Doctoral theses at NTNU, 2022:248

Jørgen Holme Qvist

Effects of hyperfine and spin-orbit interaction in multi-spin qubits

Doctoral thesis

NTNU
Norwegian University of Science and Technology
Thesis for the Degree of
Philosophiae Doctor
Faculty of Natural Sciences
Department of Physics

NTNU
Norwegian University of
Science and Technology

Jørgen Holme Qvist

Effects of hyperfine and spin-orbit interaction in multi-spin qubits

Thesis for the Degree of Philosophiae Doctor

Trondheim, August 2022

Norwegian University of Science and Technology
Faculty of Natural Sciences
Department of Physics

NTNU
Norwegian University of
Science and Technology

NTNU
Norwegian University of Science and Technology

Thesis for the Degree of Philosophiae Doctor

Faculty of Natural Sciences
Department of Physics

© Jørgen Holme Qvist

ISBN 978-82-326-6300-2 (printed ver.)
ISBN 978-82-326-6443-6 (electronic ver.)
ISSN 1503-8181 (printed ver.)
ISSN 2703-8084 (online ver.)

Doctoral theses at NTNU, 2022:248

Printed by NTNU Grafisk senter

ABSTRACT

One promising qubit implementation for the physical realization of quantum processors is spin qubits, where the qubit is encoded in the spins of electrons confined in semiconductor quantum dots. Despite considerable progress during the past decades the information stored in spin qubits is fragile and easily lost in interactions with its environment. To construct a robust spin qubit it is therefore essential to understand the details of how these interactions affect the confined electron spins, and explore approaches to mitigate the harmful interactions.

The first two papers examine potential solutions to mitigate the harmful interaction between the electron spins and the spinful nuclei in III-V semiconductors. The first paper proposes an implementation of a singlet-only qubit in a triple quantum dot with a highly tunable qubit splitting and superior coherence properties due to its singlet-only nature. The second paper shows how the harmful interaction can be quenched by applying a DC electric current through a multi-electron spin qubit tuned to the Pauli spin blockade regime, where an interplay between the hyperfine interaction and the spin dynamics effectively suppresses the harmful nuclear field gradients in the qubit.

The third paper investigates the manifestation of the anisotropic effective mass and effective g-tensor of heavy holes in two-dimensional hole gases and lateral quantum dots in group-IV semiconductors. We present a general expression for the anisotropic g-tensor, and present a straightforward way to calculate corrections to this g-tensor for localized holes due to various types of spin–orbit interaction.

The final paper develops a detailed connection between the leakage current of a double quantum dot tuned to the Pauli spin blockade regime and the underlying spin–orbit interaction in the system. We present a general analytic expression for the leakage current, allowing us to connect experimentally observable features to both the magnitude and orientation of the effective spin–orbit interaction acting on the moving carriers.

PREFACE

This thesis is submitted in partial fulfillment of the requirements for the degree philosophiae at the Norwegian University of Science and Technology (NTNU), Trondheim, Norway. The research presented herein was conducted as part of a four-year graduate programme in physics, including 30 ECTS credits of coursework and one year of undergraduate teaching duties. The research was supervised by Jeroen Danon, co-supervised by Asle Sudbø, and funded by the Research Council of Norway under FRINATEK grant no. 274853 "The way forward for exchange-only multi-spin qubits in semiconductor quantum dots".

The thesis is written to supplement the four enclosed research papers [1–4], which are the core of the thesis. The first three Chapters 1-3 are written as general as possible, giving an introduction to the relevant spin qubit systems. The later chapters 4-7 go into more detail on certain topics, and feature the main findings of the enclosed papers.

ACKNOWLEDGEMENTS

First of all, I would like to thank my supervisor Jeroen for your excellent guidance, for many interesting research projects, and for always being available for my questions. I have learned a lot from you, and your detailed feedback has always been deeply appreciated.

I would also like to thank Arnau for all your help during my first years, working with you was a true joy.

Thank you also to Jens and the rest of CMT for all the good help and exciting discussions, and to everyone at QDev for letting me join your weekly meetings. Seeing how quantum devices work in reality has been very interesting and motivating.

Thank you to everyone at QuSpin for four fantastic years. Despite the COVID-19 pandemic, the past four years have been truly enjoyable, much thanks to the wonderful people at QuSpin.

Finally, I want to thank Ingvild for all your patience and support, for many fantastic trips, and for keeping me company during the lockdowns of the COVID-19 pandemic.

CONTENTS

Publications ix

1 INTRODUCTION 1
  - 1.1 The quantum computer 1
  - 1.2 Qubits 2
  - 1.3 Spin qubits 3

2 MULTI-ELECTRON SPIN QUBITS 7
  - 2.1 The quantum dot 7
    - 2.1.1 Two-dimensional electron gases 7
    - 2.1.2 Lateral quantum dots 9
  - 2.2 Multi quantum dot devices 11
    - 2.2.1 The exchange interaction 11
    - 2.2.2 The Zeeman interaction 12
  - 2.3 Singlet-triplet qubit 13
  - 2.4 Exchange-only qubit 15
  - 2.5 Interactions of localized spins with its environment 19
    - 2.5.1 Decoherence 19
    - 2.5.2 Spin–orbit interaction 20
    - 2.5.3 Hyperfine interaction 22

3 TRANSPORT IN QUANTUM DOT SYSTEMS 25
  - 3.1 Dissipation and decay rates 25
    - 3.1.1 Single quantum dot and lead 26
  - 3.2 The Lindblad master equation 29
  - 3.3 Coulomb blockade 30
  - 3.4 Pauli spin blockade 32

4 PAULI SPIN BLOCKADE AND SPIN–ORBIT INTERACTION 35
  - 4.1 Leakage current 35
    - 4.1.1 Stopping points 38
  - 4.2 Characterizing spin–orbit coupling 39

5 MITIGATING NUCLEAR NOISE IN GAAS-BASED QUBITS 43
  - 5.1 Transport-induced suppression of nuclear field fluctuations 43
    - 5.1.1 Singlet-triplet qubit 44
    - 5.1.2 Exchange-only qubit 50
  - 5.2 Highly tunable triple dot singlet-only qubit 54
    - 5.2.1 Multi-electron quantum dots 55
    - 5.2.2 The qubit 57
    - 5.2.3 Qubit manipulation and decoherence 60

6 GROUP-IV SEMICONDUCTORS AND VALENCE BAND HOLES 63
  6.1 Bulk semiconductors and $\mathrm{k} \cdot \mathrm{p}$ theory 64
  6.2 Confined conduction band electrons and valley states 66
    6.2.1 Direct-gap semiconductors 67
    6.2.2 Indirect-gap semiconductors 69
  6.3 Confined valence band holes 70
    6.3.1 The Luttinger Hamiltonian 71
    6.3.2 Strain and the Bir-Pikus Hamiltonian 73
    6.3.3 Two-dimensional hole gases 74
    6.3.4 Quantum dots 77
7 ANISOTROPIC PROPERTIES OF CONFINED SEMICONDUCTOR HOLES 81
  7.1 Heavy-hole Zeeman effect in 2DHGs 81
    7.1.1 Spherical approximation, $\delta = 0$ 82
    7.1.2 Anisotropic Hamiltonian, $\delta \neq 0$ 83
  7.2 g-tensor corrections in quantum dots 85
  7.3 Leakage current 87
A $\mathrm{k} \cdot \mathrm{p}$ THEORY 91
B THE ROTATED LUTTINGER HAMILTONIAN 93
  B.1 Second-rank tensor operators 93
  B.2 Products of tensor operators 94
  B.3 The rotated Luttinger Hamiltonian 96
  B.4 The Bir-Pikus Hamiltonian 98
Bibliography 99
Enclosed papers 109

PUBLICATIONS

I **A. Sala*, J. H. Qvist* and J. Danon.**

Highly tunable exchange-only singlet-only qubit in a GaAs triple quantum dot.

Physical Review Research **2**, 012062 (2020).

II **J. H. Qvist and J. Danon.**

Transport-induced suppression of nuclear field fluctuations in multi-quantum-dot systems.

Physical review B **101**, 165308 (2020).

III **J. H. Qvist and J. Danon.**

Anisotropic g-tensors in hole quantum dots: The role of the transverse confinement direction.

Physical review B **105**, 075303 (2022).

IV **J. H. Qvist and J. Danon.**

Probing details of spin–orbit coupling through Pauli spin blockade.

arXiv:2204.12546 (2022).

---

* Both authors contributed equally.

1

INTRODUCTION

1.1 THE QUANTUM COMPUTER

The exponential progress of microelectronics during the past decades [5] has enabled radical advances in derivative technologies that make use of the large amount of now available computing power. Every year microprocessors are getting increasingly better and more powerful. However, despite this remarkable progress, there are still some problems that remain computationally hard or unsolvable, even for a supercomputer with millions of cores. The textbook example of a problem that is computationally hard to solve is factorizing the product of two prime numbers. Because the computational time scales exponentially with the number of digits [6], factorizing the product of two large prime numbers takes a very long time, and is therefore an essential part of some important cryptographic algorithms [7]. Another problem that computers are not able to tackle efficiently is simulating quantum mechanical systems, which could be of great use for drug and material development [8, 9], but is computationally expensive due to its exponential scaling with the number of particles [8].

A potential solution to some of these computationally challenging problems is the quantum computer. A quantum computer is not superior to classical computers in performing arbitrary tasks, but by exploiting quantum mechanical features such as superposition and entanglement, the quantum computer can vastly outperform a classical computer in certain tasks [6, 10–15]. Because a quantum computer operates according to the laws of quantum mechanics, they appear to be an effective tool for simulating quantum mechanical systems [8, 13, 16]. Furthermore, there are some specialized algorithms that can leverage the quantum mechanical properties of a quantum computer. Examples of such algorithms are Grover's algorithm [6, 17, 18] for efficient search in unsorted databases, and Shor's algorithm [6, 12, 19] for effectively factorizing the product of two large prime numbers.

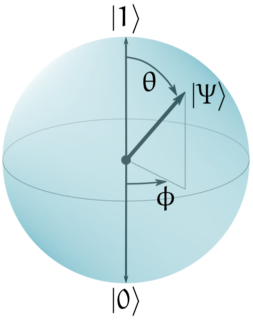

Figure 1.1: Illustration of the Bloch sphere used to represent qubit states. Any qubit state $|\Psi\rangle$ can be represented as a point on the sphere in terms of the polar angle θ and azimuthal angle ϕ of the Bloch sphere.

1.2 QUBITS

Like the classical bit is the building block of a classical computer, the quantum bit (qubit) is the fundamental building block of a quantum computer. In contrast to the classical bit, which can only take a value of either 0 or 1, the qubit is realized in a quantum mechanical two-level system, and can thus be in any superposition of these two states $|\Psi\rangle = \alpha\,|0\rangle + \beta\,|1\rangle$ [6]. A common way of visualizing the qubit is by using the Bloch sphere, as depicted in Fig. 1.1. The surface of the Bloch sphere consists of every possible qubit state, and one particular qubit state can conveniently be expressed in terms of the spherical angles of the Bloch sphere,

$$|\Psi\rangle = \cos\frac{\theta}{2}\,|0\rangle + e^{i\phi}\sin\frac{\theta}{2}\,|1\rangle\,, \tag{1.1}$$

where θ and ϕ are the polar and azimuthal angles, respectively. The poles of the Bloch sphere then define the two basis states $|0\rangle$ and $|1\rangle$, and any superposition of the two basis states can be obtained given control over two linearly-independent axes of rotation on the Bloch sphere [6].

To achieve a fully functioning quantum computer, the underlying qubit has to satisfy a given set of requirements. First stated by DiVincenzo [20], these requirements are that the qubit: (i) is encoded in a scalable two-level system, (ii) can be initiated in a fiducial state, (iii) has coherence times much longer than the operation times of the logic gates, (iv) has a universal set of logic gates from which any qubit operation can be expressed, and (v) can be readout. At present, there are several proposed physical realizations for qubits that partly satisfy the five DiVincenzo requirements.

One prominent qubit implementation at the current date is based on superconducting qubits, where the qubit is encoded in the two lowest-energy states of an anharmonic oscillator constructed from superconducting circuit elements [21, 22]. In addition to being vastly researched in academia, superconducting qubits have also gained a lot of interest from industry during the past decades, with several major technology companies developing their own superconducting quantum computers. The most noteworthy companies are Google, which claimed they demonstrated quantum supremacy for a very specific task on their 53 qubit device in 2019 [23], and IBM which provides public access to quantum computers with up to 127 qubits for testing and development of quantum algorithms [24–26]. However, despite the recent progress and interest in superconducting qubits, they suffer from being hard to scale due to their large size $\sim 300 - 500$ µm [27]. Given that a fully working quantum computer likely requires at least one million qubits [28], it will still be some time until we can experience a fully working superconducting quantum computer.

Another popular qubit implementation is spin qubits [29–33], where the qubit is encoded in the spin of electrons confined in small ~ 100 nm semiconductor structures [33]. Despite not being as developed as superconducting qubits, spin qubits could leverage the advantage of already developed semiconductor production technology and equipment [34, 35]. These commercial mass chip-manufacturing techniques, combined with the small qubit size, can enable rapid scaling and commercialization of spin qubits, superior to that of superconducting spin qubits. However, despite the promising scalability of spin qubits, there are still some challenges remaining to be solved.

1.3 SPIN QUBITS

The electron spin degree of freedom naturally provides a two-level system consisting of spin up and spin down. Originally proposed over two decades ago [36], this two-level system can be used to host a qubit by trapping a single electron in a zero-dimensional semiconductor structure called a quantum dot. Despite showing rapid experimental success with initialization, manipulation and readout [37–39], two main challenges limited further progress: (i) Manipulation of a single spin requires highly located magnetic fields, which are hard to realize in practice, and (ii) the spinful nuclei of the semiconductor couple to the electron spin as a random effective magnetic field, causing decoherence [40, 41] and relaxation [42] of the qubit.

One proposal to overcome the requirement of highly located magnetic fields was to encode the qubit in a multi-electron spin state, allowing for qubit control through gate-tunable exchange interactions [43]. With two electrons in a double quantum dot, a spin qubit can be defined in the unpolarized singlet-triplet subspace. This so-called singlet-triplet (ST) qubit enables electric control of rotations along one axis of the Bloch sphere [38, 44], partly solving the requirement for localized magnetic fields. To obtain full electric control over rotations along two independent axes of the Bloch sphere another electron and quantum dot was added. The resulting exchange-only (XO) qubit is hosted in two three-electron spin states in a triple quantum dot and can be fully controlled through exchange interactions [45–47]. Despite solving the requirement for localized magnetic fields, it came at the cost of increased sensitivity to electric noise both from the gate voltages and from environmental charge fluctuations. Luckily, recent work has shown that the sensitivity to electric noise can be greatly reduced by symmetric operation of the qubit [48–50].

High-quality III-V semiconductors, and especially GaAs, have propelled the spin qubit field forward in the past decades, being the go-to materials for hosting spin qubits due to their simple fabrication and favorable electronic properties [51]. Unfortunately, these semiconductors also have a large number of spinful nuclei, making nuclear noise a significant challenge [52–54]. Approaches to mitigate the harmful nuclear noise in GaAs-based devices have therefore been extensively explored, and have been important for the progress of the spin qubit field.

An alternative solution to the nuclear noise challenge is to host spin qubits in group-IV semiconductors such as Si and Ge. These semiconductors have only a small fraction of spinful nuclei and can be further purified to nearly nuclear-spin-free [55–59], removing the nuclear noise altogether. However, in contrast to GaAs which has a direct band-gap, Ge and Si have an indirect band-gap. When confining electrons in low-dimensional semiconductor structures this indirect band-gap gives rise to an extra valley degree of freedom [33, 60], which is both hard to control and provides an additional channel for qubit dephasing and leakage out of the qubit subspace [60, 61].

Lately, there has been substantial progress with Si- and Ge-based spin qubits that use the spin of valence band holes instead of the electron spin [62–70]. These holes provide the same protection against nuclear noise as the electrons, but without the complicating valley degrees of freedom. Because the valence band of semiconductors is of p-type [71], the corresponding hole states have a total sixfold angular momentum degree of freedom. This can lead to highly anisotropic dynamics, which again gives rise to several interesting anisotropic properties such as a highly anisotropic and tunable g-tensor [3, 72–82], and a strong effective spin-orbit coupling that allows for fast qubit operation [83–89].

In this thesis, we explore possible ways forward for spin qubits. The first two chapters give a general introduction to spin qubits and their properties, focusing on GaAs for simplicity to make the presentation as pedagogical as possible. We begin in Chapter 2 by giving a general presentation of relevant models used to describe electrons confined in quantum dots, the relevant qubits, and interactions experienced by the localized spins. In Chapter 3 we introduce interactions between the confined electrons and the leads surrounding the quantum dots, enabling dissipation and transport through quantum dots. This allows us to take a deeper look at Pauli spin blockade in double quantum dots in Chapter 4, where we focus on how spin–orbit interaction affects the leakage current. We then present two possible solutions to the nuclear noise challenge in GaAs-based devices in Chapter 5. In Chapter 6 we go beyond GaAs and look into models for describing the dynamics of group-IV semiconductors, with a special focus on valence band holes, which we then use to investigate some anisotropic properties of valence band holes in Chapter 7.

2

MULTI-ELECTRON SPIN QUBITS

Multi-electron spin qubits hosted in semiconductor quantum dots form an attractive qubit implementation that can be controlled through exchange interactions and promises easily scalable quantum processors [30, 34, 60]. In this chapter, we present a general introduction to spin qubits, where we focus on GaAs-based devices for simplicity. We begin, in Sec. 2.1, by introducing the building block of spin qubits, namely the quantum dot. In Sec. 2.2 we present the relevant models for describing devices consisting of multiple quantum dots. The two most common multi-electron spin qubits, i.e. the singlet-triplet qubit and the exchange-only qubit, are then presented in Secs. 2.3 and 2.4, respectively. Finally, in Sec. 2.5 we investigate some common interactions between the localized spins of the qubit and their environment.

2.1 THE QUANTUM DOT

A quantum dot is an approximately zero-dimensional semiconductor structure in which electrons can be confined, and thus provides an excellent platform for creating quantum devices [33]. One common quantum dot implementation is nanowires, which are one-dimensional semiconductor structures that can be further confined into quantum dots using local gates [60]. However, the most common technique for implementing quantum dots in semiconductors, and the one we will focus on in this section, are lateral quantum dots [47], where a two-dimensional electron gas is further confined by electrostatic potentials provided by metallic gates placed above/below the semiconductor heterostructure.

2.1.1 *Two-dimensional electron gases*

A common platform for creating low-dimensional semiconductor structures, such as quantum dots, is the two-dimensional electron gas (2DEG). In a 2DEG electrons are confined along one spatial direction while being free to move in

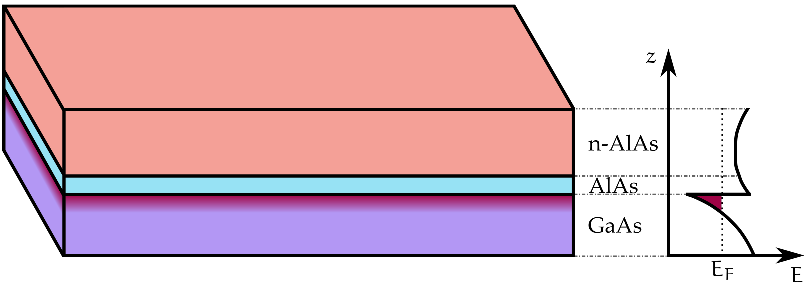

Figure 2.1: Illustration of a 2DEG in GaAs. The 2DEG is created on the GaAs side of the GaAS/AlAs interface in the region where the conduction band, as a function of the stacking direction z, drops below the Fermi level. The electrons are then confined along the stacking direction while moving freely along the interface.

the other two directions. Typically, a 2DEG is created by stacking layers of semiconductors, e.g. layers of GaAs and AlAs or Si and SiGe, where advances in semiconductor fabrication allow for atomically precise layer interfaces. By stacking semiconductors with different band structures one can create a structure where the conduction band crosses the Fermi level at one of the interfaces. This creates a quantum well (QW) along the stacking direction that confines the electrons in a ~ 10 nm thick sheet, accumulating electrons along the interface in a so-called two-dimensional electron gas. In Fig. 2.1 we illustrate how a 2DEG is created in a GaAs device by stacking layers of GaAs and AlAs, where the electrons are confined on the GaAs side of the interface, in the region where the conduction band drops below the Fermi level.

An effective Hamiltonian describing the confined electrons can be obtained by integrating out the direction of confinement, which we label z, from the bulk Hamiltonian. In most semiconductor structures, the global minimum of the conduction band is usually very parabolic and simple[1], and the dynamics of the electrons can be described fairly accurately by a simple effective-mass Hamiltonian. Integrating out the direction of confinement then yields an effective in-plane Hamiltonian,

$$H_c = E_{z,0} + \frac{\hbar^2 k_\parallel^2}{2m^*}, \tag{2.1}$$

where $k_\parallel^2 = k_x^2 + k_y^2$, and m^* is the effective mass of the electrons. Here, the first term parameterizes the confinement energy $E_{z,0}$ of the 2DEG, which

---

[1] In some semiconductors, so-called indirect-gap semiconductors, the conduction band minimum is not centered around the Γ-point $k = 0$, giving rise to additional degrees of freedom. The effects of these additional degrees of freedom are discussed in more detail in Sec. 6.2.2.

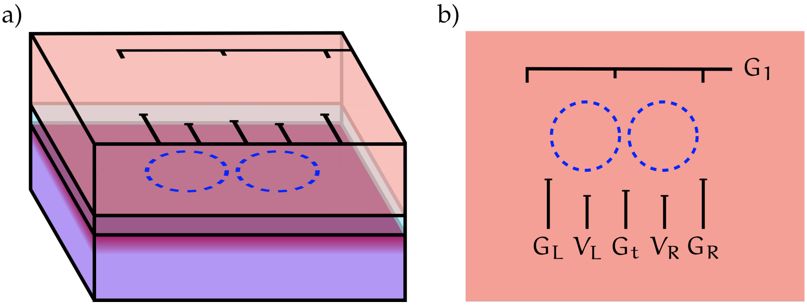

Figure 2.2: A double quantum dot is created by further confining a two-dimensional electron/hole gas using metallic gates. (a) Electrostatic gates are placed on top of the heterostructure such that the electrostatic potential creates two small islands in the two-dimensional gas where a small number of electrons/holes are confined. (b) Illustration of the gates used in (a) shown from above. Tuning the different gate voltages used to confine the quantum dots allows for control over the electrostatic potential on the dots ($V_{L(R)}$), as well as the tunneling barrier between the two dots (G_t) and the dots and leads ($G_{L(R)}$).

for an infinite-well-type confinement of width d reads $E_{z,0} = \hbar^2\pi^2/2m^*d^2$, whereas the second term governs the isotropic in-plane dynamics of the electrons confined in the electron gas.

2.1.2 *Lateral quantum dots*

A semiconductor quantum dot is a small island, often formed inside a two-dimensional electron gas, where a few electrons are trapped. The most common implementation of quantum dots is lateral quantum dots, which are created by further confining a 2DEG using electrostatic potentials. The potentials used to confine the 2DEG are usually provided by metallic gates placed on top of (and/or underneath) the heterostructure. The electrostatic potentials deplete[2] the 2DEG creating a small two-dimensional island where electrons can be trapped. An illustration of how a quantum dot can be made from a 2DEG is shown in Fig. 2.2(a).

The same gates that are used to define the quantum dot also provide tunable control over the potential landscape on and around the quantum dots. This allows for electric control over several quantum dot properties such as electrochemical potential and tunneling barriers, making the quantum dot a perfect host for creating spin-based qubits. We illustrate this control by using the example of Fig. 2.2(b), where we illustrate a possible gate configuration that can be used to confine a double quantum dot. Here, the gates labeled G_i create depletion zones in the 2DEG, giving rise to two quantum dots. By tuning the gate between the two dots G_t, one can control the tunneling barrier between the dots. Similarly, by tuning the two outer gates $G_{L(R)}$, one can control the tunneling barrier between the left(right) dot and the left(right) lead. Finally, the gates $V_{L(R)}$ can be used to control the electrochemical potential on the two dots.

---

[2] In some heterostructures, like undoped Si/SiGe, the 2DEG is typically empty in absence of gate voltages [47]. In such systems, the gate voltages are used to accumulate electrons in the 2DEG, not deplete electrons from the 2DEG.

To describe the electrons confined in a quantum dot we start with the 2DEG Hamiltonian in Eq. (2.1). By adding a circularly symmetric parabolic confinement potential $V(\mathbf{r}) = \lambda(x^2 + y^2)$, the in-plane component of the effective mass Hamiltonian reads

$$H_0 = \frac{\mathbf{p}^2}{2m^*} + \frac{m^*}{2}\omega_0^2(x^2 + y^2), \tag{2.2}$$

where $\omega_0 = \sqrt{2\lambda/m^*}$ defines the strength of the in-plane confinement, such that $\sigma_0 = \sqrt{\hbar/(m^*\omega_0)}$ gives the effective radius of the dot in the absence of a magnetic field, and $\mathbf{p} = -i\hbar\partial_{\mathbf{r}} + e\mathbf{A}(\mathbf{r})$ is the canonical momentum, with $\mathbf{A}(\mathbf{r}) = B_z(-y/2, x/2, 0)$ being the vector potential for which we use the circular gauge and neglect in-plane components of the magnetic field, assuming strong confinement along z.

The Hamiltonian in Eq. (2.2) describes an isotropic two-dimensional harmonic oscillator in the presence of a magnetic field. This Hamiltonian can be diagonalized in many different ways, straightforwardly resulting in a Hamiltonian that can be written in terms of two independent harmonic oscillators,

$$H_0 = \hbar\omega_+\left(n_+ + \frac{1}{2}\right) + \hbar\omega_-\left(n_- + \frac{1}{2}\right), \tag{2.3}$$

with $n_i = a_i^\dagger a_i$, where $a_\pm^{(\dagger)}$ are bosonic creation and annihilation operators, and the oscillator frequencies are defined through

$$\omega_\pm = \sqrt{\omega_0^2 + 2\omega_c^2 \pm 2\omega_c\sqrt{\omega_0^2 + \omega_c^2}}, \tag{2.4}$$

with the cyclotron frequency $\omega_c = eB_z/4m^*$. From the Hamiltonian in Eq. (2.3) we find that the ground state energy of an electron confined in a quantum dot is $E_0 = \hbar(\omega_+ + \omega_-)/2$, with the two closest excited states being separated from the ground state by an energy of $\omega_\pm$, respectively.

2.2 MULTI QUANTUM DOT DEVICES

Above we showed that the confined electrons in a circular quantum dot can be described in terms of two harmonic oscillators, where the oscillator frequencies $\omega_{\pm}$ are highly dependent on the size of the quantum dot. Because quantum dots are usually small, the excitation energies $\omega_{\pm}$ between the ground and excited states (typically ~ meV) are much larger than other relevant energy scales. For quantum dots in the low-electron regime hosting two electrons or less, which is most relevant for this thesis, it is therefore often a good approximation to disregard excited states and only consider the ground state[3]. The Pauli-exclusion principle then dictates that the only way two electrons can occupy the quantum dot is if their spins form a singlet. Furthermore, we also assume that all quantum dots in a device have the same size so that we can subtract the ground state energy $E_g = \hbar(\omega_+ + \omega_-)/2$, making the quantum dots effective single-levels located at zero energy.

2.2.1 *The exchange interaction*

So far we have only considered the internal dynamics of electrons confined in a quantum dot. To model spin qubits we will now have to consider systems of tunnel-coupled quantum dots, where we also have to take into account how the electrostatic potentials from the gates used to create the quantum dots affect the confined electrons. Assuming that all quantum dots in the qubit have the same ground-state energy, and thus also the same size, we can model the system as a series of tunnel-coupled single-levels (lattice sites) using a Hubbard-like Hamiltonian

$$H_{\text{Hub}} = \sum_i \left[\frac{U}{2} n_i(n_i - 1) - V_i n_i\right] + \sum_{\langle i,j\rangle} \frac{U_c}{2} n_i n_j + \sum_{\langle i,j\rangle,\eta} \frac{t_{ij}}{\sqrt{2}} c^{\dagger}_{i,\eta} c_{j,\eta}, \quad (2.5)$$

where the operator $n_i = \sum_\eta c^{\dagger}_{i,\eta} c_{i,\eta}$ accounts for the number of electrons on dot i, with $c^{\dagger}_{i,\eta}(c_{i,\eta})$ being the creation(annihilation) operator for an electron with spin-projection $\eta \in \{\uparrow, \downarrow\}$ on dot i. Here, V_i describes the electrochemical potential on dot i and t_{ij} governs the tunneling coupling between dots i and j, both of which can be tuned by changing the electric fields created by the electrostatic gates. Further, U and U_c account phenomenologically for the Coulomb potential between two electrons on the same dot and neighboring dots, respectively, where U_c is typically smaller than the on-site interaction U.

---

[3] In Sec. 5.2.1 we will consider multi-electron quantum dots where we also take into account higher orbital states.

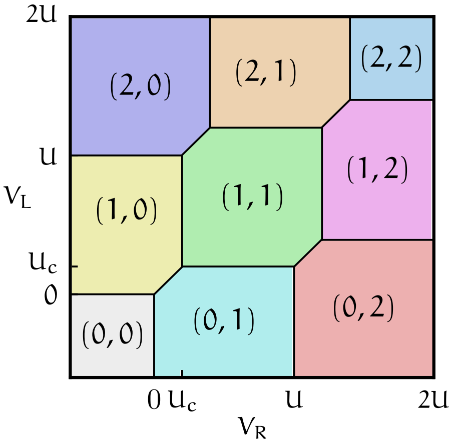

Figure 2.3: The charge stability diagram of a double quantum dot, obtained by plotting the ground state charge configuration of the electrostatic part of the Hubbard model as given in Eq. (2.5) with $U_c = U/5$.

The number of electrons in the quantum dots can be tuned by changing the voltage applied to the electrostatic gates. In general, there are 3^n available charge configurations in a system consisting of n quantum dots that contain 0, 1 or 2 electrons. Because the number of configurations grows exponentially with n, we will consider the simplest case of $n = 2$ quantum dots as an example, where there are $3^2 = 9$ different charge configurations, which we label (n_L, n_R). To see how the occupation of the double quantum dot depends on the gate voltages it is useful to investigate the electrostatic properties of the Hubbard model (i.e. we set $t_{ij} = 0$). We can do this by plotting the charge configuration of the ground state as a function of the electrostatic potentials $V_{L,R}$, which gives the so-called charge stability diagram as shown in Fig. 2.3, where we used the parameters $U_c = U/5$.

2.2.2 *The Zeeman interaction*

As we showed above, the gate voltages can be tuned to change the charge configuration of a quantum dot system. However, different spin states with the same charge configuration can not be separated using the electrostatic gates alone. An applied magnetic field is therefore often used to separate states with different spin-projections. The coupling between the magnetic field and the spin of the electron can be described using the Zeeman Hamiltonian[4],

$$H_Z = \frac{1}{2} g \mu_B \sum_i B_i^z \left(n_{i,\uparrow} - n_{i,\downarrow} \right), \tag{2.6}$$

where g is the effective g-factor, μ_B is the Bohr magneton, and B_i is the magnetic field on dot i which we assume to be pointing along the z-coordinate. Throughout the thesis we will see that the Zeeman interaction between a magnetic field and the spin of an electron is essential for both defining the qubit states, as well as for many of the qubits' properties.

2.3 SINGLET-TRIPLET QUBIT

The first qubit we consider is the singlet-triplet (ST) qubit, which is hosted by two electrons residing in a double quantum dot as shown in Fig. 2.4(a). By using the gate voltages, the double quantum dot is tuned close to the transition between the $(1,1)$ and $(0,2)$ charge configurations, see the red line in Fig. 2.4(b). Since we are only considering the low-energy part of the spectrum, i.e. only a single level on each dot, the two charge regions $(1,1)$ and $(0,2)$ consist of a total of five states. In the $(1,1)$ charge configuration all four states are available,

$$|T^+\rangle = |\uparrow,\uparrow\rangle, \tag{2.7}$$

$$|T^0\rangle = \frac{1}{\sqrt{2}} \left(|\uparrow,\downarrow\rangle + |\downarrow,\uparrow\rangle \right), \tag{2.8}$$

$$|T^-\rangle = |\downarrow,\downarrow\rangle, \tag{2.9}$$

$$|S\rangle = \frac{1}{\sqrt{2}} \left(|\uparrow,\downarrow\rangle - |\downarrow,\uparrow\rangle \right), \tag{2.10}$$

whereas in the $(0,2)$ charge configuration the Pauli exclusion principle dictates that only the doubly-occupied singlet is accessible,

$$|S_{02}\rangle = |0,\uparrow\downarrow\rangle. \tag{2.11}$$

---

[4] The Zeeman Hamiltonian describing valence band holes may be highly anisotropic, depending on details of the confinement of the quantum dots. An anisotropic Zeeman Hamiltonian should therefore be used to describe the coupling between a magnetic field and the spin of valence band holes, see Chapter 7 for more details.

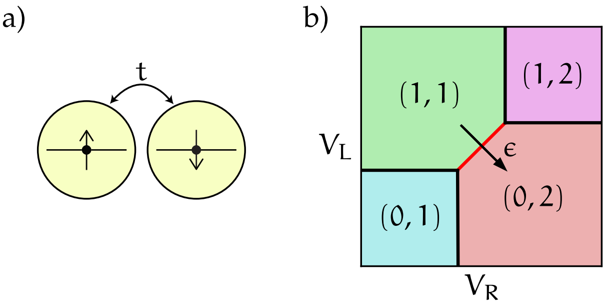

Figure 2.4: (a) Sketch of a tunnel coupled double quantum dot hosting two electrons. (b) Charge stability diagram of the double dot in the region close to the $(1,1)$-$(0,2)$ transition, where the singlet-triplet qubit is defined.

To describe this five-level subspace we use the Hubbard and Zeeman models described above. Writing the total Hamiltonian $H = H_{\text{Hub}} + H_Z$ in the basis of the five relevant states we get

$$\begin{aligned} H = -\epsilon \left|S_{02}\right\rangle \left\langle S_{02}\right| &+ t\big(\left|S\right\rangle \left\langle S_{02}\right| + \left|S_{02}\right\rangle \left\langle S\right|\big) \\ &+ \frac{1}{2} g\mu_B \left(B_L^z + B_R^z\right) \big(\left|T^+\right\rangle \left\langle T^+\right| - \left|T^-\right\rangle \left\langle T^-\right|\big) \\ &+ \frac{1}{2} g\mu_B \left(B_L^z - B_R^z\right) \big(\left|S\right\rangle \left\langle T^0\right| + \left|T^0\right\rangle \left\langle S\right|\big), \end{aligned} \tag{2.12}$$

where we have subtracted a constant energy of $V_L + V_R + U_c$, and $\epsilon = V_R - V_L$ is the detuning of the electrostatic potential between the two dots, which we have shifted by $U - U_c$ for a simpler notation. Here, the first term accounts for the potential difference between the two dots, which can be tuned via the electrostatic gates. The second term governs the tunneling between the two dots, and the third term describes the splitting of the polarized spin states due to the external magnetic field. Finally, the last term shows how the two unpolarized states are mixed by a magnetic field gradient $\Delta B^z = B_L^z - B_R^z$. In Fig. 2.5 we plot a typical spectrum of H as a function of ϵ, where we have used $\Delta B^z = 0$, $t = 0.6|g\mu_B B^z|$ and $g < 0$.

The ST qubit is defined in the two two-particle spin states with spin projection $S_z = 0$. Close to the transition between the two charge configurations (around $\epsilon = 0$) the tunnel coupling t between the two singlet states makes them hybridize. The effective singlet states can be written as $\left|S_1\right\rangle = \cos\frac{\theta}{2}\left|S_{02}\right\rangle + \sin\frac{\theta}{2}\left|S\right\rangle$ and $\left|S_2\right\rangle = \cos\frac{\theta}{2}\left|S\right\rangle - \sin\frac{\theta}{2}\left|S_{02}\right\rangle$, where $\tan\theta = 2t/\epsilon$. The two qubit states of the ST qubit are shown as stippled lines in Fig. 2.5, and consist of the unpolarized triplet $\left|1\right\rangle = \left|T^0\right\rangle$ and the lower of the two hybridized singlet states $\left|0\right\rangle = \left|S_1\right\rangle$. Projecting the Hamiltonian

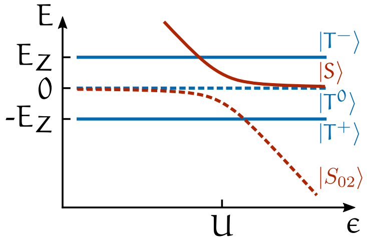

Figure 2.5: Typical energy spectrum of the five relevant states of the double quantum dot plotted as a function of the detuning between the two dots ϵ. The red(blue) lines correspond to spin singlet(triplet) states and the stippled lines indicate the two qubit states.

in Eq. (2.12) to the subspace of the two qubit states we obtain the qubit Hamiltonian of the ST qubit

$$H_{qb} = \frac{1}{2}\omega_q \sigma^z + \frac{1}{2} g\mu_B \Delta B^z \sin\frac{\theta}{2}\sigma^x, \tag{2.13}$$

where the qubit splitting $\omega_q = \epsilon/2 + \sqrt{(\epsilon/2)^2 + t^2}$ is determined by the detuning of the two singlet states and the exchange interaction. Because the qubit splitting ω_q can be tuned via the gates $V_{L,R}$, the ST qubit provides electric control over the z-axis of the Bloch sphere. Rotation over the x-axis, however, requires control over the localized magnetic field gradient ΔB^z between the two dots, which is hard to do in practice. Because the ST qubit only provides electric control over one of the axes of the Bloch sphere, the exchange-only qubit is often preferred as it provides full electric control over the Bloch sphere, despite having a more complicated design.

2.4 EXCHANGE-ONLY QUBIT

The exchange-only (XO) qubit is usually hosted in a linear triple quantum dot, containing one electron on each dot, as illustrated in Fig. 2.6(a). Unlike the ST qubit, which had to be defined close to the transition between the $(1,1)$-$(0,2)$ charge configurations, the XO qubit can be defined at several regions of the charge stability diagram. The most common regions to operate the XO qubit are the resonant-exchange (RX) regime which provides fast operation times and the sweet spot (SS) which offers less sensitivity to charge noise, both of which are marked in the charge stability diagram in Fig. 2.6(b). For simplicity we will here focus on the lower RX regime close to the $(1,1,1)$-$(2,0,1)$-$(1,0,2)$ triple point, where the central electron can be delocalized between all three dots, yielding strong exchange interactions.

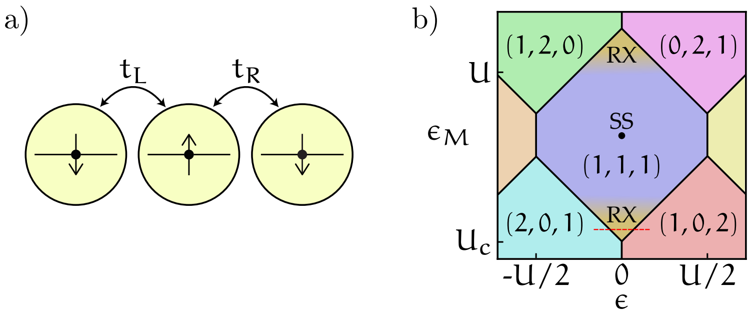

Figure 2.6: (a) Sketch of a tunnel coupled triple quantum dot hosting three electrons. (b) Charge stability diagram of the triple dot in the region where the exchange-only qubit is defined, where we have marked the resonant-exchange (RX) regimes and the sweet spot (SS).

Tuning the triple dot to the $(1,1,1)$ regime there are a total of $2^3 = 8$ available states, consisting of one spin quadruplet $|Q\rangle$ and two spin doublets $|D_{1,2}\rangle$,

$$|Q^{+3/2}\rangle = |\uparrow,\uparrow,\uparrow\rangle\,, \tag{2.14}$$

$$|Q^{+1/2}\rangle = \frac{1}{\sqrt{3}}\big(|\uparrow,\uparrow,\downarrow\rangle + |\downarrow,\uparrow,\uparrow\rangle + |\uparrow,\downarrow,\uparrow\rangle\big), \tag{2.15}$$

$$|Q^{-1/2}\rangle = \frac{1}{\sqrt{3}}\big(|\downarrow,\downarrow,\uparrow\rangle + |\uparrow,\downarrow,\downarrow\rangle + |\downarrow,\uparrow,\downarrow\rangle\big), \tag{2.16}$$

$$|Q^{-3/2}\rangle = |\downarrow,\downarrow,\downarrow\rangle\,, \tag{2.17}$$

$$|D_2^{+}\rangle = \frac{1}{\sqrt{2}}\big(|\uparrow,\uparrow,\downarrow\rangle - |\downarrow,\uparrow,\uparrow\rangle\big), \tag{2.18}$$

$$|D_2^{-}\rangle = \frac{1}{\sqrt{2}}\big(|\downarrow,\downarrow,\uparrow\rangle - |\uparrow,\downarrow,\downarrow\rangle\big), \tag{2.19}$$

$$|D_1^{+}\rangle = \frac{1}{\sqrt{6}}\big(|\uparrow,\uparrow,\downarrow\rangle + |\downarrow,\uparrow,\uparrow\rangle - 2\,|\uparrow,\downarrow,\uparrow\rangle\big), \tag{2.20}$$

$$|D_1^{-}\rangle = \frac{1}{\sqrt{6}}\big(|\downarrow,\downarrow,\uparrow\rangle + |\uparrow,\downarrow,\downarrow\rangle - 2\,|\downarrow,\uparrow,\downarrow\rangle\big). \tag{2.21}$$

where we have used the simplified notation $|D_i^{\pm}\rangle = |D_i^{\pm 1/2}\rangle$. In the RX regime close to the $(1,1,1)$-$(2,0,1)$-$(1,0,2)$ triple point we also have to take into account the neighboring charge configurations $(2,0,1)$ and $(1,0,2)$, which are made up of the two doublets $|D_L\rangle$ and $|D_R\rangle$, respectively,

$$|D_L^+\rangle = |\uparrow\downarrow, 0, \uparrow\rangle\,, \qquad |D_R^+\rangle = |\uparrow, 0, \uparrow\downarrow\rangle\,, \tag{2.22}$$

$$|D_L^-\rangle = |\uparrow\downarrow, 0, \downarrow\rangle\,, \qquad |D_R^-\rangle = |\downarrow, 0, \uparrow\downarrow\rangle\,. \tag{2.23}$$

As for the ST qubit, we describe this 12-level system using the Hubbard and Zeeman model such that the total Hamiltonian of the triple dot reads $H = H_{\mathrm{Hub}} + H_Z$. In the basis of the twelve states defined above the contribution from the Hubbard model reads

$$\begin{aligned} H_{\mathrm{Hub}} = &\sum_{\pm} \left\{ (\epsilon_M + \epsilon)\, |D_L^{\pm}\rangle \langle D_L^{\pm}| + (\epsilon_M - \epsilon)\, |D_R^{\pm}\rangle \langle D_R^{\pm}| \right\} \\ &+ \frac{t}{2} \sum_{\pm} \pm \left\{ \sqrt{3}\, |D_1^{\pm}\rangle \left[\langle D_R^{\pm}| - \langle D_L^{\pm}| \right] + |D_2^{\pm}\rangle \left[\langle D_R^{\pm}| + \langle D_L^{\pm}| \right] \right\} + \text{h.c.}, \end{aligned} \tag{2.24}$$

where we again subtracted an energy offset of $V_L + V_C + V_R + 2U_c$, and assumed the two tunnel couplings to be equal $t = t_L = t_R$. Furthermore, $\epsilon = (V_R - V_L)/2$ and $\epsilon_M = V_C - (V_R + V_L)/2$ are the detunings[5] of the electrostatic potentials, with $V_{L,C,R}$ denoting the gate-induced potentials on the left, central, and right dot, respectively. In the same basis, we find the Zeeman Hamiltonian

$$\begin{aligned} H_Z = g\mu_B B^z \sum_{\pm} \Bigg\{ &\pm \frac{3}{2} |Q^{\pm 3/2}\rangle \langle Q^{\pm 3/2}| \pm \frac{1}{2} \Big[|Q^{\pm 1/2}\rangle \langle Q^{\pm 1/2}| \\ &+ |D_1^{\pm}\rangle \langle D_1^{\pm}| + |D_2^{\pm}\rangle \langle D_2^{\pm}| + |D_L^{\pm}\rangle \langle D_L^{\pm}| + |D_R^{\pm}\rangle \langle D_R^{\pm}| \Big] \Bigg\}, \end{aligned} \tag{2.25}$$

where we have assumed that the magnetic field is homogeneous over the three dots, i.e. no magnetic field gradients[6]. The spectrum of H is plotted in Fig. 2.7 as a function of ϵ in the RX regime, corresponding to the red stippled line in Fig. 2.6(b), where we set $t = 3|g\mu_B B^z|$ and $g < 0$.

The qubit states of the XO qubit are defined in the two doublet states having the same spin projection, $|0^{\pm}\rangle = |D_1^{\pm}\rangle$ and $|1^{\pm}\rangle = |D_2^{\pm}\rangle$. Because there are four available doublet states, two with $S_z = +1/2$ and two with $S_z = -1/2$, the qubit states can be defined in either subspace. In this text we will use $|0^+\rangle$ and $|1^+\rangle$ as qubit states, which are shown as the stippled lines in the spectrum

---

[5] Like for the ST qubit, we have here shifted the gradient ϵ_M by $2U_c - U$ for a simpler and more convenient notation.

[6] In Sec. 5.1.2 we use a more general Zeeman Hamiltonian, that also includes magnetic field gradients, to describe the XO qubit.

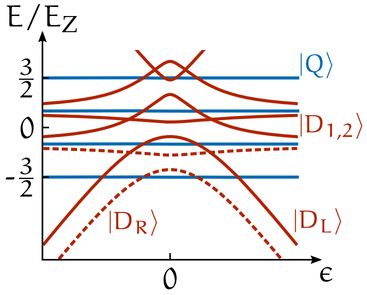

Figure 2.7: Typical energy spectrum of the triple quantum dot tuned to the RX regime plotted as a function of the detuning between the two outer dots ϵ. The red(blue) lines correspond to spin doublet(quadruplet) states and the stippled lines indicate the two qubit states.

in Fig. 2.7. To describe the interactions of the two qubit states we only have to consider the eight doublet states as there is no coupling between the two qubit states and the quadruplet. Furthermore, since the tunnel coupling t conserves spin, we can also neglect the $S_z = -1/2$ doublet states. Then, we can write an effective 4×4 Hamiltonian describing the four $S_z = +1/2$ doublet states $\{|0^+\rangle, |1^+\rangle, |D_L^+\rangle, |D_R^+\rangle\}$,

$$H_D^+ = \begin{pmatrix} 0 & 0 & -\frac{\sqrt{3}}{2}t & \frac{\sqrt{3}}{2}t \\ 0 & 0 & \frac{1}{2}t & \frac{1}{2}t \\ -\frac{\sqrt{3}}{2}t & \frac{1}{2}t & \epsilon_M + \epsilon & 0 \\ \frac{\sqrt{3}}{2}t & \frac{1}{2}t & 0 & \epsilon_M - \epsilon \end{pmatrix}. \tag{2.26}$$

From the Hamiltonian we can see how both of the qubit states hybridize with the two doublets with different charge configurations, $D_{L,R}^+$. Because the couplings between the two qubit states and $D_{L,R}^+$ are different, the exchange energies provided by the hybridization splits the two qubit states. If the tunnel coupling is not too large $t \ll \epsilon, \epsilon_M$, we can evaluate the exchange interactions perturbatively. To lowest order in t we then find an effective qubit Hamiltonian,

$$H_{qb} = \frac{1}{2}J\sigma^z - \frac{\sqrt{3}}{2}j\sigma^x, \tag{2.27}$$

with $J = (J_L + J_R)/2$ and $j = (J_L - J_R)/2$, where the exchange energies associated with virtual tunneling to the left or right dot read $J_{L,R} = t^2/(\epsilon_M \pm \epsilon)$, respectively. From the qubit Hamiltonian one can see that the XO qubit allows for full electric control of rotations around the Block sphere by tuning

J and j through ϵ and ϵ_M, which is in contrast to the ST qubit which only offered electric control over one axis.

2.5 INTERACTIONS OF LOCALIZED SPINS WITH ITS ENVIRONMENT

So far we have only described the basics of the ST and XO spin qubits using the Hubbard and Zeeman models, which is accurate if the confined electrons are only affected by electrostatic potentials and external magnetic fields. In reality, however, the confined electrons experience additional interactions that need to be considered to get an accurate description of spin qubits. Here we will consider the two most important interactions that affect spin qubits, both of which will play important roles later in the thesis. We begin by briefly explaining the concept of decoherence, focusing on the two common cases of relaxation and dephasing. Then, we investigate how the spin–orbit interaction changes the properties of the tunnel coupling between the quantum dots, allowing for spin-flip processes during a tunneling event which drastically changes the dynamics of spin qubits. Finally, we consider the hyperfine interaction between the nuclear and electronic spins, which is an important source of decoherence in spin qubits hosted in semiconductors with non-zero nuclear spin.

2.5.1 *Decoherence*

The information stored in a qubit is fragile, and is easily lost in interactions with its environment. The process of losing the stored information is often called decoherence, and can happen in many ways. To illustrate how the random noise of the environment affects a qubit we use the simple model Hamiltonian,

$$H = \frac{1}{2}\omega_q \sigma^z + \boldsymbol{\sigma} \cdot \boldsymbol{\delta}(t), \tag{2.28}$$

describing a qubit with a qubit splitting ω_q, with $\boldsymbol{\sigma}$ being the vector of Pauli spin matrices, and $\boldsymbol{\delta}(t)$ representing how the time-dependent noise of the fluctuating environment degrees of freedom couple to the qubit. In general, any random noise $\boldsymbol{\delta}(t)$ coupling to the qubit will be a source of decoherence through random rotations on the Bloch sphere.

To exemplify how qubit information is lost due to noise in the environment we here consider two common cases of decoherence, namely relaxation and depashing. If the qubit is coupled to a dissipative environment the qubit will at some point relax to its ground state, which we here assume to be $|0\rangle$, by exchanging energy to the environment via e.g. phonons. This process is called

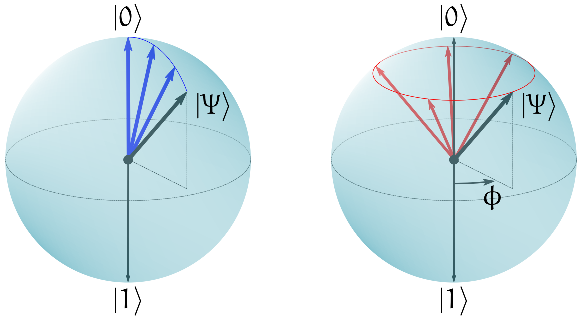

Figure 2.8: Two common cases of decoherence of a qubit. (a) Relaxation from $|\Psi\rangle$ to the ground state $|0\rangle$. (b) Dephasing, losing the phase information ϕ of $|\Psi\rangle$.

relaxation, and results in a loss of qubit information as depicted in Fig. 2.8(a). The time scale on which an arbitrary qubit state relaxes to its ground state is often denoted T_1. In the process of dephasing, on the other hand, only the phase information ϕ is lost, see Fig. 2.8(b). In contrast to relaxation, energy is conserved during dephasing. To explain the process of dephasing we consider the simple model Hamiltonian in Eq. (2.28) with noise coupling to σ^z only. The qubit state $|\Psi\rangle$ will then precess with a time-dependent and fluctuating frequency $\omega_q + 2\delta^z(t)$ around the z-axis. The randomly fluctuating frequency leads to an unpredictable offset in the phase ϕ, typically with a magnitude $\sim \delta^z$, and the phase information is completely lost on a time scale $T_2 \sim \hbar/2\delta^z$, corresponding to a random phase change of $\sim \pi$.

2.5.2 *Spin–orbit interaction*

Spin–orbit interaction (SOI) is an important ingredient in condensed matter physics, and couples the motion of the electron to its spin degree of freedom. It enters as a relativistic correction to the non-relativistic Pauli-Schrödiger equation [90], giving rise to the Pauli spin–orbit Hamiltonian,

$$H_{SO} = \frac{\hbar}{4m_0^2c^2}\mathbf{p}\cdot\boldsymbol{\sigma}\times(\nabla V), \tag{2.29}$$

where m_0 is the rest mass of the electron, c is the velocity of light, and V is the effective electric field created by the gradient of the Coulomb potential V of the atomic core.

For electrons confined in a semiconductor 2DEG, there are two main contributions to this electric field ∇V [71]: (i) If the lattice of the semiconductor lacks inversion symmetry, e.g. like the Zinc-Blende lattice of GaAs, the electrons experience a local electric field created by the atoms in the lattice, giving rise to the so-called Dresselhaus SOI. (ii) The electrons can also experience the electric field caused by an asymmetric confinement potential of the quantum well, known as the Rashba SOI. Assuming the confinement of the 2DEG to be along the *z*-coordinate, the electrons of the 2DEG can only move in-plane, and the SOI Hamiltonian takes the form of

$$H_{so} = \alpha\,(p_x\sigma^y - p_y\sigma^x) + \beta\,(-p_x\sigma^x + p_y\sigma^y)\,, \tag{2.30}$$

where the first term describes the Rashba SOI, the second term describes the Dresselhaus SOI, and α and β are the Rashba and Dresselhaus SOI coefficients, respectively. From Eq. (2.30) one can see that spin–orbit coupling affects the electrons moving through the 2DEG by rotating their spin, with the speed of the rotation proportional to their momentum.

Further confining the electrons in quantum dots, where the electrons are localized in a small region of space, the average motion of the electrons $\langle \mathbf{p} \rangle$ vanishes. However, despite this, SOI still affects the confined electrons in several ways. Most importantly for this thesis are: (i) Small inhomogeneities in the confining potentials on different quantum dots can result in different effective g-factors on the dots, and (ii) the finite momentum due to the displacement of the electron associated with tunneling between different quantum dots can induce a spin–orbit assisted spin-flip.

By changing the effective g-tensors on the dots, SOI also changes the magnetic properties of the system. To model how the magnetic properties are changed, we replace the Zeeman Hamiltonian in Eq. (2.6) of Sec. 2.2.2 with a Zeeman Hamiltonian that allows for different g-factors,

$$H_Z = \frac{1}{2}\mu_B \sum_i g_i B_i^z (n_{i,\uparrow} - n_{i,\downarrow}). \tag{2.31}$$

Applying the same magnetic field over several quantum dots can then potentially lead to different Zeeman fields on the different dots. Most importantly for spin qubits, this can give rise to field gradients over neighboring dots that effectively change the dynamics of the qubits.

The spin–orbit induced spin-flip tunneling will become an important part of the discussion when we investigate transport and spin-blockade in ST qubits in Chapter. 3. To model this effect we replace the tunneling term in the Hubbard model in Eq. (2.5) with a general non-spin-conserving tunneling Hamiltonian that also parametrizes the effect of spin–orbit interaction on the interdot tunneling, effectively yielding spin-non-conserving tunneling terms,

$$H_t = \frac{1}{\sqrt{2}} \hat{c}^\dagger_{i,\alpha} [t_s \mathbb{1} + i\mathbf{t}_{so} \cdot \boldsymbol{\sigma}]_{\alpha\beta} \hat{c}_{j,\beta} + \text{h.c.}, \tag{2.32}$$

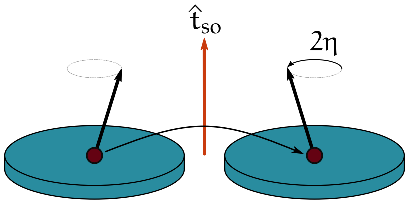

Figure 2.9: Spin–orbit induced spin-flip tunneling. The charge tunneling between the two quantum dots is accompanied by a 2η spin rotation around the spin–orbit vector $\mathbf{t}_{so}$.

where t_s is the magnitude of the spin-conserved tunnel coupling between dot i and j, and the magnitude and orientation of the vector $\mathbf{t}_{so}$ depend on microscopic details of the spin–orbit interaction. With the z-axis oriented along $\mathbf{t}_{so}$ we see that this tunneling Hamiltonian reduces to $H_t = \frac{1}{\sqrt{2}}\hat{c}^\dagger_{i,\alpha}[t\, e^{i\eta\sigma_z}]_{\alpha\beta}\hat{c}_{j,\beta} + \text{h.c.}$, which describes charge tunneling with amplitude t that is accompanied by a z-rotation of the spin over an angle of $\pm 2\eta$ depending on the direction of tunneling, as illustrated in Fig. 2.9. Projecting the Hamiltonian in Eq. (2.32) to the five-level basis of the ST qubit, the Hamiltonian reads as

$$H_{so} = i\mathbf{t}_{so} \cdot |\mathbf{T}\rangle \langle S_{02}| , \tag{2.33}$$

where $|\mathbf{T}\rangle = \{|T^x\rangle, |T^y\rangle, |T^z\rangle\}$ is the vector of unpolarized triplet states along the three orthogonal coordinate axes [91], with $|T^{x,y}\rangle = i^{1/2\mp 1/2}(|T^-\rangle \mp |T^+\rangle)/\sqrt{2}$ and $|T^z\rangle = |T^0\rangle$.

2.5.3 *Hyperfine interaction*

In many semiconductor systems, especially in devices based on III-V materials such as GaAs and InAs, but also in some Si- and Ge-based systems, atoms that carry finite nuclear spin set up a small magnetic field usually of the order ~ mT. This magnetic field, often called the Overhauser field, acts on the localized electron spins through the hyperfine interaction as illustrated in Fig. 2.10, and is an important source of decoherence in spin-based qubits. The dominating contribution from the hyperfine interaction in spin qubits is the contact interaction, described by the Hamiltonian

$$H_{hf} = \sum_{i,k} A_k \mathbf{S}_i \cdot \mathbf{I}_{i,k}, \tag{2.34}$$

where $\mathbf{S}_i$ is the electron spin operator on dot i, $\mathbf{I}_{i,k}$ the nuclear spin operator for nucleus k on dot i, and $A_k = A\nu_0|\psi(\mathbf{r}_k)|^2$ is the coupling constant between

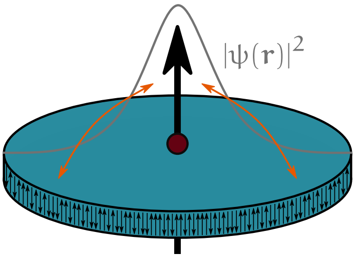

Figure 2.10: Illustration of hyperfine interaction in a quantum dot. In semiconductors with non-zero nuclear spins the small magnetic moment of the nuclear spins couple to the spin of the confined electrons.

the electrons and nucleus k, written in terms of the hyperfine coupling energy, typically $A \sim 100$ μeV, the density of spinful nuclei $1/\nu_0$, and the electron density of the envelope function at the position of the nucleus $|\psi(\mathbf{r}_k)|^2$.

Because of the small nuclear magnetic moment, the nuclear spin ensemble is in a fully mixed state in equilibrium at typical dilution fridge temperatures. Within a mean-field approximation we can therefore write

$$H_{\mathrm{hf,mf}} = \sum_i \mathbf{K}_i \cdot \mathbf{S}_i, \tag{2.35}$$

where the nuclear fields $\mathbf{K}_i$, also called Overhauser fields, are random with a root mean square (rms) value $\sim A/\sqrt{N}$, where N is the number of spinful nuclei on a dot, typically $N \sim 10^5 - 10^6$ when there is a significant fraction of spinful nuclei. These fields are thus usually of the order $\sim$ mT when translated to an effective magnetic field. Within this approximation, the hyperfine interaction takes the same form as the Zeeman interaction with an external magnetic field, which we discussed in Sec. 7.1. It can therefore often be useful to define a total Zeeman field $\mathbf{B}_i$, containing both the externally applied field $\mathbf{B}_i^{\mathrm{ext}}$ and the random nuclear field $\mathbf{K}_i$.

To investigate how hyperfine interaction affects a spin qubit it is often useful to project the Hamiltonian to the qubit subspace. Projecting the mean-field hyperfine Hamiltonian in Eq. (2.35) to the ST qubit subspace yields

$$H_{\mathrm{hf,ST}} = \delta K^z \sin\frac{\theta}{2}\,\sigma_x, \tag{2.36}$$

where $\delta K^z = \frac{1}{2}(K_L^z - K_R^z)$ is a quasistatic random field gradient between the two quantum dots. In general this field gradient presents a main source of decoherence in ST qubits due to its random nature, but it can also be used for initialization along the ±x-axis of the Bloch sphere [92].

Similarly, the hyperfine Hamiltonian can also be projected onto the XO qubit subspace,

$$\hat{H}_{\mathrm{hf,XO}} = -\frac{2}{3}\delta K^z_M \hat{\sigma}_z - \frac{1}{\sqrt{3}}\delta K^z_{LR} \hat{\sigma}_x, \tag{2.37}$$

where $\delta K^z_M = -\frac{1}{2}(\delta K^z_{LC} - \delta K^z_{CR})$ and $\delta K^z_{LR} = \frac{1}{2}\left(K^z_L - K^z_R\right)$, in terms of the field gradients $\delta K^z_{ij} = \frac{1}{2}(K^z_i - K^z_j)$ over neighboring dots. We thus see that, also for the XO qubit, the random nuclear fields can be an important source of qubit decoherence. In addition, the two gradients δK^z_M and δK^z_{LR} also couple the qubit states $|0\rangle$ and $|1\rangle$ to the quadruplet state $|Q^{+1/2}\rangle$ that cannot be split off by increasing the external field B^{ext}, making the hyperfine interaction a source of leakage out of the qubit subspace.

3

TRANSPORT IN QUANTUM DOT SYSTEMS

So far we have only considered quantum dot systems where a given number of electrons is confined. The electrons have been restricted to only be able to tunnel between different quantum dots, i.e. we have assumed that the quantum dots are not coupled to the reservoirs of the 2DEG. By now allowing electrons to also tunnel between the reservoirs of the 2DEG, often called leads, and the quantum dots, new interesting dynamics are introduced to the quantum dots.

There are several approaches that can be used to describe electrons confined in a dissipative quantum dot system. What approach is applicable depends on the complexity of the system and on what properties one wants to calculate. In this chapter we present two different approaches. In Sec. 3.1 we describe a confined electron using a single-particle Green function [93], which gives an accurate description of the interaction between the confined electron and the lead. From this approach we are able to analytically calculate the finite lifetime of the confined electron. However, this approach quickly becomes complicated when introducing several electrons and quantum dots, and fails to predict the internal spin dynamics within the quantum dots. The second approach solves this problem, and is presented in Sec. 3.2. This approach is based on a Lindblad master equation [94, 95], where the coupling between the quantum dot and lead is included as an effective decay rate using a so-called superoperator. Despite simplifying the details of the leads, this approach has the advantage that it is not limited by the dynamics and interactions of the quantum dots.

3.1 DISSIPATION AND DECAY RATES

Green functions are a powerful tool in condensed matter physics, providing a framework that allows for calculating many observables of interest. The single-particle Green function is often defined as a correlation function between two annihilation operators, with the most common type of Green function, and the only one we will encounter here, being the retarded Green function [93],

$$G^R(\nu, t; \nu', t') = -i\theta(t - t') \left\langle \left\{ c_\nu(t), c^\dagger_{\nu'}(t') \right\} \right\rangle, \tag{3.1}$$

describing the two-point correlation between having an electron in state ν at time t and in state ν' at t'. Here, $\theta(t)$ is the Heaviside step function, and $\{A, B\} = AB + BA$ is the anti-commutator.

In order to evaluate the retarded Green functions it is necessary to find their equation of motion, which can be obtained by differentiating Eq. (3.1) with respect to t. For a non-interacting Hamiltonian,

$$H_0 = \sum_{\nu\nu'} t_{\nu'\nu} c^\dagger_{\nu'} c_\nu, \tag{3.2}$$

which can include both kinetic terms and single-particle potentials, the equation of motion becomes

$$\sum_{\nu''} (i\delta_{\nu\nu''}\partial_t - t_{\nu\nu''}) G^R(\nu'', \nu', t - t') = \delta(t - t')\delta_{\nu\nu'}. \tag{3.3}$$

Although writing the Green functions in time domain is useful to understand some of the Green functions' properties, it is often more useful to represent them in frequency space. Taking the Fourier transform of Eq. (3.3) gives

$$\sum_{\nu''} \left(\delta_{\nu\nu''}(\omega + i\eta) - t_{\nu\nu''}\right) G^R(\nu'', \nu'; \omega) = \delta_{\nu\nu'}, \tag{3.4}$$

where the small imaginary part $\eta = 0^+$ is added to ensure proper convergence.

The process of calculating the retarded Green function from the equation of motion is as follows: By applying the equation of motion to several different Green functions, one obtains a set of coupled differential equations that can be solved for the relevant Green function. We will show a simple example of this approach below when we calculate the Green function of an electron confined in a quantum dot.

3.1.1 *Single quantum dot and lead*

Using the simple framework of Green functions presented above, we can now explore how the coupling between quantum dots and leads affects the electrons confined on the quantum dot. We start by considering the simplest case of a single quantum dot connected to a lead, as illustrated in Fig. 3.1.

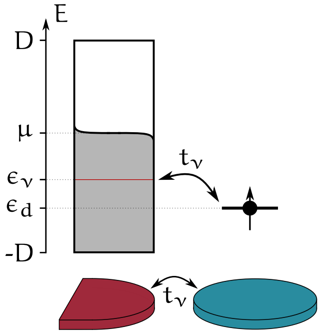

Figure 3.1: The single level of a quantum dot with energy ϵ_d is tunnel coupled to the states of the lead. This coupling is here illustrated for one of the states ν with energy ϵ_ν (marked in red).

This system can be described by the quadratic Hamiltonian (assuming no spin for simplicity)

$$H = \epsilon_d c_d^\dagger c_d + \sum_\nu (\epsilon_\nu - \mu) c_\nu^\dagger c_\nu + \sum_\nu \left(t_\nu^* c_\nu^\dagger c_d + t_\nu c_d^\dagger c_\nu \right), \tag{3.5}$$

where the first term gives the energy ϵ_d of the single level of the quantum dot, the second term governs the energies of all states ν of the lead relative to the chemical potential μ, and the last term describes the tunneling between the quantum dot and the states of the lead.

To describe an electron confined on the quantum dot, we need to calculate the retarded Green function that is diagonal in the label d of the single level of the quantum dot. To do so we will use the equation of motion, as given by Eq. (3.4), on the two Green functions $G^R(d, d; \omega)$ and $G^R(\nu, d; \omega)$. This is done by simply substituting $\{\nu, \nu'\} \to \{d, d\}$ and $\{\nu, \nu'\} \to \{\nu, d\}$ in Eq. (3.4), giving two coupled equations,

$$(\omega + i\eta - \epsilon_d) G^R(d, d; \omega) - \sum_\nu t_\nu G^R(\nu, d; \omega) = 1, \tag{3.6}$$

$$(\omega + i\eta - \epsilon_\nu + \mu) G^R(\nu, d; \omega) - t_\nu^* G^R(d, d; \omega) = 0. \tag{3.7}$$

Solving the two coupled equations for $G^R(d, d; \omega)$ then yields the retarded Green function describing the single level of the quantum dot,

$$G^R(d, d; \omega) = \frac{1}{\omega - \epsilon_d + i\eta - \Sigma^R(\omega)}, \tag{3.8}$$

where

$$\Sigma^R(\omega) = \sum_{\nu} \frac{|t_\nu|^2}{\omega - \epsilon_\nu + \mu + i\eta}, \tag{3.9}$$

is the so-called self-energy which contains all information about how the lead affects the confined electron. The self-energy changes the Green function by shifting the pole of the Green function $G^R(d, d; \omega)$. This affects the dynamics of the confined electron in two ways: (i) The real part of $\Sigma^R(\omega)$ changes the energy of the single level state d from ϵ_d to $\epsilon_d + \mathrm{Re}[\Sigma^R]$, and (ii) the imaginary part gives rise to an effective decay rate of the state which in the time domain translates into a finite lifetime.

To evaluate the self-energy we replace the sum over the states ν in the lead with an integral over the density of states $d(\epsilon)$. Assuming that the tunneling couplings t_ν only depend on ν through the energies ϵ_ν [93] the self-energy then reads

$$\Sigma^R(\omega) = \int_{-D}^{D} d\epsilon \; d(\epsilon) \frac{|t(\epsilon)|^2}{\omega - \epsilon + \mu + i\eta} \tag{3.10}$$

where $\pm D$ are the band limits of the lead (see Fig. 3.1). By further assuming that $d(\epsilon)|t(\epsilon)|^2$ changes slowly in the region of interest, we define

$$2\pi d(\epsilon)|t(\epsilon)|^2 = \begin{cases} \Gamma, & \epsilon \in [-D, D], \\ 0, & |\epsilon| > D. \end{cases} \tag{3.11}$$

This allows us to solve the integral in Eq. (3.10), giving

$$\Sigma^R(\omega) = -\frac{\Gamma}{\pi} \ln \left| \frac{D + \omega + \mu}{D - \omega - \mu} \right| - i\frac{\Gamma}{2}. \tag{3.12}$$

For all quantum dot systems considered in this thesis we will have $D \gg \omega + \mu$, and we can therefore safely neglect the real part of $\Sigma^R(\omega)$. Inserting the self-energy back into the Green function in Eq. (3.8) then gives

$$G^R(d, d; \omega) = \frac{1}{\omega - \epsilon_d + i\Gamma/2}, \tag{3.13}$$

showing how the coupling between the quantum dot and the lead effectively induces an effective decay rate Γ, and thus also a lifetime broadening, of the quantum dot single level. Note also that we would have obtained the same Green function by replacing the Hamiltonian in Eq. (3.5) by the non-hermitian Hamiltonian $H = (\epsilon_d - i\Gamma/2)c_d^\dagger c_d$.

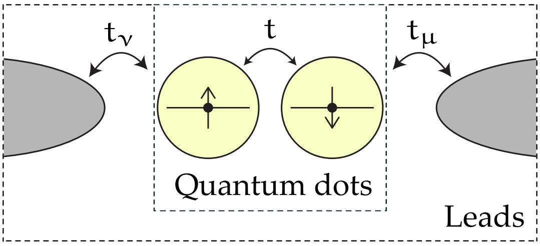

Figure 3.2: A double quantum dot coupled to two leads. The subsystem of the quantum dots belongs to a larger total system that also contains the leads. Integrating out the environment (leads) degrees of freedom enables the dynamics of the quantum dots to be described by a master equation.

3.2 THE LINDBLAD MASTER EQUATION

Green functions give a detailed description of how a single electron interacts with leads. However, when considering multi-dot systems with many electrons and many states the approach quickly becomes tedious and falls apart. For such multi-dot systems a master equation approach is very useful, where the dynamics within the quantum dots are described accurately and transitions to and from the leads are considered probabilistic through a transition rate matrix. In this section we will focus solely on the Lindblad master equation, which is especially useful for describing quantum dot systems.

The Lindblad master equation is a differential equation for the density matrix $\rho(t)$ describing a subsystem that belongs to a more complicated total system. In our case the subsystem we want to describe is the quantum dots and the environment is the leads, together they make up the total system as illustrated in Fig. 3.2. The derivation of the Lindblad equation starts with the time-evolution of the total system given by the von Neumann equation, and is obtained by tracing out the environment's degrees of freedom. We will not go into details on the derivation here, but more details can be found in Ref. [94]. In the high bias limit [94], where all relevant states lie well within the chemical potential of the leads, all Fermi functions take a value of either 0 or 1. Then, the resulting Lindblad equation that describes the time-evolution of the quantum dot system can be written as

$$\partial_t \rho = -i[H, \rho] + \sum_{j,\eta} \left\{ \Gamma_j^{\text{out}} D[c_{j,\eta}^\dagger](\rho) + \Gamma_j^{\text{in}} D[c_{j,\eta}](\rho) \right\}, \tag{3.14}$$

where H is the Hamiltonian governing the quantum dot subsystem, j labels the quantum dots that are coupled to the leads, η is the spin-projection, and

$$D[O](\rho) = O^\dagger \rho O - \frac{1}{2}\left(\rho O O^\dagger + O O^\dagger \rho\right), \tag{3.15}$$

is a superoperator, i.e. an operator that acts on an operator. The first term in Eq. (3.14) governs the coherent time-evolution of the quantum dots according to the von Neumann equation[1], whereas the second term describes transitions between different quantum dot states induced by interactions with the leads.

The rate Γ_j is here the effective rate between quantum dot j and a neighboring lead, which we derived using the Green function formalism in the previous section. However, because the explicit dependence on the leads has been traced out in the Lindblad master equation, the effective rates are separated into in-going and out-going rates, which are determined manually depending on the system at hand. Considering the example of a single quantum dot coupled to a lead studied in the previous section, a natural choice would be to use

$$\Gamma_j^{\mathrm{in(out)}} = \Gamma_j\,\Theta(\mp\{\epsilon_d - \mu\}), \tag{3.16}$$

where an electron can only tunnel into(out of) the quantum dot if the single level is below(above) the chemical potential.

The Lindblad master equation is a powerful tool when investigating dissipative systems where the internal dynamics within the quantum dots are important. An example of such a system, which we will encounter later in the thesis, is a double quantum dot tuned to the regime of Pauli spin blockade, where the current through the system is determined mainly by spin dynamics within the double dot.

3.3 COULOMB BLOCKADE

In the above, we showed that the tunnel coupling between a quantum dot and a lead introduces an effective decay rate to the level of the quantum dot. In the framework of the Lindblad master equation, the occupancy of the single-level of the spinless quantum dot can then be determined simply from the relative position of the level and the lead. By now introducing spin, a second electron is allowed to tunnel into the quantum dot if the relative detuning of the level and the lead is larger than the Coulomb repulsion U. Any further occupancy of the quantum dot, above two electrons, relies on

---

[1] Note that for a quantum dot system in absence of leads the Lindblad equation is simply reduced to the von Neumann equation.

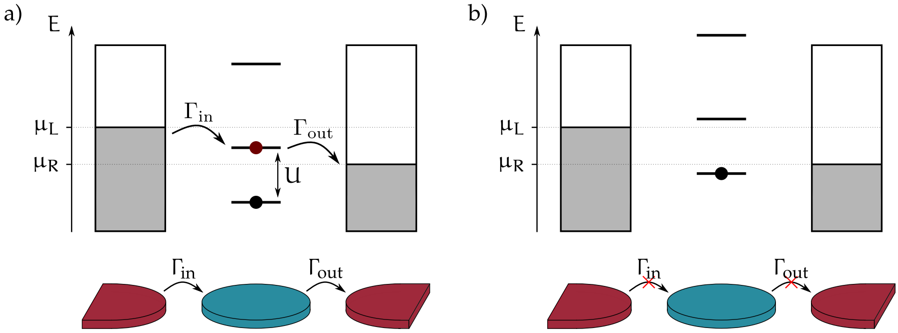

Figure 3.3: Illustration of Coulomb blockade in a single quantum dot. (a) The bias voltage from the left drain to the right drain allows a current to run through the quantum dot if there is an available level within the bias window. (b) If there is no level within the bias window the current is blocked in Coulomb blockade.

occupying higher orbitals. Thus, changing the relative energy of the quantum dot levels and the lead, e.g. through the electrochemical potential V, provides a practical way to tune the occupancy of the quantum dot.

In most quantum dot devices there is usually more than one lead. If all the leads have the same Fermi level, the system is qualitatively identical to the single lead system discussed above. However, if the leads have different Fermi levels, this allows a current to run from one lead to another through the quantum dot. For a quantum dot coupled to two leads, as depicted in Fig. 3.3(a), a current can run through the quantum dot if there is an available level within the bias window between the chemical potentials μ_L and μ_R of the two leads. However, if there is no available level in the bias window, the current is blocked in the so-called Coulomb blockade, as illustrated in Fig. 3.3(b). This can be observed in experiments by measuring the current as a function of V, where for a very small bias voltage the current peaks when the levels of the quantum dot cross the bias window. The distance between these so-called Coulomb peaks can then be used to determine the level structure of the quantum dot.

The current through the single quantum dot depicted in Fig. 3.3(a) follows the simple transport cycle $(1) \rightarrow (2) \rightarrow (1)$, where (n) labels the charge configuration of the quantum dot. For a system consisting of several quantum dots, the transport cycle is more complex and involves more than two different charge configurations. The slightly more complicated double quantum dot illustrated in Fig. 3.4, for instance, follows the transport cycle $(1,1) \rightarrow (2,1) \rightarrow (1,2) \rightarrow (1,1)$. Because of the larger number of charge configurations involved,

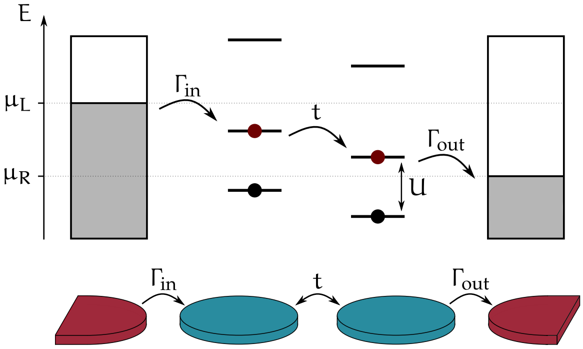

Figure 3.4: Illustration of Coulomb blockade in a double quantum dot. The current is only allowed to run through the double quantum dot when all levels involved in the transport cycle lie within the bias window.

there are more configurations for which the system is stuck in Coulomb blockade. In general, if any of the levels involved in the transport cycle lies outside the bias window, electrons can not tunnel from one lead to the other, and the system is stuck in Coulomb blockade.

3.4 PAULI SPIN BLOCKADE

In multi-dot structures the current also relies on the internal spin dynamics during tunneling events between different quantum dots, which introduce additional mechanisms that can block the current. An important exchange effect that affects the current through multi-quantum dot structures is the Pauli spin blockade, which in addition to being important for the understanding of the current through multi-quantum dot systems, also is an essential tool for spin qubits, enabling spin-to-charge conversion for qubit initialization and readout.

In the simplest case of a double quantum dot connected to two leads, Pauli spin blockade arises when the double dot is tuned to the so-called Pauli spin blockade regime, where electron transport follows the transport cycle $(0.1) \rightarrow (1,1) \rightarrow (0,2) \rightarrow (0,1)$; the energy level of the left dot satisfies $\mu_L > \epsilon_L > \epsilon_R$, whereas the energy level on the right dot is tuned to the Coulomb blockade $\epsilon_R + U > \mu_R > \epsilon_R$, assuring that there is always one electron on the right dot (see Fig. 3.5). When an electron tunnels into the left dot the double dot can be in either of the four $(1,1)$ spin states $|S\rangle$ or $|T^{\pm,0}\rangle$. In the $(0,2)$ charge configuration only the singlet state $|S_{02}\rangle$ is accessible, any $(0,2)$ triplet state requires occupation of a higher orbital state at a much higher

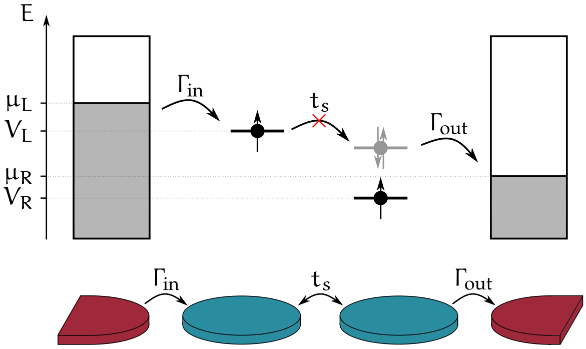

Figure 3.5: Illustration of Pauli spin-blockade in a double quantum dot. The bias voltage from the left drain to the right drain allows a current to run through the double dot. However, because the two electrons on the two dots (black dots) form a $|T^+\rangle$ spin state, which is not coupled to $|S_{02}\rangle$ (grey dot) through the spin-conserved tunneling t_s, the current is blocked.

energy. Assuming no SOI, where only the $(1,1)$ singlet state $|S\rangle$ is coupled to the energetically favorable $|S_{02}\rangle$, we then have two different situations: (i) If the two $(1,1)$ electrons form a singlet state, the left electron can tunnel to the right dot, thereby contributing to the current. (ii) If the two electrons form a triplet state, the left electron is not allowed to tunnel to the right dot, and the current is blocked in the Pauli spin blockade, as illustrated in Fig. 3.5.

Assuming that the double quantum dot is in the open regime where the transport rates $\Gamma_{L,R}$ are the largest relevant energy scales, ensures that the transitions $(0,2) \to (0,1) \to (1,1)$ are effectively instantaneous, and all the interesting dynamics happen during the $(1,1) \to (0,2)$ process. This allows us to model the tunneling to and from the leads using an effective rate $\Gamma = \Gamma_L^{in} = \Gamma_R^{out}$ which characterizes the decay of $|S_{02}\rangle$ and the subsequent reloading of one of the $(1,1)$ states. We can then describe the dynamics of the double dot by considering only the basis of the ST qubit, which we discussed in detail in Sec. 2.3. Like before, we describe the five-level system of the ST qubit using a simple model Hamiltonian containing contributions from the Hubbard and Zeeman models,

$$H = H_{Hub} + H_B, \tag{3.17}$$

where we for simplicity assume no SOI,

$$H_{Hub} = -\epsilon\, |S_{02}\rangle\langle S_{02}| + t_s\, |S\rangle\langle S_{02}| + \text{h.c.} \tag{3.18}$$

and a homogeneous magnetic field pointing along the z-coordinate,

$$H_B = B^z\big[\,|T^+\rangle\langle T^+| - |T^-\rangle\langle T^-|\,\big]. \tag{3.19}$$

The dynamics of the double dot can then be described using the Lindblad master equation in Eq. (3.14), which in the basis of the ST qubit reads

$$\partial_t \rho = -i[H, \rho] + \boldsymbol{\Gamma}(\rho), \tag{3.20}$$

where ρ is the five-level density matrix, and $\boldsymbol{\Gamma}(\rho) = -\frac{1}{2}\Gamma\{P_{02}, \rho\} + \frac{1}{4}\Gamma(\mathbb{1} - P_{02})\rho_{02,02}$ is the superoperator describing the tunneling processes to and from the reservoirs, with $P_{02} = |S_{02}\rangle\langle S_{02}|$ being the projector onto state $|S_{02}\rangle$. By solving Eq. (3.20) for the steady-state density matrix ρ^{ss}, the current through the double dot can be calculated from the expression $I = e\Gamma\rho^{ss}_{02,02}$. Since only the $(1,1)$ singlet $|S\rangle$ is in this case coupled to $|S_{02}\rangle$, there is no way for the system to transition from the triplet states $|T^{\pm,0}\rangle$ to $|S_{02}\rangle$, and the system is trapped in Pauli spin blockade, resulting in zero leakage current.

In general, any spin-mixing mechanism can break the spin-blockade by introducing a finite coupling between the blocked triplet states and $|S_{02}\rangle$. In this thesis we include two such mechanisms: (i) Allowing the Zeeman fields to be different on the two dots $\mathbf{B}_{L,R}$, the Zeeman interaction mixes the four $(1,1)$ spin states. These fields can originate from externally applied magnetic fields, nearby on-chip micromagnets, or the hyperfine interaction coupling the localized electronic spins and the nuclear spins of the host material. (ii) Strong spin–orbit coupling can result in spin-flip tunneling, effectively coupling the three triplet states directly to $|S_{02}\rangle$. In addition, SOI can also renormalize the g-tensors on the two dots, contributing to making the Zeeman fields different. In the next chapter we will consider a model where all the above-mentioned spin-mixing mechanisms are included, making the current through the double dot, and thus the degree of spin-blockade, dependent on a complex interplay between the non-spin-conserved tunneling Hamiltonian, which couples the $(1,1)$ subspace to $|S_{02}\rangle$, and the effective Zeeman Hamiltonian that mixes the four $(1,1)$ states.

4

PAULI SPIN BLOCKADE AND SPIN–ORBIT INTERACTION

The complex connection between the leakage current and the internal spin-dynamics of quantum dots enables current-measurements to probe spin properties of quantum dot systems [96–99]. Knowing the details of how the spin-blocked current behaves is therefore essential to uncovering new measurement techniques. In Paper IV we presented an analytical model for the leakage current through a double quantum dot with arbitrary Zeeman fields and strong spin–orbit coupling. Based on our model we proposed a method for characterizing both the magnitude and orientation of the spin–orbit vector $\mathbf{t}_{so}$ by simply measuring the current as a function of the orientation of the external magnetic fields.

4.1 LEAKAGE CURRENT

Like in the previous chapter, we describe the spin blocked double quantum dot in the basis of the ST qubit, using the model Hamiltonian,

$$H = H_{\text{Hub}} + H_B. \tag{4.1}$$

In contrast to the prior chapter, we now include both SOI and two arbitrary oriented Zeeman fields on the two dots. The Hubbard-like Hamiltonian then takes the form of

$$H_{\text{Hub}} = -\epsilon \left|S_{02}\right\rangle \left\langle S_{02}\right| + t_s \left|S\right\rangle \left\langle S_{02}\right| + i\mathbf{t}_{so} \cdot \left|\mathbf{T}\right\rangle \left\langle S_{02}\right| + \text{h.c.}, \tag{4.2}$$

where the effect of spin–orbit interaction on the interdot tunneling is added as described in Sec. 2.5.2. Because of the singlet nature of $|S_{02}\rangle$, the magnetic interactions only act within the $(1,1)$ subspace, described by the Zeeman Hamiltonian

$$H_B = \frac{1}{2}\left[(\mathbf{B}_L \cdot \boldsymbol{\sigma}_L) \otimes \mathbb{1}_R + \mathbb{1}_L \otimes (\mathbf{B}_R \cdot \boldsymbol{\sigma}_R)\right], \tag{4.3}$$

with $\boldsymbol{\sigma}_{L(R)}$ being the vector of Pauli matrices acting on the left(right) spin, and $\mathbf{B}_{L(R)}$ being the total Zeeman field on the left(right) dot. As discussed in

Sec. 2.5.3, these fields can contain contributions from externally applied magnetic fields as well as the Overhauser fields due to the hyperfine interaction with the nuclear spins in the quantum dots.

Because of the complexity of our model, containing three arbitrary vectors $\mathbf{t}_{so}$ and $\mathbf{B}_{L,R}$, it will be convenient to perform a basis transformation which makes the Hamiltonian take a simple form, from which the current can be calculated analytically. The first step is to define the z-direction of our coordinate system to point along $\mathbf{t}_{so}$, which rotates the Hubbard-like Hamiltonian into

$$H_{Hub} = -\epsilon \left|S_{02}\right\rangle \left\langle S_{02}\right| + t_s \left|S\right\rangle \left\langle S_{02}\right| + i t_{so} \left|T_0\right\rangle \left\langle S_{02}\right| + \text{h.c.}, \tag{4.4}$$

where t_{so} is the magnitude of the spin–orbit vector $\mathbf{t}_{so}$.

We then introduce a dimensionless parameter $\eta = \arctan\left[t_{so}/t_s\right]$ that parameterizes the relative strength of the spin–orbit-induced tunnel coupling and apply a basis transformation to all $(1,1)$ states

$$|\tilde{\psi}\rangle = e^{i\frac{\eta}{2}(\sigma_L^z - \sigma_R^z)} |\psi\rangle . \tag{4.5}$$

In this new basis we find that $|B\rangle = \cos\eta\ |S\rangle + i\sin\eta\ |T_0\rangle$ is a "bright" state that is coupled to $|S_{02}\rangle$ with strength $t \equiv \sqrt{t_s^2 + t_{so}^2}$, and $|D\rangle = i\sin\eta\ |S\rangle + \cos\eta\ |T_0\rangle$ is a "dark" state that is not coupled; the polarized triplet states $|\tilde{T}_\pm\rangle = |T_\pm\rangle$ are unchanged by the transformation. Thus, only one $(1,1)$ state is coupled to $|S_{02}\rangle$ in the new basis, with the cost being that the transformed Zeeman Hamiltonian $e^{-i\frac{\eta}{2}(\sigma_L^z - \sigma_R^z)} H_B e^{i\frac{\eta}{2}(\sigma_L^z - \sigma_R^z)}$ acquired an η-dependence and now incorporates all spin–orbit effects included in our model.

By further introducing the (anti)symmetric magnetic fields $\mathbf{B}_\pm = \frac{1}{2}(\mathbf{B}_L \pm \mathbf{B}_R)$, we define the auxiliary fields $\mathbf{E}_\pm = \{B_\pm^x \cos\eta - B_\mp^y \sin\eta, B_\pm^y \cos\eta + B_\mp^x \sin\eta, B_\pm^z\}$ that incorporate the η-dependence of the Zeeman Hamiltonian. In terms of these new auxiliary fields, the Zeeman Hamiltonian can be written as

$$\begin{aligned} H_B = \frac{1}{\sqrt{2}} \sum_\pm \Big[& (E_+^x \pm i E_+^y) |\tilde{T}_0\rangle \langle \tilde{T}_\pm| + (\mp E_-^x - i E_-^y) |\tilde{S}\rangle \langle \tilde{T}_\pm| + \text{h.c.} \Big] \\ & + E_+^z \{ |\tilde{T}_+\rangle \langle \tilde{T}_+| - |\tilde{T}_-\rangle \langle \tilde{T}_-| \} + E_-^z \{ |\tilde{S}\rangle \langle \tilde{T}_0| + |\tilde{T}_0\rangle \langle \tilde{S}| \}, \end{aligned} \tag{4.6}$$

which has the exact same form as the usual $(1,1)$ Zeeman Hamiltonian (4.3) when written in a singlet-triplet basis [100], under the substitution $\mathbf{B}_\pm \to \mathbf{E}_\pm$. The transformation thus gauges away the spin–orbit interaction, yielding a Hamiltonian that can be mapped exactly to the case without spin–orbit coupling ($\mathbf{t}_{so} = 0$), simply by redefining the two effective Zeeman fields.

The 3×3 block of the Hamiltonian governing the subspace $\{|\tilde{T}_+\rangle, |\tilde{T}_0\rangle, |\tilde{T}_-\rangle\}$ describes a spin-1 system coupled to the spin–orbit-rotated effective field $\mathbf{E}_+$.

We can diagonalize this block by applying the appropriate spin-1 rotation $\exp(i\alpha \mathbf{J}\cdot\hat{\mathbf{n}})$, where $\mathbf{J}$ is the vector of spin-1 matrices and $\hat{\mathbf{n}}$ is the unit vector of rotation, such that the full five-level Hamiltonian becomes

$$H = \begin{pmatrix} E_+ & 0 & 0 & c & 0 \\ 0 & 0 & 0 & -d & 0 \\ 0 & 0 & -E_+ & -c & 0 \\ c & -d & -c & 0 & t \\ 0 & 0 & 0 & t & -\delta \end{pmatrix}, \tag{4.7}$$

where $t = \sqrt{t_s^2 + t_{so}^2}$, and the (real) couplings between the triplets and the bright state $|\tilde{S}\rangle$ read

$$c = \frac{E_-}{\sqrt{2}}\Big\{ [\cos\theta_+ \sin\theta_- \cos(\phi_+ - \phi_-) - \cos\theta_- \sin\theta_+]^2 \\ + \sin^2\theta_- \sin^2(\phi_+ - \phi_-)\Big\}^{1/2}, \tag{4.8}$$

$$d = E_- \left[\cos\theta_- \cos\theta_+ + \sin\theta_- \sin\theta_+ \cos(\phi_+ - \phi_-)\right], \tag{4.9}$$

with

$$\theta_\pm = \arccos\left[\frac{E^z_\pm}{E_\pm}\right], \quad \phi_\pm = \arg\left[E^x_\pm + iE^y_\pm\right], \tag{4.10}$$

being the angles that define the orientation of the fields $\mathbf{E}_\pm$. Having the Hamiltonian on this form reduces the number of independent parameters from eight to five, and is thus advantageous when calculating the current analytically.

To obtain an analytical expression for the current through the system we then solve the steady-state master equation

$$\frac{\partial\hat{\rho}}{\partial t} = -i[H,\hat{\rho}] + \boldsymbol{\Gamma}(\hat{\rho}) = 0, \tag{4.11}$$

where again $\hat{\rho}$ is the five-level density matrix and $\boldsymbol{\Gamma}(\hat{\rho}) = -\frac{1}{2}\Gamma\{\hat{P}_{02},\hat{\rho}\} + \frac{1}{4}\Gamma(\mathbb{1} - \hat{P}_{02})\hat{\rho}_{02,02}$ the superoperator describing the fast tunneling processes to and from the reservoirs. By solving Eq. (4.11) for the steady-state density matrix $\hat{\rho}^{ss}$, the leakage current follows from $I = e\Gamma\hat{\rho}^{ss}_{02,02}$, giving in the $\Gamma \gg \epsilon, t, B_{L,R}$ limit the relatively compact expression

$$\frac{I}{e\Gamma_s} = \frac{|e^{2i\eta}B_R^- B_L^z - B_L^- B_R^z|^2 + \mathrm{Im}\{e^{2i\eta}B_R^- B_L^+\}^2}{\Gamma_s^2 Q_+^2 \left[3 + \frac{16 Q_+^2 Q_-^2}{(B_L^2 - B_R^2)^2}\right] + B_L^2 B_R^2}, \tag{4.12}$$

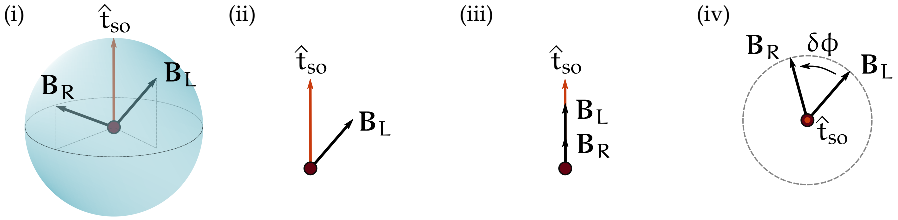

Figure 4.1: Illustration of the four stopping points. The leakage current vanishes when: (i) The magnitudes of the two Zeeman fields are equal. (ii) Either of the two fields is zero. (iii) Both fields are aligned with $\hat{t}_{so}$. (iv) The two fields have the same polar angle but a relative azimuthal angle of $\delta\phi = 2\eta$.

where $B_{L,R} = |\mathbf{B}_{L,R}|$ and we introduced the rate $\Gamma_s \equiv t^2/\Gamma$, which sets the scale of the effective decay rate of the $(1,1)$ states. We here also introduced the notations $B^\pm = B^x \pm iB^y$ and

$$Q_\pm^2 = \mathrm{Re}\{\tfrac{1}{2}e^{i\eta}(B_L^+ \pm B_R^-)\}^2 + \mathrm{Im}\{\tfrac{1}{2}e^{i\eta}(B_L^+ \mp B_R^-)\}^2 + \tfrac{1}{4}(B_L^z \pm B_R^z)^2. \quad (4.13)$$

The expression in Eq. (4.12) thus describes the current through a double quantum dot in the spin-blockade regime, including the effect of spin–orbit coupling and two possibly different Zeeman fields on the two dots (and thus generalizes the result presented in [101]).

4.1.1 *Stopping points*

Having an analytic expression for the current allows us to identify special configurations of $\mathbf{B}_{L,R}$ for which the current vanishes, so-called "stopping points" [100, 101]. These points are of interest as they enable the characterization of some double dot properties through simple current measurements, as we will show below.

From Eq. (4.12) we find four stopping points, all of which are illustrated in Fig. 4.1. (i) The first arises when the magnitude of the two Zeeman fields is equal, $B_L = B_R$, where the term $16Q_+^2Q_-^2/(B_L^2 - B_R^2)^2$ in the denominator diverge. At this point, the blockade can be understood by considering the four $(1,1)$ states in the basis of spin up and down along the local fields on the two dots. In this basis the two states $|\uparrow\downarrow\rangle$ and $|\downarrow\uparrow\rangle$ are both eigenstates of H_B with zero total Zeeman energy. This means that the two states can be rearranged into a bright and dark state, and the system will thus be blocked in the dark state. (ii) The three other points are obtained for field configurations where the numerator in Eq. (4.12) vanishes. One of these configurations is when either of the two fields is zero, $B_{L,R} = 0$, resulting in two doubly degenerate

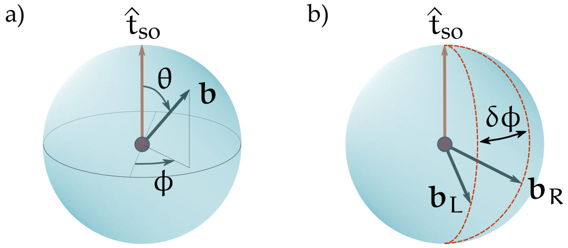

Figure 4.2: (a) For two Zeeman fields with the same orientation $\mathbf{b} = \mathbf{B}/B$ but different magnitudes the current only vanishes when the two fields are parallel to the spin–orbit vector marked in orange. (b) Orienting the Zeeman fields away from the spin–orbit vector, the current vanishes along the orange lines on the sphere where the relative orientation of the two Zeeman vectors $\mathbf{b}_{L,R}$ satisfy $\delta\phi = 2\eta$.

subspaces which can again be rearranged in dark and bright states. (iii) The numerator also vanishes when both fields are parallel or antiparallel to the spin–orbit vector $\mathbf{t}_{so}$, i.e. when $B^{\pm}_{L,R} = 0$. In this case the two triplets $|T_{\pm}\rangle$ are eigenstates of H_B that are not coupled to $|S_{02}\rangle$, resulting in a blockade of the current. (iv) The last stopping point occurs when $e^{2i\eta} = B^-_L B^z_R / B^-_R B^z_L$. To better understand this stopping point it is useful to write the two fields in spherical coordinates $\{B, \theta, \phi\}$, where $\theta = 0$ corresponds to the z-direction which is aligned with $\mathbf{t}_{so}$, as illustrated in Fig. 4.2(a). In this coordinate system the condition corresponds to having $\phi_R - \phi_L = 2\eta$ if $\theta_L = \theta_R$ and $\phi_R - \phi_L = 2\eta + \pi$ if $\theta_L = \pi - \theta_R$, i.e. the two fields having the same "latitude" but a relative azimuthal angle of $\delta\phi = 2\eta$, as illustrated in Fig. 4.2(b). For these configurations the eigenstates of H_B, where both spins are aligned with the two local fields with a relative azimuthal angle of 2η, will evolve during the interdot tunneling into a fully polarized spin-1 state, which has no overlap with $|S_{02}\rangle$.

4.2 CHARACTERIZING SPIN–ORBIT COUPLING

The collection of stopping points we identified above provides a potentially useful tool for characterizing properties of a double quantum dot, one of which is the spin–orbit interaction [96–99]. Assuming that one has full control over the two Zeeman fields on the two dots, all of the above stopping points can in principle be mapped out. This allows identifying both the orientation and magnitude of the spin–orbit tunneling vector $\mathbf{t}_{so}$.

The procedure works as follows. By making sure that the two Zeeman fields are both non-zero and have different magnitudes, we ensure that only

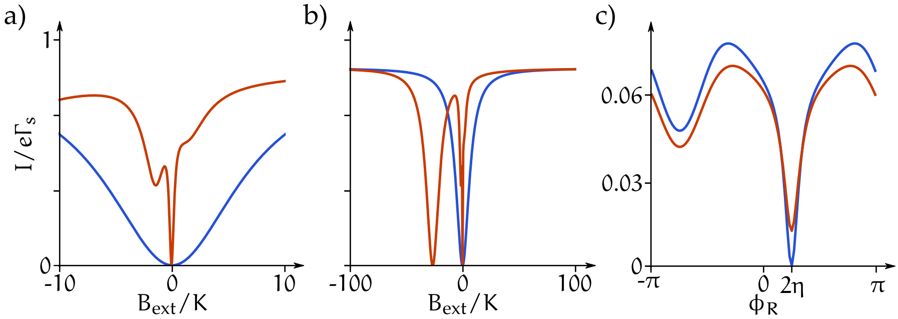

Figure 4.3: (a,b) Calculated current as a function of the magnitude of a uniform external field B_{ext} assuming different g-tensors on the two dots, where we used $\mathbf{B}_L = \{0.76, 0.32, 0.34\}B_{\text{ext}}$ and $\mathbf{B}_R = \{1, 0, 0\}B_{\text{ext}}$. The blue lines show the case with no nuclear spins present, and the red lines show how the behaviour of the double dot is drastically changed at small fields when adding two small random nuclear fields $\mathbf{K}_{L,R}$, drawn from a normal distribution with an r.m.s. value of 0.1 µeV. (c) Current as a function of ϕ_R with $\phi_L = 0$, $B_L = 0.9B_R$, and $\theta_L = \theta_R = 3\pi/8$. In the absence of nuclear fields (blue line) the current vanishes when the relative azimuthal angle $\delta\phi$ of two fields of different magnitude is equal to 2η. Averaging the current over random nuclear fields (red line) with the same distribution as used in (a,b), the current still has a minimum at $\delta\phi = 2\eta$.

the two last stopping points will be probed. The orientation of the spin–orbit vector can then be identified by making the two Zeeman fields parallel to each other and finding the field orientation for which the current vanishes, i.e. by probing stopping point (iii). Knowing the orientation of the spin–orbit vector, its magnitude can then be found by probing stopping points of type (iv). Tilting both fields away from $\mathbf{t}_{so}$ and then rotating one of the fields along $\mathbf{t}_{so}$, the leakage current vanishes when the relative orientation of the two fields satisfy $\delta\phi = 2\eta$, see Fig. 4.2(b), from which the magnitude of the SOI can be calculated. Although the procedure relies on our assumption that the two fields have different magnitudes, the stopping points related to $\mathbf{t}_{so}$ are also detectable as minima of the current if the fields are equal in magnitude, given that there is still a sizable leakage current due to e.g. spin relaxation processes.

In the above we assumed accurate control over the two Zeeman fields $\mathbf{B}_{L,R}$ separately. However, as we discussed in Sec. 2.5.3, the Overhauser field can in many systems give rise to a sizable random effective magnetic field that adds to the total Zeeman field, making it uncontrollable. Luckily, there are several ways to circumvent this problem: (i) Since only the orientation of the total

Zeeman fields matters for the procedure presented above, the random effects of the Overhauser fields can be suppressed by working in the large-field limit $B^{\mathrm{ext}}_{L,R} \gg K$. We illustrate this by exemplifying the effect of one single static configuration of nuclear fields on the leakage current in Fig. 4.3(a,b), where the blue lines show the current as given by Eq. (4.12) as a function of the applied magnetic field B_{ext} in the absence nuclear fields. For the red lines we added a random two random nuclear field configurations drawn from a normal distribution with $\langle K^2_{L,R}\rangle^{1/2} = 0.1$ μeV. The figures show a substantial difference in the current at small applied fields which indeed vanishes at larger fields. (ii) Because in typical experiments the total measurement time exceeds the correlation time of the nuclear fields, the details depending on the specific configuration of the nuclear fields average out. This averaging removes all sharp features, allowing to locate the current minimum related to the spin–orbit coupling in the same way as in the case without nuclear fields. We illustrate this in Fig. 4.3(c) by plotting the current as a function of the angle ϕ_R with $\phi_L = 0$ in the absence of nuclear fields (blue line) and after averaging over many (finite) nuclear field configurations (red line), both showing the same minimum located at $\delta\phi = 2\eta$.

5

MITIGATING NUCLEAR NOISE IN GAAS-BASED QUBITS

GaAs-based devices have propelled the spin qubit field forward for more than a decade, yielding many encouraging features such as full electric control and fast operation times [20, 47, 102–105]. However, despite the popularity and ease of use of GaAs-devices, their coherence times are intrinsically limited due to the hyperfine coupling between the electron spins and the nuclear spin bath of the host material [52–54]. We saw examples of this in Sec. 2.5.3 where we, by projecting the hyperfine Hamiltonian onto the qubit subspace, found that the random nuclear field gradients are a main source of decoherence in both the double dot ST qubit and the triple dot XO qubit.

Because the nuclear noise is one of the largest challenges for spin qubit implementations in GaAs-devices, several approaches to reduce its harmful effects have been explored. Such approaches can be roughly divided into two types: (i) Protocols for actively mitigate the nuclear noise through protocols to control or suppress the harmful nuclear field gradient δK^z, and (ii) encoding the qubit in a singlet-only subspace which is intrinsically insensitive to the fluctuating nuclear fields [1, 106–109]. In Papers II and I we proposed two approaches belonging to the former and latter types, respectively. The main ideas and findings of these papers are presented in this chapter.

5.1 TRANSPORT-INDUCED SUPPRESSION OF NUCLEAR FIELD FLUCTUATIONS

One approach to mitigate the nuclear noise in spin qubits that has been explored during the past years is active noise mitigation. By actively controlling the spin dynamics of the qubit one can use the hyperfine interaction to suppress the effects of the nuclear spins. Such methods can be roughly divided into two types: (i) By actively manipulating the spin qubit one can average out the effects of the semistatic nuclear field, e.g. by applying complex spin-echo-like pulse sequences that effectively filter out all peaks from the noise spectrum [110]. (ii) Exploiting the interplay between the electron dynamics and hyperfine interaction one can create an active feedback cycle where one uses the electron dynamics to manipulate the nuclear fields [111–115].

In this section we explore an approach that falls into the second category but is simpler to implement than other methods. A few years ago, experiments on a double quantum dot hosted in an InAs nanowire suggested that when running a DC electric current through the system in the regime of a Pauli spin blockade, an interplay between the hyperfine interaction and strong spin-orbit interaction (SOI) in InAs can give rise to a process of dynamical nuclear polarization that effectively quenches the total Zeeman gradient over the two dots [46]. In Paper II we investigated this idea in more detail, and showed how it not only works for double quantum dots with strong SOI, but also in the absence of SOI. In addition, and maybe more importantly, we showed that the idea can be implemented in a similar way in a linear triple quantum dot, where it results in a suppression of the harmful nuclear field gradients between neighboring dots.

5.1.1 *Singlet-triplet qubit*

In the previous chapter we investigated how the nuclear spins of the host material in an ST qubit affected the electron spin dynamics, and thus also the current, via the hyperfine interaction. However, this is not the full story. The flow of electrons through the qubit also induces dynamic nuclear spin polarization (DNP) that changes the nuclear spin polarizations on the dots, creating an effective feedback cycle. It turns out that in materials with a negative g-factor like e.g. GaAs, this feedback cycle tends to suppress the harmful nuclear field gradients over the two dots.

We describe the ST qubit using a similar model as in the previous chapter, i.e. the electron spin dynamics is described by a Lindblad master equation

$$\partial_t \rho = -i[H, \rho] + \Gamma(\rho) \tag{5.1}$$

with $H = H_{\rm Hub} + H_B$, where the Hubbard-like Hamiltonian reads as

$$H_{\rm Hub} = -\epsilon \left|S_{02}\right\rangle \left\langle S_{02}\right| + t_s \left|S\right\rangle \left\langle S_{02}\right| + i\mathbf{t}_{\rm so} \cdot \left|\mathbf{T}\right\rangle \left\langle S_{02}\right| + \text{h.c.}. \tag{5.2}$$

In contrast to the last chapter, we will here use a less general Zeeman Hamiltonian. By assuming that the external magnetic field is homogeneous and applied along our z-coordinate, and allowing for different g-tensors on the two dots as a result of the strong SOI, the Zeeman Hamiltonian reads as

$$H_B = E_Z\big(\left|T^+\right\rangle \left\langle T^+\right| - \left|T^-\right\rangle \left\langle T^-\right|\big) + \Delta_{\rm so}\big(\left|S\right\rangle \left\langle T^0\right| + \left|T^0\right\rangle \left\langle S\right|\big), \tag{5.3}$$

where $E_Z = \frac{1}{2}\mu_B\,(g_L + g_R)\,B^z$ is the Zeeman splitting, and $\Delta_{\rm so} = \frac{1}{2}\mu_B\,(g_L - g_R)\,B^z$ is the spin–orbit induced Zeeman gradient.

We did not consider the effects of the Overhauser fields in the Zeeman Hamiltonian above as we are interested in studying the dynamic coupling between the electron and nuclear spins in detail. The hyperfine Hamiltonian is therefore treated separately,

$$H_{\mathrm{hf}} = \sum_{i,k} \frac{A_k}{2} \left(2S_i^z I_{i,k}^z + S_i^+ I_{i,k}^- + S_i^- I_{i,k}^+ \right), \tag{5.4}$$

here written in terms of the ladder operators $O^\pm = O^x \pm iO^y,\ O \in \{S, I\}$. The first term couples the z-components of the electron and nuclear spins, and adds to the Zeeman splitting and gradient in Eq. (5.3) as the Overhauser field $K_i^z = \sum_k A_k I_{i,k}^z$. The two last terms can give rise to so-called spin flip-flop processes, where the electron on dot i exchanges one unit of angular momentum with one of the nuclei in the dot. In this way, a non-equilibrium electron spin polarization on the dots can slowly be transferred to the nuclear spin ensemble which, in turn, influences the electron dynamics yielding an intricate feedback cycle.

Before presenting analytic expressions it will be useful to develop a qualitative understanding of how this feedback cycle affects the nuclear spin polarizations. We start by investigating the simplest case without spin–orbit coupling, where only the $(1,1)$ singlet state is coupled to $|S_{02}\rangle$, and the system is stuck in spin-blockade in either of the three triplet states $|T^{\pm,0}\rangle$ with equal occupation probabilities. A non-zero Zeeman gradient $\Delta = \Delta_{\mathrm{so}} + \delta K^z$, where $\delta K^z = (K_L^z - K_R^z)/2$, can lift the spin-blockade of $|T^0\rangle$, leaving the system stuck in either of the polarized triplets $|T^\pm\rangle$ as illustrated in the spectrum in Fig. 5.1(a), where the thickness of the lines indicates the relative occupation probabilities. The only mechanisms that can then lift the blockade of the polarized triplets are the spin flip-flop processes, which couple the polarized states to the decaying unpolarized states through exchanging angular momentum with the nuclear spins ensemble, effectively changing the nuclear spin polarization.

By investigating the spin structure of the electronic states, we can then say something about the preferred direction of nuclear spin polarization. For a positive gradient $\Delta > 0$, the triplet state $|T^0\rangle$ evolves into state with a slightly stronger $|{\downarrow},{\uparrow}\rangle$ component, whereas the singlet state $|S\rangle$ acquires a slight $|{\uparrow},{\downarrow}\rangle$ character. Furthermore, because of the stronger coupling of $|S\rangle$ to $|S_{02}\rangle$ compared to $|T^0\rangle$ close to $\Delta = 0$, transitions to $|S\rangle$ are favored for lifting the spin-blockade. This makes flip-flop processes involving $S_L^+ K_L^-$ and $S_R^- K_R^+$ more likely than the opposite ones, as illustrated by the grey lines in Fig. 5.1(a). This results in a net negative(positive) pumping of nuclear spin in the left(right) dot, effectively driving δK^z, and thus also Δ, towards smaller values. Similarly, for a negative gradient $\Delta < 0$, $|T^0\rangle$ and $|S\rangle$ acquire a slight

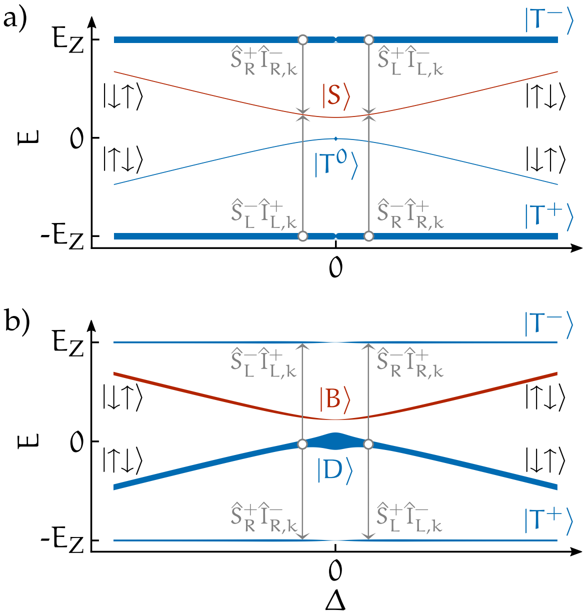

Figure 5.1: Energy spectrum of the four $(1,1)$ states as a function of Δ (a) without and (b) with spin-orbit coupling. The thickness of the lines indicates the occupation probability of the eigenstates, and the grey arrows indicate preferred electron-nuclear spin-flip rates close to $\Delta = 0$. We have here set $t = 0.6E_Z$, and in (b) we used $\mathbf{t} = \{0.4, 0.4, 0.4\}t_s$.

$|\uparrow,\downarrow\rangle$ and $|\downarrow,\uparrow\rangle$ character, respectively, resulting in a net positive pumping of δK^z and Δ. We thus see that independent of the sign of Δ, the nuclear field gradient δK^z is pumped towards $\Delta = 0$.

Similarly, we can develop a qualitative understanding for finite spin–orbit interaction. Including spin–orbit interaction lifts also the blockade of the two polarized triplets $|T^\pm\rangle$. However, if the total gradient Δ vanishes, the two unpolarized states can again be combined into a bright state $|B\rangle = \cos\eta\,|S\rangle + i\sin\eta\,|T^0\rangle$ that is coupled to $|S_{02}\rangle$ with strength $t = \sqrt{t_s^2 + (t_{so}^z)^2}$ and a dark state $|D\rangle = i\sin\eta\,|S\rangle + \cos\eta\,|T^0\rangle$ that is uncoupled and thus spin-blocked, see the spectrum in Fig 5.1(b). To escape spin blockade, spin flip-flop processes couple the blocked dark state $|D\rangle$ and the two polarized triplets $|T^\pm\rangle$ which are now coupled to $|S_{02}\rangle$ due to the finite spin–orbit interaction. We can thus develop a similar picture as for the spin–orbit free case by considering how $|D\rangle$ qualitatively changes for a non-zero Δ. Making Δ larger(smaller) than zero, $|D\rangle$ acquires a slightly larger $|\downarrow,\uparrow\rangle(|\uparrow,\downarrow\rangle)$ component. This in turn favors spin flip-flop processes that drives the gradient Δ towards zero, as illustrated by the grey arrows in Fig. 5.1(b).

Now that we have a brief understanding of the process behind the nuclear spin pumping, we can investigate the dynamics of the nuclear spin polarization analytically. We will do this by first calculating the occupancy and effective decay rates of the electronic states, which we in turn use to calculate the spin-flip rates of the nuclear spins perturbatively using Fermi's golden rule. Assuming that the decay rate Γ is the largest energy scale in the Lindblad master equation, we can separate the timescales of ρ involving $|S_{02}\rangle$ and the $(1,1)$ subspace, and describe the system using an effective model for the $(1,1)$ subspace. To include the effects of the decay rate Γ of $|S_{02}\rangle$ we add the term $-\frac{i}{2}\Gamma|S_{02}\rangle\langle S_{02}|$ to the Hamiltonian H. Then, projecting the now non-hermitian Hamiltonian H onto the $(1,1)$ subspace yields exchange terms on the form $(H_{ex})_{ij} = 4\epsilon T_{ij}/(4\epsilon^4 + \Gamma^2)$, with

$$T_{ij} = \langle i| H_{Hub} |S_{02}\rangle \langle S_{02}| H_{Hub} |j\rangle \,. \tag{5.5}$$

Further assuming that the Zeeman splitting E_Z is much larger than these exchange energies, we only need to consider the exchange energy $E_B = 4\epsilon(t_s^2 + t^{z2})/(4\epsilon^2 + \Gamma^2)$, yielding an effective Hamiltonian for the $(1,1)$ subspace,

$$H^{(1,1)} = \begin{pmatrix} E_Z & 0 & 0 & 0 \\ 0 & E_B & \Delta & 0 \\ 0 & \Delta & 0 & 0 \\ 0 & 0 & 0 & -E_Z \end{pmatrix}, \tag{5.6}$$

written in the basis $\{|T^+\rangle, |B\rangle, |D\rangle, |T^-\rangle\}$. In addition to the exchange energies, the projection also gives the $(1,1)$ state effective decay rates $\Gamma_i = 4\Gamma T_{ii}/(4\epsilon^2 + \Gamma^2)$, where we denote $\Gamma_{T^\pm} = \Gamma_t$. Using the effective Hamiltonian in Eq. (5.6) together with the effective decay rates, we write a time-evolution equation for the density matrix of the $(1,1)$ subspace $\rho^{(1,1)}$ similar to the Lindblad master equation in Eq. (5.1). Solving for steady-state $\partial_t\rho^{(1,1)} = 0$ we find the equilibrium density matrix $\rho_{eq}^{(1,1)}$, which by diagoalization yields the occupation probabilities p_i of the eigenstates $|i\rangle$.

The occupation probabilities and decay rates describe the dynamics of the four relevant $(1,1)$ spin states including the z-component of the quasistatic nuclear spins. We now add the in-plane contributions described by the flip-flop terms in Eq. (5.4) perturbatively to investigate how the electron spin dynamics affect the polarization of the nuclear spins. Assuming for simplicity nuclear spin 1/2, we express the flip rates of the nuclear spins on dot d using Fermi's golden rule

$$\gamma_d^{\pm} = \frac{A^2}{4N^2} N_d^{\mp} \sum_{i,j} p_i \frac{\Gamma_j}{E_Z^2} \left|\langle j| S_d^{\mp} |i\rangle\right|^2 + \gamma N_d^{\mp}, \tag{5.7}$$

where $N_d^{\pm}$ is the number of spinful nuclei on dot d, and we have assumed that all nuclei are coupled equally strong to the electron spin, $A_k = A/N$, for simplicity. Here, the factor Γ_j/E_Z^2 accounts for the lifetime broadening of the final state $|j\rangle$, assuming a Lorentzian level broadening in the limit $E_Z \gg \Gamma_j$. Furthermore, we also added a term that describes random nuclear spin flips with a rate γ to account phenomenologically for the slow relaxation of the nuclear spins to their fully mixed equilibrium state.

The flip rates can be translated into evolution equations for the dot polarizations $P_d = (N_d^+ - N_d^-)/N$. For the polarization gradient $P_\Delta = (P_L - P_R)/2$ and the average polarization $P_\Sigma = (P_L + P_R)/2$ we find the nonlinear evolution equations

$$\partial_t P_\Delta = -\left[F(\Delta) + \frac{1}{\tau}\right] P_\Delta - \frac{2F(\Delta)E_B\Delta}{E_B^2 + \Gamma_B^2/4 + 4\Delta^2}, \tag{5.8}$$

$$\partial_t P_\Sigma = -\left[F(\Delta) + \frac{1}{\tau}\right] P_\Sigma, \tag{5.9}$$

with

$$F(\Delta) = \frac{A^2}{4N^2E_Z^2} \frac{\Gamma_t^2(4E_B^2 + \Gamma_B^2 + 16\Delta^2) + 4\Gamma_B^2\Delta^2}{\Gamma_t(4E_B^2 + \Gamma_B^2 + 16\Delta^2) + 8\Gamma_B\Delta^2}, \tag{5.10}$$

and $1/\tau = 2\gamma/N$ being the phenomenological relaxation rate of the polarizations, usually $\tau \sim 1 - 10$ s. The evolution equations show how the polarizations acquire an enhanced relaxation rate $\tau^{-1} \to \tau^{-1} + F(\Delta)$ as a result of the electron dynamics, with $\partial_t P_\Delta$ having an additional term that drives the gradient towards $\Delta = 0$, which for typical parameters where $E_B \sim \Gamma_B \ll A$ dominates.

To illustrate these results we plot the pumping curves for the polarization gradient and average polarization in Fig. 5.2 for three different magnitudes of SOI, where we used as parameters $A = 250$ μeV, $E_Z = -5$ μeV, $N = 4^5$, and $\tau = 5$ s. For the curve without SOI (green) we used $E_B = 0.5$ μeV, $\Gamma_B = 0.25$ μeV, and $\Gamma_t = \Delta_{so} = 0$. The other two curves have $\Gamma_t = 0.01$ μeV, $\Delta_{so} = 0.5$ μeV (red) and $\Gamma_t = 0.0625$ μeV, $\Delta_{so} = 1$ μeV (blue). The plots indeed show that the polarization gradient is pumped towards $\delta K^z = -\Delta_{so}$, and the average polarization is pumped towards zero.

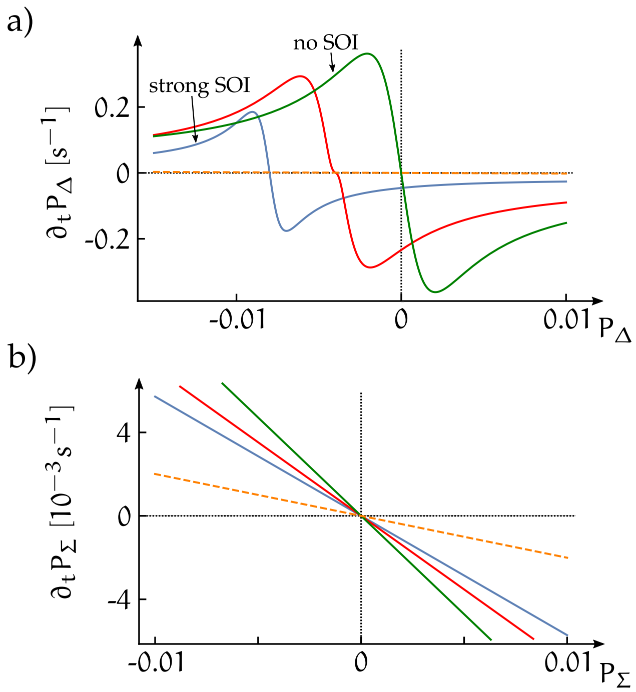

Figure 5.2: Pumping curves for the polarization gradient and the average polarization as given by (5.8) and (5.9). (a) $\partial_t P_\Delta$ as a function of P_Δ and (b) P_Σ as a function of P_Σ. Both plots show three curves corresponding to no SOI (green), intermediate SOI (red), and strong SOI (blue), compared to a reference without any spin pumping (orange dashed line).

5.1.2 *Exchange-only qubit*

Above we showed that running an electric current through a double quantum dot can drive the harmful nuclear field gradient in the ST qubit towards zero, resulting in an effective reduction of the nuclear noise fluctuations. We here show that we can implement a similar approach in a linear triple quantum dot which suppresses both of the two nuclear field gradients of the XO qubit.

Like for the ST qubit, we model the XO qubit using the model Hamiltonian

$$H = H_{\text{Hub}} + H_{B}, \tag{5.11}$$

where we use the same Hubbard-like and Zeeman Hamiltonian that we used to describe the XO qubit in Sec. 2.4, which explicitly read

$$\begin{aligned} H_{\text{Hub}} = &\sum_{\alpha=\pm} \left\{ (\epsilon_M + \epsilon) |D^{\alpha}_{L}\rangle \langle D^{\alpha}_{L}| + (\epsilon_M - \epsilon) |D^{\alpha}_{R}\rangle \langle D^{\alpha}_{R}| \right\} \\ &+ \frac{t}{2} \sum_{\alpha=\pm} \alpha \left\{ \sqrt{3} |D^{\alpha}_{1}\rangle \left[\langle D^{\alpha}_{R}| - \langle D^{\alpha}_{L}| \right] + |D^{\alpha}_{2}\rangle \left[\langle D^{\alpha}_{R}| + \langle D^{\alpha}_{L}| \right] \right\} + \text{h.c.}, \end{aligned} \tag{5.12}$$

and

$$\begin{aligned} H_{Z} = g\mu_B B^z &\sum_{\alpha=\pm} \left\{ \alpha\frac{3}{2} |Q^{\alpha 3/2}\rangle \langle Q^{\alpha 3/2}| + \alpha\frac{1}{2} \Big[|Q^{\alpha 1/2}\rangle \langle Q^{\alpha 1/2}| \right. \\ &\left. + |D^{\alpha}_{1}\rangle \langle D^{\alpha}_{1}| + |D^{\alpha}_{2}\rangle \langle D^{\alpha}_{2}| + |D^{\alpha}_{L}\rangle \langle D^{\alpha}_{L}| + |D^{\alpha}_{R}\rangle \langle D^{\alpha}_{R}| \Big] \right\}, \end{aligned} \tag{5.13}$$

respectively. For the XO qubit we will neglect SOI because a finite SOI always lifts the spin blockade and thus competes with the flip-flop terms in the hyperfine interaction, thereby reducing the efficiency of the spin pumping.

We add the effects of hyperfine interaction using the Hamiltonian in Eq. (5.4), where we again assume that the average nuclear polarization over the dots K_{Σ} is much smaller than the Zeeman energy E_Z and can be neglected. The hyperfine interaction then affects the XO qubit in two ways: (i) The flip-flop terms $S^{\pm}_{i} I^{\mp}_{i,k}$ exchange angular momentum between the confined electrons and the nuclei on the same dot, and (ii) the two nuclear field gradients $\delta K^z_M = (\delta K^z_{LC} - \delta K^z_{CR})/2$ and $\delta K^z_{LR} = (K^z_L - K^z_R)/2$, where $\delta K^z_{ij} = (K^z_i - K^z_j)/2$, couple states with the same spin projection, which effect can be described by the Hamiltonian

$$H^{\pm 1/2}_{\text{hf}} = \pm \begin{pmatrix} 0 & -\frac{\sqrt{2}}{3}\delta K_M & \sqrt{\frac{2}{3}}\delta K_{LR} \\ -\frac{\sqrt{2}}{3}\delta K_M & -\frac{1}{3}\delta K_M & -\frac{1}{\sqrt{3}}\delta K_{LR} \\ \sqrt{\frac{2}{3}}\delta K_{LR} & -\frac{1}{\sqrt{3}}\delta K_{LR} & \frac{1}{3}\delta K_M \end{pmatrix} \tag{5.14}$$

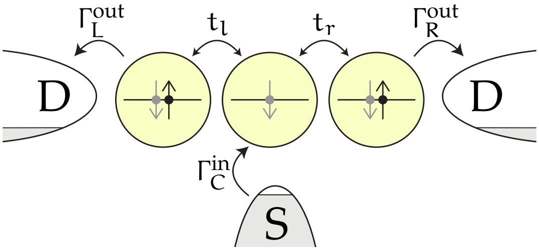

Figure 5.3: The triple quantum dot of the XO qubit with the central dot connected to a source and the two outer dots connected to drains. An applied bias voltage enables electrons to flow from the source to either of the drains.

acting on the two $S^z = \pm 1/2$ subspaces $\{|Q^{\pm 1/2}, |D_1^{\pm 1/2}\rangle, |D_2^{\pm 1/2}\rangle\rangle\}$.

Adding the effects of the three leads, we apply a source-drain bias voltage as shown in Fig. 5.3, enabling a current to flow from the center lead to the two outer leads. The current through the linear triple dot can follow one of the two possible transport cycles $(1,1,1) \to (2,0,1)/(1,0,2) \to (1,0,1) \to (1,1,1)$. By again assuming that the system is in the open regime, where the rates $\Gamma = \Gamma_C^{in} = \Gamma_{L,R}^{out}$ are the largest energy scales, the interesting dynamics happen during the $(1,1,1) \to (2,0,1)/(1,0,2)$ transition, which involves the 12 states discussed above. We can then describe the dynamics of these 12 states using the Lindblad master equation as before,

$$\partial_t \rho = -i[H, \rho] + \boldsymbol{\Gamma}(\rho), \tag{5.15}$$

where the superoperator reads $\boldsymbol{\Gamma}(\rho) = -\frac{1}{2}\Gamma\{P_{dec}, \rho\} + \frac{1}{8}\Gamma(\mathbb{1} - P_{dec})\rho_{dec}$, with the projection operator $P_{dec} = \sum_{i=D_{L,R}^{\alpha}} |i\rangle\langle i|$ projecting on the subspace $\{D_L, D_R\}$ that that can decay by having an electron tunnel to the drain leads, and $\rho_{dec} = \sum_{i=D_{L,R}^{\alpha}} \rho_{i,i}$.

Like for the ST qubit, it will be useful to first develop a qualitative understanding of how the feedback cycle affects the nuclear spin polarizations in the XO qubit, before presenting analytic expressions. When the gradients $\Delta_{LR} = \delta K_{LR}$ and $\Delta_M = \delta K_M$ are zero, the electrons are trapped in one of the four quadruplet states. A non-zero gradient mixes states with equal spin polarization, giving all states with $S_z = \pm 1/2$ a finite coupling to $|D_{L,R}\rangle$, leaving the electrons trapped in the fully polarized quadruplet states $|Q^{\pm 3/2}\rangle$. For small gradients, the doublets have a much stronger coupling to $|D_{L,R}\rangle$ than $|Q^{\pm 1/2}\rangle$, making the spin-flip processes dominated by transitions from $|Q^{\pm 3/2}\rangle$ to a doublet states. It turns out that transitions to $|D_2\rangle$ do not contribute strongly to spin-pumping as the transitions to $|D_2^{\pm}\rangle$ cancel out. Transitions to $|D_1\rangle$, however, which have the largest coupling to $|D_{L,R}\rangle$,

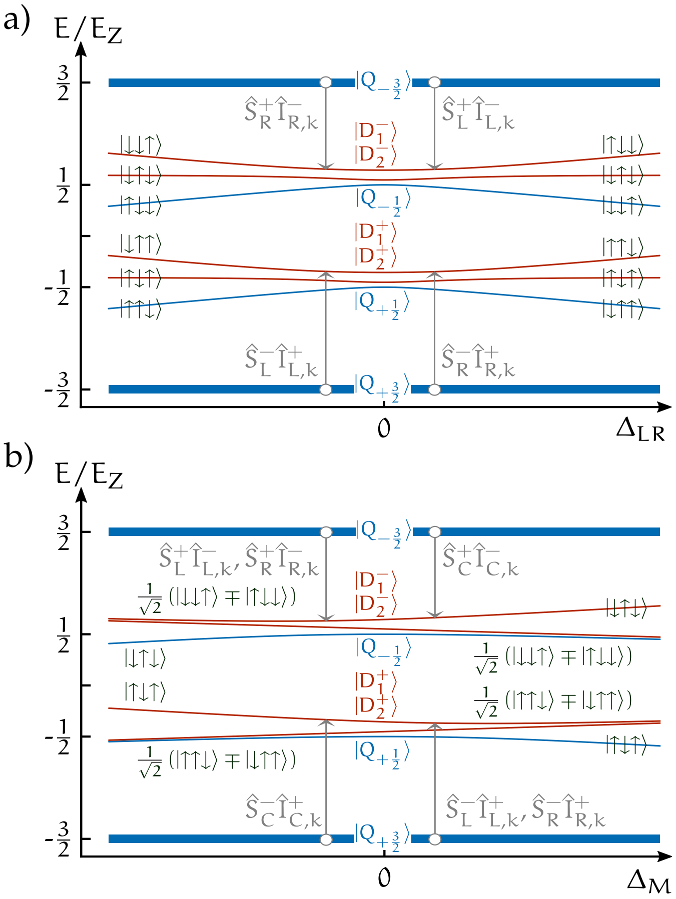
a)
E/E_Z
$\frac{3}{2}$
$\frac{1}{2}$
$-\frac{1}{2}$
$-\frac{3}{2}$
$|Q_{-\frac{3}{2}}\rangle$
$\hat{S}_R^+\hat{I}_{R,k}^-$
$\hat{S}_L^+\hat{I}_{L,k}^-$
$|D_1^-\rangle$
$|D_2^-\rangle$
$|\downarrow\downarrow\uparrow\rangle$
$|\downarrow\uparrow\downarrow\rangle$
$|\uparrow\downarrow\downarrow\rangle$
$|Q_{-\frac{1}{2}}\rangle$
$|\downarrow\uparrow\uparrow\rangle$
$|D_1^+\rangle$
$|D_2^+\rangle$
$|\uparrow\uparrow\downarrow\rangle$
$|\uparrow\downarrow\uparrow\rangle$
$|\uparrow\uparrow\downarrow\rangle$
$|Q_{+\frac{1}{2}}\rangle$
$|\downarrow\uparrow\uparrow\rangle$
$\hat{S}_L^-\hat{I}_{L,k}^+$
$\hat{S}_R^-\hat{I}_{R,k}^+$
$|Q_{+\frac{3}{2}}\rangle$
0
Δ_{LR}
b)
E/E_Z
$\frac{3}{2}$
$\frac{1}{2}$
$-\frac{1}{2}$
$-\frac{3}{2}$
$|Q_{-\frac{3}{2}}\rangle$
$\hat{S}_L^+\hat{I}_{L,k}^-, \hat{S}_R^+\hat{I}_{R,k}^-$
$\hat{S}_C^+\hat{I}_{C,k}^-$
$\frac{1}{\sqrt{2}}(|\downarrow\downarrow\uparrow\rangle \mp |\uparrow\downarrow\downarrow\rangle)$
$|D_1^-\rangle$
$|D_2^-\rangle$
$|\downarrow\uparrow\downarrow\rangle$
$|\downarrow\uparrow\downarrow\rangle$
$|Q_{-\frac{1}{2}}\rangle$
$\frac{1}{\sqrt{2}}(|\downarrow\downarrow\uparrow\rangle \mp |\uparrow\downarrow\downarrow\rangle)$
$|\uparrow\downarrow\uparrow\rangle$
$|D_1^+\rangle$
$|D_2^+\rangle$
$\frac{1}{\sqrt{2}}(|\uparrow\uparrow\downarrow\rangle \mp |\downarrow\uparrow\uparrow\rangle)$
$\frac{1}{\sqrt{2}}(|\uparrow\uparrow\downarrow\rangle \mp |\downarrow\uparrow\uparrow\rangle)$
$|Q_{+\frac{1}{2}}\rangle$
$|\uparrow\downarrow\uparrow\rangle$
$\hat{S}_C^-\hat{I}_{C,k}^+$
$\hat{S}_L^-\hat{I}_{L,k}^+, \hat{S}_R^-\hat{I}_{R,k}^+$
$|Q_{+\frac{3}{2}}\rangle$
0
Δ_M

Figure 5.4: Energy spectrum of the eight $(1,1,1)$ states as a function of (a) Δ_{LR} and (b) Δ_M, where the thickness of the lines indicates the occupation probability of the eigenstates, and the grey arrows indicate preferred electron-nuclear spin-flip rates.

effectively pump the two gradients towards zero in a similar way as for the ST qubit, as illustrated in Fig. 5.4.

To derive analytic expressions describing the dynamics of the polarization gradients we again assume that Γ is the largest energy scale, and project the Hamiltonian onto the $(1,1,1)$ subspace. The projection introduces an exchange energy $E_{1,2} = (2 \pm 1)\zeta_D \epsilon_M$ and decay rate $\Gamma_{1,2} = (2 \pm 1)\zeta_D \Gamma$ to the doublet states $|D_{1,2}\rangle$, respectively, where the unit-less parameter,

$$\zeta_D = \frac{2t^2}{4\epsilon_M^2 + \Gamma^2}, \tag{5.16}$$

characterizes the relative strength of the coupling to $|D_{L,R}\rangle$. By further assuming that the exchange energies $E_{1,2}$ are much larger than the gradients ϵ and ϵ_M, the Hamiltonian H is diagonalized using second-order perturbation theory. The resulting eigenstates and their respective decay rates can then be inserted into Fermi's golden rule in Eq. (5.7) to obtain the hyperfine-induced flip-flop rates to lowest order in the field gradients ϵ and ϵ_M. Translating the flip-flop rates into evolution equations for the average polarization P_Σ and the polarization gradients $P_{LR} = (P_L - P_R)/2$ and $P_M = (P_L + P_R)/2 - P_C$ then yields

$$\partial_t P_{LR} = -\left[G + \frac{1}{\tau}\right] P_{LR} - \frac{\Gamma}{\epsilon_M}\Delta_{LR}, \tag{5.17}$$

$$\partial_t P_M = -\left[\frac{5}{3}G + \frac{1}{\tau}\right] P_M - G P_\Sigma - \frac{2\Gamma}{3\epsilon_M}\Delta_M, \tag{5.18}$$

$$\partial_t P_\Sigma = -\left[\frac{4}{3}G + \frac{1}{\tau}\right] - \frac{2}{9} G P_M, \tag{5.19}$$

with $G = A^2\zeta_D\Gamma/4N^2E_Z^2$, where we have again assumed equal N on all dots, for simplicity.

The evolution equations show that, similar to in the double dot, the polarization gradients acquire an effectively enhanced relaxation rate. In addition, we find that the polarization dynamics of the two gradients are coupled, which is a result of the geometry of the source and drains. However, for typical parameters the last terms in Eqs. (5.17) and (5.18) dominate, effectively suppressing both nuclear field gradients of the XO qubit. In Fig. 5.5 we plot the nuclear polarization gradients (a) $\partial_t P_{LR}$ and (b) $\partial_t P_M$ calculated numerically using Eq. (5.7), where the black lines represent the vector field $(\partial_t P_M, \partial_t P_{LR})$, showing how both polarization gradients are pumped towards 0. Furthermore, the indents show line cuts along the red dashed lines, where the orange lines show the slope of $\partial_t P$ as predicted by Eqs. (5.17) and (5.18), thus confirming the validity of our analytic expressions at small fields.

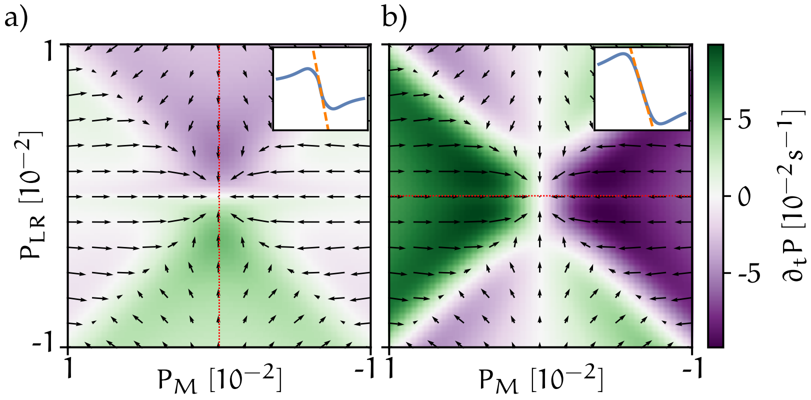

Figure 5.5: (a) $\partial_t P_{LR}$ and (b) $\partial_t P_M$ as a function of P_{LR} and P_M, calculated numerically using Eq. (5.7). The indents show line cuts along the red dashed lines, where the orange dashed lines show the slope of $\partial_t P$ as predicted by Eqs. (5.17) and (5.18). In both plots we include the black arrows representing the same vector field ($\partial_t P_M$, $\partial_t P_{LR}$).

As parameters we used $P_\Sigma = 0$, $A = 125$ µeV, $E_Z = 12.5$ µeV, $N = 4 \times 10^5$, $\tau = 5$ s, $\epsilon_M = 100$ µeV, $\epsilon = 0$, $\Gamma = 75$ µeV, and $t = 7.5$ µeV.

5.2 HIGHLY TUNABLE TRIPLE DOT SINGLET-ONLY QUBIT

The second approach we will explore that aims to mitigate nuclear noise in spin qubits are the so-called singlet-only (SO) qubits [1, 108, 109]. The idea behind the SO qubit is simple; by encoding the qubit in a decoherence-free subspace consisting of two singlet states, the qubit states will not be coupled to each other via the hyperfine interaction. The first SO qubit that was proposed was the exchange-only singlet-only (XOSO) spin qubit [108], where the two singlet states were created using four electrons in a quadruple quantum dot formed in a T-shape. By tuning one of the tunnel barriers unequal to the two other barriers, the two singlets acquire different exchange energies, making them a good basis for a fully-controllable spin qubit.

Despite promising drastically improved coherence times compared to the XO qubit, the XOSO qubit had the drawbacks of a relatively small qubit splitting and requiring a new four-quantum dot device for realization. In Paper I we sought to solve both these drawbacks by creating a SO qubit with a tunable qubit splitting hosted in a triple quantum dot that can straightforwardly be implemented in already existing triple-dot devices. The qubit is constructed by tuning the three quantum dots to the $(1,4,1)$ charge configura-

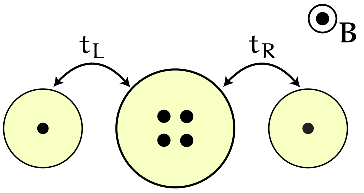

Figure 5.6: Sketch of the linear triple quantum dot tuned to the $(1,4,1)$ charge configuration with a perpendicular applied magnetic field.

tion, see Fig. 5.6, where an interplay between an external magnetic field and the Coulomb interaction results in a magnetic-field-dependent singlet-triplet crossing on the center dot. Coupling the four-electron states on the center dot to the two spins on the outer dots then creates two singlet states that form the basis of our SO qubit. Before presenting the details of the qubit in Sec. 5.2.2 we briefly explore the multi-electron states used to create it.

5.2.1 *Multi-electron quantum dots*

So far we have only considered the ground state orbital in quantum dots due to the large excitation energy. For multi-electron (above 2) quantum dots we will now have to include the orbital effects of higher-lying orbitals. In addition to the added orbital effects, we also need to take the Coulomb interaction between the electrons seriously in multi-electron quantum dots.

To calculate an approximate spectrum for the multi-electron states we start by describing a single electron (labeled i) using the single-particle Hamiltonian,

$$H_0^{(i)} = \frac{1}{2m^*}\left[\mathbf{p}_i + e\mathbf{A}(\mathbf{r}_i)\right]^2 + \frac{1}{2}m^*\omega_0^2\mathbf{r}_i^2 + \frac{1}{2}g\mu_B B\sigma_i^z, \tag{5.20}$$

where $\mathbf{A}(\mathbf{r}) = \frac{1}{2}B(x\hat{y} - y\hat{x})$ is the vector potential, ω_0 sets the effective radius of the dot in the absence of a magnetic field $\sigma_0 = \sqrt{\hbar/m^*\omega_0}$, g is the g-factor of the host material, σ^z is the third Pauli matrix, and we assumed parabolic confinement. The eigenstates of $H_0^{(i)}$ are the well-known Fock-Darwin states,

$$\psi_{n,l,\eta}(\mathbf{r}_i) = \sqrt{\frac{n!}{\pi\sigma^2(n+|l|)!}}\rho_i^{|l|}e^{-\rho_i^2/2}L_n^{|l|}\left(\rho_i^2\right)e^{-il\theta_i}, \tag{5.21}$$

written in terms of the dimensionless polar coordinates $\rho = r/\sigma$ and θ, where $L_a^b(x)$ is the associated Laguerre polynomial, and $\sigma = \sqrt{\hbar/m^*\Omega}$, with $\Omega = \sqrt{\omega_0^2 + \omega_c^2/4}$ and $\omega_c = eB/m^*$. Here, the quantum numbers $n \in \mathbb{N}_0$,

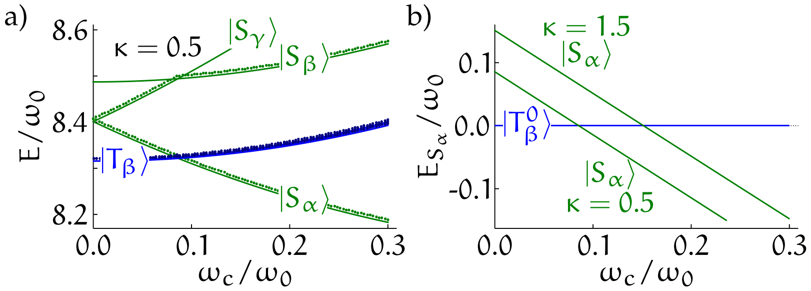

Figure 5.7: (a) Low-energy part of the four-electron spectrum as a function of the applied magnetic field with $\kappa = 0.5$ and $g = -0.4$, where the dots(lines) represent the numerical(perturbative) results. (b) The numerically calculated energy of the lowest singlet $|S_\alpha\rangle$ relative to the unpolarized triplet $|T^0_\beta\rangle$ for $\kappa = 0.5$ and $\kappa = 1.5$.

$l \in \mathbb{Z}$, and $\eta = \pm 1$ label the radial state, orbital angular momentum, and spin of the electron, respectively. The eigenenergies corresponding to the Fock-Darwin states are

$$E^{(i)}_{n,l,\eta} = \Omega(2n + |l| + 1) - \frac{1}{2}\omega_c l + \frac{1}{4} g \frac{m^*}{m_e}\omega_c \eta, \tag{5.22}$$

where the first term gives the regular two-dimensional harmonic-oscillator energies, but with a magnetic-field-dependent oscillator frequency Ω, the second term describes the coupling between the angular momentum l and the external magnetic field, and the third term accounts for the Zeeman effect.

From the lowest energetic Fock-Darwin states, with quantum numbers $n \leqslant 1$ and $|l| \leqslant 3$, we create antisymmterized product states that we use as basis for our many-particle states. In the new many-particle basis we then evaluate all matrix elements of the Coulomb interaction Hamiltonian

$$V = \sum_{i<j} \frac{e^2}{4\pi\epsilon_r |\mathbf{r}_i - \mathbf{r}_j|}, \tag{5.23}$$

with ϵ_r being the effective dielectric constant of the surroundings of the quantum dot. The eigenstates and -energies of the many-particle states are then obtained by diagonalizing the full Hamiltonian $H_1 = \sum_i H^{(i)}_0 + V$, which can be done numerically or, in the weak-interaction limit characterized by $\kappa \equiv e^2/4\pi\epsilon_r\sigma_0\omega_0 \ll 1$, using perturbation theory in κ.

In Fig. 5.7(a) we present a typical spectrum for the lowest six multi-electron states of a quantum dot hosting four interacting electrons, where we used $\kappa = 0.5$ and $g = -0.4$, and the blue and green lines label the singlet and triplet states, respectively. The three triplet states labeled $|T_\beta^{\pm,0}\rangle$ live mostly in the orbital configuration $(0,0)^2(0,1)^1(0,-1)^1$, where $(n,l)^m$ denotes m electrons in orbital state (n,l). The three singlet states $|S_{\alpha,\beta,\gamma}\rangle$ have the largest weight in the orbital configurations $(0,0)^2(0,1)^2$, $(0,0)^2(0,1)^1(0,-1)^1$ and $(0,0)^2(0,-1)^2$, respectively. Furthermore, the solid lines are the perturbative results, which are in good agreement with the dots indicating the numerical results.

To create our singlet-only qubit we will utilize the lowest energy singlet $|S_\alpha\rangle$ and the unpolarized triplet $|T_\beta^0\rangle$. We therefore plot the numerically calculated energy of $|S_\alpha\rangle$ relative to $|T_\beta^0\rangle$ as a function of $\omega_c = eB/m^*$ in Fig. 5.7(b) for $\kappa = 0.5$ and $\kappa = 1.5$. For both values of κ the singlet-triplet splitting $E_{ST} = E_{T_\beta^0} - E_{S_\alpha}$ is to good approximation linear in ω_c in the region of interest, and becomes zero around $\omega_c/\omega_0 \sim 0.1$. Both of these features are key ingredients for our singlet-only qubit. Finally, for small $\kappa \lesssim 0.5$ we find a short and compact expression for the singlet-triplet splitting[1],

$$E_{ST} \approx \gamma_0\omega_0 + \omega_c, \tag{5.24}$$

with $\gamma_0 = -0.235\,\kappa + 0.128\,\kappa^2$.

5.2.2 *The qubit*

As above-mentioned, the qubit is defined in two six-electron singlet states hosted in a linear triple quantum dot with a perpendicular magnetic field. Like for the XO qubit presented in Sec. 2.4, we describe the triple quantum dot using a Hubbard-like Hamiltonian,

$$H = \sum_{i=1}^{3}\left(H_1^{(i)} - V_i n_i\right) + \sum_{\langle i,j\rangle}\frac{U_c}{2}n_i n_j - \sum_{\langle i,j\rangle,\eta}\frac{t_{ij}}{\sqrt{2}}c_{i\eta}^\dagger c_{j\eta}, \tag{5.25}$$

where the on-site Coulomb interaction that we previously described by the charging energy U has been replaced by the many-particle Hamiltonian $H_1^{(i)}$ for dot i as described above. By using a Hubbard-like Hamiltonian like Eq. (5.25) we effectively assume that: (i) The separation between the dots is large enough to allow us to treat the interdot electrostatic energy as being independent of the exact orbital configuration of the electrons on neighboring dots. (ii) All tunneling processes we will consider mostly involve the same orbital structures allowing us to use tunneling coefficients t_{ij} that are independent of the exact electronic orbitals involved. (iii) The gate-induced

---

[1] See supplementary material for Paper I for all derivations and an explicit expression for γ_0.

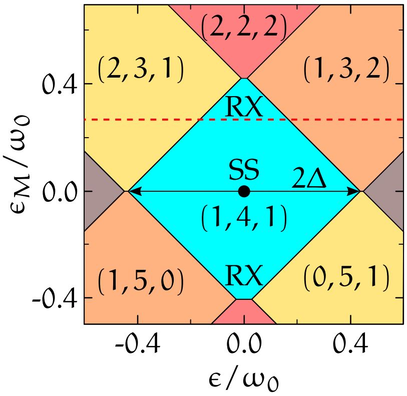

Figure 5.8: Six-electron charge stability diagram around the $(1,4,1)$ region, as a function of the two detuning potentials ϵ_M and ϵ.

potentials are smooth enough so that all electronic orbitals are affected in the same way.

Neglecting the tunneling term in the Hamiltonian, we study the electrostatic properties by diagonalizing the first two terms in Eq. (5.25). The resulting charge stability diagram, showing the charge configuration of the ground state, is shown Fig. 5.8 as a function of the two detuning potentials $\epsilon_M = (V_1 + V_3)/2 - V_2$ and $\epsilon = (V_3 - V_1)/2$, where we fixed $V_1 + 4V_2 + V_3 = -E_{S_\alpha} - 8U_c$ to focus on the regime around $(1,4,1)$. We here assumed different dot sizes, $\sigma_0 = 30$ nm for the central dot and $\sigma_0 = 20$ nm for the outer dots, and further used $U_c = 0.2\omega_0$, $\omega_c/\omega_0 = 0.1$, $\kappa = 0$ and $m^*/m_e = 0.067$ with ω_0 being the bare level splitting on the central dot.

Within the $(1,4,1)$ charge region the four lowest-energy singlet states that can be written as

$$|0\rangle = |S_\alpha S_{(13)}\rangle, \tag{5.26}$$

$$|1\rangle = \frac{1}{\sqrt{3}}\left[|T^0_\beta T^0_{(13)}\rangle - |T^-_\beta T^+_{(13)}\rangle - |T^+_\beta T^-_{(13)}\rangle\right], \tag{5.27}$$

$$|2\rangle = |S_\beta S_{(13)}\rangle, \tag{5.28}$$

$$|3\rangle = |S_\gamma S_{(13)}\rangle, \tag{5.29}$$

where $|S_{(13)}\rangle$ and $|T_{(13)}\rangle$ indicate that the two electrons in the outer dots are paired in a singlet and triplet state, respectively. By tuning the central dot close to the singlet-triplet crossing, which for a central dot of $\sigma_0 = 30$ nm happens at $B \approx 75$ mT, the two lowest-energy singlet states $|0\rangle$ and $|1\rangle$ can be used as qubit states, with the two other singlets $|2\rangle$ and $|3\rangle$ being split off by

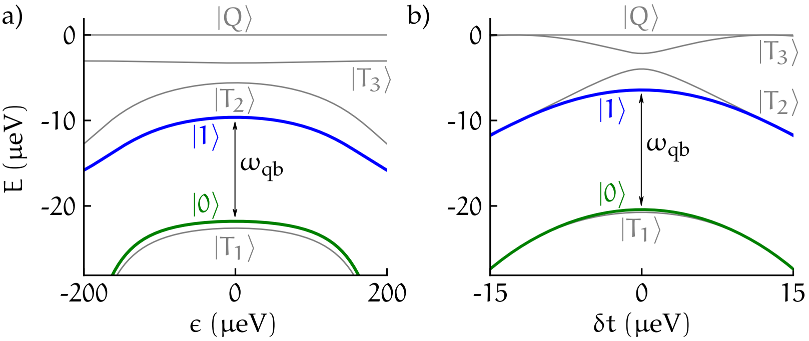

Figure 5.9: Low-energy part of the spectrum of the Hubbard-like Hamiltonian in Eq. (5.25) as a function of (a) ϵ at $\epsilon_M/\omega_0 = 0.27$ and (b) δt at the SS. The green and blue lines show the singlet qubit states $|0\rangle$ and $|1\rangle$, respectively, and the grey lines show the close-lying triplet and quintuplet states.

an energy much larger than the qubit splitting as shown by the spectrum in Fig. 5.7(a).

We then investigate the low-energy spectrum of the Hamiltonian in Eq. (5.25) for the two regions of interest: (i) In the RX regime, close to the top and bottom of the $(1,4,1)$ region, the strong exchange interaction provides fast qubit control through ϵ. Here the low-energy spectrum is plotted in Fig. 5.9(a) as a function of ϵ along the red line in Fig. 5.8, corresponding to $\epsilon_M/\omega_0 = 0.27$, where we ignored the Zeeman splitting for clarity and used the same parameters as in Fig. 5.8 with $t_{12} = t_{23} = 25$ μeV. (ii) At the SS in the center of the $(1,4,1)$ region the qubit is to linear order in the potentials V_i protected from charge noise. Using as parameters $\epsilon = \epsilon_M = 0$ and $t = (t_{12} + t_{23})/2 = 25$ μeV we plot the low-energy spectrum as a function of $\delta t = t_{12} - t_{23}$ in Fig. 5.9(b).

Assuming that the tunnel couplings t_{ij}, which are typically $t_{ij} \sim 10$ μeV, are much smaller than the width of the $(1,4,1)$ region 2Δ as defined in Fig. 5.8, we treat the tunnel couplings perturbatively and project the full Hamiltonian in Eq. (5.25) onto the qubit subspace by means of a Schrieffer-Wolff transformation [116]. To second order in t_{ij} this yields the qubit Hamiltonian

$$H_{qb} = \frac{1}{2}\left(E_{ST} + J_z\right)\sigma^z + J_x\sigma^x, \tag{5.30}$$

where the qubit splitting is dominated by the magnetic-field-dependent singlet-triplet splitting E_{ST} as given by Eq. (5.24). We emphasize that this magnetic field dependence arises due to the coupling between the magnetic field and the orbital degrees of freedom of the electrons; the singlet-only qubit subspace remains insensitive to the coupling of magnetic fields to the spin of the electrons. For approximately symmetric tunnel couplings $t_{12} \approx t_{23}$ and close to the line where $\epsilon = 0$, the two exchange terms read as

$$J_z \approx -t^2 \left[\frac{\Delta}{\Delta^2 - \epsilon_M^2} + \frac{3(\Delta + \omega_c)}{(\Delta + \omega_c)^2 - \epsilon_M^2} \right], \tag{5.31}$$

$$J_x \approx \frac{\sqrt{6} t \Delta}{\Delta^2 - \epsilon_M^2} \left[\delta t + \frac{2t\epsilon_M}{\Delta^2 - \epsilon_M^2} \epsilon \right]. \tag{5.32}$$

The J_z term provides a small tuning-dependent correction to the qubit splitting, which is mainly determined by E_{ST}, whereas the J_x provides a coupling to σ^x that is linear in ϵ and δt, which can be used to drive Rabi oscillations in the RX regime and at the SS, respectively.

5.2.3 *Qubit manipulation and decoherence*

Single-qubit rotations can be performed via resonant Rabi driving using a sinusoidal modulation $q(t) = q_0 + \tilde{q} \sin(\omega t)$ of a tuning parameter $q = \{\epsilon, \delta t\}$. For small enough amplitudes $\tilde{q}$ the qubit Hamiltonian in Eq. (5.30) can be approximated as

$$H_{qb} = \frac{1}{2} (E_{ST} + J_z) \sigma^z + A_q \sin(\omega t) \sigma^x, \tag{5.33}$$

where $A_q = \tilde{q}\,(dJ_x/dq)_{q=q_0}$. Resonantly driving the qubit with frequency $\omega = E_{ST} + J_z$ then induces Rabi oscillations with a frequency A_q, providing single-qubit manipulation. By picking the right tuning parameter we can obtain fast qubit operation at both the RX regime and at the SS. At the RX regime we can use $q = \epsilon$ as tuning parameter, which for an amplitude of $\tilde{\epsilon} = 5 - 10$ μeV gives a Rabi period of $T_{\text{Rabi}} \approx 20 - 40$ ns. At the SS, the tuning parameter $q = \delta t$ is more efficient, yielding a Rabi period of $T_{\text{Rabi}} = 20$ ns for an amplitude of $\tilde{\delta t} = 2$ μeV.

Finally, we investigate the coherence properties of the qubit. Because both qubit states are singlets, there is no direct coupling between the qubit states via the hyperfine interaction to lowest order. Couplings to other states, however, can give rise to energy shifts in the qubit splitting that are of a higher order in the hyperfine coupling, potentially leading to dephasing. To get a rough estimate for the scale of this dephasing we consider their effect on Rabi oscillations during resonant driving, and find an estimated dephasing time of $T_2^* \sim A_q (E_0 - E_{T_1^0})^2 / \sigma_K^4$, where $\sigma_K = A/\sqrt{N}$ and E_i is the energy of state $|i\rangle$ with $|T_1^0\rangle = |S_\alpha T^0_{(13)}\rangle$ being the closest lying triplet state. Based

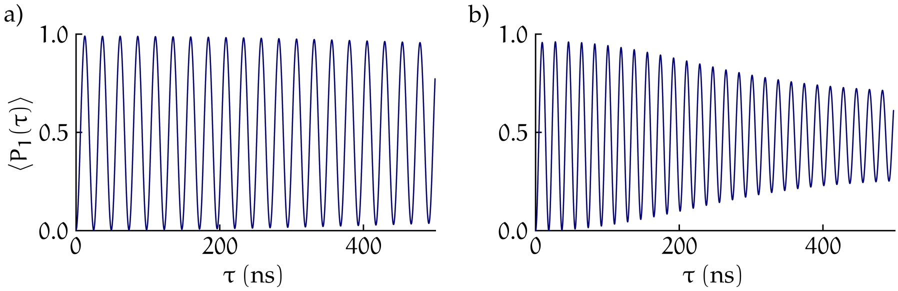

Figure 5.10: Time-dependent return probability $\langle P_1(\tau)\rangle$ after averaging over 2500 nuclear configurations with zero mean and $\sigma_K = 0.07$, (a) in the RX regime with $\bar{\epsilon} = 10$ μeV and (b) at the SS with $\delta\bar{t} = 2$ μeV.

on the low-energy spectra in Fig. 5.9 we therefore expect less nuclear noise induced dephasing at the RX regime than at the SS, a result of the larger exchange interaction that determines the splitting of $|0\rangle$ and $|T_1^0\rangle$. To illustrate the coherence properties we plot the probability $\langle P_1(\tau)\rangle$ of finding the qubit in $|1\rangle$ after initializing in $|0\rangle$ and resonantly driving for a time τ. In Fig. 5.10 we show the resulting time-dependent probabilities for (a) driving ϵ in the RX regime and (b) driving δt at the SS, after averaging over 2500 random nuclear configurations with $g\mu_B K^{x,y,z}$ each taken from a normal distribution with zero mean and $\sigma_K = 0.07$ μeV, where we used the same parameters as above with driving amplitudes $\tilde{\epsilon} = 10$ μeV and $\tilde{\delta t} = 2$ μeV. The plots indeed agree with our rough estimate, showing that the qubit is less sensitive to nuclear noise in the RX regime than at the SS.

6

GROUP-IV SEMICONDUCTORS AND VALENCE BAND HOLES

Although GaAs-based devices have propelled the spin qubit field forward for more than a decade, their coherence times are intrinsically limited by the nuclear noise [52–54]. A potential solution to this problem is to host the qubits in group-IV materials, such as Si or Ge, which can be made almost nuclear-spin-free by isotopic purification [55–59], removing the nuclear noise altogether. There has therefore been a lot of interest recently in Si- and Ge-based spin qubits, where Si also has the advantage of leveraging already developed commercial mass chip-manufacturing techniques. However, using group-IV semiconductors also comes with the complication of extra valley degrees of freedom, providing additional channels for leakage and dephasing [60, 61].

Lately, there has been substantial progress with Si- and Ge-based spin qubits that use the spin of valence-band holes instead of the electron spin [62–70]. These holes do not have the complicating valley degree of freedom of the electrons while still benefiting from the protection against nuclear noise due to the absence of nuclear spins in purified samples. Moreover, since the orbitals that make up the valence band are of p type [71], the valence band holes have the additional advantage of weaker coupling to any residual nuclear spins due to the wave function vanishing at the atomic site [117]. However, since the orbitals that constitute the valence band are of p-type [71], the corresponding states have a total six-fold angular momentum degree of freedom, possibly leading to highly anisotropic dynamics. Compared to the valley mixing of the electronic states, however, these dynamics are relatively predictable, and the built-in mixing of orbital and spin degrees of freedom can yield strong effective spin–orbit coupling that allows for fast qubit operation [83–89].

In this chapter, we investigate the properties of group-IV semiconductors in more detail. We start by presenting the very useful framework of $k \cdot p$ theory which is often used to describe the band structure of semiconductors. Based on this framework we briefly explore the dynamics of confined electrons in Sec. 6.2, including the origin and properties of the valley degrees of freedom.

Finally, in Sec. 6.3 we use $k \cdot p$ theory to derive the Luttinger Hamiltonian describing the valence band holes in confined semiconductor structures.

6.1 BULK SEMICONDUCTORS AND $k \cdot p$ THEORY

To get a good grasp of the origin of the properties of confined electrons and holes we will in this chapter derive a series of Hamiltonians that describes the dynamics of electrons and holes in confined semiconductors structures. Our derivations are based on the framework of $k \cdot p$ theory [71], which serves as a starting point to obtain smaller $k \cdot p$ models describing the confined carriers.

The derivation of the $k \cdot p$ dispersion relation is given in Appendix A, and can be briefly summarized as follows: We start from the Schrödinger equation for the lattice periodic part of the Bloch function $|\nu\mathbf{k}\rangle$ in a lattice-periodic crystal potential $V(r)$, to which we add Pauli SOI, which makes $|\nu\mathbf{k}\rangle$ a spinor $|n\mathbf{k}\rangle$ with n accounting for both the spin degree of freedom and the orbital motion of the electron. By then expanding the set of spinors $\{|n\mathbf{k}\rangle\}$ in terms of the eigenfunctions of the lattice-periodic functions at the Γ-point $\{|\nu 0\rangle\}$ we obtain an algebraic expression for the dispersion relation of the bands $E_n(\mathbf{k})$,

$$\sum_{\nu',\sigma'} \left\{ \left[E_{\nu'}(0) + \frac{\hbar^2 k^2}{2m_0} \right] \delta_{\nu\nu'}\delta_{\sigma\sigma'} + \frac{\hbar}{m_0}\mathbf{k} \cdot \mathbf{P}^{\nu\nu'}_{\sigma\sigma'} + \Delta^{\nu\nu'}_{\sigma\sigma'} \right\} c_{n\nu'\sigma'}(\mathbf{k}) \\ = E_n(\mathbf{k}) c_{n\nu\sigma}(\mathbf{k}), \quad (6.1)$$

where $c_{n\nu'\sigma'}$ are the expansion coefficients, and

$$\mathbf{P}^{\nu\nu'}_{\sigma\sigma'} \equiv \langle \nu\sigma | \boldsymbol{\pi} | \nu'\sigma' \rangle, \quad (6.2)$$

$$\Delta^{\nu\nu'}_{\sigma\sigma'} \equiv \frac{\hbar}{4m_0^2c^2} \langle \nu\sigma | \mathbf{p} \cdot \boldsymbol{\sigma} \times (\nabla V) | \nu'\sigma' \rangle. \quad (6.3)$$

Here, the diagonal terms $E_{\nu'}(0) + \hbar^2 k^2/2m_0$ determine the energies of the bands edge states $|\nu 0\rangle$, and the off-diagonal terms $(\hbar/m_0)\mathbf{k} \cdot \mathbf{P}^{\nu\nu'}_{\sigma\sigma'}$ give rise to a $\mathbf{k}$-dependent mixing of the different $|\nu 0\rangle$ states. We can also see that by choosing to expand in the basis without SOI $\{\nu 0\}$, the SOI can be treated as a small perturbation. When treating the SOI as a small perturbation it is often a good approximation to neglect the SOI contribution in $\boldsymbol{\pi}$ and write $\boldsymbol{\pi} = \mathbf{p}$ [71]. Finally, the SOI terms $\Delta^{\nu\nu'}_{\sigma\sigma'}$ generally split the degenerate energy levels $E_\nu(\mathbf{k})$, even at $\mathbf{k} = 0$. We will see an example of this below when we investigate the properties of confined holes, where SOI splits the threefold degenerate $l = 1$ band into a fourfold degenerate $j = 3/2$ band and a doubly degenerate $j = 1/2$ band when we include spin.

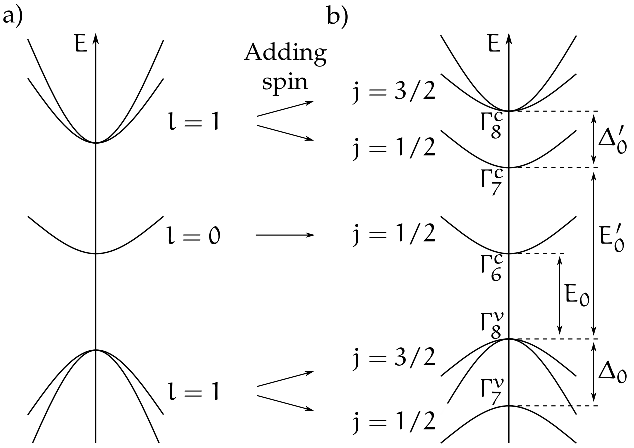

Figure 6.1: Schematic illustration of the bands included in the extended Kane model. (a) The included bands are the uppermost $l = 1$ valence band and the two lowermost $l = 0$ and $l = 1$ conduction bands. (b) Adding spin splits both of the two triply degenerate $l = 1$ bands into a doubly degenerate $j = 1/2$ band and a fourfold degenerate $j = 3/2$ band, separated by the spin–orbit splitting Δ_0. Redrawn after [71].

Diagonalizing Eq. (6.1) yields the exact dispersion relation for all wave vectors $\mathbf{k}$ and band indices n. However, we are often only interested in the dispersion relation for a finite number of adjacent bands close to the expansion point $\mathbf{k}_0 = \mathbf{0}$, e.g. the lowermost conduction band for electrons or the uppermost valence band for holes. By fully taking into account the $\mathbf{k} \cdot \mathbf{p}$ and spin–orbit interactions between those N bands of interest, and including all interactions to remote band perturbatively, one obtains a N dimensional Hamiltonian containing higher-order terms in $\mathbf{k}$ that describes the N bands. We will use this approach in Secs. 6.2.1 and 6.3.3 to obtain Hamiltonians describing two-dimensional electron and holes gases, respectively.

Before we go into detail on the properties of confined electrons and holes we take a broader look at the closest lying bands around the fundamental gap in semiconductors. To do so we take a look at the 14×14 extended Kane model, which includes the uppermost bonding p-like valence band and the antibonding s- and p-like conduction bands, as illustrated in Fig. 6.1(a). By including spin the three bands are split into five bands; the $l = 0$ band is transformed into a doubly degenerate $j = 1/2$ band denoted Γ_6^c, whereas the triply degenerate $l = 1$ conduction(valence) band is split into a fourfold degenerate $j = 3/2$ band $\Gamma_8^{c(v)}$ and a doubly degenerate $j = 1/2$ band $\Gamma_7^{c(v)}$, see Fig. 6.1(b). As already mentioned above, the splitting between the $j = 1/2$

and $j = 3/2$ bands is determined by the Pauli SOI $\Delta_{\sigma\sigma'}^{\nu\nu'}$ caused by the strong Coulomb potential close to the atomic cores, effectively coupling the $l = 1$ states. This splitting is usually large enough that one can treat the $\Gamma_8^{c(\nu)}$ band as isolated[1], and the split-of $j = 1/2$ band is therefore often called the spin–orbit split-off band.

The dispersion relation for the extended Kane model is obtained by using the approach presented above, where we include all $\mathbf{k} \cdot \mathbf{p}$ and spin–orbit interactions between the 14 bands exactly, and add all interactions with remote bands using second-order perturbation theory. The extended Kane model is a convenient tool for describing the neighbourhood around our bands of interest: The lowermost conduction band Γ_6^c and the uppermost valence band Γ_8^ν. The Γ_6^c band has an almost parabolic and isotropic dispersion relation $E(\mathbf{k})$ as it originates from the $l = 0$ band. Because of this parabolicity, electrons in the Γ_6^c band can be described fairly accurately by an effective-mass Hamiltonian. The dispersion relation for holes in Γ_8^ν on the other hand is highly nonparabolic and anisotropic because of the effective spin $j = 3/2$. This complexity gives rise to several interesting and anisotropic properties when the holes are confined, among other highly anisotropic masses and g-tensor, as we will show in Chapter 7.

Although the extended Kane model provides an accurate description of the 14 bands close to the fundamental gap, it is often convenient to consider smaller $\mathbf{k} \cdot \mathbf{p}$ models. In the two next sections we will use two such smaller models to explore two different types of two-dimensional semiconductor structures. First, we use the $\mathbf{k} \cdot \mathbf{p}$ model for the lowermost conduction band Γ_6^c to describe electrons confined in a two-dimensional electron gas, which turns out can be approximated fairly accurate by a simple effective-mass Hamiltonian. Then, we use a $\mathbf{k} \cdot \mathbf{p}$ model for the uppermost valence band Γ_8^ν to describe a two-dimensional hole gas, which in contrast to the 2DEG is complex and anisotropic.

6.2 CONFINED CONDUCTION BAND ELECTRONS AND VALLEY STATES

In most semiconductors the global minimum of the conduction band Γ_6^c is usually very parabolic and simple, and the in-plane dynamics of the electrons can be described fairly accurately by a simple effective-mass Hamiltonian. However, in some semiconductors, so-called indirect-gap semiconductors, the conduction band minimum is not centered around the Γ-point $\mathbf{k} = 0$, giving rise to additional degrees of freedom. This is shown in Fig. 6.2, where we

---

[1] This is especially relevant for holes, where Γ_8^ν is the uppermost valence band with Γ_7^ν as its closest neighbour.

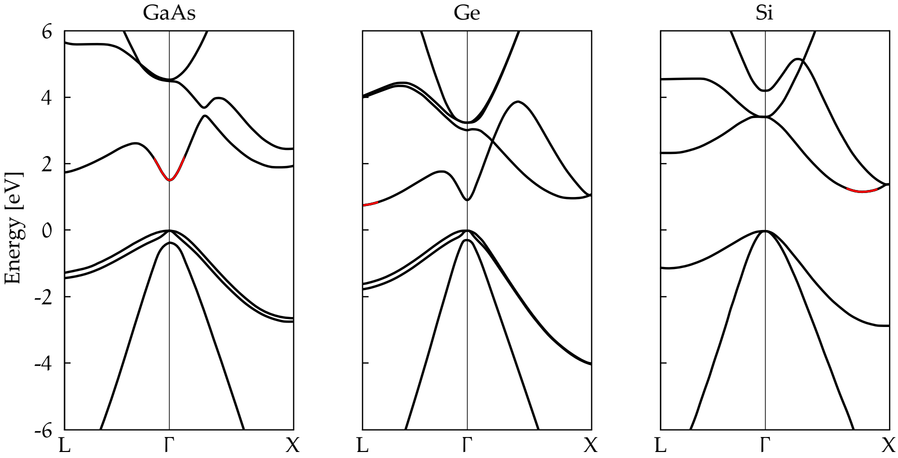

Figure 6.2: Band structure of GaAs, Ge and Si [118] with the global minimum of the conduction band marked in red. The relative position of the conduction band minimum and the valence band maximum shows that GaAs has a direct band-gap whereas Ge and Si have indirect band-gaps.

depict the band structure of the direct-gap semiconductor GaAs and the two indirect-gap semiconductors Si and Ge, where the global minima are marked in red. In this section, we derive the effective-mass Hamiltonian of direct band-gap semiconductors which we introduced already back in Sec. 2.1.1. Then, we briefly explore the origin and properties of the valley states that arise in indirect band-gap semiconductors.

6.2.1 *Direct-gap semiconductors*

In a direct band-gap semiconductor, e.g. GaAs or InAs , the conduction band minimum is centered around $\mathbf{k} = 0$. This allows us to use use the $\mathbf{k} \cdot \mathbf{p}$ results as presented above. The dispersion relation for the conduction band Γ_6^c is obtained from Eq. (A.8) by only taking into account the conduction band $\nu = c$, where all couplings to remote bands are included using second-order perturbation theory,

$$E_c(\mathbf{k}) = E_c(0) + \frac{\hbar^2 k^2}{2m_0} + \frac{\hbar^2 k^2}{m_0^2} \sum_{\nu'} \frac{P_{c\nu'}^2}{E_c(0) - E_{\nu'}(0)}, \tag{6.4}$$

with the matrix elements $P_{c\nu'} = \langle c|\mathbf{p}|\nu'\rangle$ governing the contributions from remote bands. By rewriting Eq. (6.4) we can describe the electrons in the conduction band using an effective mass Hamiltonian with a parabolic dispersion relation,

$$H_c = \frac{\hbar^2 k^2}{2m^*} \tag{6.5}$$

where we removed the constant energy offset $E_c(0)$, and the effective mass reads

$$\frac{m_0}{m^*} = 1 + \frac{2}{m_0} \sum_{\nu'} \frac{P_{c\nu'}^2}{E_c(0) - E_{\nu'}(0)}. \tag{6.6}$$

Usually, the dominating contribution to the sum over ν' in direct-gap semiconductors is the coupling to the closest lying valence band $\nu' = \nu$. It is therefore often a good approximation to write

$$\frac{m_0}{m^*} \approx \frac{2}{m_0} \frac{P_{c\nu}^2}{E_g} \tag{6.7}$$

where $E_g = E_c - E_\nu$ is the fundamental band gap, suggesting that the effective mass has a close to linear dependence on the band-gap.

To obtain an effective in-plane Hamiltonian that describes the electrons in the 2DEG we integrate out the coordinate along the direction of confinement, which we will label z. Because the Hamiltonian in Eq. (6.5) is spherically symmetric, the resulting in-plane Hamiltonian will be independent of the actual orientation of the confinement. Integrating over the ground state in z then yields

$$H_c = E_{z,0} + \frac{\hbar^2 k_\parallel^2}{2m^*}, \tag{6.8}$$

where $k_\parallel^2 = k_x^2 + k_y^2$, and $E_{z,0} = \hbar^2 \langle k_z^2 \rangle / 2m^*$ parameterizes the confinement energy of the 2DEG. The expectation value $\langle k_z^2 \rangle$ is here averaged over the ground state in z, and depends on the strength and shape of the 2DEG confinement. For example, for an infinite-well-type of confinement we have $\langle k_z^2 \rangle = \pi^2/d^2$, with d being the width of the well, giving a confinement energy of $E_{z,0} = \hbar^2 \pi^2 / 2m^* d^2$. Finally, the second term in Eq. (6.8) governs the in-plane dynamics of the electrons confined in the two-dimensional electron gas.

The 2DEG described by Eq. (6.8) can be further confined into a quantum dot by adding a circularly symmetric confinement potential $V(r) = \lambda(x^2 + y^2)$, as we showed back in Sec. 2.1 where we found that the resulting diagonal quantum dot Hamiltonian could be written in terms of two independent Harmonic oscillators,

$$H_0 = \hbar\omega_+ \left(n_+ + \frac{1}{2}\right) + \hbar\omega_- \left(n_- + \frac{1}{2}\right), \tag{6.9}$$

with $\omega_0 = \sqrt{2\lambda/m^*}$ defining the strength of the in-plane confinement such that $\sigma_0 = \sqrt{\hbar/(m^*\omega_0)}$ gives the effective radius of the quantum dot. Thus, the orbital ground state of the quantum dot has an energy of $E_0 = \hbar(\omega_+ + \omega_-)/2$, and is separated from the lowest energetic excited states by an energy of $\omega_\pm$, respectively, typically on the order $\sim$ meV.

6.2.2 *Indirect-gap semiconductors*

In contrast, in an indirect band-gap semiconductor the conduction band is centered around $\mathbf{k} = \mathbf{k}_0 \neq 0$. The most common indirect band-gap semiconductors for use in quantum devices are Si and Ge, both of which have diamond cubic lattice structures, and whose band structures are depicted in Fig. 6.2. The combination of an indirect band-gap and the cubic symmetry gives rise to six equivalent minima in the conduction band, referred to as "valleys", located at different points in k-space [33, 60]. Each of the six minima has a spheroidal constant energy surface which is oriented along a $\langle 001\rangle(\langle 111\rangle)$ crystal axis in Si(Ge), as illustrated for Si in Fig. 6.3(a).

Because the band edges are not centered around $\mathbf{k} = 0$ in an indirect semiconductor, we can not use our results in Eq. (6.1) directly to obtain the band structure; to calculate band structure we need to expand around the correct minimum $\mathbf{k}_0 \neq 0$. In this way the dispersion relation for each of the spheroids, expanded around different $\mathbf{k}_0$, can be written as an effective mass Hamiltonian. Using one of the z-valleys in Si as an example, see Fig. 6.3(a), the effective mass Hamiltonian reads

$$E_c(\mathbf{k}) = E_c(\mathbf{k}_0) + \frac{\hbar^2}{2m_t^*}\left[(k_x - k_{0,x})^2 + (k_y - k_{0,y})^2\right] + \frac{\hbar^2}{2m_l^*}(k_z - k_{0,z})^2, \tag{6.10}$$

where $m^*_{l,t}$ are the longitudinal and transverse effective masses of the spheroid, respectively.

Confining an indirect band-gap semiconductor into a 2DEG breaks the sixfold degeneracy of the conduction band [60]. Focusing especially on Si for simplicity, the strain in Si/SiGe quantum wells raises the four in-plane valleys Δ about ~ 200 meV above the two out-of-plane valleys Γ [33, 60, 119],

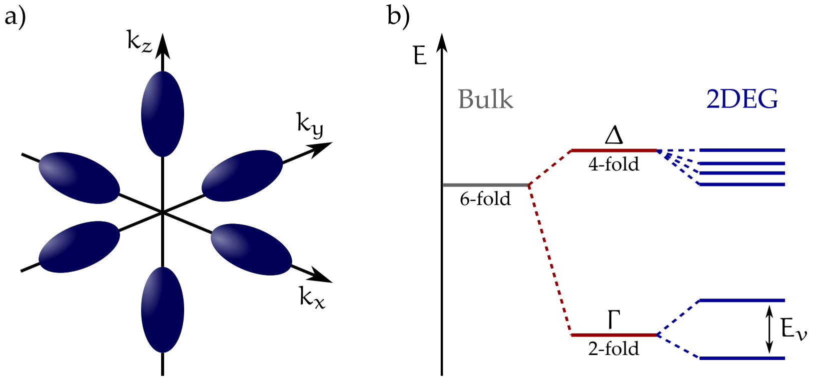

Figure 6.3: (a) Illustration of the constant energy ellipsoids centered around the global minima of the conduction band in Si. (b) The sixfold degeneracy of the bulk is split into the two Γ levels and four Δ levels by the large in-plane strain in the quantum well. The electric field and details of the confinement further splits the Γ levels by the valley splitting E_v. Redrawn after [60].

see Fig. 6.3(b). The degeneracy of the two Γ valleys is further split by details of the heterointerfaces, resulting in a valley splitting of order $\sim 0.1 - 1$ meV, usually smaller than the orbital level splitting of quantum dots. Because the valley splitting has a complex dependence on structural and environmental conditions it is hard to control, and complicates the dynamics of confined electrons. In spin qubit devices the additional degrees of freedom also provide extra channels for leakage and dephasing [60, 61]. We will not go into more detail on how to describe such confined electrons in indirect semiconductors as it is beyond the scope of this thesis, we instead refer to [33, 60] for more details.

6.3 CONFINED VALENCE BAND HOLES

Because of the complexity of the valley states there has been a massive effort with Si- and Ge-based devices that use the spin of valence-band holes instead of the electrons. These holes provide similar protection against magnetic noise as the electrons in purified samples, but without the complicating valley degrees of freedom. However, the valence band has a complex and anisotropic structure that is highly dependent on the details of the confinement. This is a result of the upper valence band having angular momentum $l = 1$, which makes the Γ_v^8 band total spin $j = 3/2$ and fourfold degenerate. Based on $\mathbf{k} \cdot \mathbf{p}$ theory and the Luttinger Hamiltonian we here discuss the dynamics of confined holes, with a special focus on the orientation of the confinement.

6.3.1 *The Luttinger Hamiltonian*

Despite having a more complicated dynamics than confined electrons, the framework of $\mathbf{k}\cdot\mathbf{p}$ theory presented in Sec. 6.1 can be used to obtain a Hamiltonian that describes the dynamics of the Γ_v^8 band. The simplest model to describe this band is the 4×4 Luttinger Hamiltonian, which is obtained from Eq. (A.8) by taking into account all interactions between the four Γ_8^v states, and including interactions to remote bands using second-order perturbation theory. This corresponds to an infinite large splitting Δ_0 to the spin–orbit split-off band, and is accurate for low-energy dynamics as the spin–orbit splitting is usually of the order ~ 100 meV. In the cubic approximation, where terms with tetrahedral symmetries are neglected [71], the Luttinger Hamiltonian reads

$$H_L = \frac{p^2}{2m_0}\left(\gamma_1 + \frac{5}{2}\gamma_2\right) - \frac{\gamma_2}{m_0}\left(p_x^2 J_x^2 + \text{c.p.}\right) - \frac{2\gamma_3}{m_0}\left(\{p_x, p_y\}\{J_x, J_y\} + \text{c.p.}\right), \quad (6.11)$$

where J_i are the three spin-$\frac{3}{2}$ matrices, and c.p. denotes cyclic permutation. Furthermore, the dimensionless constants $\gamma_{1,2,3}$ are the three so-called Luttinger parameters, and are given in Tab. 6.1 for Si, Ge, GaAs and InAs.

In (6.11) it is assumed that the coordinate system $\{x, y, z\}$ is aligned with the main crystallographic axes. This is important because the two terms proportional to $\gamma_{2,3}$ are not spherically symmetric, and the structure of these two terms thus depends on the choice of coordinate system. In many common semiconductors such as GaAs, Ge, and InAs the difference $\delta \equiv \gamma_3 - \gamma_2$ is much smaller than the (weighted) average $2\gamma_2 + 3\gamma_3$ (see Tab. 6.1). For such materials the terms with cubic symmetry, which are all $\propto \delta$ (see Appendix B of Paper III), can be neglected. Then, the remaining Hamiltonian becomes spherically symmetric and no longer depends on the orientation

Table 6.1: Luttinger parameters $\gamma_{1,2,3}$ in for selected semiconductors [71].

	Si	Ge	GaAs	InAs
γ_1	4.285	13.38	6.85	20.40
γ_2	0.339	4.24	2.10	8.30
γ_3	1.446	5.69	2.90	9.10

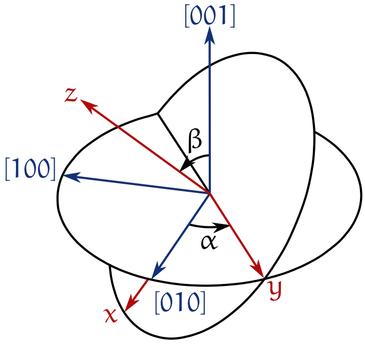

Figure 6.4: Illustration of the rotation of the coordinate system using the two Euler angles α and β. The crystallographic axes are shown in blue and the rotated coordinate system (x, y, z) is shown in red.

of the coordinate system with respect to the crystal structure. This is the so-called spherical approximation, which we discuss in more detail below.

Like for the 2DEG we will need to integrate out the coordinate along the direction of confinement to find an effective in-plane two-dimensional Hamiltonian for the 2DHG. However, since the Hamiltonian that governs valence band holes depends on the actual orientation of the coordinate system, we first need to rotate the Hamiltonian to the correct coordinate system if the confinement axis does not point along with one of the main crystallographic axes. The detailed derivation is shown in Appendix B and can be summarized as follows: (i) We separate the original Luttinger Hamiltonian in Eq. (6.11) in a spherically symmetric part, which is invariant under rotations, and a cubic part, which is decomposed into the 0 and ± 4 components of the rank-4 part of the tensor product of the two irreducible rank-2 tensors that can be formed from the elements $K_{ij} = \frac{3}{2}(p_i p_j + p_j p_i) - \delta_{ij} p^2$ and $L_{ij} = \frac{3}{2}(J_i J_j + J_j J_i) - \delta_{ij} J^2$ [120]. (ii) We rotate the cubic contribution to the new coordinate system by applying the rotation matrix for $j = 4$ angular-momentum eigenfunctions $\mathbf{D}^{(4)}(\alpha, \beta, \gamma)$ to the components of the rank-4 tensor mentioned above, where $\{\alpha, \beta, \gamma\}$ are the Euler angles of the rotation [121]. Because any plane of confinement can be defined by two angles only, we fix $\gamma = 0$ to simplify our analytic expressions. The new coordinate system then results from a rotation by α about $[001]$ followed by a rotation by β about the new y-axis, as illustrated in Fig. 6.4.

The resulting rotated Hamiltonian can always be written in the following form,

$$H(\alpha,\beta) = \begin{pmatrix} P-Q & -S & R & 0 \\ -S^\dagger & P+Q & 0 & R \\ R^\dagger & 0 & P+Q & S \\ 0 & R^\dagger & S^\dagger & P-Q \end{pmatrix}, \tag{6.12}$$

in the basis of the eigenstates $\{|\frac{3}{2}\rangle, |\frac{1}{2}\rangle, |-\frac{1}{2}\rangle, |-\frac{3}{2}\rangle\}$ of J_z with its quantization axis along the new z-direction. The matrix elements P, Q, R and S can be expressed in terms of dimensionless symmetric tensors M_{ij},

$$M = \frac{1}{2m_0} \sum_{i,j} M_{ij}\{p_i, p_j\}, \tag{6.13}$$

where $M \in \{P, Q, R, S\}$ and $i, j \in \{x, y, z\}$. The diagonal element P is invariant under rotations and follows from $P_{ij} = \delta_{ij}\gamma_1$; the other elements are more involved and explicit expressions for their M_{ij} as a function of α and β are given in Appendix B of Paper III.

6.3.2 *Strain and the Bir-Pikus Hamiltonian*

Strain is not an important topic in this thesis, however, we will here briefly explain how one can add strain effects to the rotated Luttinger Hamiltonian by using the same procedure as for the Luttinger Hamiltonian. While the physics of strain is fundamental, the origin of strain is highly device dependent, and can result from e.g. lattice-mistmatched growth in epitaxial heterostructures, intrinsic stress in deposited thin films, phonon-induced lattice vibrations in homogeneous semiconductors, or applied external stress [122]. For the $j = 3/2$ valence band holes strain is governed by the 4x4 Bir-Pikus Hamiltonian, which in the regular coordinate system aligned with the crystallographic axes reads [122]

$$H_{BP} = \left(-a + \frac{5}{4}b\right)(\epsilon_{xx} + \text{c.p.}) - b\left(\epsilon_{xx}J_x^2 + \text{c.p.}\right) - \frac{2d}{\sqrt{3}}\left(\epsilon_{xy}\{J_x, J_y\} + \text{c.p.}\right), \tag{6.14}$$

where ϵ_{ij} is the strain tensor, a is the Bir-Pikus hydrostatic deformation potential, and b and d are two Bir-Pikus shear deformation potentials [122], and are given in Tab. 6.2 for Si, Ge, GaAs and InAs. Because this Hamiltonian has the same structure as the Luttinger Hamiltonian (6.11), it allows for straightforward inclusion of strain into the rotated Luttinger Hamiltonian. Using the notation of Eq. (6.12) we add a similar contribution to the tensor elements $M \to M + \sum_{i,j} M^{BP}_{ij} \epsilon_{ij}$, where the Bir-Pikus elements M^{BP}_{ij} can be obtained from the Luttinger elements M_{ij} by the substitution $\{\gamma_1, \gamma_2, \gamma_3\} \to \{-a, \frac{1}{2}b, \frac{1}{2\sqrt{3}}d\}$.

6.3.3 *Two-dimensional hole gases*

The in-plane Hamiltonian for the confined holes in the 2DHG can now be obtained by integrating out the coordinate along with the direction of confinement, which we again label z. By assuming no strain and an infinite-well type of confinement for simplicity, all terms in the Luttinger Hamiltonian H that are linear in p_z vanish[2] and the terms quadratic in p_z integrate out to contributions $M_{zz}u_z$, where the confinement energy scale $u_z = \langle p_z^2 \rangle / 2m_0$ will be assumed much larger than the in-plane kinetic energy of the holes. We can then diagonalize the part of the Hamiltonian that is proportional to u_z, which in general leads to a basis that no longer consists of pure $m_j = \pm\frac{3}{2}$ and $m_j = \pm\frac{1}{2}$ states. The two resulting pairs of spin-mixed eigenstates are the heavy and light holes (HHs and LHs), where the terms "heavy" and "light" refer to the large and small, respectively, masses along the direction of confinement. Note that for in-plane motion, this relation is reversed; the heavy holes have a smaller in-plane mass than the light holes, as shown in the illustration of the dispersion relation for the heavy and light holes in Fig. 6.5. The heavy and light holes are splitt off by an energy $\Delta_{HL} = 2u_z\sqrt{Q_{zz}^2 + |R_{zz}|^2 + |S_{zz}|^2}$, but can become mixed by an applied magnetic field or in-plane confinement.

Before we investigate the anisotropic dynamics of the 2DHG, we briefly explore the well-known Luttinger Hamiltonian in the spherical approximation,

---

[2] This is also the case in presence of a finite magnetic field [71].

Table 6.2: Deformation potentials for selected semiconductors (eV) [122].

	Si	Ge	GaAs	InAs
a	-2.5	-1.2	-1.2	-1.0
b	-2.1	-2.9	-2.0	-1.8
d	-4.8	-5.3	-4.8	-3.6

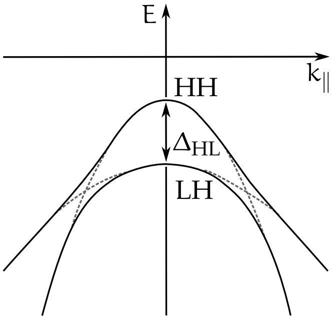

Figure 6.5: Illustration of the HH-LH anti-crossing. Confining the valence band holes in a 2DHG splits the fourfold degenerate $j = 3/2$ states, giving rise to the heavy and light hole states. Redrawn after [71].

which is obtained by neglecting all terms proportional to $\delta = \gamma_3 - \gamma_2$. Then, the HH and LH states at the band edge where $k_{||} = 0$ are pure $m_j = \pm\frac{3}{2}$ and $m_j = \pm\frac{1}{2}$ states, and we find $S = 0$ and

$$Q = \frac{4\gamma_2 + 6\gamma_3}{5} u_z - \frac{1}{10m_0}(2\gamma_2 + 3\gamma_3)(p_x^2 + p_y^2), \tag{6.15}$$

$$R = -\frac{\sqrt{3}}{10m_0}(2\gamma_2 + 3\gamma_3)(p_x - ip_y)^2, \tag{6.16}$$

so that $\Delta_{HL} = \frac{4}{5}(2\gamma_2 + 3\gamma_3)u_z$. We see that the Hamiltonian is indeed spherically symmetric in this limit and irrespective of the crystallographic orientation of the 2DHG the in-plane dynamics can be to leading order in $1/u_z$ described using an effective-mass Hamiltonian $H_{L,||}^{H(L)} = p^2/2m^{H(L)}$, where the in-plane effective masses read as

$$m^{H(L)} = m_0 / \left[\gamma_1 \pm \frac{1}{5}(2\gamma_2 + 3\gamma_3)\right], \tag{6.17}$$

for the HHs and LHs, respectively.

The spherical approximation is good in materials where $\delta/(2\gamma_2 + 3\gamma_3)$ is very small. However, in some materials the spherical approximation is not particularly good, like in Si where $\delta/(2\gamma_2 + 3\gamma_3) \approx 0.22$ which is not negligible. Because we want to specifically include Si in our consideration when investigating the g-tensor of confined holes in Chapter 7, we will go beyond the spherical approximation and not neglect δ, and we will take the actual crystal orientation into account. In general this results in a mixing of the $m_j = \pm\frac{3}{2}$ and $m_j = \pm\frac{1}{2}$ states, except for confinement along high-symmetry directions, such as [001] and [111], where the Hamiltonian becomes isotropic again.

Because of the strong confinement along z, the terms $\propto u_z$ in the Luttinger Hamiltonian dominate. To find an analytic expression for the effective in-plane Hamiltonian we therefore diagonalize the part of the Hamiltonian that is $\propto u_z$. Doing so we find that the in-plane dynamics of the holes can be modeled by an elliptical effective mass Hamiltonian,

$$H^{H(L)}_{L,\|} = \frac{p_{\tilde{x}}^2}{2m_-^{H(L)}} + \frac{p_{\tilde{y}}^2}{2m_+^{H(L)}} \tag{6.18}$$

where the two in-plane masses follow from $m_-^{H(L)} = m^{H(L)}(\zeta)$ and $m_+^{H(L)} = m^{H(L)}(\zeta + \pi/2)$, with

$$m^{H(L)}(\theta) = \frac{2m_0}{2\gamma_1 + s^{H(L)} + r^{H(L)}\cos(2\theta - 2\zeta)}. \tag{6.19}$$

Here, θ is the angle between the x-axis and the direction of motion of the hole, and

$$\begin{aligned} s^{H(L)} &= \mp \mathrm{Re}[\boldsymbol{n}_{zz} \cdot (\boldsymbol{v}_{xx} + \boldsymbol{v}_{yy})^*], \\ r^{H(L)} &= \pm \sqrt{\mathrm{Re}[\boldsymbol{n}_{zz} \cdot (\boldsymbol{v}_{xx} - \boldsymbol{v}_{yy})^*]^2 + \mathrm{Re}[\boldsymbol{n}_{zz} \cdot \boldsymbol{v}_{xy}^*]^2}, \end{aligned}$$

where we introduced the vectors $\boldsymbol{v}_{\alpha\beta} \equiv \{Q_{\alpha\beta}, R_{\alpha\beta}, S_{\alpha\beta}\}$ and $\boldsymbol{n}_{\alpha\beta} \equiv \boldsymbol{v}_{\alpha\beta}/|\boldsymbol{v}_{\alpha\beta}|$, and the new in-plane coordinate system $\{\tilde{x}, \tilde{y}\}$ is rotated over an angle

$$\zeta = \frac{1}{2}\arctan\left(\frac{\mathrm{Re}[\boldsymbol{n}_{zz} \cdot \boldsymbol{v}_{xy}^*]}{2\mathrm{Re}[\boldsymbol{n}_{zz} \cdot (\boldsymbol{v}_{yy} - \boldsymbol{v}_{xx})^*]}\right) \tag{6.20}$$

along z with respect to the original system $\{x, y\}$. ζ then determines what θ gives the smallest(largest) effective heavy(light) hole mass, while the largest(smallest) effective mass is always obtained when θ is an angle $\frac{\pi}{2}$ off from ζ. Inserting the tensor elements given in Appendix B of Paper III reveals the explicit dependence of $m^{H,L}(\theta)$ on the Euler angles that were used to rotate the Hamiltonian.

In Fig. 6.6 we illustrate how the effective HH masses in Si depend on the two Euler angles α and β. (a) and (b) show the magnitudes of the smallest effective mass $m^H(\zeta)/m_0$ and the largest effective mass $m^H(\zeta + \frac{\pi}{2})/m_0$, respectively. In (c) we plot the anisotropy of the effective masses $m^H(\zeta + \frac{\pi}{2})/m^H(\zeta)$, while (d) shows how the angle ζ depends on α and β. Because most experiments use samples grown along the common directions [001] and [110], with the confinement created along the growth direction, the respective directions are marked by the red circle and cross.

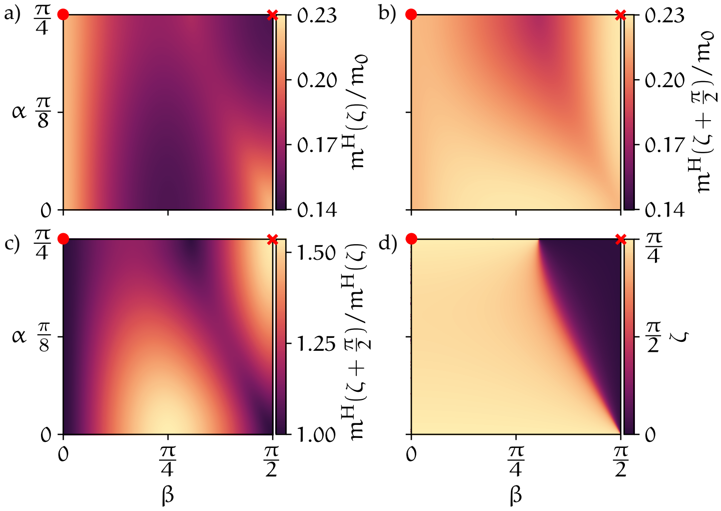

Figure 6.6: The effective hole masses of Si as predicted by Eq. (6.19), plotted against the direction of confinement. (a) and (b) show the smallest and largest effective mass $m^H(\zeta)$ and $m^H(\zeta+\pi/2)$, respectively, (c) shows the anisotropy of the effective masses $m^H(\zeta+\pi/2)/m^H(\zeta)$, and (d) shows the angle ζ.

6.3.4 *Quantum dots*

In contrast to electrons, which have a circularly symmetric effective mass, holes may have elliptic effective masses depending on the details of the confinement, as we showed in the previous section. This has to be taken into account when further confining the 2DHG into quantum dots, and we will see how the anisotropic dynamics of the holes give rise to a confinement-dependent level structure.

The Luttinger Hamiltonian that governs the in-plane motion of the effective heavy holes was in Sec. 6.3.1 obtained by transforming the in-plane part of H in Eq. (6.12) to the basis where the part of H proportional to u_z is diagonal. To confine the holes in a quantum dot, we now add additional in-plane confinement, assuming the corresponding orbital energy scale to be much smaller than the out-of-plane orbital energy. Further assuming the confinement potential to be symmetric parabolic $V(\mathbf{r}) = \lambda(x^2+y^2)$, we describe the confinement of heavy holes in a quantum dot by adding confinement terms to the 2DHG Hamiltonian in Eq. (6.18),

$$H^H_{L,\parallel} = \frac{p_{\tilde{x}}^2}{2m_-} + \frac{p_{\tilde{y}}^2}{2m_+} + \frac{m_-}{2}\omega_x^2\tilde{x}^2 + \frac{m_+}{2}\omega_y^2\tilde{y}^2, \tag{6.21}$$

where again $m_- = m^H(\zeta)$ and $m_+ = m^H(\zeta + \pi/2)$ are the minimum and maximum HH effective masses, as given by Eq. (6.19), and the new in-plane coordinate system $\{\tilde{x}, \tilde{y}\}$ is thus rotated over an angle ζ along z with respect to the original system $\{x, y\}$. Further, the frequencies $\omega_x = \sqrt{2\lambda/m_-}$ and $\omega_y = \sqrt{2\lambda/m_+}$ determine the strength of the in-plane confinement and we use the same vector potential as above $\mathbf{A}(\tilde{\mathbf{r}}) = B_z(-\tilde{y}/2, \tilde{x}/2, 0)$ in the canonical momentum $\mathbf{p} = -i\hbar\partial_{\mathbf{r}} + e\mathbf{A}(\mathbf{r})$. Although we assume a circularly symmetric confining potential, the anisotropic effective hole mass makes the confinement effectively elliptic.

The eigenstates and -energies of such an anisotropic two-dimensional oscillator in the presence of a magnetic field can be found in different ways, see e.g. Refs. [81, 123, 124]. We follow the procedure presented in [125], resulting in a Hamiltonian that can be written in terms of two independent harmonic oscillators,

$$H^H_{L,\parallel} = \hbar\omega_+ \left(n_+ + \frac{1}{2}\right) + \hbar\omega_- \left(n_- + \frac{1}{2}\right), \tag{6.22}$$

where the oscillator frequencies read as

$$\omega_\pm = \sqrt{\frac{1}{2}\omega_x^2 + \frac{1}{2}\omega_y^2 + 2\omega_c^2 \pm \frac{1}{2}\sqrt{(\omega_x^2 - \omega_y^2)^2 + 8\left(\omega_x^2 + \omega_y^2 + 2\omega_c^2\right)\omega_c^2}}, \tag{6.23}$$

with $\omega_c^2 = e^2B_z^2/4m_+m_-$. Because the confinement of the 2DHG is usually much stronger than the in-plane confinement of the quantum dot, we will assume that the oscillator energies $\hbar\omega_\pm$ are much smaller than the energy u_z associated with the transverse confinement.

Since the masses $m_\pm$ depend on the orientation of the plane of the 2DHG through the angles α and β, the level splitting in the dot will also vary as a function of that orientation. This can be shown explicitly by inserting the maximum and minimum masses as given by Eq. (6.19), yielding

$$\omega_\pm^2 = \frac{\lambda}{m_0}(2\gamma_1 + s + 2\chi_c^2 \pm \eta), \tag{6.24}$$

where we introduced the notation

$$\eta = \sqrt{b^2 + 4\chi_c^2(2\gamma_1 + s + \chi_c^2)}, \tag{6.25}$$

and used the dimensionless parameter

$$\chi_c = \frac{eB_z}{4\sqrt{\lambda m_0}}\sqrt{(2\gamma_1 + s)^2 - r^2}, \tag{6.26}$$

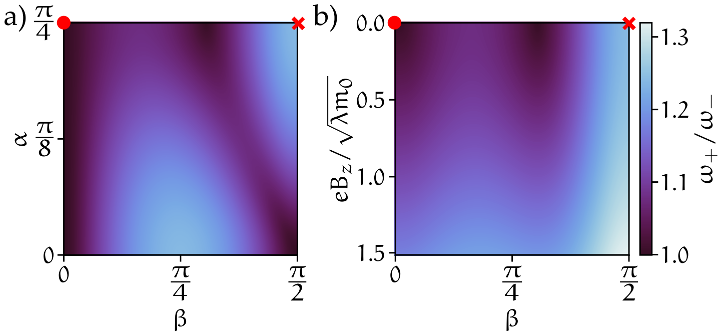

Figure 6.7: Asymmetry in the confinement energy ω_+/ω_- as given by Eq. (6.24). (a) ω_+/ω_- as a function of the direction of confinement in the absence of a vector potential. (b) ω_+/ω_- as a function of the angle β and applied magnetic field $eB_z/\sqrt{\lambda m_0}$, setting $\alpha = \pi/4$ (which corresponds to focusing on confinement directions $[nnm]$). In both plots we used parameters for Si.

characterizing the magnitude of the cyclotron frequency compared to the harmonic oscillator frequencies. We used the same notation as in Sec. 6.3.3, where we omitted the superscript H from the coefficients r and s.

To illustrate the dependence of the confinement energies on the orientation of the 2DHG explicitly, we plot in Fig. 6.7(a) the anisotropy of the level splitting ω_+/ω_- as a function of the angles α and β in the absence of a vector potential, where we used parameters for Si. Naturally, since this anisotropy stems from the orientation dependence of the effective mass, it strongly resembles the results shown in Fig. 6.6(c). Fig. 6.7(b) shows how a non-zero vector potential affects the anisotropy. We plot ω_+/ω_- as a function of $eB_z/\sqrt{\lambda m_0}$ and the angle β, fixing $\alpha = \pi/4$, which captures all confinement directions of the form $[nnm]$. We see that, as expected, the magnetic field increases the anisotropy, while retaining some of the orientation dependence. As we will see in Sec. 7.2, this magnetic field dependence becomes important when we investigate the g-tensor of holes confined in quantum dots.

7

ANISOTROPIC PROPERTIES OF CONFINED SEMICONDUCTOR HOLES

In the previous chapter we showed how terms in the Luttinger Hamiltonian that broke spherical symmetry allowed the confinement of the 2DHG to mix states with different angular momentum along the out-of-plane direction. This mixing introduces an interesting anisotropy into many of the effective hole parameters. Indeed, recent experiments on two-dimensional hole quantum wells and quantum dots have shown wildly varying and anisotropic effective hole masses [126–128] and g-factors [72–76, 78–80, 129–132], depending on choice of material, hole densities, and on the details of the confinement.

In Paper III we theoretically investigated the anisotropic properties of the g-tensor of confined holes in detail, again with a focus on the role of the precise orientation of the confinement potentials with respect to the crystal orientation, where we paid special attention to the case of Si, which has particularly strong anisotropic properties as compared to most other common materials, such as Ge, GaAs and InAs [71]. Here, we present our main findings from the paper, and further discuss how these anisotropic properties affects the leakage current. In Sec. 7.1 we present the main findings on the g-tensor arising from rotating the Zeeman Hamiltonian to the "eigenbasis" defined by the transverse confinement of the holes. Then, in Sec. 7.2 we add in-plane confinement into quantum dots which induces SOI corrections to the g-tensor of holes localized in quantum dots. Finally, in Sec. 7.3 we investigate how this highly anisotropic g-tensor affects the leakage current of holes through a double quantum dot.

7.1 HEAVY-HOLE ZEEMAN EFFECT IN 2DHGS

In Sec. 6.3.1 we showed that the dynamics of holes confined in a 2DHG is governed by a rotated Luttinger Hamiltonian as given in Eq. (6.12). We will now add an external magnetic field, and investigate how it couples to the angular momentum of the heavy holes (HH) through the Zeeman effect. We do this by transforming the Zeeman Hamiltonian to the basis where the Luttinger Hamiltonian is diagonal, from which we can then find the HH g-tensor. The Zeeman Hamiltonian that describes the coupling of the four $j = \frac{3}{2}$ states in the upper valence band due to the external magnetic field reads as [71, 133]

$$H_Z = 2\kappa \mathbf{B} \cdot \mathbf{J} + 2q\mathbf{B} \cdot \mathcal{J}, \tag{7.1}$$

where κ is the effective g-factor of the isotropic coupling, $\mathbf{B}$ is the applied magnetic field, q sets the strength of the anisotropic coupling, $\mathcal{J} = \{J_x^3, J_y^3, J_z^3\}$, and we use units where the Bohr magneton $\mu_B = 1$. Since κ is usually two orders of magnitude larger than q (see Tab. 7.1) we neglect the anisotropic contribution to H_Z.

The goal of this section is to derive an effective g-tensor $\bar{g}$ for the HH subspace, such that the linear Zeeman Hamiltonian (7.1) for the HHs can be written as

$$H_Z^H = \frac{1}{2}\boldsymbol{\sigma} \cdot \bar{g} \cdot \mathbf{B}, \tag{7.2}$$

where $\boldsymbol{\sigma} = \{\sigma_x, \sigma_y, \sigma_z\}$ is the vector of Pauli matrices, acting in the HH subspace. We start by deriving the g-tensor obtained for the spherical approximation discussed in Sec. 7.1.1. Then, by also including the cubic terms of the Luttinger Hamiltonian we investigate the full orientation-dependence of the g-tensor in Sec. 7.1.2.

7.1.1 *Spherical approximation, $\delta = 0$*

Like when investigating the anisotropic dynamics of the valence band holes, we first review the case of the spherical approximation, which we in Sec. 6.3.1 obtained by neglecting all terms proportional to $\delta = \gamma_3 - \gamma_2$. We found that at the top of the valence band, i.e. where $k_x = k_y = 0$ and $R = 0$, the HH

Table 7.1: Bare effective g-factors κ and q for selected semiconductors [71].

	Si	Ge	GaAs	InAs
κ	−0.42	3.41	1.20	7.60
q	0.01	0.06	0.01	0.39

and LH states are the pure $m_j = \pm\frac{3}{2}$ and $m_j = \pm\frac{1}{2}$ states. This makes the effective HH Zeeman, to leading order in $1/u_z$,

$$H_Z^H = 3\kappa B_z \sigma_z, \tag{7.3}$$

with the coupling to the in-plane components of the magnetic field $B_{x,y}$ being a higher-order effect via the LH states, and thus being proportional to $B_{x,y}^3/u_z^2$. In terms of the g-tensor this means that $g_{zz} = 6\kappa$ and all other elements are much smaller.

Away from the top of the valence band, i.e. for a 2DHG with a finite density, also the holes with non-zero in-plane momentum have a non-zero matrix element R [see Eq. (6.16)]. Thus, close to the Fermi level the HH-LH mixing adds a finite coupling to the in-plane field which yields an effective direction-dependent g-tensor

$$\bar{g} = \begin{pmatrix} g_{\|}\cos 2\varphi & -g_{\|}\sin 2\varphi & 0 \\ g_{\|}\sin 2\varphi & g_{\|}\cos 2\varphi & 0 \\ 0 & 0 & g_{\perp} \end{pmatrix}, \tag{7.4}$$

with $g_\perp = 6\kappa$ and $g_\| = 6\kappa p_F^2/2m_0 u_z$, again up to order $\mathcal{O}(1/u_z)$, where p_F is the Fermi momentum and φ is the direction of propagation of the hole under consideration.

Finally, by using that $u_z = \langle p_z^2 \rangle/2m_0$, we find an elegant expression for the ratio of the magnitudes of the in-plane and out-of-plane g-factors in the spherical approximation [71, 77],

$$\frac{g_\|}{g_\perp} = \frac{p_F^2}{\langle p_z^2 \rangle}. \tag{7.5}$$

By further assuming parabolic dispersion for the range of energies of interest, we can consider a finite two-dimensional density of HHs ρ in the valence band and thus write for the ratio of g-factors at the Fermi level

$$\frac{g_\|}{g_\perp} = \frac{2\pi\rho}{\langle k_z^2 \rangle} = \frac{2}{\pi}\rho d^2, \tag{7.6}$$

where we again used our assumption of an infinite-well type of confinement along z such that $\langle k_z^2 \rangle = \pi^2/d^2$, where d is the width of the well.

7.1.2 *Anisotropic Hamiltonian, $\delta \neq 0$*

Going beyond the spherical approximation, which is especially relevant for Si, all HHs and LHs are mixtures of the $m_j = \pm\frac{3}{2}$ and $m_j = \pm\frac{1}{2}$ states.

This results in general in a finite coupling to $B_{x,y}$ within the HH subspace, also in the absence of finite in-plane momentum. Transforming the Zeeman Hamiltonian in Eq. (7.1) to the basis where the part of H proportional to u_z is diagonal, which we then project to the HH subspace, we find to leading order in $1/u_z$ the relatively compactly expression for the g-tensor,

$$\frac{g_{zz}}{\kappa} = 2\frac{Q_{zz}}{\nu} + 4\frac{\nu}{\mu}, \tag{7.7}$$

$$\frac{g_{zx} - ig_{zy}}{\kappa} = 2\sqrt{3}\frac{S_{zz}}{\nu} - 2\frac{R_{zz}S^*_{zz}}{\mu\nu}, \tag{7.8}$$

$$\frac{g_{xz} + ig_{yz}}{\kappa} = 2\frac{R_{zz}S_{zz}}{\mu\nu}, \tag{7.9}$$

$$g_{xx} - ig_{xy} = g_{-+} + g_{++}, \tag{7.10}$$

$$g_{yy} + ig_{yx} = g_{-+} - g_{++}, \tag{7.11}$$

with

$$\frac{g_{-+}}{\kappa} = -\sqrt{3}\frac{R^*_{zz}}{\mu}\left(1 + \frac{Q_{zz}}{\nu}\right) - \frac{(S^*_{zz})^2}{|S_{zz}|^2}\left(1 - \frac{Q_{zz}}{\nu}\right)\left(1 + \frac{\nu}{\mu}\right),$$

$$\frac{g_{++}}{\kappa} = \sqrt{3}\frac{R_{zz}}{\mu}\frac{S^2_{zz}}{|S_{zz}|^2}\left(1 - \frac{Q_{zz}}{\nu}\right) + \frac{R^2_{zz}}{|R_{zz}|^2}\left(1 + \frac{Q_{zz}}{\nu}\right)\left(1 - \frac{\nu}{\mu}\right),$$

where we introduced the shorthand notation $\mu = \sqrt{Q^2_{zz} + |S_{zz}|^2 + |R_{zz}|^2}$ and $\nu = \sqrt{Q^2_{zz} + |S_{zz}|^2}$. Note that Eqs. (7.7-7.11) successfully reproduce the result of the spherical approximation where $S_{zz} = R_{zz} = 0$, yielding $g_{zz} = 6\kappa$ as the only non-zero element, as expected.

In Fig. 7.1 we plot the magnitude of all nine components of the HH g-tensor at the band edge as a function of the two confinement angles α and β, as given by Eqs. (7.7)–(7.11), where we again used parameters for Si. The plots show that by controlling the orientation of the confining potential one can design the qualitative form of the g-tensor, ranging from purely diagonal for high-symmetry directions like [001] to highly anisotropic for less common directions.

Although we here focused on the leading order terms $\propto 1/u_z$, we note that the expressions in Eqs. (7.7)-(7.11) can be generalized to describe the g-tensor of any heavy hole governed by a Hamiltonian in the form of Eq. (6.12) by simply substituting $\{Q_{zz}, R_{zz}, S_{zz}\} \to \{Q, R, S\}$. By doing so the g-tensor becomes valid also including e.g. in-plane momenta and strain. The contribution from in-plane momenta typically becomes important and comparable to the $\propto 1/u_z$ contribution when $k_\parallel d \sim 1$, however, the exact number is highly material-dependent.

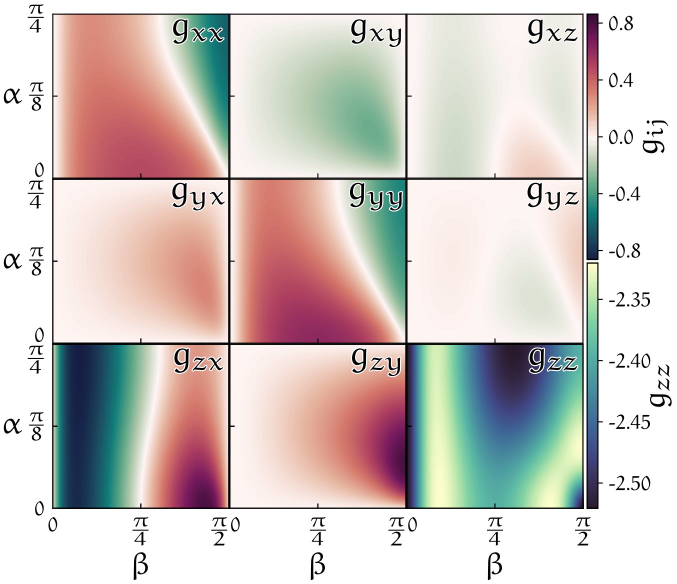

Figure 7.1: The nine components of the heavy hole g-tensor given by Eqs. (7.7)-(7.11) plotted against the direction of confinement, where we used parameters for Si, see Tab. 6.1.

7.2 g-TENSOR CORRECTIONS IN QUANTUM DOTS

In the previous section we investigated the effects of confinement along the z-direction on the g-tensor in a 2DHG. Further confinement along the in-plane coordinates x and y into quantum dots can give rise to SOI that affects the effective g-tensor of the localized holes [134]. Such SOI-induced corrections to the g-tensor are interesting for the spin qubit field as they can be used for fast spin manipulation through electrical g-tensor modulation [76, 130, 135, 136]. It is therefore crucial to understand the detailed interplay of SOI, confinement, and applied magnetic fields [137–139].

We here restrict ourselves to a general linear Rashba-type SOI, which could be caused by e.g. the 2DHG confinement potential [140, 141], and neglect all other sources of SOI. This choice is not meant to indicate that this type of SOI is dominant most often in realistic systems, but it makes the presentation as pedagogical as possible: the straightforward derivation that follows below can serve as a clear blueprint for how the approach can be adapted to other, possibly more complex types of SOI[1]. The Hamiltonian describing the linear Rashba-type SOI for the $j = \frac{3}{2}$ states in the upper valence band reads as [71, 142, 143]

$$H_{so} = \beta_{so}(p_y J_x - p_x J_y), \tag{7.12}$$

where we neglected the contribution proportional to $\mathcal{J}$, which is usually much weaker, and we assumed the electric field associated with the confining potential to point along z. The parameter β_{so} is material-dependent and depends also in an intricate way on the exact shape of the transverse confining potential.

In Sec. 6.3.4 we showed that the Hamiltonian that governs the in-plane motion of the heavy holes confined in a circularly symmetric quantum dot can be written in terms of two independent harmonic oscillators. Knowing the level structure of the holes allows us to project the spin–orbit Hamiltonian in Eq. (7.12) to this basis of the localized heavy-hole states. By then expressing the hole momentum operators in terms of the ladder operators of the level structure allows for a straightforward and versatile perturbative evaluation of the effect of spin–orbit interaction (SOI) on the dynamics of the confined holes, from which we can calculate the SOI-induced corrections to the g-tensor,

$$\begin{aligned} g^{so}_{ij} = \frac{1}{16\kappa^2}\frac{l_0^2}{l_{so}^2}\Bigg[&\cos^2\zeta\left(\frac{g_{ix}g_{jx}}{L_-^3}+\frac{g_{iy}g_{jy}}{L_+^3}\right)+\sin^2\zeta\left(\frac{g_{ix}g_{jx}}{L_+^3}+\frac{g_{iy}g_{jy}}{L_-^3}\right) \\ &+\sin(2\zeta)\frac{L_+ + L_-}{L_+^2 L_-^2}\epsilon_{ikl}g_{kx}g_{ly}\delta_{jz}\Bigg], \end{aligned} \tag{7.13}$$

where

$$L_\pm = \sqrt{2\gamma_1 + s \pm r}, \tag{7.14}$$

and we used the length scales $l_0 = (\hbar^2/m_0\lambda)^{\frac{1}{4}}$ (characterizing the in-plane confinement) and $l_{so} = \hbar/m_0\beta_{so}$ (the spin–orbit length). The first two terms in (7.13) arise due to the Zeeman shift of the ground and excited spin states, whereas the last term contains the contribution linear in ω_c and couples therefore only to B_z.

In Fig. 7.2 we show an example of the orientation dependence of the elements g^{so}_{ij} as given by Eq. (7.13), where we used parameters for Si for consistency. The nine elements are plotted in units of the dimensionless ratio l_0/l_{so} which characterizes the effect of the spin–orbit interaction in

---

[1] Depending on the details of the material and confinement potential of the hole gas, other types of SOI than the linear Rashba type could be dominating, such as an effectively cubic Rashba interaction $\propto p_+^3\sigma_- - p_-^3\sigma_+$.

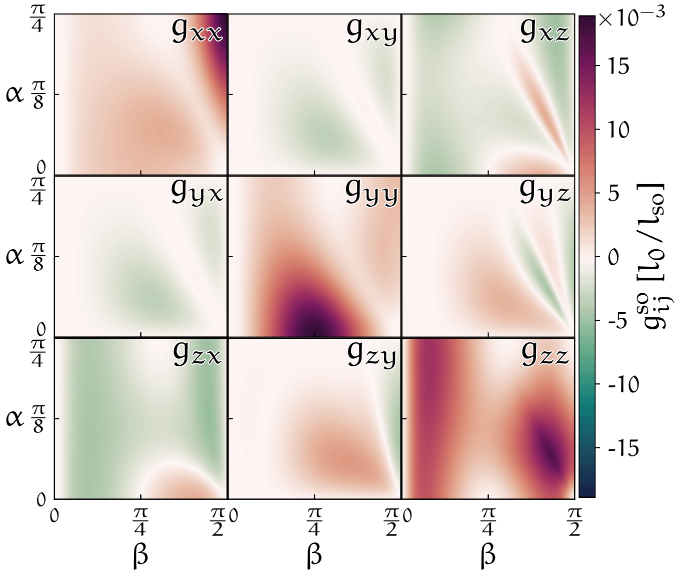

Figure 7.2: The nine elements of the spin–orbit correction to the g-tensor, as given by Eq. (7.13), plotted against the direction of the confinement plane. The correction is shown in units of l_0/l_{so}, and we again used parameters for Si.

the quantum dots. We emphasize that the elements g^{so}_{ix} and g^{so}_{iy} are solely determined by the first two terms in Eq. (7.13), whereas the elements g^{so}_{iz} also include contributions from the last term. Similar to the unperturbed g-tensor as investigated in Sec. 7.1.2, many elements of the spin–orbit correction $\bar{g}^{so}$ also vanish for high-symmetry confinement directions such as [001].

7.3 LEAKAGE CURRENT

In the previous sections we have seen how the anisotropic dynamics of confined valence band holes give rise to highly anisotropic magnetic properties. Using this knowledge we can predict how the Zeeman fields will manifest in multi-quantum dot devices, which is important when investigating the leakage current through a double quantum dot. Here, we present an analytic expression for the hole current through a double quantum dot, which results are included in Paper IV.

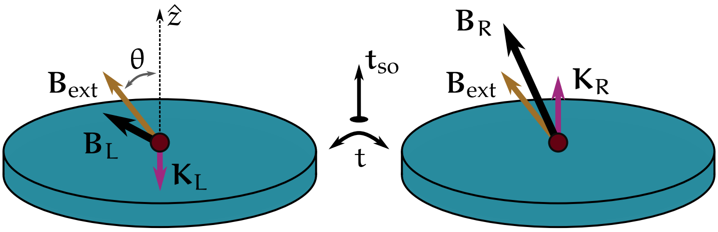

Figure 7.3: Illustration of the orientation of the fields used for the analytical derivation. The spin-orbit vector $\mathbf{t}_{\text{so}}$ and the Overhauser fields $\mathbf{K}_i$ are assumed to be pointing along $\hat{z}$, whereas the orientation of the external Zeeman field B_{ext} is the same on the two dots, and depend on the orientation of the external magnetic field and on the details of the g-tensor.

In Sec. 4.1 we presented a general expression for the current through a double quantum dot for a given realization of Zeeman fields $\mathbf{B}_{L,R}$,

$$\frac{I}{e\Gamma_s} = \frac{|e^{2i\eta}B_R^- B_L^z - B_L^- B_R^z|^2 + \text{Im}\{e^{2i\eta}B_R^- B_L^+\}^2}{\Gamma_s^2 Q_+^2 \left[3 + \frac{16 Q_+^2 Q_-^2}{(B_L^2 - B_R^2)^2}\right] + B_L^2 B_R^2}, \tag{7.15}$$

where

$$Q_\pm^2 = \text{Re}\{\tfrac{1}{2}e^{i\eta}(B_L^+ \pm B_R^-)\}^2 + \text{Im}\{\tfrac{1}{2}e^{i\eta}(B_L^+ \mp B_R^-)\}^2 + \tfrac{1}{4}(B_L^z \pm B_R^z)^2. \tag{7.16}$$

Assuming that one can only control a homogeneous external magnetic field, the Zeeman fields are more or less equal on the two dots. In order to then avoid the stopping point $B_L = B_R$ (which we discussed back in Sec. 4.1) and obtain a non-zero leakage current, finite nuclear fields are required. In a typical experiment, the total measurement time exceeds the correlation time of the nuclear fields, and details depending on the specific configurations of $\mathbf{K}_{L,R}$ average out. Calculating the leakage current that would be measured in a typical experiment can therefore be done by averaging Eq. (7.15) over the random fields nuclear fields $\mathbf{K}_{L,R}$.

For valence band holes that are strongly confined, the HH-LH splitting can become significant, making the heavy holes almost purely the $\pm\frac{3}{2}$ angular momentum states. Because these states are not coupled by the in-plane angular momentum operators $J_\pm$, hyperfine interaction with the residual nuclear spins could become effectively almost purely Ising-like[2] [117, 146–148], and also spin–orbit coupling inside the HH subspace will in general be more efficient along J^z. We can thus assume that the two nuclear fields are purely out-of-plane and the spin–orbit vector $\mathbf{t}_{so}$ is also most likely to be out-of-plane. In that case, the current (4.12) becomes a function of the fields $\mathbf{B}_{L,R} = \mathbf{B}_{ext} + K^z_{L,R}\hat{z}$, as illustrated in Fig. 7.3, where $\mathbf{B}_{ext}$ includes also the effects of the anisotropic g-tensor.

---

[2] Although some experiments and theories suggest that a significant d-shell state admixture can result in a much less anisotropic coupling than naively expected [144, 145].

The leakage current then follows from averaging Eq. (7.15) over $K^z_{L,R}$,

$$\mathcal{I}_{av} = \int dK^z_L dK^z_R \, \frac{e^{-[(K^z_L)^2+(K^z_R)^2]/2K^2}}{4\pi K^2} \, I(\mathbf{B}_L, \mathbf{B}_R), \tag{7.17}$$

where we have assumed the nuclear-field distributions to be Gaussian with mean zero and variance K^2. Signatures of the hyperfine interaction that survive this averaging are again expected to be most prominent at small fields where $B_{ext} \lesssim K$. We will thus focus on the small-field limit, $\Gamma_s \gg K, B_{ext}$, where we find the approximate analytic result

$$\begin{aligned}\frac{\mathcal{I}_{av}\Gamma_s}{eK^2} = 2f\left(\alpha + ib^z\right)\left\{1 + 6f\left(\tfrac{1}{2}\beta\right)\beta^2\right\} \\ - f\left(\tfrac{1}{2}\alpha + ib^z\right)\left\{2 + 3f\left(\tfrac{1}{2}\beta\right)\beta^2\right\},\end{aligned} \tag{7.18}$$

where we have used the function

$$f(x) = \frac{\sqrt{\pi}}{3}\,\mathrm{Re}\{x\}\,\mathrm{Re}\left\{e^{x^2}\mathrm{erfc}\left(x\right)\right\} - \frac{1}{3}, \tag{7.19}$$

with erfc(x) being the complementary error function. Furthermore, we introduced $\alpha = b^{\parallel}\cos\eta$ and $\beta = b^{\parallel}\sin\eta$, where $b^z = B^z_{ext}/K$ and $b^{\parallel} = \sqrt{(B^x_{ext})^2 + (B^y_{ext})^2}/K$ give the out-of-plane and in-plane component of the external Zeeman field, respectively, in units of K, and $\eta = \arctan(t_{so}/t_s)$ parameterize the relative strength of the spin–orbit induced tunnel coupling.

In Fig. 7.4 we plot the current given by Eq. (7.18) as a function of the magnitude of the external magnetic field, for different orientations of the external magnetic field and different strengths of spin–orbit coupling. The four plots (a–d) show the current for different magnitudes of spin–orbit coupling ($\eta = 0$, $\eta = 0.02$, $\eta = 0.1$ and $\eta = 0.5$, respectively) and each plot contains four traces that assume a different orientation of $\mathbf{B}_{ext}$, the angle θ being the polar angle of the applied field (see Fig. 7.3). In all plots we used as parameters $\Gamma_s = 15$ µeV and $K = 0.1$ µeV. From the plots we can observe three main features: (i) The nuclear field peak, with width $\sim K$, that is split into a double peak by the stopping point at $B_{ext} = 0$, (ii) the current converges towards a direction-dependent limiting value at large fields, still smaller than Γ_s, and (iii) finite spin–orbit coupling introduces a characteristic spin–orbit-induced low-field current dip on top of the narrow current peaks caused by the nuclear fields.

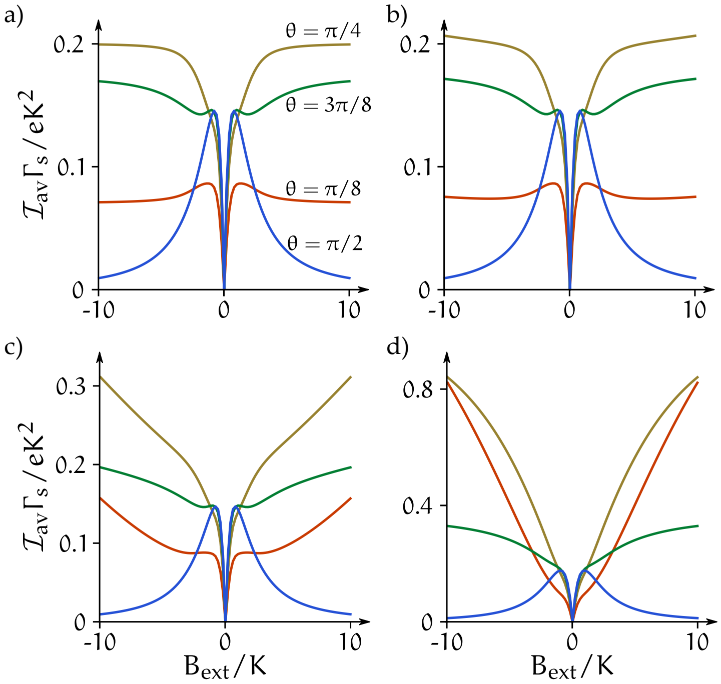

Figure 7.4: Plots of the current as given by Eq. (7.15) as function of the magnitude of the Zeeman field E_s for four different orientations of the Zeeman field where the same colors represent the same orientations in all plots. (a) - (d) show current profiles for four different magnitudes of spin–orbit interaction, $\eta = 0$, $\eta = 0.02$, $\eta = 0.1$ and $\eta = 0.5$, respectively.

A

$k \cdot p$ THEORY

A very useful framework to describe the band structure of semiconductors is the $k \cdot p$ theory. In this appendix we derive a general $k \cdot p$ dispersion relation that is used as a starting point to obtain smaller $k \cdot p$ models in chapter 6.

The derivation of the $k \cdot p$ framework is based on the time-independent Schrödinger equation, which for a free particle in a position-dependent potential $V(r)$ reads

$$\left[-\frac{p^2}{2m_0} + V(\mathbf{r})\right] \Psi_\nu(\mathbf{r}) = E_\nu(\mathbf{r})\Psi_\nu(\mathbf{r}), \tag{A.1}$$

where m_0 is the free electron mass, ν is the band index, and $p = \|\mathbf{p}\|$, with $\mathbf{p}$ being the momentum operator. For a periodic potential $V(\mathbf{r} + \mathbf{T}) = V(\mathbf{r})$, with $\mathbf{T}$ being a translation vector between different lattice sites, the solution to the Schrödinger equation is the Bloch function $\Psi_\nu(\mathbf{r}) = e^{i\mathbf{k}\cdot\mathbf{r}}u_{\nu\mathbf{k}}(\mathbf{r})$, where $\mathbf{k}$ is the wave vector, in which the wave-function takes the form of a plane wave $e^{i\mathbf{k}\cdot\mathbf{r}}$ modulated by a periodic function $u_{\nu\mathbf{k}}(\mathbf{r}) = \langle\mathbf{r}|\nu\mathbf{k}\rangle$ with the same periodicity as the potential $V(\mathbf{r})$. Inserting the Bloch function into Eq. (A.1), the Schrödinger equation for the Bloch function is

$$\left[-\frac{p^2}{2m_0} + V(\mathbf{r})\right] e^{i\mathbf{k}\cdot\mathbf{r}}u_{\nu\mathbf{k}}(\mathbf{r}) = E_\nu(\mathbf{k})e^{i\mathbf{k}\cdot\mathbf{r}}u_{\nu\mathbf{k}}(\mathbf{r}). \tag{A.2}$$

Because it is easy to evaluate the effect of the momentum operator $\mathbf{p}$ on the plane-wave part of the Bloch function we can obtain a Schrödinger equation for the lattice-periodic part of the Bloch function $|\nu\mathbf{k}\rangle$,

$$\left[-\frac{p^2}{2m_0} + V + \frac{\hbar^2k^2}{2m_0} + \frac{\hbar}{m_0}\mathbf{k}\cdot\mathbf{p}\right] |\nu\mathbf{k}\rangle = E_\nu(\mathbf{k})|\nu\mathbf{k}\rangle. \tag{A.3}$$

Since we also want to include the effects of Pauli SOI (first presented in Sec. 2.5.2), we add to Eq. (A.2) the Pauli spin–orbit term,

$$H_{SO} = \frac{\hbar}{4m_0^2c^2}\mathbf{p}\cdot\boldsymbol{\sigma}\times(\nabla V). \tag{A.4}$$

The Pauli SOI couples to both the momentum $\mathbf{p}$ and the wave vector $\mathbf{k}$, and the Schrödinger equation reads

$$\left[-\frac{p^2}{2m_0} + V + \frac{\hbar^2 k^2}{2m_0} + \frac{\hbar}{m_0}\mathbf{k}\cdot\boldsymbol{\pi} + \frac{\hbar}{4m_0^2c^2}\mathbf{p}\cdot\boldsymbol{\sigma}\times(\nabla V)\right]|n\mathbf{k}\rangle = E_n(\mathbf{k})|n\mathbf{k}\rangle, \quad \text{(A.5)}$$

where

$$\boldsymbol{\pi} \equiv \mathbf{p} + \frac{\hbar}{4m_0c^2}\boldsymbol{\sigma}\times(\nabla V), \quad \text{(A.6)}$$

and the spin-dependence makes the lattice-periodic part of the Bloch function a spinor $|n\mathbf{k}\rangle$, where the index n accounts for both the spin degree of freedom and the orbital motion of the electron.

Because the set of lattice-periodic functions $\{|n\mathbf{k}_0\rangle\}$ provide a complete and orthonormal basis for a given wave vector $\mathbf{k}_0$, we can expand $\{|n\mathbf{k}\rangle\}$ in terms of the eigenfunctions $\{|\nu 0\rangle\}$[1] of the Hamiltonian without SOI,

$$|n\mathbf{k}\rangle = \sum_{\nu',\sigma'} c_{n\nu'\sigma'}(\mathbf{k})|\nu'\sigma'\rangle, \quad \text{(A.7)}$$

where $|\nu'\sigma'\rangle \equiv |\nu' 0\rangle \otimes |\sigma'\rangle$, and $c_{n\nu'\sigma'}$ are the expansion coefficients. Multiplying by $\langle \nu\sigma|$ from the left we obtain an algebraic expression for the dispersion relation of the bands $E_n(\mathbf{k})$,

$$\sum_{\nu',\sigma'}\left\{\left[E_{\nu'}(0) + \frac{\hbar^2k^2}{2m_0}\right]\delta_{\nu\nu'}\delta_{\sigma\sigma'} + \frac{\hbar}{m_0}\mathbf{k}\cdot\mathbf{P}^{\nu\nu'}_{\sigma\sigma'} + \Delta^{\nu\nu'}_{\sigma\sigma'}\right\}c_{n\nu'\sigma'}(\mathbf{k}) = E_n(\mathbf{k})c_{n\nu\sigma}(\mathbf{k}), \quad \text{(A.8)}$$

where

$$\mathbf{P}^{\nu\nu'}_{\sigma\sigma'} \equiv \langle \nu\sigma|\boldsymbol{\pi}|\nu'\sigma'\rangle, \quad \text{(A.9a)}$$

$$\Delta^{\nu\nu'}_{\sigma\sigma'} \equiv \frac{\hbar}{4m_0^2c^2}\langle \nu\sigma|\mathbf{p}\cdot\boldsymbol{\sigma}\times(\nabla V)|\nu'\sigma'\rangle. \quad \text{(A.9b)}$$

Here we can see that by choosing to expand in the basis $\{\nu 0\}$ without SOI, the SOI can now be treated as a small perturbation. The diagonal terms $E_{\nu'}(0) + \hbar^2k^2/2m_0$ in Eq. (A.8) determine the energies of the bands edge states $|\nu 0\rangle$, and the off-diagonal terms $(\hbar/m_0)\mathbf{k}\cdot\mathbf{P}^{\nu\nu'}_{\sigma\sigma'}$ give rise to a $\mathbf{k}$-dependent mixing of the different $|\nu 0\rangle$ states.

---

[1] Note that this expansion can be done around any $\mathbf{k}_0$, which is especially relevant when investigating electrons in indirect band-gap semiconductors where the global minimum of the conduction band is not centered around $\mathbf{k} = 0$.

B

THE ROTATED LUTTINGER HAMILTONIAN

In this appendix we show how to write the Luttinger Hamiltonian presented in Sec. 6.3.1 in terms of products of rank-2 spherical tensors. The resulting Hamiltonian is then rotated to an arbitrary coordinate system using the rotation matrix for the $j = 4$ angular-momentum eigenfunctions.

B.1 SECOND-RANK TENSOR OPERATORS

A tensor that is a vector product of two vectors u_i and v_i can be written as a sum over terms that behave differently under rotation [149],

$$T_{ij} = u_i v_j = \frac{\mathbf{u}\cdot\mathbf{v}}{3}\delta_{ij} + \frac{1}{2}\left(u_i v_j - u_j v_i\right) + \left[\frac{1}{2}\left(u_i v_j + u_j v_i\right) - \frac{\mathbf{u}\cdot\mathbf{v}}{3}\delta_{ij}\right]. \quad \text{(B.1)}$$

Here, the first term behaves as a scalar, the second term is anti-symmetric and behaves as a vector, while the third term is a second-rank tensor

$$\Xi_{ij} = \frac{3}{2}\left(\Xi_i \Xi_j + \Xi_j \Xi_i\right) - \delta_{ij}\Xi^2, \quad \text{(B.2)}$$

which is both symmetric and has zero trace. The second-rank tensor can be decomposed further into irreducible spherical tensors of rank 0, 1 and 2, denoted $\Xi^{(0)}$, $\Xi^{(1)}$ and $\Xi^{(2)}$, respectively, where $\Xi^{(0)}$ has one component, $\Xi^{(1)}$ has three components and $\Xi^{(2)}$ has five components. Because the second-rank tensor Ξ_{ij} is symmetric and has zero trace, both $\Xi^{(0)}$ and $\Xi^{(1)}$ are zero. Ξ_{ij} can therefore be decomposed into the five second-rank spherical tensors only, which explicitly read

$$\Xi^{(2)}_{0} = \sqrt{\frac{3}{2}}\Xi_{zz}, \quad \text{(B.3)}$$

$$\Xi^{(2)}_{\pm 1} = \mp\left(\Xi_{xz} \pm i\Xi_{yz}\right), \quad \text{(B.4)}$$

$$\Xi^{(2)}_{\pm 2} = \frac{1}{2}\left(\Xi_{xx} - \Xi_{yy} \pm 2i\Xi_{xy}\right). \quad \text{(B.5)}$$

We now use the relations above to calculate the products of the two tensors p_{ij} and J_{ij} that appear in the Luttinger Hamiltonian in Eq. (6.11) in Sec. 6.3.1,

$$\begin{aligned} H_L = \frac{p^2}{2m_0}\left(\gamma_1 + \frac{5}{2}\gamma_2\right) - \frac{\gamma_2}{m_0}\left(p_x^2 J_x^2 + \text{c.p.}\right) \\ - \frac{2\gamma_3}{m_0}\left(\{p_x, p_y\}\{J_x, J_y\} + \text{c.p.}\right), \end{aligned} \quad \text{(B.6)}$$

so that we can write the Hamiltonian in terms of second-rank tensor operators. We start by using Eq. (B.2) to write the second-rank tensor operators of p_i and J_i,

$$p_{ij} = 3p_i p_j - \delta_{ij} p^2, \quad \text{(B.7)}$$

$$J_{ij} = \frac{3}{2}\left(J_i J_j + J_j J_i\right) - \delta_{ij} J^2, \quad \text{(B.8)}$$

where we used that $[p_i, p_j] = 0$ and $[J_i, J_j] = iJ_z$. Further, by inserting these second-rank tensor operators into the definition of the second-rank spherical tensors in Eqs. (B.3-B.5), we find the second-rank spherical tensors of p_{ij} and J_{ij},

$$p_0^{(2)} = \sqrt{\frac{3}{2}}\left(3p_z^2 - p^2\right), \quad J_0^{(2)} = \sqrt{\frac{3}{2}}\left(3J_z J_z - J^2\right), \quad \text{(B.9)}$$

$$p_{\pm 1}^{(2)} = \mp 3p_{\pm} p_z, \quad J_{\pm 1}^{(2)} = \mp\frac{3}{2}\{J_x J_z + J_z J_x \pm i\left(J_y J_z + J_z J_y\right)\}, \quad \text{(B.10)}$$

$$p_{\pm 2}^{(2)} = \frac{3}{2} p_{\pm}^2, \quad J_{\pm 2}^{(2)} = \frac{3}{2}\left\{J_x^2 - J_y^2 \pm i\left(J_x J_y + J_y J_x\right)\right\}, \quad \text{(B.11)}$$

where we defined $p_{\pm} \equiv p_x \pm i p_y$.

B.2 PRODUCTS OF TENSOR OPERATORS

Now that we know how the second-rank spherical tensors of p_{ij} and J_{ij} look, we can investigate their products. Here we calculate all products of the spherical tensor operators of p_{ij} and J_{ij} that we will need to rewrite the Luttinger Hamiltonian. The first product we need is the scalar product, which reads

$$p^{(2)} \cdot J^{(2)} = p_0^{(2)} J_0^{(2)} - \left(p_1^{(2)} J_{-1}^{(2)} + p_{-1}^{(2)} J_1^{(2)}\right) + p_2^{(2)} J_{-2}^{(2)} + p_{-2}^{(2)} J_2^{(2)}. \quad \text{(B.12)}$$

Secondly, we need all nine components of the tensor product $[p^{(2)} \otimes J^{(2)}]^{(4)}$, where we will use the following short-hand notation $T_M = [p^{(2)} \otimes J^{(2)}]^{(4)}_M$, and the pre-factors are simply the Clebsch–Gordan coefficients [150],

$$T_0 = \frac{1}{\sqrt{70}} \left(p_2^{(2)} J_{-2}^{(2)} + 4p_1^{(2)} J_{-1}^{(2)} + 6p_0^{(2)} J_0^{(2)} + 4p_{-1}^{(2)} J_1^{(2)} + p_{-2}^{(2)} J_2^{(2)} \right), \tag{B.13}$$

$$T_{\pm 1} = \frac{1}{\sqrt{7}} \left(\frac{1}{\sqrt{2}} p_{\pm 2}^{(2)} J_{\mp 1}^{(2)} + \sqrt{3} p_{\pm 1}^{(2)} J_0^{(2)} + \sqrt{3} p_0^{(2)} J_{\pm 1}^{(2)} \frac{1}{\sqrt{2}} p_{\mp 1}^{(2)} J_{\pm 2}^{(2)} \right), \tag{B.14}$$

$$T_{\pm 2} = \frac{1}{\sqrt{7}} \left(\sqrt{\frac{3}{2}} p_{\pm 2}^{(2)} J_0^{(2)} + 2p_{\pm 1}^{(2)} J_{\pm 1}^{(2)} + \sqrt{\frac{3}{2}} p_0^{(2)} J_{\pm 2}^{(2)} \right), \tag{B.15}$$

$$T_{\pm 3} = \frac{1}{\sqrt{2}} \left(p_{\pm 2}^{(2)} J_{\pm 1}^{(2)} + p_{\pm 1}^{(2)} J_{\pm 2}^{(2)} \right), \tag{B.16}$$

$$T_{\pm 4} = p_{\pm 2}^{(2)} J_{\pm 2}^{(2)}. \tag{B.17}$$

Using these products we can now rewrite the terms in the Luttinger Hamiltonian in Eq. (B.6) that are not spherically symmetric (second and third terms) in terms of second-rank spherical tensor operators, which are much easier to rotate than the Cartesian tensors. Doing so we find that the second term reads

$$p_x^2 J_x^2 + \text{c.p.} = \frac{1}{3} p^2 J^2 + \frac{2}{45} p^{(2)} \cdot J^{(2)} + \frac{1}{18} \left(T_4 + \frac{\sqrt{70}}{5} T_0 + T_{-4} \right), \tag{B.18}$$

while the third term becomes

$$p_x p_y \left(J_x J_y + J_y J_x \right) + \text{c.p.} = \frac{1}{15} p^{(2)} \cdot J^{(2)} - \frac{1}{18} \left(T_4 + \frac{\sqrt{70}}{5} T_0 + T_{-4} \right). \tag{B.19}$$

Note here that we only need the rank 4 spherical tensor product, in addition to the scalar product, to represent the cubic Luttinger Hamiltonian when the coordinate system is aligned with the crystallographic axes. Although it might be hard to see how to get from the left-hand side of Eqs. (B.18) and (B.19) to the right-hand side without doing the calculation explicitly, the equations can easily be verified by inserting for the second-rank spherical tensors.

B.3 THE ROTATED LUTTINGER HAMILTONIAN

By inserting the relations in Eqs. (B.18) and (B.19) into the Luttinger Hamiltonian in Eq. (B.6) we obtain

$$\begin{aligned} H_L[001] = \frac{p^2}{2m_0}\gamma_1 - \frac{1}{45}\left(2\gamma_2 + 3\gamma_3\right) k^{(2)} \cdot J^{(2)} \\ + \frac{\delta}{18}\left(T_4 + \frac{\sqrt{70}}{5}T_0 + T_{-4}\right), \end{aligned} \tag{B.20}$$

where $\delta = \gamma_3 - \gamma_2$. Here, the first two terms have axial symmetry (spherically symmetric) and behave as a scalar, while the last term has cubic symmetry and behaves as a rank 4 spherical tensor. Note that by setting $\delta = 0$ here, one effectively removes all cubic terms from the Hamiltonian, resulting in the spherical approximation as discussed in Sec. 6.3.1.

Because only the last term in Eq. (B.20) depends on the actual orientation of the coordinate system, the whole Hamiltonian can be rotated by simply rotating the spherical tensor operators T_0 and $T_{\pm 4}$. We do this using the rotation matrix for $j = 4$ angular-momentum eigenfunctions [121],

$$\begin{aligned} \mathbf{D}^{(j)}(\alpha, \beta, \gamma)_{m',m} = e^{-im'\alpha} e^{-im\gamma} \sum_{\kappa=0}^{\infty} C(j, m', m, \kappa) \\ \times \left(\cos\frac{\beta}{2}\right)^{2j-2\kappa-m'+m} \left(-\sin\frac{\beta}{2}\right)^{2\kappa+m'-m}, \end{aligned} \tag{B.21}$$

where

$$C(j, m', m, \kappa) = \frac{(-1)^{\kappa}\sqrt{(j+m)!(j-m)!(j+m')!(j-m')!}}{\kappa!(j+m-\kappa)!(j-m'-\kappa)!(\kappa+m'+m)!}, \tag{B.22}$$

such that the rotated tensor operators are written as

$$T_M[001] = \sum_{M'=-4}^{4} T_{M'} D^{(4)}_{MM'}(-\alpha, -\beta, -\gamma), \tag{B.23}$$

where $\{\alpha, \beta, \gamma\}$ are the Euler angles of the rotation [121]. Since any plane of confinement can be defined by two angles only, we fix $\gamma = 0$ to simplify our analytic expressions. The new coordinate system then results from a rotation by α about [001] followed by a rotation by β about the new y-axis, as illustrated in Fig. B.1. In this thesis we will explore the full range of possible confinement planes and thus not restrict ourselves to the common crystal

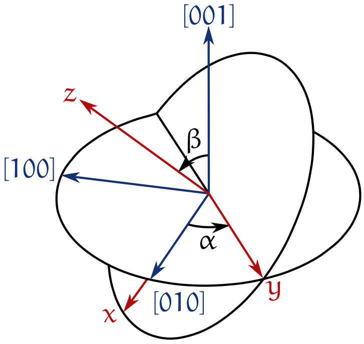

Figure B.1: Illustration of the rotation using the two Euler angles α and β. The crystallographic axes are shown in blue, the rotated coordinate system (x, y, z) is shown in red.

growth directions such as $[nnm]$, as investigated in [71, 120], which can be obtained by simply setting $\alpha = \pi/4$.

The resulting rotated Hamiltonian, as given in Eq. (6.12) of the main text, can always be written in the following form,

$$H(\alpha, \beta) = \begin{pmatrix} P-Q & -S & R & 0 \\ -S^\dagger & P+Q & 0 & R \\ R^\dagger & 0 & P+Q & S \\ 0 & R^\dagger & S^\dagger & P-Q \end{pmatrix}, \tag{B.24}$$

in the basis of the eigenstates $\{|\frac{3}{2}\rangle, |\frac{1}{2}\rangle, |-\frac{1}{2}\rangle, |-\frac{3}{2}\rangle\}$ of J_z with its quantization axis along the new z-direction. The matrix elements P, Q, R and S can be written in terms of the dimensionless symmetric tensors M_{ij},

$$M = \frac{1}{2m_0} \sum_{i,j} M_{ij} \{p_i, p_j\}, \tag{B.25}$$

with $M \in \{P, Q, R, S\}$ and $i, j \in \{x, y, z\}$. The diagonal element P is invariant under rotations and follows from $P_{ij} = \delta_{ij}\gamma_1$. The other elements are more involved and are given in Appendix B of Paper III.

B.4 THE BIR-PIKUS HAMILTONIAN

The Bir-Pikus Hamiltonian can also easily be obtained from the tensor elements above. The matrix elements of the Hamiltonian takes the form

$$M = \sum_{i,j} M_{ij}^{BP} \epsilon_{ij}, \tag{B.26}$$

where $\bar{\epsilon}$ is the strain tensor, and M_{ij}^{BP} can be obtained from M_{ij} by the substitution $\{\gamma_1, \gamma_2, \gamma_3\} \to \{-a, \frac{1}{2}b, \frac{1}{2\sqrt{3}}d\}$. Adding the Bir-Pikus matrix elements to the Luttinger Hamiltonian is then done by substituting $M \to M + \sum_{i,j} M_{ij}^{BP} \epsilon_{ij}$.

BIBLIOGRAPHY

[1] A. Sala, J. H. Qvist, and J. Danon,
Phys. Rev. Res. **2**, 012062 (2020).

[2] J. H. Qvist and J. Danon,
Phys. Rev. B **101**, 165308 (2020).

[3] J. H. Qvist and J. Danon,
Phys. Rev. B **105**, 075303 (2022).

[4] J. H. Qvist and J. Danon,
arXiv, `10.48550/arXiv.2204.12546` (2022).

[5] S. Furber,
Proc. R. Soc. A. **473**, 20160893 (2017).

[6] M. A. Nielsen and I. L. Chuang,
Quantum computation and quantum information, 2000.

[7] J. A. Buchmann, D. Butin, F. Göpfert, and A. Petzoldt,
in *The New Codebreakers* (Springer, Berlin, Germany, Mar. 2016), pp. 88–108.

[8] L. Bassman, M. Urbanek, M. Metcalf, et al.,
Quantum Sci. Technol. **6**, 043002 (2021).

[9] M. P. Andersson, M. N. Jones, K. V. Mikkelsen, et al.,
Curr. Opin. Chem. Eng. **36**, 100754 (2022).

[10] A. M. Childs and W. van Dam,
Rev. Mod. Phys. **82**, 1 (2010).

[11] D. P. DiVincenzo,
Science **270**, 255 (1995).

[12] A. Ekert and R. Jozsa,
Rev. Mod. Phys. **68**, 733 (1996).

[13] R. P. Feynman,
Int. j. Theor. phys **21** (1982).

[14] S. Jordan,
Quantum Algorithm Zoo, [Online; accessed 21. May 2022], Feb. 2021.

[15] A. Montanaro,
npj Quantum Inf. **2**, 1 (2016).

[16] S. Lloyd,
Science **273**, 1073 (1996).

[17] L. K. Grover,
in Proceedings of the twenty-eighth annual acm symposium on theory of computing (1996), pp. 212–219.

[18] L. K. Grover,
Phys. Rev. Lett. **80**, 4329 (1998).

[19] P. W. Shor,
in *Proceedings 35th Annual Symposium on Foundations of Computer Science* (IEEE, Nov. 1994), pp. 124–134.

[20] D. P. DiVincenzo, D. Bacon, J. Kempe, et al.,
Nature **408**, 339 (2000).

[21] G. Wendin,
Rep. Prog. Phys. **80**, 106001 (2017).

[22] P. Krantz, M. Kjaergaard, F. Yan, et al.,
Appl. Phys. Rev. **6**, 021318 (2019).

[23] F. Arute, K. Arya, R. Babbush, et al.,
Nature **574**, 505 (2019).

[24] U. Alvarez-Rodriguez, M. Sanz, L. Lamata, and E. Solano,
Sci. Rep. **8**, 1 (2018).

[25] R. Harper and S. T. Flammia,
Phys. Rev. Lett. **122**, 080504 (2019).

[26] B. K. Behera, T. Reza, A. Gupta, and P. K. Panigrahi,
Quantum Inf. Process. **18**, 1 (2019).

[27] C. Wang, X. Li, H. Xu, et al.,
npj Quantum Inf. **8**, 1 (2022).

[28] A. G. Fowler, M. Mariantoni, J. M. Martinis, and A. N. Cleland,
Phys. Rev. A **86**, 032324 (2012).

[29] D. Loss and D. P. DiVincenzo,
Phys. Rev. A **57**, 120 (1998).

[30] R. Hanson, L. P. Kouwenhoven, J. R. Petta, et al.,
Rev. Mod. Phys. **79**, 1217 (2007).

[31] C. Kloeffel and D. Loss,
Annu. Rev. Condens. Matter Phys. **4**, 51 (2013).

[32] A. Chatterjee, P. Stevenson, S. De Franceschi, et al.,
Nat. Rev. Phys. **3**, 157 (2021).

[33] G. Burkard, T. D. Ladd, J. M. Nichol, et al.,
arXiv:2112.08863 (2021).

[34] L. M. K. Vandersypen, H. Bluhm, J. S. Clarke, et al.,
npj Quantum Information **3**, 34 (2017).

[35] M. F. Gonzalez-Zalba, S. de Franceschi, E. Charbon, et al.,
Nat. Electron. **4**, 872 (2021).

[36] D. Loss and D. P. DiVincenzo,
Phys. Rev. A **57**, 120 (1998).

[37] J. M. Elzerman, R. Hanson, L. H. Willems van Beveren, et al.,
Nature **430**, 431 (2004).

[38] J. R. Petta, A. C. Johnson, J. M. Taylor, et al.,
Science **309**, 2180 (2005).

[39] F. H. L. Koppens, C. Buizert, K. J. Tielrooij, et al.,
Nature **442**, 766 (2006).

[40] I. A. Merkulov, A. L. Efros, and M. Rosen,
Phys. Rev. B **65**, 205309 (2002).

[41] A. V. Khaetskii, D. Loss, and L. Glazman,
Phys. Rev. Lett. **88**, 186802 (2002).

[42] S. I. Erlingsson and Y. V. Nazarov,
Phys. Rev. B **66**, 155327 (2002).

[43] D. P. DiVincenzo, D. Bacon, J. Kempe, et al.,
Nature **408**, 339 (2000).

[44] J. M. Taylor, J. R. Petta, A. C. Johnson, et al.,
Phys. Rev. B **76**, 035315 (2007).

[45] E. A. Laird, J. M. Taylor, D. P. DiVincenzo, et al.,
Phys. Rev. B **82**, 075403 (2010).

[46] J. Medford, J. Beil, J. M. Taylor, et al.,
Nat. Nanotechnol. **8**, 654 (2013).

[47] M. Russ and G. Burkard,
J. Phys.: Condens. Matter **29**, 393001 (2017).

[48] Y.-P. Shim and C. Tahan,
Phys. Rev. B **93**, 121410 (2016).

[49] M. D. Reed, B. M. Maune, R. W. Andrews, et al.,
Phys. Rev. Lett. **116**, 110402 (2016).

[50] F. Martins, F. K. Malinowski, P. D. Nissen, et al.,
Phys. Rev. Lett. **116**, 116801 (2016).

[51] F. Kuemmeth and H. Bluhm,
arXiv, `10.48550/arXiv.2011.13907` (2020).

[52] A. V. Khaetskii, D. Loss, and L. Glazman,
Phys. Rev. Lett. **88**, 186802 (2002).

[53] J.-T. Hung, J. Fei, M. Friesen, and X. Hu,
Phys. Rev. B **90**, 045308 (2014).

[54] C. G. Péterfalvi and G. Burkard,
Phys. Rev. B **96**, 245412 (2017).

[55] M. Veldhorst, J. C. C. Hwang, C. H. Yang, et al.,
Nat. Nanotechnol. **9**, 981 (2014).

[56] J. T. Muhonen, J. P. Dehollain, A. Laucht, et al.,
Nat. Nanotechnol. **9**, 986 (2014).

[57] K. Eng, T. D. Ladd, A. Smith, et al.,
Sci. Adv. **1**, e1500214 (2015).

[58] J. Yoneda, K. Takeda, T. Otsuka, et al.,
Nat. Nanotechnol. **13**, 102 (2018).

[59] R. W. Andrews, C. Jones, M. D. Reed, et al.,
Nat. Nanotechnol. **14**, 747 (2019).

[60] F. A. Zwanenburg, A. S. Dzurak, A. Morello, et al.,
Rev. Mod. Phys. **85**, 961 (2013).

[61] D. Culcer, X. Hu, and S. Das Sarma,
Phys. Rev. B **82**, 205315 (2010).

[62] R. Maurand, X. Jehl, D. Kotekar-Patil, et al.,
Nat. Comm. **7**, 13575 (2016).

[63] S. D. Liles, R. Li, C. H. Yang, et al.,
Nat. Comm. **9**, 3255 (2018).

[64] H. Watzinger, J. Kukučka, L. Vukušić, et al.,
Nat. Comm. **9**, 3902 (2018).

[65] L. Vukušić, J. Kukučka, H. Watzinger, et al.,
Nano Lett. **18**, 7141 (2018).

[66] A. Crippa, R. Ezzouch, A. Aprá, et al.,
Nat. Comm. **10**, 2776 (2019).

[67] G. Scappucci, C. Kloeffel, F. A. Zwanenburg, et al.,
Nat. Rev. Mat. **6**, 926 (2020).

[68] D. Jirovec, A. Hofmann, A. Ballabio, et al.,
Nat. Mat. **20**, 1106 (2021).

[69] W. I. L. Lawrie, M. Russ, F. v. Riggelen, et al.,
arXiv:2109.07837 (2021).

[70] N. W. Hendrickx, W. I. L. Lawrie, M. Russ, et al.,
Nature **591**, 580 (2021).

[71] R. Winkler,
Spin–Orbit Coupling Effects in Two-Dimensional Electron and Hole Systems
(Springer Berlin Heidelberg, 2003).

[72] H. Watzinger, C. Kloeffel, L. Vukušić, et al.,
Nano Lett. **16**, 6879 (2016).

[73] M. Brauns, J. Ridderbos, A. Li, et al.,
Phys. Rev. B **93**, 121408(R) (2016).

[74] A. Bogan, S. A. Studenikin, M. Korkusinski, et al.,
Phys. Rev. Lett. **118**, 167701 (2017).

[75] T. M. Lu, C. T. Harris, S.-H. Huang, et al.,
Appl. Phys. Lett. **111**, 102108 (2017).

[76] A. Crippa, R. Maurand, L. Bourdet, et al.,
Phys. Rev. Lett. **120**, 137702 (2018).

[77] E. Marcellina, A. Srinivasan, D. S. Miserev, et al.,
Phys. Rev. Lett. **121**, 077701 (2018).

[78] C. Gradl, R. Winkler, M. Kempf, et al.,
Phys. Rev. X **8**, 021068 (2018).

[79] A. Hofmann, D. Jirovec, M. Borovkov, et al.,
arXiv:1910.05841 (2019).

[80] A. J. Miller, M. Brickson, W. J. Hardy, et al.,
arXiv:2102.01758 (2021).

[81] F. N. M. Froning, M. J. Ran či ć, B. Hetényi, et al.,
Phys. Rev. Research **3**, 013081 (2021).

[82] S. D. Liles, F. Martins, D. S. Miserev, et al.,
Phys. Rev. B **104**, 235303 (2021).

[83] N. Ares, G. Katsaros, V. N. Golovach, et al.,
Appl. Phys. Lett. **103**, 263113 (2013).

[84] C. Kloeffel, M. Trif, and D. Loss,
Phys. Rev. B **84**, 195314 (2011).

[85] C. Kloeffel, M. J. Rančić, and D. Loss,
Phys. Rev. B **97**, 235422 (2018).

[86] S. Bosco, M. Benito, C. Adelsberger, and D. Loss,
arXiv:2103.16724 (2021).

[87] S. Bosco, B. Hetényi, and D. Loss,
PRX Quantum **2**, 010348 (2021).

[88] F. N. M. Froning, L. C. Camenzind, O. A. H. v. d. Molen, et al.,
Nat. Nanotech. **16**, 308 (2021).

[89] Z. Wang, E. Marcellina, A. R. Hamilton, et al.,
npj Quant. Inf. **7**, 54 (2021).

[90] J. J. Sakurai,
Advanced quantum mechanics (Pearson Education India, 2006).

[91] J. Danon and Y. V. Nazarov,
Phys. Rev. B **80**, 041301 (2009).

[92] J. R. Petta, A. C. Johnson, J. M. Taylor, et al.,
Science **309**, 2180 (2005).

[93] H. Bruus and K. Flensberg,
Many-body quantum theory in condensed matter physics: an introduction
(OUP Oxford, 2004).

[94] U. Harbola, M. Esposito, and S. Mukamel,
Phys. Rev. B **74**, 235309 (2006).

[95] M. Russ, C. G. Péterfalvi, and G. Burkard,
J. Phys.: Condens. Matter **32**, 165301 (2020).

[96] D. Q. Wang, O. Klochan, J.-T. Hung, et al.,
Nano Lett. **16**, 7685 (2016).

[97] J.-Y. Wang, G.-Y. Huang, S. Huang, et al.,
Nano Lett. **18**, 4741 (2018).

[98] M. Marx, J. Yoneda, Á. G. Rubio, et al.,
arXiv:2003.07079 (2020).

[99] A. Sala and J. Danon,
Phys. Rev. B **104**, 085421 (2021).

[100] O. N. Jouravlev and Y. V. Nazarov,
Phys. Rev. Lett. **96**, 176804 (2006).

[101] J. Danon, X. Wang, and A. Manchon,
Phys. Rev. Lett. **111**, 066802 (2013).

[102] E. A. Laird, J. M. Taylor, D. P. DiVincenzo, et al.,
Phys. Rev. B **82**, 75403 (2010).

[103] L. Gaudreau, G. Granger, A. Kam, et al.,
Nat. Phys. **8**, 54 (2011).

[104] J. Medford, J. Beil, J. M. Taylor, et al.,
Nat. Nanotechnol. **8**, 654 (2013).

[105] J. Medford, J. Beil, J. M. Taylor, et al.,
Phys. Rev. Lett. **111**, 50501 (2013).

[106] D. Bacon, J. Kempe, D. A. Lidar, and K. B. Whaley,
Phys. Rev. Lett. **85**, 1758 (2000).

[107] M. Friesen, J. Ghosh, M. A. Eriksson, and S. N. Coppersmith,
Nat. Commun. **8**, 1 (2017).

[108] A. Sala and J. Danon,
Phys. Rev. B **95**, 241303 (2017).

[109] M. Russ, J. R. Petta, and G. Burkard,
Phys. Rev. Lett. **121**, 177701 (2018).

[110] F. K. Malinowski, F. Martins, P. D. Nissen, et al.,
Nat. Nano. **12**, 16 (2016).

[111] J. R. Petta, J. M. Taylor, A. C. Johnson, et al.,
Phys. Rev. Lett. **100**, 067601 (2008).

[112] D. J. Reilly, J. M. Taylor, J. R. Petta, et al.,
Science **321**, 817 (2008).

[113] S. Foletti, H. Bluhm, D. Mahalu, et al.,
Nat. Phys. **5**, 903 (2009).

[114] H. Bluhm, S. Foletti, D. Mahalu, et al.,
Phys. Rev. Lett. **105**, 216803 (2010).

[115] C. Echeverrıa-Arrondo and E. Y. Sherman,
Phys. Rev. B **87**, 081410 (2013).

[116] S. Bravyi, D. P. DiVincenzo, and D. Loss,
Ann. Phys. **326**, 2793 (2011).

[117] J. Fischer, W. A. Coish, D. V. Bulaev, and D. Loss,
Phys. Rev. B **78**, 155329 (2008).

[118] S. Richard, F. Aniel, and G. Fishman,
Phys. Rev. B **70**, 235204 (2004).

[119] F. Schäffler,
Semicond. Sci. Technol. **12**, 1515 (1997).

[120] G. Fishman,
Phys. Rev. B **52**, 11132 (1995).

[121] M. Tinkham,
Group Theory and Quantum Mechanics (McGraw-Hill Book Company, 1964).

[122] Y. Sun, S. E. Thompson, and T. Nishida,
Strain effect in semiconductors: theory and device applications (Springer Science & Business Media, 2009).

[123] T. Rebane,
Theor. Exp. Chem. **5**, 1 (1972).

[124] B. Schuh,
J. Phys. A: Math. Gen. **18**, 803 (1985).

[125] L. Qiong-Gui,
Commun. Theor. Phys. **38**, 667 (2002).

[126] Y. Chiu, M. Padmanabhan, T. Gokmen, et al.,
Phys. Rev. B **84**, 155459 (2011).

[127] W. J. Hardy, C. T. Harris, Y. H. Su, et al.,
Nanotechnology **30**, 215202 (2019).

[128] M. Lodari, A. Tosato, D. Sabbagh, et al.,
Phys. Rev. B **100**, 041304(R) (2019).

[129] S. P. Koduvayur, L. P. Rokhinson, D. C. Tsui, et al.,
Phys. Rev. Lett. **100**, 126401 (2008).

[130] B. Voisin, R. Maurand, S. Barraud, et al.,
Nano Lett. **16**, 88 (2016).

[131] F. K. de Vries, J. Shen, R. J. Skolasinski, et al.,
Nano Lett. **18**, 6483 (2018).

[132] A. Sammak, D. Sabbagh, N. W. Hendrickx, et al.,
Adv. Funct. Mat. **29**, 1807613 (2019).

[133] R. Winkler, S. J. Papadakis, E. P. DePoortere, and M. Shayegan,
Phys. Rev. Lett. **85**, 4574 (2000).

[134] R. Hanson, L. P. Kouwenhoven, J. R. Petta, et al.,
Rev. Mod. Phys. **79**, 1217 (2007).

[135] Y. Kato, R. C. Myers, D. C. Driscoll, et al.,
Science **299**, 1201 (2003).

[136] B. Venitucci, L. Bourdet, D. Pouzada, and Y.-M. Niquet,
Phys. Rev. B **98**, 155319 (2018).

[137] L. A. Terrazos, E. Marcellina, Z. Wang, et al.,
Phys. Rev. B **103**, 125201 (2021).

[138] V. P. Michal, B. Venitucci, and Y.-M. Niquet,
Phys. Rev. B **103**, 045305 (2021).

[139] C. Adelsberger, M. Benito, S. Bosco, et al.,
arXiv:2110.15039 (2021).

[140] H. Nakamura, T. Koga, and T. Kimura,
Phys. Rev. Lett. **108**, 206601 (2012).

[141] R. Moriya, K. Sawano, Y. Hoshi, et al.,
Phys. Rev. Lett. **113**, 086601 (2014).

[142] R. Winkler,
Phys. Rev. B **62**, 4245 (2000).

[143] R. Winkler, D. Culcer, S. J. Papadakis, et al.,
Semicond. Sci. Technol. **23**, 114017 (2008).

[144] E. A. Chekhovich, M. M. Glazov, A. B. Krysa, et al.,
Nat. Phys. **9**, 74 (2013).

[145] P. Machnikowski, K. Gawarecki, and Ł. Cywi ński,
Phys. Rev. B **100**, 085305 (2019).

[146] C. Testelin, F. Bernardot, B. Eble, and M. Chamarro,
Phys. Rev. B **79**, 195440 (2009).

[147] J. H. Prechtel, A. V. Kuhlmann, J. Houel, et al.,
Nat. Mat. **15**, 981 (2016).

[148] S. Bosco and D. Loss,
Phys. Rev. Lett. **127**, 190501 (2021).

[149] M. Tinkham,
Group theory and quantum mechanics (Courier Corporation, 2003).

[150] A. Baldereschi and N. O. Lipari,
Phys. Rev. B **8**, 2697 (1973).

Paper I

A. Sala, J. H. Qvist and J. Danon.

Highly tunable exchange-only singlet-only qubit in a GaAs triple quantum dot.

Physical Review Research **2**, 012062 (2020).

PHYSICAL REVIEW RESEARCH **2**, 012062(R) (2020)

Rapid Communications

Highly tunable exchange-only singlet-only qubit in a GaAs triple quantum dot

Arnau Sala, Jørgen Holme Qvist, and Jeroen Danon
Center for Quantum Spintronics, Department of Physics, Norwegian University of Science and Technology, NO-7491 Trondheim, Norway

(Received 22 November 2019; revised manuscript received 26 February 2020; accepted 27 February 2020; published 13 March 2020)

We propose an implementation of a singlet-only spin qubit in a GaAs-based triple quantum dot with a (1, 4, 1) charge occupation. In the central multielectron dot, the interplay between Coulomb interaction and an out-of-plane magnetic field creates an energy spectrum with a tunable singlet-triplet splitting, which can be exploited to create a six-particle singlet-only qubit with a qubit splitting that can straightforwardly be tuned over tens of μeV by adjusting the external magnetic field. We confirm the full exchange-based electric control of the qubit and demonstrate its superior coherence properties due to its singlet-only nature.

DOI: 10.1103/PhysRevResearch.2.012062

Introduction. Semiconductor spin qubits are among the most promising candidates for the physical realization of quantum processors [1,2]. Multispin exchange-only (XO) qubits, in particular, have drawn much attention in recent years since they offer fast qubit manipulation and full electric control [3–10]. However, rapid decoherence of the qubit—due to magnetic noise from randomly fluctuating nuclear spins [11,12], electric noise in the qubit's environment [13–15], electron-phonon coupling [16–18], and other spin-mixing mechanisms [19–22]—still causes the usable operation time of most XO qubits to be too short for scaling up. Besides, the typically small qubit splitting [4,8] hinders the long-distance coupling of XO qubits via, e.g, microwave resonators, where a large qubit splitting is required for fast two-qubit gates [23–25].

There have been several proposals put forward to increase the coherence time of quantum-dot-based XO qubits while retaining their conceptual simplicity and ease of manipulation. Of special interest are (i) proposals to suppress the effects of charge noise and electron-phonon interaction, via a symmetric operation of the qubit or operating at a sweet spot (SS) [17,26–28], and (ii) proposals to reduce magnetic noise or suppress its effects, either by isotope purification or by constructing decoherence-free qubit subspaces [9,29–32].

In the exchange-only singlet-only (XOSO) spin qubit proposed in Ref. [31], the leading effects of magnetic noise are suppressed by encoding the qubit states in a four-electron singlet-only subspace, while electric noise can be mitigated by operating the system symmetrically at a SS. However, the exceptionally long coherence time of the qubit comes at the cost of an increase in device complexity (a quadruple quantum dot in a T geometry) and the proposal suffers from the common problem with XO qubits of having a relatively small qubit splitting.

Here, we propose a GaAs-based implementation of the XOSO qubit that overcomes both drawbacks and, furthermore, has a qubit splitting that is straightforwardly tunable over a large range of energies. The reason why the XOSO qubit of Ref. [31] used a fourth quantum dot is that the qubit splitting scales with the singlet-triplet splitting of the "central" two electrons: Implementing the same qubit in a linear triple dot in a (1, 2, 1) charge configuration is in principle possible but results in a qubit with a splitting of the order of the orbital level splitting on the central dot (∼ meV), which is too large for practical purposes. In Ref. [32], it was pointed out that one can implement the same qubit in a Si-based triple dot, where the on-site singlet-triplet splitting is typically set by the valley splitting, which can be 20–200 μeV. The drawback of this proposal is that (i) the magnitude of the valley splitting is hard to control or predict in practice [2] and (ii) uncontrollable phase differences between valley couplings on different dots can severely affect the exchange effects used to define and operate the qubit [33]. Besides, Si can be purified to be almost nuclear spin free, which eradicates the need for a singlet-only qubit [9].

The solution is to tune the triple quantum dot to a (1, 4, 1) charge configuration and apply an out-of-plane magnetic field. On the central dot, the interplay between the magnetic field and the Coulomb interaction between the electrons results in an energy spectrum with many crossings between levels with different total spin and orbital angular momentum. For the case of four electrons, the ground state changes from a triplet to a singlet character, typically at a moderate field of ≈ 100 mT [34]. Tuning close to this crossing and adding the singly occupied outer dots to the picture yields a XOSO qubit where the singlet-triplet splitting on the central dot, and thus the qubit splitting, can be tuned by adjusting the external magnetic field. This yields a superior GaAs-based XOSO qubit that is not more complicated to create or operate than existing spin qubits and has a qubit splitting that is straightforwardly tunable from zero to tens of μeV [35]. This high degree of tunability could also be beneficial for a Si-based version of this qubit.

Multielectron dot. The single-particle Hamiltonian of an electron labeled i in a two-dimensional planar quantum dot,

Published by the American Physical Society under the terms of the Creative Commons Attribution 4.0 International license. Further distribution of this work must maintain attribution to the author(s) and the published article's title, journal citation, and DOI.

assuming a parabolic confinement and an external magnetic field perpendicular to the plane, is

$$H_0^{(i)} = \frac{[\mathbf{p}_i + e\mathbf{A}(\mathbf{r}_i)]^2}{2m^*} + \frac{1}{2}m^*\omega_0^2 r_i^2 + \frac{1}{2}g\mu_{\rm B}B\sigma_i^z, \qquad (1)$$

where $\mathbf{A}(\mathbf{r}) = \frac{1}{2}B(x\hat{y} - y\hat{x})$ is the vector potential, ω_0 sets the effective radius of the dot in the absence of a magnetic field $\sigma_0 = \sqrt{\hbar/m^*\omega_0}$, g is the g factor of the host material, and σ^z is the third Pauli matrix. The eigenstates of this Hamiltonian are the Fock-Darwin states

$$\psi_{n,l,\eta}(\mathbf{r}) = \sqrt{\frac{n!}{\pi\sigma^2(n+|l|)!}}\,\rho^{|l|}e^{-\rho^2/2}L_n^{|l|}(\rho^2)e^{-il\theta}, \qquad (2)$$

in terms of the dimensionless polar coordinates $\rho = r/\sigma$ and θ. We used $\sigma = \sqrt{\hbar/m^*\Omega}$, with $\Omega = \sqrt{\omega_0^2 + \omega_c^2/4}$ and $\omega_c = eB/m^*$, and $L_a^b(x)$ is the associated Laguerre polynomial. The quantum numbers $n \in \mathbb{N}_0$, $l \in \mathbb{Z}$, and $\eta = \pm 1$ label the radial state, orbital angular momentum, and spin of the electron, respectively. The corresponding eigenenergies are (we will set $\hbar = 1$ from now on)

$$E_{n,l,\eta} = \Omega(2n + |l| + 1) - \frac{1}{2}\omega_c l + \frac{1}{4}g\omega_c\frac{m^*}{m_e}\eta. \qquad (3)$$

In order to find the approximate eigenenergies and spin structure of multielectron states in the presence of electron-electron interactions, we follow the method used in Refs. [34,36]; see the Supplemental Material [37] for the details. We create a many-particle basis of antisymmetrized products of single-particle states (2), where we restrict ourselves to the states with $n \leqslant 1$ and $|l| \leqslant 3$, which corresponds to including all single-particle levels up to $\approx 4\ \Omega$ at small fields. In the thusly constructed basis, we evaluate all matrix elements of the interaction Hamiltonian

$$V = \sum_{i<j}\frac{e^2}{4\pi\varepsilon|\mathbf{r}_i - \mathbf{r}_j|}, \qquad (4)$$

and the eigenstates and eigenenergies of the full many-particle Hamiltonian $H_1 = \sum_i H_0^{(i)} + V$ can then be found from numerical diagonalization or, in the weak-interaction limit characterized by $\kappa \equiv e^2/4\pi\varepsilon\sigma_0\omega_0 \ll 1$, from perturbation theory in κ. For few particles and not too large κ (we consider up to five electrons and $\kappa \leqslant 1.5$), the low-energy part of the spectrum of H_1 will resemble the exact many-particle spectrum fairly accurately [34,44].

In Fig. 1(a), we present typical results for the lowest few levels for the case of four electrons, where we set $\kappa = 0.5$ and $g = -0.4$. The dots show the numerically calculated lowest five eigenenergies, where green (blue) dots indicate a state with a four-particle spin singlet (triplet) structure. The three triplet states are labeled $|T_\beta\rangle$ and have the largest weight in the orbital configuration $(0,0)^2(0,1)^1(0,-1)^1$, where $(n,l)^m$ means m electrons in the orbital state (n,l) [34]. The three lowest singlet states, labeled $|S_{\alpha,\beta,\gamma}\rangle$, live mostly in the orbital configurations $(0,0)^2(0,1)^2$, $(0,0)^2(0,1)^1(0,-1)^1$, and $(0,0)^2(0,-1)^2$, respectively.

For small κ, these lowest eigenenergies can also be approximated through perturbation theory in the interaction Hamiltonian V. Up to second order in κ, this yields for the lowest six states the generic expression

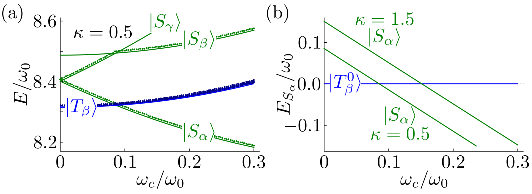

FIG. 1. (a) Field-dependent low-energy part of the spectrum of a four-electron quantum dot with $\kappa = 0.5$ and $g = -0.4$. Dots present numerical results and solid lines show the perturbative results of (5). (b) The numerically evaluated energy of the state $|S_\alpha\rangle$ (green lines) relative to $|T_\beta^0\rangle$ for two values of κ.

$$E_\nu = 6\Omega - \frac{L}{2}\omega_c + \frac{S}{2}g\omega_c\frac{m^*}{m_e} + c_1^{(\nu)}\kappa\sqrt{\Omega\omega_0} + c_2^{(\nu)}\kappa^2\omega_0, \qquad (5)$$

where L and S denote the total orbital and spin angular momentum along $\hat{z}$ of the four electrons. The coefficients $c_{1,2}^{(\nu)} \sim 1$ differ per state $|\nu\rangle$ but can be found explicitly; see Ref. [37] for their exact values. The resulting energies E_ν are plotted in Fig. 1(a) as solid lines and show good agreement with the numerics. For larger κ, the perturbation theory breaks down, but the low-energy part of the spectrum is qualitatively the same. This suggests that one can use Eq. (5) to describe the E_ν if one treats the coefficients $c_{1,2}^{(\nu)}$ as fit parameters to the numerical data. As illustrated in Ref. [37] for the case $\kappa = 1.5$, this still leads to excellent agreement. In Fig. 1(b), we show the numerically evaluated energy of the state $|S_\alpha\rangle$ relative to $|T_\beta^0\rangle$ as a function of ω_c, for $\kappa = 0.5$ and $\kappa = 1.5$. In both cases, the splitting between $|S_\alpha\rangle$ and $|T_\beta^0\rangle$ is to good approximation linear in ω_c in the regime of interest, and the ground state changes from a spin triplet to a singlet around $\omega_c/\omega_0 \sim 0.1$. These two generic features are the key ingredients for our qubit proposal.

Triple-dot six-electron states. We will construct our qubit in two *six*-electron states hosted in a linear arrangement of three quantum dots with a perpendicular magnetic field applied, such as sketched in Fig. 2(a), where the effective on-site potentials V_i and the interdot tunnel couplings t_{ij} can be controlled through nearby gate electrodes, as schematically

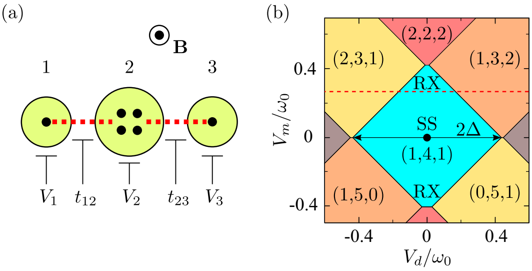

FIG. 2. (a) Sketch of the linear triple-dot setup in a (1, 4, 1) charge configuration with a perpendicular magnetic field applied. (b) Six-electron charge stability diagram around the (1, 4, 1) ground state, as a function of V_m and V_d.

indicated. We describe this system using a simple Hubbard-like Hamiltonian [16,31,45],

$$H = \sum_{i=1}^{3} \left(H_1^{(i)} - V_i n_i\right) + \sum_{\langle i,j\rangle} U_c n_i n_j - \sum_{\langle i,j\rangle,\eta} \frac{t_{ij}}{\sqrt{2}} c_{i\eta}^\dagger c_{j\eta}, \quad (6)$$

where $n_i = \sum_\eta c_{i\eta}^\dagger c_{i\eta}$ is the number operator for dot i, $c_{i\eta}$ annihilates an electron on dot i with spin η, U_c accounts for the cross capacitance between neighboring dots, and $H_1^{(i)}$ is the single-dot many-particle Hamiltonian for dot i as described above. We thus made several simplifying assumptions: (i) The gate-induced potentials are smooth enough so that they affect all electronic orbitals in the same way. (ii) The separation between the dots is large enough to allow us to treat the *inter*dot electrostatic energy as being dependent only on the n_i and not on the exact orbital configuration of the electrons on the neighboring dots. (iii) All tunneling processes we will consider below mostly involve a (0, 0) orbital on a lateral dot and a (0, ±1) orbital on the central dot; since all (0, ±1) orbitals have the same radial structure, we assume that this allows us to use tunneling coefficients t_{ij} that are independent of the exact electronic orbitals involved.

We first study the electrostatic properties of H by diagonalizing the first two terms in Eq. (6). The charge stability diagram in Fig. 2(b) shows the resulting six-electron ground-state charge configuration (n_1, n_2, n_3), where n_i is the number of electrons on dot i, as a function of the detuning parameters $V_d = \frac{1}{2}(V_3 - V_1)$ and $V_m = \frac{1}{2}(V_1 + V_3) - V_2$. We fixed $V_1 + 4V_2 + V_3$ and focused on the regime around the (1, 4, 1) state. As indicated in Fig. 2(a), we assumed different dot sizes, $\sigma_0 = 30$ nm for the central dot and $\sigma_0 = 20$ nm for the lateral dots, which results in a good ratio between the orbital splitting on the outer dots and the splitting of the many-electron states in the middle dot [46]. Furthermore, we used $U_c = 0.2\,\omega_0$ (where ω_0 is the bare level splitting on the *central* dot) and set $\omega_c/\omega_0 = 0.1$, $\kappa = 0.5$, and $m^*/m_e = 0.067$.

In the (1, 4, 1) region, the four lowest-energy six-particle states with $S^2 = 0$ can be written as

$$|0\rangle = |S_\alpha S_{(13)}\rangle, \quad (7)$$

$$|1\rangle = \frac{1}{\sqrt{3}}\left[\left|T_\beta^0 T_{(13)}^0\right\rangle - |T_\beta^- T_{(13)}^+\rangle - |T_\beta^+ T_{(13)}^-\rangle\right], \quad (8)$$

$$|2\rangle = |S_\beta S_{(13)}\rangle, \quad (9)$$

$$|3\rangle = |S_\gamma S_{(13)}\rangle, \quad (10)$$

where $|S_{(13)}\rangle$ and $|T_{(13)}\rangle$ indicate pairing in a singlet or triplet state of the two electrons in the outer dots, and $|S_{\alpha,\beta,\gamma}\rangle$ and $|T_\beta\rangle$ are the lowest four-particle singlets and triplet on the central dot, see above.

The qubit. We propose to tune close to the degeneracy of $|S_\alpha\rangle$ and $|T_\beta\rangle$ on the central dot, which for $\sigma_0 = 30$ nm happens at $B \approx 75$ mT. The two lowest-energy singlet states $|0\rangle$ and $|1\rangle$ can then be used as qubit basis, and the singlets $|2\rangle$ and $|3\rangle$ will be split off by an energy much larger than the qubit splitting.

We assume that $t/\Delta \ll 1$, with t the magnitude of the tunnel couplings (typically $t \sim 10$ μeV) and 2Δ the width of the (1, 4, 1) region; see its definition in Fig. 2(b). Then we can treat the tunnel coupling perturbatively for most of the (1, 4, 1) region, and we thus project the full Hamiltonian (6) onto the qubit subspace by means of a Schrieffer-Wolff transformation [37], yielding to order t^2

$$H_{\rm qb} = \tfrac{1}{2}(E_{ST} + J_z)\sigma_z + J_x\sigma_x, \quad (11)$$

where $\sigma_{x,z}$ are Pauli matrices. The qubit splitting is dominated by the singlet-triplet splitting on the central dot $E_{ST} = E_{T_\beta^0} - E_{S_\alpha}$ [see Fig. 1(b)], which follows to good approximation from the expressions given in Eq. (5),

$$E_{ST} \approx \gamma_0\omega_0 + \omega_c, \quad (12)$$

with $\gamma_0 = -0.235\,\kappa + 0.128\,\kappa^2$, accurate for $\kappa \lesssim 0.5$ (see Ref. [37] for all derivations and an explicit expression for γ_0). We wrote E_{ST} here up to linear order in ω_c/ω_0; the next correction is smaller by a factor $\approx 10^{-2}\kappa\omega_c/\omega_0$. Through $\omega_c \propto B$, this term, and thus the qubit splitting, can be easily tuned over tens of μeV. We emphasize that this magnetic field dependence arises through coupling of the field to the *orbital* degrees of freedom of the electrons; the (singlet-only) qubit subspace is insensitive to the coupling of magnetic fields to the *spin* of the electrons.

Close to the line where $V_d = 0$ and assuming approximately symmetric tunnel couplings $t_{12} \approx t_{23}$, the two exchange terms read as [37]

$$J_z \approx -t^2\left[\frac{\Delta}{\Delta^2 - V_m^2} + \frac{3(\Delta + \omega_c)}{(\Delta + \omega_c)^2 - V_m^2}\right], \quad (13)$$

$$J_x \approx \frac{\sqrt{6}t\,\Delta}{\Delta^2 - V_m^2}\left[\delta t + \frac{2tV_m}{\Delta^2 - V_m^2}V_d\right], \quad (14)$$

for Δ as defined in Fig. 2(b) and with $t = \frac{1}{2}(t_{12} + t_{23})$ and $\delta t = t_{12} - t_{23}$. We see that J_z in general presents a small tuning-dependent correction to the qubit splitting, which is dominated by E_{ST}, whereas J_x provides a coupling to σ_x linear in δt and/or V_d (depending on tuning), which can be used to drive Rabi oscillations.

We now discuss two regimes of special interest in the charge stability diagram shown in Fig. 2(b): (i) In the resonant-exchange (RX) regime, close to the top and bottom of the (1, 4, 1) region, the strong coupling to the other charge states offers fast qubit control through V_d [8]. In Fig. 3(a), we show the lowest-lying states as a function of V_d along the horizontal dashed line in Fig. 2(b) ($V_m/\omega_0 = 0.27$) calculated from the Hamiltonian as given in (6), where we ignored the Zeeman splitting for clarity. We used the same parameters as in Fig. 2(b) and further set $t = 25$ μeV and $\delta t = 0$. We labeled the two qubit states $|0\rangle$ and $|1\rangle$, three spin triplets $|T_{1,2,3}\rangle$, and a spin quintuplet $|Q\rangle$; including the Zeeman effect, a triplet (quintuplet) acquires an additional threefold (fivefold) splitting of 1.7 μeV for $\omega_c/\omega_0 = 0.1$. (ii) In the center of the (1, 4, 1) region, we find a SS where the qubit is to linear order insensitive to fluctuations of the potentials V_i, offering some protection against charge noise. In Fig. 3(b), we show the spectrum at the SS for the same parameters as in Fig. 3(a), now as a function of δt while setting $V_d = 0$. At the SS exchange effects are much smaller and thus the qubit splitting is closer to E_{ST} ($\approx$18.3 μeV for $\omega_c/\omega_0 = 0.1$), but apart from that the spectrum looks similar to the RX regime.

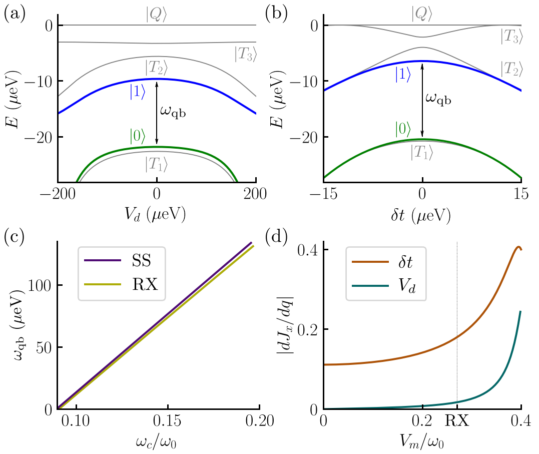

FIG. 3. Low-energy part of the spectrum of the Hamiltonian (6) (a) as a function of V_d at $V_m/\omega_0 = 0.27$ and (b) as a function of δt at the SS, $V_d = V_m = 0$. The green and blue lines show the spin-singlet qubit states $|0\rangle$ and $|1\rangle$ respectively; the gray lines show the spin triplet and quintuplet states. (c) The qubit splitting as a function of the magnetic field, where $\omega_c/\omega_0 = 0.1$ corresponds to $B \approx 75$ mT. (d) The derivative dJ_x/dq for $q \in \{\delta t, V_d\}$ as a function of V_m and at $V_d = 0$.

In Fig. 3(c), we plot the qubit splitting $\omega_{\rm qb}$ as a function of the magnetic field, in the RX regime ($V_m = 0.27$, $V_d = 0$, yellow line) and at the SS (purple line). This confirms the high degree of tunability of our qubit. We further note how the spectra in Figs. 3(a) and 3(b) strongly resemble those in the XOSO spin-qubit proposals of Refs. [31,32], the main difference being the large and straightforwardly tunable qubit splitting $\omega_{\rm qb} \propto B$ in our proposal. This permits an efficient and adaptable coupling to other systems such as microwave cavities which can be used to couple distant qubits [47–50].

Qubit operation. Single-qubit rotations can be performed via resonant Rabi driving, using a sinusoidal modulation of a tuning parameter $q = \{V_d, V_m, t, \delta t\}$ with a small amplitude $\tilde{q}$ and frequency ω, i.e., $q(t) = q_0 + \tilde{q}\,\sin(\omega t)$. For small enough $\tilde{q}$, the qubit Hamiltonian (11) can be approximated as

$$H_{\rm qb} = \tfrac{1}{2}\omega_{\rm qb}\sigma_z + A_q \sin(\omega t)\sigma_x, \qquad (15)$$

where $A_q = \tilde{q}\,(dJ_x/dq)_{q=q_0}$. Driving the qubit resonantly, $\omega = \omega_{\rm qb}$, then induces Rabi oscillations with a frequency A_q. At the RX regime, where we can use V_d as the driving parameter, an amplitude of $\tilde{V}_d = 5$–10 μeV gives a Rabi period of $T_{\rm Rabi} \approx 20$–40 ns. At the SS, Rabi rotations are much more efficient via a driving of δt, which gives a period of $T_{\rm Rabi} \approx 20$ ns for an amplitude $\delta\tilde{t} = 2$ μeV. Fast qubit rotations can therefore be achieved both in the RX regime and at the SS. In Fig. 3(d), we plot the "efficiency" dJ_x/dq of the two driving parameters $q \in \{\delta t, V_d\}$ as a function of V_m, along the line $V_{d,0} = 0$. We see that at the SS the sensitivity to V_d vanishes, in accordance with Eq. (14), whereas driving of δt stays effective all the way down to $V_m = 0$.

Qubit initialization and readout can be accomplished by standard spin-to-charge conversion, i.e., pulsing the qubit to one of the neighboring charge configurations that has only one low-lying six-particle singlet state. For example, when tuning into the (1, 3, 2)/(2, 3, 1) charge regions, only the qubit state $|0\rangle$ is adiabatically connected to the new ground-state charge configuration. This allows for initialization in $|0\rangle$ as well as readout of the qubit by means of charge detection.

Decoherence. In most GaAs-based spin qubits, the main source of decoherence is the fluctuating bath of nuclear spins that couples to the electron spins via contact hyperfine interaction. On a mean-field level, the effect of this interaction can be described by the Hamiltonian $H_{\rm hf} = \frac{1}{2}g\mu_{\rm B}\sum_i \mathbf{K}_i \cdot \boldsymbol{\sigma}_i$, with $\mathbf{K}_i$ being a random effective nuclear field acting on electron i, typically of the order of a few mT. In the device we propose in this paper, both qubit states are singlets and therefore the qubit splitting is not directly influenced by any intrinsic or external (gradient) of Zeeman fields acting on the electrons, thereby reducing the hyperfine-induced decoherence dramatically [31,32]. We estimate the coupling between the nuclear magnetic moments and the *orbital* degrees of freedom of the electrons to be negligible and dominated by hyperfine coupling of the qubit states to nearby triplet states, which leads to random higher order shifts of the qubit levels [31]. The timescale of this residual hyperfine-induced dephasing can be estimated as $T_2^* \sim A_q\hbar(\delta\varepsilon)^2/\sigma_K^4$, where $\delta\varepsilon$ is the energy splitting between $|0\rangle$ and $|T_1\rangle$; see Figs. 3(a) and 3(b) [37]. For the range of parameters considered here, we find $T_2^* \sim 0.5$–5 μs [37], giving a number of visible, coherent Rabi oscillations of $n_{\rm coh} = T_2^*/T_{\rm Rabi} \sim 25$–$250$.

Another source of decoherence for exchange-based qubits are low-frequency fluctuations in the electrostatic environment of the system. A common way to mitigate such charge noise is to operate the qubit at the SS [Fig. 3(b)], where the qubit splitting is insensitive to fluctuations in the potentials V_i to leading order; there we find a dephasing time of $T_2^* \gg 10$ μs. Away from the SS, the effects of charge noise are larger. At the RX regime [Fig. 3(a)], far away from the SS, the contribution from charge noise to dephasing becomes similar to that of nuclear noise, with a dephasing time of $T_2^* \sim 0.5$ μs [37].

Finally, qubit relaxation via electron-phonon coupling causes qubit decoherence. The relaxation rate can be estimated using Fermi's golden rule and depends on the qubit splitting and on the strength of the exchange interaction [31]. In the RX regime, where the qubit splitting can be extensively tuned through ω_c, we estimate relaxation rates from $\Gamma_{\rm rel} \sim 1$ GHz for $\omega_{\rm qb} \sim 50$ μeV to $\Gamma_{\rm rel} \sim 1$ MHz for $\omega_{\rm qb} \sim 10$ μeV. And, as is common in exchange-based qubits [18,31], the relaxation rate is strongly suppressed as we approach the SS.

Conclusions. We propose a six-electron exchange-only singlet-only spin qubit hosted in a GaAs linear triple quantum dot. Its singlet-only nature makes the qubit intrinsically insensitive to randomly fluctuating nuclear fields. The qubit can be operated fully electrically, either in an RX regime which enables fast qubit operations or at a SS where the qubit is better protected against charge noise. Furthermore, the fact that the qubit splitting is highly tunable over a large range of energies allows for efficient and adaptable coupling to microwave resonators, enabling coupling of distant qubits. The only ingredient on which this tunability relies is the appearance of a ground-state singlet-triplet transition at finite magnetic field in the multiparticle spectrum of the central dot. This is a very commonly observed feature in quantum dots of various shapes and sizes.

Acknowledgments. This work is part of FRIPRO Project No. 274853, which is funded by the Research Council of Norway (RCN), and was also partly supported by the Centers of Excellence funding scheme of the RCN, Project No. 262633, QuSpin.

A.S. and J.H.Q. contributed equally to this work.

---

[1] R. Hanson, L. P. Kouwenhoven, J. R. Petta, S. Tarucha, and L. M. K. Vandersypen, Rev. Mod. Phys. **79**, 1217 (2007).

[2] F. A. Zwanenburg, A. S. Dzurak, A. Morello, M. Y. Simmons, L. C. L. Hollenberg, G. Klimeck, S. Rogge, S. N. Coppersmith, and M. A. Eriksson, Rev. Mod. Phys. **85**, 961 (2013).

[3] D. P. DiVincenzo, D. Bacon, J. Kempe, G. Burkard, and K. B. Whaley, Nature (London) **408**, 339 (2000).

[4] M. Russ and G. Burkard, J. Phys.: Condens. Matter **29**, 393001 (2017).

[5] E. A. Laird, J. M. Taylor, D. P. DiVincenzo, C. M. Marcus, M. P. Hanson, and A. C. Gossard, Phys. Rev. B **82**, 075403 (2010).

[6] L. Gaudreau, G. Granger, A. Kam, G. C. Aers, S. A. Studenikin, P. Zawadzki, M. Pioro-Ladrière, Z. R. Wasilewski, and A. S. Sachrajda, Nat. Phys. **8**, 54 (2011).

[7] J. Medford, J. Beil, J. M. Taylor, S. D. Bartlett, A. C. Doherty, E. I. Rashba, D. P. DiVincenzo, H. Lu, A. C. Gossard, and C. M. Marcus, Nat. Nanotechnol. **8**, 654 (2013).

[8] J. Medford, J. Beil, J. M. Taylor, E. I. Rashba, H. Lu, A. C. Gossard, and C. M. Marcus, Phys. Rev. Lett. **111**, 050501 (2013).

[9] K. Eng, T. D. Ladd, A. Smith, M. G. Borselli, A. A. Kiselev, B. H. Fong, K. S. Holabird, T. M. Hazard, B. Huang, P. W. Deelman, I. Milosavljevic, A. E. Schmitz, R. S. Ross, M. F. Gyure, and A. T. Hunter, Sci. Adv. **1**, e1500214 (2015).

[10] R. W. Andrews, C. Jones, M. D. Reed, A. M. Jones, S. D. Ha, M. P. Jura, J. Kerckhoff, M. Levendorf, S. Meenehan, S. T. Merkel, A. Smith, B. Sun, A. J. Weinstein, M. T. Rakher, T. D. Ladd, and M. G. Borselli, Nat. Nanotechnol. **14**, 747 (2019).

[11] J.-T. Hung, J. Fei, M. Friesen, and X. Hu, Phys. Rev. B **90**, 045308 (2014).

[12] C. G. Péterfalvi and G. Burkard, Phys. Rev. B **96**, 245412 (2017).

[13] M. Russ and G. Burkard, Phys. Rev. B **91**, 235411 (2015).

[14] F. Martins, F. K. Malinowski, P. D. Nissen, E. Barnes, S. Fallahi, G. C. Gardner, M. J. Manfra, C. M. Marcus, and F. Kuemmeth, Phys. Rev. Lett. **116**, 116801 (2016).

[15] J. Yoneda, K. Takeda, T. Otsuka, T. Nakajima, M. R. Delbecq, G. Allison, T. Honda, T. Kodera, S. Oda, Y. Hoshi, N. Usami, K. M. Itoh, and S. Tarucha, Nat. Nanotechnol. **13**, 102 (2018).

[16] J. M. Taylor, V. Srinivasa, and J. Medford, Phys. Rev. Lett. **111**, 050502 (2013).

[17] C. Zhang, X. C. Yang, and X. Wang, Phys. Rev. A **97**, 042326 (2018).

[18] A. Sala and J. Danon, Phys. Rev. B **98**, 245409 (2018).

[19] V. N. Golovach, A. Khaetskii, and D. Loss, Phys. Rev. Lett. **93**, 016601 (2004).

[20] M. Raith, P. Stano, F. Baruffa, and J. Fabian, Phys. Rev. Lett. **108**, 246602 (2012).

[21] M. Raith, P. Stano, and J. Fabian, Phys. Rev. B **86**, 205321 (2012).

[22] A. Hofmann, V. F. Maisi, T. Krähenmann, C. Reichl, W. Wegscheider, K. Ensslin, and T. Ihn, Phys. Rev. Lett. **119**, 176807 (2017).

[23] V. Srinivasa, J. M. Taylor, and C. Tahan, Phys. Rev. B **94**, 205421 (2016).

[24] A. J. Landig, J. V. Koski, P. Scarlino, U. C. Mendes, A. Blais, C. Reichl, W. Wegscheider, A. Wallraff, K. Ensslin, and T. Ihn, Nature (London) **560**, 179 (2018).

[25] S. P. Harvey, C. G. L. Bøttcher, L. A. Orona, S. D. Bartlett, A. C. Doherty, and A. Yacoby, Phys. Rev. B **97**, 235409 (2018).

[26] M. D. Reed, B. M. Maune, R. W. Andrews, M. G. Borselli, K. Eng, M. P. Jura, A. A. Kiselev, T. D. Ladd, S. T. Merkel, I. Milosavljevic, E. J. Pritchett, M. T. Rakher, R. S. Ross, A. E. Schmitz, A. Smith, J. A. Wright, M. F. Gyure, and A. T. Hunter, Phys. Rev. Lett. **116**, 110402 (2016).

[27] Y.-P. Shim and C. Tahan, Phys. Rev. B **93**, 121410(R) (2016).

[28] F. K. Malinowski, F. Martins, P. D. Nissen, S. Fallahi, G. C. Gardner, M. J. Manfra, C. M. Marcus, and F. Kuemmeth, Phys. Rev. B **96**, 045443 (2017).

[29] D. Bacon, J. Kempe, D. A. Lidar, and K. B. Whaley, Phys. Rev. Lett. **85**, 1758 (2000).

[30] M. Friesen, J. Ghosh, M. A. Eriksson, and S. N. Coppersmith, Nat. Commun. **8**, 15923 (2017).

[31] A. Sala and J. Danon, Phys. Rev. B **95**, 241303(R) (2017).

[32] M. Russ, J. R. Petta, and G. Burkard, Phys. Rev. Lett. **121**, 177701 (2018).

[33] D. Culcer, X. Hu, and S. Das Sarma, Phys. Rev. B **82**, 205315 (2010).

[34] M. Eto, J. Phys. Soc. Jpn. **66**, 2244 (1997).

[35] An in-plane magnetic field would also induce crossings between singlet and triplet many-particle states, but due to the strong confinement of the electrons along one of the axes perpendicular to the field, a much larger magnetic field would be required to achieve the same effect.

[36] M. Rontani, F. Rossi, F. Manghi, and E. Molinari, Phys. Rev. B **59**, 10165 (1999).

[37] See Supplemental Material at http://link.aps.org/supplemental/10.1103/PhysRevResearch.2.012062 which includes Refs. [38–43], for more detailed discussions and derivations of the equations presented in the main text.

[38] V. N. Golovach, A. Khaetskii, and D. Loss, Phys. Rev. B **77**, 045328 (2008).

[39] L. P. Kouwenhoven, T. H. Oosterkamp, M. W. S. Danoesastro, M. Eto, D. G. Austing, T. Honda, and S. Tarucha, Science **278**, 1788 (1997).

[40] M. Rontani, Electronic states in semiconductor quantum dots, Ph.D. thesis, Università degli Studi di Modena e Reggio Emilia, Modena, Italy, 1999.

[41] F. C. Zhang and S. Das Sarma, Phys. Rev. B **33**, 2903 (1986).

[42] L. Jacak, J. Krasnyj, D. Jacak, W. Salejda, and A. Mituś, Acta Phys. Pol. A **99**, 277 (2001).

[43] V. Srinivasa, H. Xu, and J. M. Taylor, Phys. Rev. Lett. **114**, 226803 (2015).

[44] S. M. Reimann and M. Manninen, Rev. Mod. Phys. **74**, 1283 (2002).

[45] G. Burkard, D. Loss, and D. P. DiVincenzo, Phys. Rev. B **59**, 2070 (1999).

[46] The dependence of the orbital spacing on the dot size allows us to design a device with an orbital splitting on the outer dots larger than the level splittings in the central multielectron dot, which enables full spin blockade in the regime where the qubit is operated.

[47] M. Russ and G. Burkard, Phys. Rev. B **92**, 205412 (2015).

[48] M. Russ, F. Ginzel, and G. Burkard, Phys. Rev. B **94**, 165411 (2016).

[49] A. J. Landig, J. V. Koski, P. Scarlino, C. Müller, J. C. Abadillo-Uriel, B. Kratochwil, C. Reichl, W. Wegscheider, S. N. Coppersmith, M. Friesen, A. Wallraff, T. Ihn, and K. Ensslin, Nat. Commun. **10**, 5037 (2019).

[50] G. Burkard, M. J. Gullans, X. Mi, and J. R. Petta, Nat. Rev. Phys. **2**, 129 (2020).

Highly tunable exchange-only singlet-only qubit in a GaAs triple quantum dot: Supplemental Material

Arnau Sala, Jørgen Holme Qvist, and Jeroen Danon
Center for Quantum Spintronics, Department of Physics,
Norwegian University of Science and Technology, NO-7491 Trondheim, Norway

In this supplemental material we complement the results presented in the main text with several more detailed discussions. We included (*i*) a detailed explanation of how to construct the many-electron Hamiltonian and the derivation of analytical approximate expressions for the energy spectrum of a multi-electron quantum dot; (*ii*) the derivation of the qubit Hamiltonian via a Schrieffer-Wolff transformation; and (*iii*) an estimate of the residual effects of the hyperfine coupling to the fluctuating nuclear spin baths on the qubit's coherence properties.

ELECTRONIC STATES IN A MULTI-ELECTRON QUANTUM DOT

Single-particle states in the presence of a perpendicular magnetic field

In this section we investigate the spectrum of a multi-electron quantum dot in the presence of a magnetic field perpendicular to the plane of the dot, where we will largely follow the method used in Ref. 1. We assume strong confinement of the electrons along the z-direction, perpendicular to the plane, and a circularly symmetric parabolic in-plane confinement. Under these assumptions we write a single-particle Hamiltonian in the xy-plane for electron i:

$$H_0^{(i)} = \frac{1}{2m^*}[\mathbf{p}_i + e\mathbf{A}(\mathbf{r}_i)]^2 + \frac{1}{2}m^*\omega_0^2\mathbf{r}_i^2 + \frac{1}{2}g\mu_\mathrm{B}B\sigma_i^z, \tag{S1}$$

where $\mathbf{A}(\mathbf{r}) = \frac{1}{2}B(x\hat{y} - y\hat{x})$ is the vector potential describing the magnetic field $\mathbf{B} = B\hat{z}$, m^* is the effective mass of the electrons, ω_0 defines the strength of the in-plane confinement, such that $\sigma_0 = \sqrt{\hbar/(m^*\omega_0)}$ gives the effective radius of the dot in the absence of a magnetic field, and g is the effective g-factor of the host material.

The eigenstates of this Hamiltonian are the Fock-Darwin states,

$$\psi_{n,l,\eta}(\mathbf{r}_i) = \sqrt{\frac{n!}{\pi\sigma^2(n+|l|)!}}\,\rho_i^{|l|}e^{-\rho_i^2/2}L_n^{|l|}\left(\rho_i^2\right)e^{-il\theta_i}, \tag{S2}$$

written in terms of polar coordinates $\rho_i = r_i/\sigma$ and θ_i. Here, $\sigma = \sqrt{\hbar/m^*\Omega}$ is the magnetic-field-dependent effective dot radius, with $\Omega = \sqrt{\omega_0^2 + \omega_c^2/4}$ and $\omega_c = eB/m^*$, and $L_a^b(x)$ is the associated Laguerre polynomial. The quantum number $n = 0, 1, 2, \dots$ labels the radial orbital degree of freedom, the quantum number $l \in \mathbb{Z}$ the orbital angular momentum, and $\eta = \pm 1$ the spin of the electron. The corresponding eigenenergies are

$$E_{n,l,\eta}^{(i)} = \hbar\Omega(2n + |l| + 1) - \frac{1}{2}\hbar\omega_c l + \frac{1}{4}g\frac{m^*}{m_e}\hbar\omega_c\eta, \tag{S3}$$

where m_e is the bare electron rest mass. The first term contributes the regular two-dimensional harmonic-oscillator energies, but with a magnetic-field-dependent oscillator frequency Ω, the second term adds the direct coupling of the angular momentum l to the perpendicular magnetic field, and the last term accounts for the Zeeman effect. In Fig. 1 we show this spectrum as a function of ω_c, where the boxed labels indicate the quantum numbers (n, l) of the lowest few states. For clarity we omitted the Zeeman effect, i.e., we set $g = 0$, meaning that all lines are still twofold degenerate. The levels plotted in red are the ones we used to construct the many-particles states that formed the basis for our analytic and numerical calculations, see below.

Many-particle Hamiltonian including interactions

In a quantum dot with more than one electron one has to account for electron-electron interactions as well, which we describe by the Hamiltonian

$$V = \sum_{i<j}\frac{e^2}{4\pi\varepsilon|\mathbf{r}_i - \mathbf{r}_j|}, \tag{S4}$$

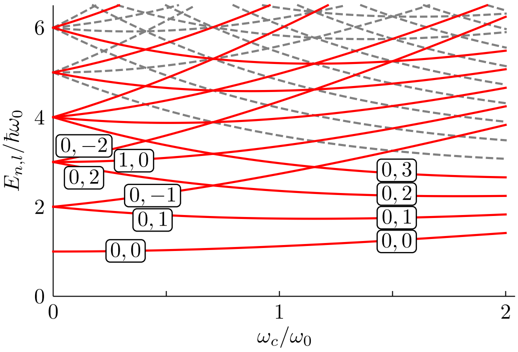

FIG. 1. The Fock-Darwin spectrum as a function of $\omega_c = eB/m^*$ for $g = 0$, see Eq. (S3), where the boxed labels indicate the orbital and angular momentum quantum numbers (n, l). The levels plotted in red are the ones we included in constructing the many-particle states that we used as a basis for our calculations.

where ε is the effective dielectric constant of the surroundings of the quantum dot. For a system with two electrons analytical diagonalization of the Hamiltonian $\sum_i H_0^{(i)} + V$ is possible [2], but for more than two electrons there is no obvious solution. We thus treat this many-body problem by working in a restricted configuration space, where we construct a basis of many-particle states from products of single-particle states and impose a cutoff on the quantum numbers n and l as was done in Ref. [1]. In this basis, we can write explicit expressions for the matrix elements of the interaction Hamiltonian (S4). We then proceed by (i) numerical diagonalization of the resulting Hamiltonian matrix and (ii) applying perturbation theory in the interaction Hamiltonian V, which works best in the weak-coupling limit, where $e^2/4\pi\varepsilon\sigma_0 \ll \hbar\omega_0$ [3].

We start by constructing a basis of many-particle states from antisymmetrized products of Fock-Darwin states. For a system of M electrons one such product state, which we denote $|s\rangle$, is characterized by a set of quantum numbers $s = \{n_{s_1}, l_{s_1}, \eta_{s_1}; n_{s_2}, l_{s_2}, \eta_{s_2}; \ldots; n_{s_M}, l_{s_M}, \eta_{s_M}\}$. The antisymmetrized wave function in position space $\langle \mathbf{r}_1, \mathbf{r}_2, \ldots \mathbf{r}_M|s\rangle = \phi_s(\mathbf{r}_1, \mathbf{r}_2, \ldots \mathbf{r}_M)$ can then be written as

$$\phi_s(\mathbf{r}_1, \mathbf{r}_2, \ldots \mathbf{r}_M) = \mathcal{A}[\psi_{n_{s_1},l_{s_1},\eta_{s_1}}(\mathbf{r}_1)\psi_{n_{s_2},l_{s_2},\eta_{s_2}}(\mathbf{r}_2)\ldots\psi_{n_{s_M},l_{s_M},\eta_{s_M}}(\mathbf{r}_M)], \tag{S5}$$

where $\mathcal{A}$ is the antisymmetrization operator.

Since $\sum_i H_0^{(i)}$ is diagonal in the basis of these product states, we can write the full Hamiltonian as

$$H = \sum_s \left[\hbar\Omega(2N_s + K_s + M) - \frac{1}{2}\hbar\omega_c L_s + \frac{1}{2}g\frac{m^*}{m_e}\hbar\omega_c S_s + V_{ss}\right]|s\rangle\langle s| + \sum_{s\neq r} V_{sr}|s\rangle\langle r|, \tag{S6}$$

where $N_s = \sum_i n_{s_i}$, $K_s = \sum_i |l_{s_i}|$, $L_s = \sum_i l_{s_i}$, $S_s = \frac{1}{2}\sum_i \eta_{s_i}$, and $V_{sr} = \langle s|V|r\rangle$. To write an explicit matrix form of this Hamiltonian we therefore need to evaluate the integrals

$$V_{sr} = \sum_{i<j}^{M} \int d\mathbf{r}_1 \cdots d\mathbf{r}_M\, \phi_s^*(\mathbf{r}_1, \ldots \mathbf{r}_M)\frac{e^2}{4\pi\varepsilon|\mathbf{r}_i - \mathbf{r}_j|}\phi_r(\mathbf{r}_1, \ldots \mathbf{r}_M) \tag{S7}$$

for all sets of quantum numbers s and r. Since the Coulomb potential couples electrons pairwise, we only need to evaluate integrals of the form

$$v_{n_1,l_1;n_2,l_2;n_3,l_3;n_4,l_4} \equiv \int d\mathbf{r}_1 d\mathbf{r}_2\, \psi^*_{n_1,l_1,\eta}(\mathbf{r}_1)\psi^*_{n_2,l_2,\eta'}(\mathbf{r}_2)\psi_{n_3,l_3,\eta'}(\mathbf{r}_2)\psi_{n_4,l_4,\eta}(\mathbf{r}_1)\frac{e^2}{4\pi\varepsilon|\mathbf{r}_1 - \mathbf{r}_2|}. \tag{S8}$$

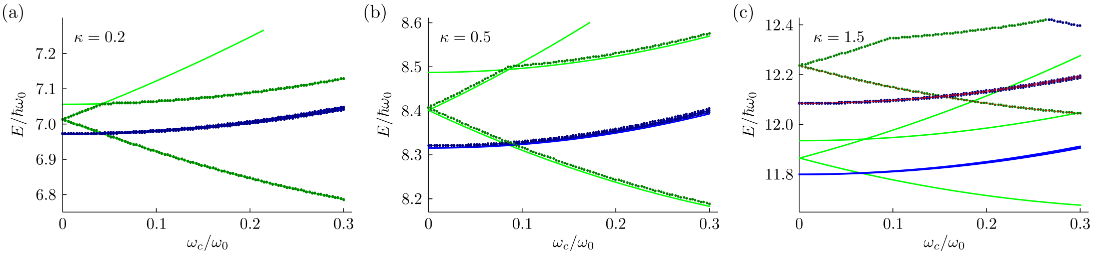

FIG. 2. The lowest few four-electron levels in a single planar quantum dot as a function of the applied perpendicular magnetic field $\omega_c = eB/m^*$ with $g = -0.4$, for three different interaction parameters: (a) $\kappa = 0.2$, (b) $\kappa = 0.5$, and (c) $\kappa = 1.5$. The dots are the result of numerical diagonalization of the Hamiltonian (S6) written in the basis of antisymmetrized product states of the 28 single-particle states with $n \in \{0, 1\}$, $l \in \{0, \pm 1, \pm 2, \pm 3\}$, and $\eta = \pm 1$. States that have a singlet spin configuration are plotted in green and states with a triplet spin configuration are plotted in blue. The solid lines show the analytic expressions for the field-dependent energies (S10–S15) as found from second-order perturbation theory in κ. The thin red dashed lines in (c) show the result of fitting the numerical data to Eqs. (S18) and (S19), which have the same algebraic structure as the perturbative results given in (S10) and (S12).

Using the Fock-Darwin states as given in Eq. (S2) the result of the integral can be written in a closed form [4],

$$v_{n_1,l_1;n_2,l_2;n_3,l_3;n_4,l_4} = \frac{e^2}{4\sqrt{2}\pi\varepsilon\sigma}\delta_{l_1+l_2,l_3+l_4}\sqrt{\prod_{i=1}^{4}\frac{n_i!}{2^{|l_i|}(n_i+|l_i|)!}}\sum_{j_1=0}^{n_1}\sum_{j_2=0}^{n_2}\sum_{j_3=0}^{n_3}\sum_{j_4=0}^{n_4}\left[\prod_{k=1}^{4}\frac{(-\frac{1}{2})^{j_k}}{j_k!}\binom{n_k+|l_k|}{n_k-j_k}\right]$$

$$\times\sum_{\lambda_1=0}^{\alpha_1}\sum_{\lambda_2=0}^{\alpha_2}\sum_{\lambda_3=0}^{\alpha_3}\sum_{\lambda_4=0}^{\alpha_4}\delta_{\lambda_1+\lambda_2,\lambda_3+\lambda_4}\left[\prod_{t=1}^{4}\binom{\alpha_t}{\lambda_t}\right](-1)^{\alpha_2+\alpha_3-\lambda_2-\lambda_3}\,\Gamma\left(\frac{\Lambda+2}{2}\right)\Gamma\left(\frac{A-\Lambda+1}{2}\right), \tag{S9}$$

where $\alpha_i = j_i + j_{5-i} + \frac{1}{2}(|l_i| + l_i + |l_{5-i}| - l_{5-i})$, $\Lambda = \sum_{i=1}^{4}\lambda_i$, and $A = \sum_{i=1}^{4}\alpha_i$. This allows us to find analytic expressions for all V_{sr} in (S6) and thus to write H in a closed matrix form.

Numerical results

We will investigate many-particle states with up to 5 electrons in a single quantum dot, assuming relatively small applied magnetic fields, $\omega_c/\omega_0 \leq 0.3$, and not too strong interactions, characterized by the dimensionless parameter $\kappa = e^2/4\pi\varepsilon\sigma_0\hbar\omega_0 \lesssim 1$. Since we are only interested in finding the lowest few levels for $M \leq 5$, the 28 single-particle states with $n \in \{0, 1\}$, $l \in \{0, \pm 1, \pm 2, \pm 3\}$ and $\eta = \pm 1$ (the levels plotted in red in Fig. 1, which all still have a twofold spin degeneracy) form in this case a reasonable set to construct our basis of many-particle states from.

We now focus on the case of four electrons and proceed by diagonalizing the Hamiltonian numerically to obtain the eigenstates and -energies of the lowest electronic states in the multi-electron quantum dot. The results are shown as dots in Fig. 2, where we used (a) $\kappa = 0.2$, (b) $\kappa = 0.5$, and (c) $\kappa = 1.5$, and we set $g = -0.4$. Green dots correspond to eigenstates that have a many-particle spin-singlet structure and blue dots to states with a spin-triplet structure. Under the simplest assumptions that the surroundings of the dot are made of pure GaAs and that there are no additional screening effects, we use $\varepsilon = 12.9\,\varepsilon_0$ and $m^* = 0.067\,m_e$ to estimate the dot size and orbital level splitting corresponding to these two values of κ, giving $E_{\text{orb}} \approx 40$ meV for $\kappa = 0.5$ and $E_{\text{orb}} \approx 5$ meV for $\kappa = 1.5$. For the most common gate-defined dots $\kappa = 1.5$ seems thus to be more realistic, although we note that the actual value of ε is probably hard to predict since it can be affected severely by structural inhomogeneities, screening effects due to nearby metallic gates, or the underlying three-dimensional nature of the electronic wave function [5].

The overall structure of the low-field part of the spectra shown in Fig. 2 is, however, the same for all values of κ: At zero field, exchange effects arising from the Coulomb interaction favor a spin triplet ground state, which for small κ has the orbital configuration $(0, 0)^2(0, 1)^1(0, -1)^1$, where the superscript denotes the number of electrons in the state (n, l) [1]. The first excited states are two spin singlets with the configurations $(0, 0)^2(0, 1)^2$ and $(0, 0)^2(0, -1)^2$, and the next excited state is the singlet with the configuration $(0, 0)^2(0, 1)^1(0, -1)^1$. When the field is increased, the most pronounced effects are: (i) all orbital energies increase due to the magnetic compression of the wave functions, i.e., the dependence of Ω on ω_c, (ii) the first two excited singlets split in energy due to their total projected orbital angular momentum of $L_z = \pm 2\hbar$, and (iii) the three triplet states split due to the Zeeman effect.

All together, this leads to a singlet-triplet crossing at $\omega_c/\omega_0 \sim 0.1$ after which a four-particle singlet becomes the ground state. Close to this degeneracy the next excited state is typically $\sim 0.2\,\hbar\omega_0$ higher in energy, which is far enough to treat the lowest four levels to first approximation as a well-separated subsystem. The magnitude of the magnetic field, through ω_c, that forces a singlet-triplet crossing also depends on κ. Therefore, for larger quantum dots, with a smaller $E_{\text{orb}} = \hbar\omega_0$, a smaller ω_c will be needed.

One could alternatively use levels that cross in this subsystem to construct a singlet-triplet qubit [6], but in this case qubit control would still rely on modulation of the magnetic field. If, instead, we add two more quantum dots with a single electron on each, then we can create a triple-dot exchange-only singlet-only qubit similar to the quadruple-dot qubit proposed in Ref. 7, where the tunability of the singlet-triplet splitting of the two central electrons, through the detuning and coupling between the two central dots, is now replaced by tunability of the splitting through the external magnetic field.

Analytic results

Since we have closed-form expressions for all elements of the interaction Hamiltonian, we can do perturbation theory in small κ to arrive at analytic expressions for the lowest few eigenenergies in a multi-electron quantum dot [8]. For the four-electrons case studied above we find for the three lowest triplet levels

$$E_{T_\beta^{(S)}} = 6\hbar\Omega + \frac{S}{2} g \frac{m^*}{m_e} \hbar\omega_c + \gamma_T^{(1)} \kappa\hbar\sqrt{\Omega\omega_0} + \gamma_T^{(2)} \kappa^2 \hbar\omega_0, \tag{S10}$$

where $S \in \{-1, 0, 1\}$ labels the total spin projection of the triplet and we used the coefficients

$$\gamma_T^{(1)} = 2\sqrt{2\pi}, \qquad \gamma_T^{(2)} = -\frac{195893509\pi}{805306368} \approx -0.764, \tag{S11}$$

that determine the prefactor of the first- and second-order correction, respectively. The two lowest singlet levels have

$$E_{S_{\alpha,\gamma}} = 6\hbar\Omega - \frac{L}{2}\hbar\omega_c + \gamma_{S1}^{(1)} \kappa\hbar\sqrt{\Omega\omega_0} + \gamma_{S1}^{(2)} \kappa^2 \hbar\omega_0, \tag{S12}$$

where L labels the total orbital angular momentum projection of the state, i.e., $L = 2$ for the lowest singlet $|S_\alpha\rangle$ and $L = -2$ for the first excited singlet $|S_\gamma\rangle$. Further,

$$\gamma_{S1}^{(1)} = \frac{67}{16}\sqrt{\frac{\pi}{2}}, \qquad \gamma_{S1}^{(2)} = -\frac{38109479\pi}{134217728} \approx -0.892. \tag{S13}$$

Finally, for the singlet $|S_\beta\rangle$ that lives in the same combination of orbital states as the lowest triplet we find

$$E_{S_\beta} = 6\hbar\Omega + \gamma_{S2}^{(1)} \kappa\hbar\sqrt{\Omega\omega_0} + \gamma_{S2}^{(2)} \kappa^2 \hbar\omega_0, \tag{S14}$$

with

$$\gamma_{S2}^{(1)} = \frac{35}{8}\sqrt{\frac{\pi}{2}}, \qquad \gamma_{S2}^{(2)} = -\frac{1391260025\pi}{4294967296} \approx -1.02. \tag{S15}$$

These results are shown as solid lines in Fig. 2(a,b) and match the numerical data reasonably well—better for smaller values of κ—but for $\kappa = 1.5$ the perturbative results are off by $\sim 5\%$. Using these results, we can also easily write down an expression for the singlet-triplet splitting denoted E_{ST} in the main text,

$$E_{T_\beta^0} - E_{S_\alpha} = \hbar\omega_c - \frac{3}{16}\sqrt{\frac{\pi}{2}}\kappa\hbar\sqrt{\Omega\omega_0} + \frac{32763365\pi}{805306368}\kappa^2\hbar\omega_0, \tag{S16}$$

which for small ω_c/ω_0 can be very well approximated by

$$E_{T_\beta^0} - E_{S_\alpha} \approx \hbar\omega_c + \left(-\frac{3}{16}\sqrt{\frac{\pi}{2}}\kappa + \frac{32763365\pi}{805306368}\kappa^2 \right) \hbar\omega_0 \approx \hbar\omega_c + \left(-0.235\,\kappa + 0.128\,\kappa^2 \right) \hbar\omega_0. \tag{S17}$$

For larger κ, such as $\kappa = 1.5$, the level structure of the low-energy part of the spectrum still looks qualitatively very similar to the small-κ case, which suggests that we can use the same type of algebraic expression to describe the energies. If we write for the lowest four levels

$$E_{T_\beta^{(S)}} = 6\hbar\Omega + \frac{S}{2} g \frac{m^*}{m_e} \hbar\omega_c + a_1 \hbar\sqrt{\Omega\omega_0} + b_1 \hbar\omega_0, \tag{S18}$$

$$E_{S_\alpha} = 6\hbar\Omega - \hbar\omega_c + a_2 \hbar\sqrt{\Omega\omega_0} + b_2 \hbar\omega_0, \tag{S19}$$

then we can use a least-square fit to the numerical data shown in Fig. 2(b) to extract the four parameters

$$a_1 = 7.383, \qquad b_1 = -1.146, \qquad a_2 = 7.123, \qquad b_2 = -1.037, \tag{S20}$$

resulting in the red dashed curves shown in the Figure, which agree very well with the numerically calculated results.

SINGLET BASIS STATES AND SCHRIEFFER-WOLFF TRANSFORMATION

As explained in the main text, the system is modeled using a Hubbard-like Hamiltonian,

$$H = \sum_i^3 \left(H_1^{(i)} - V_i n_i \right) + \sum_{\langle i,j \rangle} U_c n_i n_j - \sum_{\langle i,j \rangle,\eta} \frac{t_{ij}}{\sqrt{2}} c^\dagger_{i,\eta} c_{j,\eta}, \tag{S21}$$

where $H_1^{(i)}$ is the many-particle Hamiltonian in Eq. (S6) acting on the electrons in dot i, the V_i describe the gate-tunable offset voltages on the three dots, $n_i = \sum_\eta c^\dagger_{i,\eta} c_{i,\eta}$ is the electron number operator for dot i, U_c characterizes the interdot electrostatic coupling between the electrons, the t_{ij} describe tunneling between neighboring dots i and j, and $c_{i,\eta}$ annihilates an electron on dot i with spin η.

We assume six electrons occupying a linear array of three quantum dots. Our qubit is defined in the singlet subspace of the (1,4,1) charge configuration, the lowest four singlet states being

$$|0\rangle = |S_\alpha S_{(13)}\rangle, \tag{S22}$$

$$|1\rangle = \frac{1}{\sqrt{3}} \left[|T^0_\beta T^0_{(13)}\rangle - |T^-_\beta T^+_{(13)}\rangle - |T^+_\beta T^-_{(13)}\rangle \right], \tag{S23}$$

$$|2\rangle = |S_\beta S_{(13)}\rangle, \tag{S24}$$

$$|3\rangle = |S_\gamma S_{(13)}\rangle, \tag{S25}$$

where $|S_{(13)}\rangle$ and $|T_{(13)}\rangle$ indicate pairing in a singlet or triplet state of the two electrons in the outer dots, and $|S_{\alpha,\beta,\gamma}\rangle$ and $|T_\beta\rangle$ are the lowest four-particle singlets and triplet on the central dot, see the main text and above. In the absence of interdot tunneling, i.e., for $t_{12} = t_{23} = 0$, the energies of these four states are

$$E_0 = 2E_{D_0^{(1,1)}} + E_{S_\alpha^{(4,2)}} - V_1 - 4V_2 - V_3 + 8U_c, \tag{S26}$$

$$E_1 = 2E_{D_0^{(1,1)}} + E_{T_\beta^{(4,2)}} - V_1 - 4V_2 - V_3 + 8U_c, \tag{S27}$$

$$E_2 = 2E_{D_0^{(1,1)}} + E_{S_\beta^{(4,2)}} - V_1 - 4V_2 - V_3 + 8U_c, \tag{S28}$$

$$E_3 = 2E_{D_0^{(1,1)}} + E_{S_\gamma^{(4,2)}} - V_1 - 4V_2 - V_3 + 8U_c. \tag{S29}$$

Here, $E_{D_0^{(n,i)}}$ denotes the lowest doublet eigenenergy of the many-particle Hamiltonian (S6) for the case of n electrons on dot i, where we assumed that dots 1 and 3 are identical. Note that these energies do not include the Zeeman energy, i.e., they represent the case $E_Z = 0$ [9]. Since the corresponding state $|D_0^{(1,1)}\rangle$ has the exact orbital configuration $(0,0)^1$ this means that we simply have $E_{D_0^{(1,1)}} = \hbar\Omega^{(1)}$, where the superscript (1) indicates that we have to use the orbital energy of dot 1 (we assume the lateral dots to have a slightly smaller size than the central one). Similarly, $E_{S_\alpha^{(4,2)}}$ is the eigenenergy of the lowest four-particle singlet state on the central dot, such as investigated above, etc.

We would now like to introduce the effect of the tunnel coupling between the dots, to leading order in the coupling parameters $t_{l,r}$ denoting the tunneling coupling between the leftmost and rightmost two dots, respectively. For that purpose, we need to consider virtual transitions to the neighboring charge configurations (1,3,2), (2,3,1), (1,5,0), and

(0,5,1). (The charge states (2,2,2) and (0,6,0) also border the (1,4,1) region, but a transition to one of these requires *two* tunneling events.) The states that are directly coupled to the four basis states (S22–S25) are

$$|4\rangle = |\{D_0^{(1,1)} D_0^{(3,2)}\}_S S_0^{(2,3)}\rangle, \tag{S30}$$

$$|5\rangle = |\{D_0^{(1,1)} D_1^{(3,2)}\}_S S_0^{(2,3)}\rangle, \tag{S31}$$

$$|6\rangle = |\{D_0^{(1,1)} D_0^{(5,2)}\}_S\rangle, \tag{S32}$$

$$|7\rangle = |\{D_0^{(1,1)} D_1^{(5,2)}\}_S\rangle, \tag{S33}$$

where we used the same notation as above, i.e., $|S_0^{(2,3)}\rangle$ denotes the ground state singlet formed by two electrons in dot 3, in addition to which we used $|\{D_a D_b\}_S\rangle$ to denote the spin singlet formed by the two doublets $|D_a\rangle$ and $|D_b\rangle$. We see that states $|4\rangle$ and $|5\rangle$ are (1,3,2) states and $|6\rangle$ and $|7\rangle$ (1,5,0) states, and there are thus four more states, $|8\rangle$–$|11\rangle$, that are exactly the same but with the dot indices 1 and 3 interchanged. The three- and five-particle doublet ground states $|D_0^{(3,2)}\rangle$ and $|D_0^{(5,2)}\rangle$ have a dominating orbital configuration of $(0,0)^2(0,1)^1$ and $(0,0)^2(0,1)^2(0,-1)^1$, respectively, and since the splitting to the first excited doublet states with main configurations $(0,0)^2(0,-1)^1$ and $(0,0)^2(0,1)^1(0,-1)^2$ is relatively small we included them in the perturbation theory; these first excited doublets are indicated with a subscript 1. Using the same notation as before, the energies of these virtual states follow straightforwardly as

$$E_4 = E_{D_0^{(1,1)}} + E_{D_0^{(3,2)}} + E_{S_0^{(2,3)}} - V_1 - 3V_2 - 2V_3 + 9U_c, \tag{S34}$$

$$E_5 = E_{D_0^{(1,1)}} + E_{D_1^{(3,2)}} + E_{S_0^{(2,3)}} - V_1 - 3V_2 - 2V_3 + 9U_c, \tag{S35}$$

$$E_6 = E_{D_0^{(1,1)}} + E_{D_0^{(5,2)}} - V_1 - 5V_2 + 5U_c, \tag{S36}$$

$$E_7 = E_{D_0^{(1,1)}} + E_{D_1^{(5,2)}} - V_1 - 5V_2 + 5U_c, \tag{S37}$$

and the energies $E_{8,9,10,11}$ again by interchanging the dot indices 1 and 3.

We now include the tunnel couplings $t_{12} \equiv t_l$ and $t_{23} \equiv t_r$, and assuming that we are deep enough in the (1,4,1) region so that the energy differences to the other four charge states is much larger than the tunnel couplings we can evaluate the exchange effects perturbatively in $t_{l,r}$. This is done using a Schrieffer-Wolff transformation, and gives up to second order in $t_{l,r}$ the effective (1,4,1) Hamiltonian

$$H^{(1,4,1)} = \begin{pmatrix} 0 & J_x & J_{0,2} & 0 \\ J_x & E_{ST} + J_1 - J_0 & J_{1,2} & J_{1,3} \\ J_{2,0} & J_{2,1} & E_{S_\beta^{(4,2)}} - E_{S_\alpha^{(4,2)}} + J_2 - J_0 & J_{2,3} \\ 0 & J_{3,1} & J_{3,2} & E_{S_\gamma^{(4,2)}} - E_{S_\alpha^{(4,2)}} + J_3 - J_0 \end{pmatrix}, \tag{S38}$$

where we subtracted $E_0 + J_0$ as a constant and defined $E_{ST} \equiv E_{T_\beta^{(4,2)}} - E_{S_\alpha^{(4,2)}}$. The qubit regime we consider is where $(E_{S_{\beta,\gamma}^{(4,2)}} - E_{S_\alpha^{(4,2)}}) \gg E_{ST}$: the magnetic field is tuned not too far from the $S_\alpha T_\beta^0$-crossing in the four-electron central dot, so that the splitting between $|S_\alpha\rangle$ and $|T_\beta^0\rangle$ (~ 10 μeV) is much smaller than the distance to the other two singlets $|S_\beta\rangle$ and $|S_\gamma\rangle$ (~ 0.5 meV). Since typical exchange energies are $J \sim 1$ μeV, we can, to first approximation, neglect the exchange-induced coupling of the qubit to the states $|2\rangle$ and $|3\rangle$; they would lead to small corrections of the order $\sim J^2/(E_{S_{\beta,\gamma}^{(4,2)}} - E_{S_\alpha^{(4,2)}})$. A second (more practical) reason to neglect these couplings is that these corrections are $\propto J^2 \propto t^4$, and for consistency one would then also have to perform the original Schrieffer-Wolff transformation to order t^4, now including the charge states (2,2,2) and (0,6,0) as well.

We then arrive at the effective qubit Hamiltonian

$$H_{\rm qb} = \frac{1}{2}(E_{ST} + J_z)\sigma_z + J_x\sigma_x, \tag{S39}$$

where

$$\begin{aligned} J_z = & \frac{3t_r^2}{4}\left(\frac{1}{E_1-E_4}+\frac{1}{E_1-E_5}+\frac{1}{E_1-E_6}+\frac{1}{E_1-E_7}\right) \\ & +\frac{3t_l^2}{4}\left(\frac{1}{E_1-E_8}+\frac{1}{E_1-E_9}+\frac{1}{E_1-E_{10}}+\frac{1}{E_1-E_{11}}\right) \\ & -\frac{t_r^2}{2}\left(\frac{1}{E_0-E_4}+\frac{1}{E_0-E_6}\right)-\frac{t_l^2}{2}\left(\frac{1}{E_0-E_8}+\frac{1}{E_0-E_{10}}\right), \end{aligned} \tag{S40}$$

$$\begin{aligned} J_x = & \frac{\sqrt{3}t_r^2}{4\sqrt{2}}\left(\frac{1}{E_0-E_6}+\frac{1}{E_0-E_4}+\frac{1}{E_1-E_6}+\frac{1}{E_1-E_4}\right) \\ & -\frac{\sqrt{3}t_l^2}{4\sqrt{2}}\left(\frac{1}{E_0-E_8}+\frac{1}{E_0-E_{10}}+\frac{1}{E_1-E_8}+\frac{1}{E_1-E_{10}}\right). \end{aligned} \tag{S41}$$

The largest term in the Hamiltonian (S39) is

$$E_{ST}=\hbar\omega_c+(a_1-a_2)\hbar\sqrt{\Omega^{(2)}\omega_0^{(2)}}+(b_1-b_2)\hbar\omega_0^{(2)}, \tag{S42}$$

in terms of the notation of Eqs. (S18–S19), where $\Omega^{(2)}$ and $\omega_0^{(2)}$ are the oscillator frequencies (with and without magnetic field) of the central dot. Here one can use $a_1=\kappa\gamma_T^{(1)}$, $b_1=\kappa^2\gamma_T^{(2)}$, $a_2=\kappa\gamma_{S1}^{(1)}$, and $b_2=\kappa^2\gamma_{S1}^{(2)}$ for $\kappa\lesssim 0.5$.

The exchange terms are relatively small and their approximate magnitude can be related to the width (and "height") 2Δ of the stable (1,4,1) region in terms of the tuning parameters $V_d=\frac{1}{2}(V_3-V_1)$ and $V_m=\frac{1}{2}(V_1+V_3)-V_2$, respectively. We assume that we can neglect the difference between E_0 and E_1 compared to the splitting to the other eight states. For a given tuning (V_m,V_d) the splitting to the states $|4\rangle$, $|6\rangle$, $|8\rangle$, and $|10\rangle$ then equals the distance to the corresponding excited charge state in the charge stability diagram. The energies of the four states that involve one excited orbital state, $|5\rangle$, $|7\rangle$, $|9\rangle$, and $|11\rangle$, are higher in energy by $\hbar\omega_c$. Assuming that the stable (1,4,1) region is roughly symmetric in V_d and V_m, we then arrive at the approximate expressions

$$E_{0,1}-E_4 = -\Delta+V_d+V_m, \tag{S43}$$

$$E_{0,1}-E_5 = -\Delta+V_d+V_m-\hbar\omega_c, \tag{S44}$$

$$E_{0,1}-E_6 = -\Delta-V_d-V_m, \tag{S45}$$

$$E_{0,1}-E_7 = -\Delta-V_d-V_m-\hbar\omega_c, \tag{S46}$$

$$E_{0,1}-E_8 = -\Delta-V_d+V_m, \tag{S47}$$

$$E_{0,1}-E_9 = -\Delta-V_d+V_m-\hbar\omega_c, \tag{S48}$$

$$E_{0,1}-E_{10} = -\Delta+V_d-V_m, \tag{S49}$$

$$E_{0,1}-E_{11} = -\Delta+V_d-V_m-\hbar\omega_c, \tag{S50}$$

With these approximations we find

$$J_z=\frac{1}{2}\left(\frac{t_l^2\Delta}{(V_d-V_m)^2-\Delta^2}+\frac{t_r^2\Delta}{(V_d+V_m)^2-\Delta^2}+\frac{3t_l^2(\Delta+\omega_c)}{(V_d-V_m)^2-(\Delta+\omega_c)^2}+\frac{3t_r^2(\Delta+\omega_c)}{(V_d+V_m)^2-(\Delta+\omega_c)^2}\right), \tag{S51}$$

$$J_x=\sqrt{\frac{3}{2}}\left(\frac{t_r^2\Delta}{(V_d+V_m)^2-\Delta^2}-\frac{t_l^2\Delta}{(V_d-V_m)^2-\Delta^2}\right). \tag{S52}$$

Assuming approximately equal tunnel couplings $t_{l,r}$ and qubit operation near the "line" where $V_d=0$, we define $t=\frac{1}{2}(t_l+t_r)$ and $\delta t=t_l-t_r$, and expand the exchange energies to leading order in δt and V_d,

$$J_z \approx -t^2\left[\frac{\Delta}{\Delta^2-V_m^2}+\frac{3(\Delta+\hbar\omega_c)}{(\Delta+\hbar\omega_c)^2-V_m^2}\right], \tag{S53}$$

$$J_x \approx \frac{\sqrt{6}t\Delta}{\Delta^2-V_m^2}\left[\delta t+\frac{2tV_m}{\Delta^2-V_m^2}V_d\right]. \tag{S54}$$

HIGHER-ORDER HYPERFINE INTERACTION AND DEPHASING

Hosting the qubit in singlet states only results in having no direct coupling between the qubit states via the hyperfine interaction to lowest order. Higher-order effects, however, can give rise to energy shifts of the qubit splitting that may lead to qubit dephasing.

We treat the hyperfine interaction between the electron spins and the spins of the many nuclei on a mean-field level, resulting in a Zeeman-like Hamiltonian

$$H_{\rm hf} = \frac{g\mu_B}{2}\sum_i \mathbf{K}_i\cdot\boldsymbol{\sigma}_i, \tag{S55}$$

where $\mathbf{K}_i$ is the effective nuclear field acting on electron i and $(\hbar/2)\boldsymbol{\sigma}_i$ is the spin operator for electron i. Due to the tiny nuclear magnetic moments, the nuclear-spin density matrix will be in a high-temperature mixed state for all experimentally relevant temperatures. This results in random nuclear fields $\mathbf{K}_i$ that have zero mean and a standard deviation $\sigma_K \sim A/\sqrt{N}$, where A is an effective material-dependent hyperfine coupling parameter and N the number of nuclear spins the electron is coupled to. For typical GaAs-based quantum dots $\sigma_K \sim$ 1–5 mT.

The main contribution to higher-order hyperfine terms in the qubit subspace comes from other (non-qubit) spin states that are close in energy. There are three triplets that are energetically close to the qubit states (labeled $|T^0_{1,2,3}\rangle$ in Fig. 3 in the main text), one lying below $|0\rangle$ and two in between $|1\rangle$ and the quintuplet $|Q\rangle$. The energy splitting between the qubit states and the triplets are governed by exchange effects, where the splitting between $|0\rangle$ and $|T^0_1\rangle$ goes as $\sim t^4/\Delta^3$ [10] and the splitting between $|1\rangle$ and $|T^0_2\rangle$ and $|T^0_3\rangle$ as $\sim t^2/\Delta$. Thus, the hyperfine-induced shift in the qubit splitting is dominated by the coupling between $|0\rangle$ and the triplet states

$$|T_1^+\rangle = |S_\alpha T^+_{(13)}\rangle, \tag{S56}$$
$$|T_1^0\rangle = |S_\alpha T^0_{(13)}\rangle, \tag{S57}$$
$$|T_1^-\rangle = |S_\alpha T^-_{(13)}\rangle. \tag{S58}$$

We project the hyperfine Hamiltonian (S55) to the subspace $\{|0\rangle, |T_1^+\rangle, |T_1^0\rangle, |T_1^-\rangle\}$, yielding

$$H_{\rm hf} = \begin{pmatrix} 0 & \iota^-_{13} & \kappa_{13} & \iota^+_{13} \\ \iota^+_{13} & 0 & 0 & 0 \\ \kappa_{13} & 0 & 0 & 0 \\ \iota^-_{13} & 0 & 0 & 0 \end{pmatrix}, \tag{S59}$$

where we defined the gradients

$$\kappa_{13} = \frac{g\mu_B}{2}\left(K_1^z - K_3^z\right), \tag{S60}$$
$$\iota^\pm_{13} = \frac{g\mu_B}{2\sqrt{2}}\left(K_1^\pm - K_3^\pm\right) = \frac{g\mu_B}{2\sqrt{2}}\left(K_1^x \pm iK_1^y - K_3^x \mp iK_3^y\right). \tag{S61}$$

Using perturbation theory, we find that, to leading order in $K_i^{x,y,z}$ the energy shift of $|0\rangle$ is

$$\delta E_0 = \frac{\kappa_{13}^2}{E_0 - E_{T_1^0}} + \frac{\iota^+_{13}\iota^-_{13}}{E_0 - E_{T_1^+}} + \frac{\iota^+_{13}\iota^-_{13}}{E_0 - E_{T_1^-}}, \tag{S62}$$

where the E_ν are the unperturbed energy levels. Due to the larger separation between $|1\rangle$ and $|T^0_{2,3}\rangle$, the hyperfine-induced shift of $|1\rangle$ is much smaller. The shifts caused by the coupling to the polarized triplets $|T_1^\pm\rangle$, i.e. the two last terms, can be reduced by tuning the Zeeman energy, which can be done independently from ω_c by tilting the total externally applied field. The energy of $|T_1^0\rangle$ is not affected by the Zeeman effect, and the shift caused by the coupling to this state is thus solely determined by exchange effects.

To obtain a very rough estimate for the scale of the dephasing time caused by these higher-order hyperfine fields, we consider their effect on the Rabi oscillations when the system is driven resonantly. Following the approach of Ref. [7] we find the estimate $T_2^* \sim A_q\hbar(E_0 - E_{T_1^0})^2/\sigma_K^4$, which indeed predicts a shorter dephasing time the closer the state $|T_1^0\rangle$ is to $|0\rangle$, i.e., a shorter hyperfine-induced T_2^* at the sweet spot than in the resonant-exchange regime.

To illustrate, we calculate numerically the probability $\langle P_1(\tau)\rangle$ of finding the qubit in $|1\rangle$ after initializing in $|0\rangle$ and resonantly driving either V_d or δt for a time τ, focusing on the two cases illustrated in Fig. 3(a,b) in the main text.

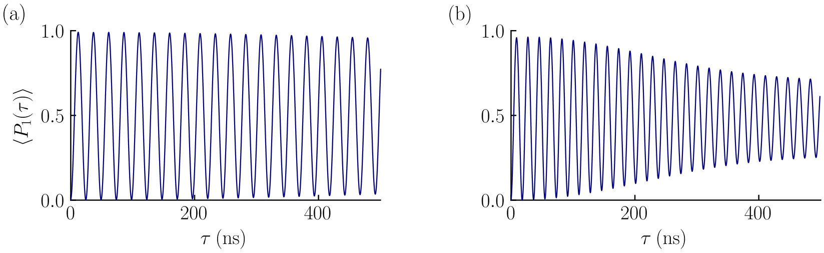

FIG. 3. Time dependent probability $\langle P_1(\tau)\rangle$ after averaging over 2500 random nuclear field configurations, (a) in the resonant-exchange regime and (b) at the sweet-spot. We used the same parameters as in the main text, with $\tilde{V}_d = 10\ \mu$eV, $\delta\tilde{t} = 2\ \mu$eV, and $g\mu_B K_i^{x,y,z}$ taken from a normal distribution with zero mean and $\sigma_K = 0.07\ \mu$eV.

In Fig. 3 we show the resulting time-dependent probabilities for (a) driving V_d in the resonant-exchange regime, and (b) driving δt at the sweet spot, after averaging over 2500 random nuclear configurations with $g\mu_B K_i^{x,y,z}$ each taken from a normal distribution with mean zero and $\sigma_K = 0.07\ \mu$eV (corresponding to 3 mT for $|g| = 0.4$). We used the same parameters as in the main text, with driving amplitudes $\tilde{V}_d = 10\ \mu$eV and $\delta\tilde{t} = 2\ \mu$eV. The results show that the hyperfine-induced dephasing, even at the sweet spot, is small compared to the Rabi period.

We finally compare this with the rough estimate $T_2^* \sim A_q\hbar(E_0 - E_{T_1^0})^2/\sigma_K^4$. Using the fact that the Rabi period is given by $T_{\text{Rabi}} = h/A_q$, we find for the approximate number of coherent Rabi oscillations that should be visible

$$n_{\text{coh}} \equiv \frac{T_2^*}{T_{\text{Rabi}}} \sim \frac{1}{2\pi}\frac{A_q^2(E_0 - E_{T_1^0})^2}{\sigma_K^4} = \frac{1}{2\pi}\frac{h^2(E_0 - E_{T_1^0})^2}{T_{\text{Rabi}}^2\sigma_K^4}. \tag{S63}$$

For the resonant-exchange regime of Fig. 3(a) we read off $T_{\text{Rabi}} \approx 25$ ns and we find $E_0 - E_{T_1^0} \approx 0.80\ \mu$eV which yields $n_{\text{coh}} \sim 120$, whereas at the sweet spot, see Fig. 3(b), we have $T_{\text{Rabi}} \approx 19$ ns and $E_0 - E_{T_1^0} \approx 0.32\ \mu$eV giving $n_{\text{coh}} \sim 30$. We see that these estimates are indeed roughly agreeing with the dephasing observed in Fig. 3.

We perform a similar analysis for the dephasing caused by charge noise affecting the gate potentials. In the RX regime (along $V_d = 0$) we find a shift in the qubit splitting given by the first-order derivatives of J_z with respect to the gate potentials V_i:

$$\hbar\delta\omega_q = \sqrt{6}t^2V_m\delta V\left[-\frac{\Delta}{(V_m^2 - \Delta^2)^2} - \frac{3(\Delta + \omega_c)}{(V_m^2 - (\Delta + \omega_c)^2)^2}\right], \tag{S64}$$

where δV is a (Gaussian) random fluctuation in the gates, with a standard deviation σ_e typically of the order of μeV. The charge noise induced dephasing can be estimated as

$$T_2^* \simeq \frac{A_q\hbar}{6t^4V_m^2\sigma_e^2}\left[\frac{\Delta}{(V_m^2 - \Delta^2)^2} + \frac{3(\Delta + \omega_c)}{(V_m^2 - (\Delta + \omega_c)^2)^2}\right]^{-2}. \tag{S65}$$

At the RX regime, with $T_2^* \sim 0.5\ \mu$eV, the effects of charge noise can be comparable to those of the nuclear spin bath, but as we approach the SS, where the first derivative of J_z vanishes, the coherence time increases substantially. A similar analysis yields $T_2^* \gg 10\ \mu$s, suggesting that the higher-order effects of the nuclear spin noise become the dominant source of decoherence at the SS.

[1] M. Eto, J. Phys. Soc. Jpn. **66**, 2244 (1997).
[2] V. N. Golovach, A. Khaetskii, and D. Loss, Phys. Rev. B **77**, 045328 (2008).
[3] L. P. Kouwenhoven, T. H. Oosterkamp, M. W. S. Danoesastro, M. Eto, D. G. Austing, T. Honda, and S. Tarucha, Science **278**, 1788 (1997).
[4] M. Rontani, *Electronic States in Semiconductor Quantum Dots*, Ph.D. thesis, Università degli Studi di Modena e Reggio Emilia (1999).
[5] F. C. Zhang and S. Das Sarma, Phys. Rev. B **33**, 2903 (1986).
[6] L. Jacak, J. Krasnyj, D. Jacak, W. Salejda, and A. Mituś, Acta Phys. Pol. A **99**, 277 (2001).

[7] A. Sala and J. Danon, Phys. Rev. B **95**, 241303(R) (2017).
[8] M. Rontani, F. Rossi, F. Manghi, and E. Molinari, Phys. Rev. B **59**, 10165 (1999).
[9] We can safely ignore the Zeeman energy here since all states we will consider in this section have a six-particle spin singlet structure.
[10] V. Srinivasa, H. Xu, and J. Taylor, Phys. Rev. Lett. **114**, 226803 (2015).

Paper II

J. H. Qvist and J. Danon.

Transport-induced suppression of nuclear field fluctuations in multi-quantum-dot systems.

Physical review B **101**, 165308 (2020).

PHYSICAL REVIEW B **101**, 165308 (2020)

Transport-induced suppression of nuclear field fluctuations in multi-quantum-dot systems

Jørgen Holme Qvist and Jeroen Danon
Center for Quantum Spintronics, Department of Physics, Norwegian University of Science and Technology, NO-7491 Trondheim, Norway

(Received 16 January 2020; revised manuscript received 24 March 2020; accepted 27 March 2020; published 17 April 2020)

Magnetic noise from randomly fluctuating nuclear spin ensembles is the dominating source of decoherence for many multi-quantum-dot multielectron spin qubits. Here, we investigate in detail the effect of a DC electric current on the coupled electron-nuclear spin dynamics in double and triple quantum dots tuned to the regime of a Pauli spin blockade. We consider both systems with and without significant spin-orbit coupling and find that in all cases the flow of electrons can induce a process of dynamical nuclear spin polarization that effectively suppresses the nuclear polarization gradients over neighboring dots. Since exactly these gradients are the components of the nuclear fields that act harmfully in the qubit subspace, we believe that this presents a straightforward way to extend coherence times in multielectron spin qubits by at least one order of magnitude.

DOI: 10.1103/PhysRevB.101.165308

I. INTRODUCTION

Spin qubits hosted in semiconductor quantum dots form an attractive qubit implementation that promises easily scalable quantum processors [1–3]. One drawback of the originally proposed single-spin single-quantum-dot qubit is that it requires highly localized magnetic fields for qubit control [4,5]. To overcome the practical challenge of creating such fields, qubits can also be encoded in a *multielectron* spin state hosted in a multi-quantum-dot structure. If one defines a qubit in the unpolarized singlet-triplet subspace of two spins in a double quantum dot, then the field along one axis of the Bloch sphere can be controlled fully electrically, but the second control axis is still set by the magnetic field gradient over the two dots [6,7]. Adding one more spin to the setup, one can create a three-electron double-dot hybrid qubit [8,9] or a triple-dot exchange-only qubit [10–14], offering electric control over the full Bloch sphere through exchange interactions [15,16].

An important remaining challenge for many multispin qubit implementations is their rapid decoherence. Its two main sources are (i) hyperfine coupling of the electronic spins to the randomly fluctuating nuclear spin baths in the quantum dots [17–20] and (ii) charge fluctuations in the environment that interfere with exchange-based qubit control [21,22]. The latter could be mitigated by enhancing the device quality or operating the qubit at a (higher-order) sweet spot [23–27], which leaves the nuclear spin noise as an important intrinsic obstacle for further progress.

Several approaches to reducing the harmful effects of nuclear spin fluctuations in exchange-only qubits are being explored: (i) One can host the qubits in quantum dots created in isotopically purified ^{28}Si, which can be made nearly nuclear spin free [2,28–31]. However, silicon comes with the complication of the extra valley degree of freedom [2], which is hard to control [32–34] and provides an extra channel for leakage and dephasing [35,36]. (ii) It is possible to encode the qubit in a four-electron singlet-only subspace [37–39], which makes it intrinsically insensitive to the fluctuating nuclear fields. This, however, presents significant complications for device design and tuning. (iii) One can actively mitigate the nuclear spin noise, e.g., by applying complex spin-echo-like pulse sequences that effectively filter out all peaks from the noise spectrum [40] or with an active feedback cycle exploiting an interplay between the electron dynamics and hyperfine interaction [41–45].

In this paper, we propose another approach that falls in the last category but is much simpler to implement. A few years ago, experiments on a double quantum dot hosted in an InAs nanowire suggested that when running a DC electric current through the system in the regime of a Pauli spin blockade, an interplay between the hyperfine interaction and strong spin-orbit interaction (SOI) in InAs can give rise to a process of dynamical nuclear polarization that effectively quenches the total Zeeman gradient over the two dots [46]. Here, we investigate this idea in more detail, and we show how it not only works for double quantum dots with strong SOI, but also in the absence of SOI and—maybe more importantly—can be implemented in a similar way in a linear triple quantum dot, where it results in a suppression of *both* nuclear field gradients between neighboring dots. For all mechanisms we investigate, we present a simple intuitive picture as well as analytic and numerical results that support this picture and predict a suppression of the fluctuations of the nuclear field gradients of one to two orders of magnitude. Since the hyperfine-induced decoherence of both singlet-triplet and exchange-only qubits originates mainly from these gradients, we believe that this current-induced suppression mechanisms yields a straightforward way to significantly extend the coherence time of multielectron qubits.

The rest of this paper is separated into two main parts, Secs. II and III, which discuss the double-dot and triple-dot setup, respectively. Both parts are organized as follows: In Secs. II A and III A we briefly review the definition of the respective qubit and present a description of the system in terms of a simple model Hamiltonian. In Secs. II B and III B we then present an intuitive picture of the mechanism behind the suppression

©2020 American Physical Society

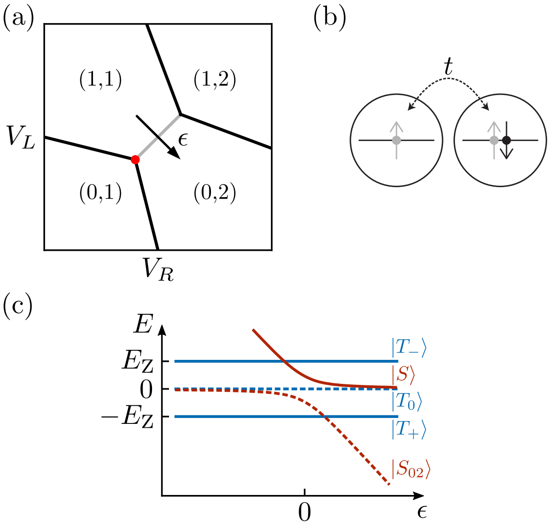

FIG. 1. (a) Typical charge stability diagram of a double quantum dot, showing the ground-state charge configuration of the system as a function of the local dot potentials V_L and V_R. (b) Sketch of the double quantum dot. If the system is in a (0,2) charge state, the two electrons must have opposite spin. (c) Energy spectrum along the detuning axis indicated in (a) showing the relevant (1,1) and (0,2) states, where a finite interdot tunnel coupling and Zeeman splitting were included. The blue (red) lines correspond to spin triplet (singlet) states.

of the gradients. Sections II C and III C contain approximate analytic expressions for the current-induced dynamics of the nuclear polarizations, which we corroborate in Secs. II D and III D with numerical simulations of the stochastic nuclear spin dynamics. Sections II E and III E contain a short conclusion, and a final general conclusion is presented in Sec. IV.

II. SINGLET-TRIPLET QUBIT

A. The qubit

The singlet-triplet qubit is usually hosted by two electrons residing in a double quantum dot and is defined in two two-particle spin states with total spin projection $S_z = 0$. Using gate voltages, the double dot is tuned close to the (1,1)-(0,2) charge transition [the gray line in the charge stability diagram shown in Fig. 1(a)]. Here, the low-energy part of the spectrum consists of five states: The large orbital level splitting on the dots (typically ∼meV) allows us to disregard states involving excited orbital states; the Pauli exclusion principle then dictates that the two electrons in the (0,2) configuration must be in a spin-singlet state $|S_{02}\rangle$. In the (1,1) charge configuration all four spin states are accessible: one singlet state $|S\rangle$, and three triplet states $|T_\pm\rangle$ and $|T_0\rangle$.

We describe this five-level subspace with a simple model Hamiltonian,

$$\hat{H}_0 = \hat{H}_e + \hat{H}_t + \hat{H}_Z. \tag{1}$$

Here,

$$\hat{H}_e = -\epsilon|S_{02}\rangle\langle S_{02}| \tag{2}$$

describes the relative energy detuning of the (1,1) and (0,2) charge states as a function of the detuning parameter ϵ (see Fig. 1). Further,

$$\hat{H}_t = t_s[|S\rangle\langle S_{02}| + |S_{02}\rangle\langle S|] \tag{3}$$

accounts for spin-conserving interdot tunneling, and

$$\hat{H}_Z = g\mu_B B[|T_+\rangle\langle T_+| - |T_-\rangle\langle T_-|] \tag{4}$$

describes the Zeeman effect due to a homogeneous magnetic field. A typical spectrum of $\hat{H}_0$ as a function of ϵ is shown in Fig. 1(c), where we have set $t_s = 0.6E_Z$ with $E_Z = |g\mu_B B|$ the Zeeman splitting, and we assumed $g < 0$.

The qubit is defined in an unpolarized subspace consisting of a triplet, $|1\rangle = |T_0\rangle$, and the lower of the two singlet branches, $|0\rangle = |S_2\rangle = \cos\frac{\theta}{2}|S_{02}\rangle + \sin\frac{\theta}{2}|S\rangle$ [dashed levels in Fig. 1(c)] where $\tan\theta = 2t_s/\epsilon$. From the projected qubit Hamiltonian

$$\hat{H}_q = \frac{\omega_q}{2}\hat{\sigma}_z, \tag{5}$$

with $\omega_q = \epsilon/2 + \sqrt{(\epsilon/2)^2 + t_s^2}$, we see that the qubit has a splitting that is tunable electrically via $V_{L,R}$, presenting an advantage over the single-spin qubit, which requires magnetic control.

In semiconductors with nonzero nuclear spin, such as GaAs and InAs, an important source of decoherence for such a qubit is the hyperfine interaction between the nuclear and electronic spins. The dominating term is the contact interaction, described by

$$\hat{H}_{\mathrm{hf}} = \sum_{d,k}\frac{A_k}{2}\left(2\hat{S}_d^z\hat{I}_{d,k}^z + \hat{S}_d^+\hat{I}_{d,k}^- + \hat{S}_d^-\hat{I}_{d,k}^+\right), \tag{6}$$

where $\hat{\mathbf{S}}_d$ is the electron spin operator on dot d, $\hat{\mathbf{I}}_{d,k}$ the nuclear spin operator for nucleus k on dot d, and $A_k = Av_0|\psi(\mathbf{r}_k)|^2$ is the coupling constant between the electrons and nucleus k, written in terms of the hyperfine coupling energy, typically $A \sim 100\ \mu\mathrm{eV}$, the density of spinful nuclei $1/v_0$, and the electron density at the position of the nucleus. Due to the small nuclear magnetic moment, the nuclear spin ensemble is in a fully mixed state in equilibrium at typical dilution fridge temperatures, and within a mean-field approximation we can then write

$$\hat{H}_{\mathrm{hf,mf}} = \mathbf{K}_L\cdot\hat{\mathbf{S}}_L + \mathbf{K}_R\cdot\hat{\mathbf{S}}_R, \tag{7}$$

where the nuclear fields $\mathbf{K}_{L,R}$ are random with an rms value $\sim A/\sqrt{N}$, where N is the number of spinful nuclei on a dot, typically $N \sim 10^5$–10^6. These fields are thus usually of the order ∼mT when translated to an effective magnetic field. Projecting this Hamiltonian to the qubit subspace yields

$$\hat{H}_{\mathrm{hf,q}} = \delta K^z \sin\frac{\theta}{2}\hat{\sigma}_x, \tag{8}$$

where $\delta K^z = \frac{1}{2}(K_L^z - K_R^z)$ is a quasistatic random field gradient. For the singlet-triplet qubit this gradient can be used for initialization along the $\pm\hat{x}$ axis of the Bloch sphere [6], but in general its random nature presents a main source of qubit decoherence. Protocols how to control or suppress the gradient δK^z could lead to significant improvement of the qubit coherence time.

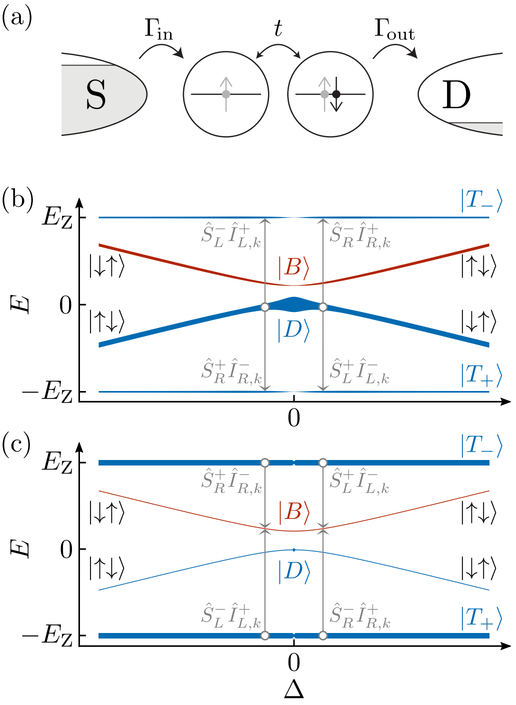
(a)
$\Gamma_{\rm in}$
t
$\Gamma_{\rm out}$
S
D
(b)
E_Z
E
0
$-E_Z$
$|T_-\rangle$
$|B\rangle$
$|D\rangle$
$|T_+\rangle$
$|\downarrow\uparrow\rangle$
$|\uparrow\downarrow\rangle$
$\hat{S}_L^-\hat{I}^+_{L,k}$
$\hat{S}_R^-\hat{I}^+_{R,k}$
$\hat{S}_R^+\hat{I}^-_{R,k}$
$\hat{S}_L^+\hat{I}^-_{L,k}$
(c)
$\hat{S}_R^+\hat{I}^-_{R,k}$
$\hat{S}_L^+\hat{I}^-_{L,k}$
$\hat{S}_L^-\hat{I}^+_{L,k}$
$\hat{S}_R^-\hat{I}^+_{R,k}$
Δ

FIG. 2. (a) The double quantum dot is tunnel coupled to source and drain reservoirs, and in the presence of a bias voltage electrons can flow from source to drain. Energy spectrum as a function of Δ for the (1,1) spin states: (b) with and (c) without spin-orbit coupling. The thickness of the lines indicates the occupation probability of the eigenstates as given by Eqs. (15)–(17). Preferred electron-nuclear spin-flip rates close to $\Delta = 0$ are indicated by the gray arrows.

B. Transport-induced nuclear spin pumping: Qualitative picture

In Ref. [46] it was shown how such a gradient can get suppressed naturally in the presence of a strong spin-orbit interaction, when the double dot is embedded in a transport setup. We will first review here the intuitive picture of the underlying mechanism, as outlined in Ref. [46], and then show how it also works in the absence of a spin-orbit interaction. In the next sections we will support this with an analytic investigation and numerical simulations of the coupled electron-nuclear spin dynamics.

We assume the double dot to be connected in a linear arrangement to source and drain reservoirs, as sketched in Fig. 2(a), and to be tuned close to the so-called "triple point" (where three stable charge regions meet) indicated by the red dot in Fig. 1(a). Then, a finite bias voltage over the source and drain can give rise to a current through the system, via the transport cycle (0, 1) → (1, 1) → (0, 2) → (0, 1). We assume that the system is tuned to the open regime, where the couplings to the reservoirs, characterized by the rates $\Gamma_{\rm in,out}$, are the largest relevant energy scales. This ensures that the tunneling processes (0, 2) → (0, 1) → (1, 1) are effectively instantaneous, and the interesting dynamics happen during the transition (1, 1) → (0, 2) which involves the same five levels as before, $\{|T_{\pm,0}\rangle, |S\rangle, |S_{02}\rangle\}$.

In the absence of spin-mixing processes, the only available transport path is (0, 1) → $|S\rangle \to |S_{02}\rangle$ → (0, 1) and population of one of the (1,1) triplet states results in a spin blockade of the current. The effect of SOI in this context is twofold: (i) Small inhomogeneities in the confining potential can result in different effective g-factors $g_{L,R}$ on the two dots, and (ii) tunneling from one dot to the other can now be accompanied by a spin flip [47]. These two effects can be described by the Hamiltonian

$$\hat{H}_{\rm so} = it^+|T_-\rangle\langle S_{02}| - it^-|T_+\rangle\langle S_{02}| \\ + it_z|T_0\rangle\langle S_{02}| + \Delta_{\rm so}|T_0\rangle\langle S| + {\rm H.c.}, \qquad (9)$$

where $t^\pm = \frac{1}{\sqrt{2}}(t_x \pm it_y)$, with the real vector $\mathbf{t}$ characterizing the spin-orbit-induced spin-flip tunnel coupling, and $\Delta_{\rm so} = \frac{1}{2}(g_L - g_R)\mu_{\rm B}B$ accounting for the difference in g-factors on the dots. The magnitude of the vector $\mathbf{t}$ can be estimated as $\sim(d/l_{\rm so})t_s$, where d is the distance between the two dots and $l_{\rm so}$ the spin-orbit length in the direction of the interdot axis.

We see that SOI can lift the blockade of the polarized states $|T_\pm\rangle$. But if the total Zeeman gradient Δ vanishes, $\Delta = \Delta_{\rm so} + \delta K^z = 0$, the two unpolarized (1,1) states can still be combined into a bright state $|B\rangle = [t_s|S\rangle + it_z|T_0\rangle]/\sqrt{t_s^2 + t_z^2}$ (that is coupled to $|S_{02}\rangle$ with strength $\sqrt{t_s^2 + t_z^2}$) and a dark state $|D\rangle = [it_z|S\rangle + t_s|T_0\rangle]/\sqrt{t_s^2 + t_z^2}$ (that is not coupled). So in this case there is still one spin-blocked state left, $|D\rangle$, which, as a consequence, will be populated with high probability, whereas the other three states $|T_\pm\rangle$ and $|B\rangle$ have a vanishing population. Adding a finite Zeeman gradient $\Delta \neq 0$ mixes the states $|T_0\rangle$ and $|S\rangle$, and thus $|B\rangle$ and $|D\rangle$, lifting the blockade of $|D\rangle$ which results in a more evenly distributed population of the levels. These observations are illustrated in Fig. 2(b), where we show the energy spectrum of the four (1,1) states as a function of Δ: The thickness of the lines indicates the relative occupation probabilities of the four states when embedded in a transport setup. We have set $t_s = 0.6E_Z$ and $\mathbf{t} = \{0.4, 0.4, 0.4\}t_s$, and we assumed the escape rates of every state to be proportional to the modulo square of its total coupling to $|S_{02}\rangle$ given by $\hat{H}_t + \hat{H}_{\rm so}$, which is valid in the limit of large $\Gamma_{\rm out}$.

Based on this, we can now develop a qualitative understanding of the resulting coupled electron-nuclear spin dynamics. The hyperfine Hamiltonian (6) contains terms $\hat{S}_d^\pm\hat{I}_{d,k}^\mp$ which can give rise to so-called spin flip-flop processes in which the electron on dot d exchanges one unit of angular momentum with one of the nuclei in the dot, which changes the value of the effective nuclear field K_d^z by a small amount. A nonequilibrium electron spin polarization on the dots can thus be slowly transferred to the nuclear spin ensemble which, in turn, can influence the electron dynamics, potentially yielding an intricate feedback cycle.

To see if there is a preferred direction of nuclear spin polarization, we investigate the spin structure of the most strongly occupied electronic state: At $\Delta = 0$ the state $|D\rangle$ contains equally large components of $|\uparrow\downarrow\rangle$ and $|\downarrow\uparrow\rangle$, i.e., $|\langle D|\uparrow\downarrow\rangle|^2 = |\langle D|\downarrow\uparrow\rangle|^2 = \frac{1}{2}$, where $|\alpha\beta\rangle$ denotes the (1,1) state with a spin-α electron on the left dot and a spin-β electron on the right dot. Due to these equal weights, all possible hyperfine-induced flip-flop processes are to first approximation equally likely, and the net nuclear spin-flip rates on both dots thus vanish. However, when $\Delta > 0$ the most strongly occupied state acquires a slightly $\downarrow\uparrow$-polarized character [see Fig. 2(b)] and then the flip-flop processes caused by $\hat{S}_L^+\hat{I}_{L,k}^-$ and $\hat{S}_R^-\hat{I}_{R,k}^+$ (illustrated by the gray arrows in the figure) are more likely than the opposite ones. This results in a net negative (positive) nuclear spin pumping rate in the left (right) dot, which reduces δK^z and thus Δ. Similarly, we see that when $\Delta < 0$, the small polarization of the most strongly occupied state will drive δK^z and thus Δ to larger values. All together, this indeed suggests that the specific manifestation of spin blockade in the presence of strong SOI can result in a self-quenching of the Zeeman gradient over the dots. The experimental results presented in Ref. [46] were consistent with this picture.

Let us now turn to the limit of very weak SOI, where we set $\mathbf{t} = \Delta_{\text{so}} = 0$. In that case we see that at $\Delta = 0$ there are three spin-blocked states, the (1,1) triplet states $|T_{\pm,0}\rangle$. At this special point one thus finds an occupation probability of $\frac{1}{3}$ for each of the triplet states and zero for the coupled state $|S\rangle$. But again, due to the symmetric polarization of all four states, there will be no net nuclear spin pumping at this point. Away from the special point $\Delta = 0$, the Zeeman gradient mixes the states $|S\rangle$ and $|T_0\rangle$ and both unpolarized eigenstates end up having a finite coupling to $|S_{02}\rangle$, whereas the polarized triplets remain uncoupled. This results in an occupation probability of approximately $\frac{1}{2}$ for $|T_+\rangle$ and $|T_-\rangle$ and zero for the two unpolarized states. We first focus on the case $\Delta > 0$, where $|D\rangle$ evolves into a state with a slightly stronger $\downarrow\uparrow$ component, whereas $|B\rangle$ acquires a slight $\uparrow\downarrow$ character [see Fig. 2(c)]. Flip flops from the blocked states can cause transitions to both unpolarized states, but due to its stronger coupling to $|S_{02}\rangle$ transitions to the state $|B\rangle$ at $\Delta = 0$ are favored. This means that the flip-flop processes caused by $\hat{S}_L^+\hat{I}_{L,k}^-$ and $\hat{S}_R^-\hat{I}_{R,k}^+$ are most likely, which again result in a pumping of δK^z toward smaller values of Δ. At $\Delta < 0$ a similar reasoning results in positive pumping of δK^z toward higher values of Δ. So, we see that also in the case of vanishing SOI a naive qualitative investigation of the spin dynamics predicts a transport-induced self-quenching of the Zeeman gradient.

In the next two sections we will present analytic and numerical investigations that support the simple picture presented above.

C. Analytic results

We start by deriving evolution equations for the nuclear polarizations in the two dots, similar to those derived in Ref. [46] but now including the effect of the strong couplings $\Gamma_{\text{in,out}}$ in a more general way and not solely focusing on the case of strong SOI. From the flip-flop rates we thus find, we derive an expression for the fluctuations around the stable point at $\Delta = 0$ using a Fokker-Planck equation to describe the stochastic dynamics of the nuclear fields $K_{L,R}^z$.

We start from a time-evolution equation for the electronic density matrix (we use $\hbar = 1$),

$$\frac{d\hat{\rho}}{dt} = -i[\hat{H}, \hat{\rho}] + \mathbf{\Gamma}\hat{\rho}, \tag{10}$$

where $\hat{H} = \hat{H}_0 + \hat{H}_{\text{so}} + \delta K^z[|T_0\rangle\langle S| + |S\rangle\langle T_0|]$. We neglect all other components of $\mathbf{K}_{L,R}$ since they lead to small corrections that are of the order K/E_Z, where K is the typical magnitude of the nuclear fields. The term $\mathbf{\Gamma}\hat{\rho} = -\frac{1}{2}\Gamma\{\hat{P}_{02}, \hat{\rho}\} + \frac{1}{4}\Gamma(\mathbb{1} - \hat{P}_{02})\rho_{02,02}$ describes the transitions $|S_{02}\rangle \to (0, 1) \to (1, 1)$, using the projector onto the (0,2) singlet state $\hat{P}_{02} = |S_{02}\rangle\langle S_{02}|$, where $\Gamma = \Gamma_{\text{out}}$ and we assume that tunneling into the system is instantaneous.

Assuming that the rate Γ is the largest energy scale in Eq. (10), we can separate the timescales of the part of $\hat{\rho}$ involving $|S_{02}\rangle$ and the part describing the dynamics in the (1,1) subspace. This yields an effective Hamiltonian for that subspace,

$$\hat{H}^{(1,1)} = \begin{pmatrix} E_Z & 0 & 0 & 0 \\ 0 & E_B & \Delta & 0 \\ 0 & \Delta & 0 & 0 \\ 0 & 0 & 0 & -E_Z \end{pmatrix}, \tag{11}$$

written in the basis $\{|T_-\rangle, |B\rangle, |D\rangle, |T_+\rangle\}$, where we assumed $g < 0$ and $B > 0$. The projection onto the (1,1) subspace resulted in exchange terms of the form $(\hat{H}_{\text{ex}})_{ij} = 4\epsilon T_{ij}/(4\epsilon^2 + \Gamma^2)$, with

$$T_{ij} = \langle i|(\hat{H}_t + \hat{H}_{\text{so}})|S_{02}\rangle\langle S_{02}|(\hat{H}_t + \hat{H}_{\text{so}})|j\rangle, \tag{12}$$

and thus $E_B = 4\epsilon(t_s^2 + t_z^2)/(4\epsilon^2 + \Gamma^2)$, where i, j can represent any of the four basis states. Assuming that E_Z is much larger than all exchange corrections, we neglected the terms coupling $|T_\pm\rangle$ to $|B, D\rangle$. The four (1,1) states also acquire a finite lifetime that can be characterized by the four decay rates $\Gamma_i = 4\Gamma T_{ii}/(4\epsilon^2 + \Gamma^2)$, where we note that $\Gamma_+ = \Gamma_- \equiv \Gamma_t$ and $\Gamma_B = 4\Gamma(t_s^2 + t_z^2)/(4\epsilon^2 + \Gamma^2)$.

Using Eq. (11) and the decay rates Γ_i, we can write a time-evolution equation for $\hat{\rho}^{(1,1)}$ similar to Eq. (10). Solving $d\hat{\rho}^{(1,1)}/dt = 0$ we find the equilibrium density matrix, which can be written $\hat{\rho}_{\text{eq}}^{(1,1)} = \sum_i p_i|i\rangle\langle i|$ in the basis $\{|T_+\rangle, |1\rangle, |2\rangle, |T_-\rangle\}$, where

$$|1\rangle = \cos\frac{\theta}{2}|D\rangle + e^{i\varphi}\sin\frac{\theta}{2}|B\rangle, \tag{13}$$

$$|2\rangle = \cos\frac{\theta}{2}|B\rangle - e^{-i\varphi}\sin\frac{\theta}{2}|D\rangle, \tag{14}$$

in terms of the angles $\varphi = \arg(-i\Gamma_B\Delta - 2E_B\Delta)$ and $\theta = \arctan(4|\Delta|/\sqrt{\Gamma_B^2 + 4E_B^2})$. The occupation probabilities p_i of the four states read

$$p_\pm = \frac{4\Gamma_B\Delta^2}{\Gamma_t E_2^2 + 8\Gamma_B\Delta^2}, \tag{15}$$

$$p_1 = \frac{1}{2} - \frac{4\Gamma_B\Delta^2 - \frac{1}{2}\Gamma_t\sqrt{(4E_B^2 + \Gamma_B^2)E_2^2}}{\Gamma_t E_2^2 + 8\Gamma_B\Delta^2}, \tag{16}$$

$$p_2 = \frac{1}{2} - \frac{4\Gamma_B\Delta^2 + \frac{1}{2}\Gamma_t\sqrt{(4E_B^2 + \Gamma_B^2)E_2^2}}{\Gamma_t E_2^2 + 8\Gamma_B\Delta^2}, \tag{17}$$

with $E_2 = \sqrt{4E_B^2 + \Gamma_B^2 + 16\Delta^2}$. In contrast to Ref. [46], we included the effect Γ_{out} here, resulting in a different basis of unpolarized states $|1, 2\rangle$.

We now add the flip-flop terms in Eq. (6) in a perturbative way where we use Fermi's golden rule to calculate the rates for the resulting nuclear spin flips. Assuming for simplicity nuclear spin $\frac{1}{2}$ [48], we write for the flip rates up and down on dot d,

$$\gamma_d^{\pm} = \frac{A^2}{4N^2} N_d^{\mp} \sum_{i,j} p_i \frac{\Gamma_j}{E_Z^2} |\langle j|\hat{S}_d^{\mp}|i\rangle|^2 + \gamma N_d^{\mp}, \tag{18}$$

where $N_d^{\pm}$ is the number of nuclei with spin $\pm\frac{1}{2}$ on the dot, and we assumed for simplicity that all nuclei in a dot are coupled equally strong to the electron spin, $A_k = A/N$. The factor Γ_j/E_Z^2 accounts for the finite lifetime of the final electronic state $|j\rangle$, assuming a Lorentzian level broadening in the limit $E_Z \gg \Gamma_j$. We also added a term that describes random nuclear spin flips with a rate γ to account phenomenologically for the slow relaxation of the nuclear spins to their fully mixed equilibrium state. Typically, this process is dominated by diffusion of nuclear spin polarization out of the quantum dots, resulting in relaxation of the nuclear spin polarization on a timescale of 1–10 s [49].

We can translate these flip rates to evolution equations for the dot polarizations $P_d = (N_d^+ - N_d^-)/N$. For the polarization gradient $P_\Delta = \frac{1}{2}(P_L - P_R)$ and the average polarization $P_\Sigma = \frac{1}{2}(P_L + P_R)$ we find

$$\frac{dP_\Delta}{dt} = -\left[F(\Delta) + \frac{1}{\tau}\right]P_\Delta - \frac{2F(\Delta)E_B\Delta}{E_B^2 + \frac{1}{4}\Gamma_B^2 + 4\Delta^2}, \tag{19}$$

$$\frac{dP_\Sigma}{dt} = -\left[F(\Delta) + \frac{1}{\tau}\right]P_\Sigma, \tag{20}$$

with

$$F(\Delta) = \frac{A^2}{4N^2E_Z^2}\frac{\Gamma_t^2\left(4E_B^2 + \Gamma_B^2 + 16\Delta^2\right) + 4\Gamma_B^2\Delta^2}{\Gamma_t\left(4E_B^2 + \Gamma_B^2 + 16\Delta^2\right) + 8\Gamma_B\Delta^2},$$

and $1/\tau = 2\gamma/N$ the phenomenological relaxation rate of the polarizations, usually $\tau \sim 1$–10 s. We note that these equations are nonlinear, since $\Delta = \Delta_{\rm so} + \delta K^z = \Delta_{\rm so} + (A/2)P_\Delta$.

From Eqs. (19) and (20) we see that both polarizations acquire effectively an enhanced relaxation rate, $\tau^{-1} \to \tau^{-1} + F(\Delta)$, which does depend on P_Δ but always drives the polarizations toward zero. Furthermore, Eq. (19) has an extra term that pumps the polarization gradient to the point where the *total* Zeeman gradient Δ is zero. For typical parameters, where $E_B \sim \Gamma_B \ll A$, this term dominates and the result is a stable polarization close to $\Delta = 0$. In the limit of vanishing SOI, we can set $\Gamma_t \to 0$ and then find $F(\Delta) = A^2\Gamma_B/8N^2E_Z^2$. These results are illustrated in Fig. 3, where in Fig. 3(a) we plot dP_Δ/dt as a function of P_Δ and in Fig. 3(b) we plot dP_Σ/dt as a function of P_Σ for three different strengths of SOI (green, red, and blue lines) as well as without any spin pumping (orange dashed line). We used $A = 250$ μeV, $E_Z = 5$ μeV, $N = 4 \times 10^5$, and $\tau = 5$ s. For the curve without SOI (green) we used $E_B = 0.5$ μeV, $\Gamma_B = 0.25$ μeV, and $\Gamma_t = \Delta_{\rm so} = 0$. The other two curves have $\Gamma_t = 0.01$ μeV, $\Delta_{\rm so} = 0.5$ μeV (red) and $\Gamma_t = 0.0625$ μeV, $\Delta_{\rm so} = 1$ μeV (blue). In these two cases, we adjusted Γ_B and E_B such that the total coupling $\sqrt{t_s^2 + |\mathbf{t}|^2}$ remains constant; this amounts to assuming that the SOI "converts" part of the tunnel coupling to a non-spin-conserving coupling but it does not affect the total coupling energy. In the next section, we will show that these analytic results also agree well with numerical simulations of the dynamics of the polarizations [see Fig. 5(a)].

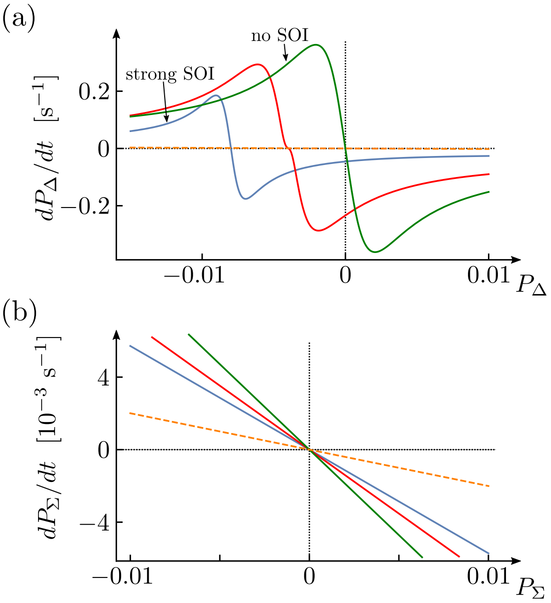

FIG. 3. Pumping curves for the polarization gradient and average polarization, as given by Eqs. (19) and (20). (a) dP_Δ/dt as a function of P_Δ. (b) dP_Σ/dt as a function of P_Σ. In both plots we show three curves: without SOI (green), with intermediate SOI (red), and with strong SOI (blue); see the main text for the parameters used. As a reference, we also added the result without any spin pumping, i.e., with $F(\Delta) = 0$ (orange dashed line).

Finally, we investigate the stochastic fluctuations of the polarization gradient around the stable point using a Fokker-Planck equation to describe the (time-dependent) probability distribution function $\mathcal{P}(n, t)$, where the integer $n = NP_\Delta$ labels the allowed polarization gradients [50,51]. Going to the continuum limit, we can find the equilibrium distribution

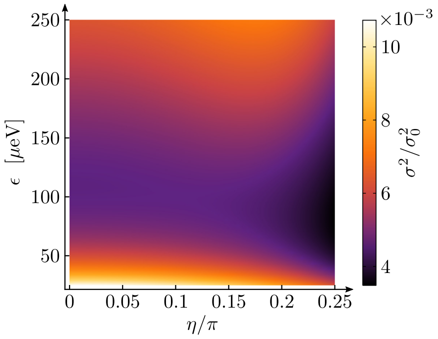

FIG. 4. Suppression of the fluctuations of the nuclear field gradient, as given in Eq. (22), as a function of ϵ and η, where η characterizes the strength of the SOI. See the main text for the parameters used and the exact definition of η.

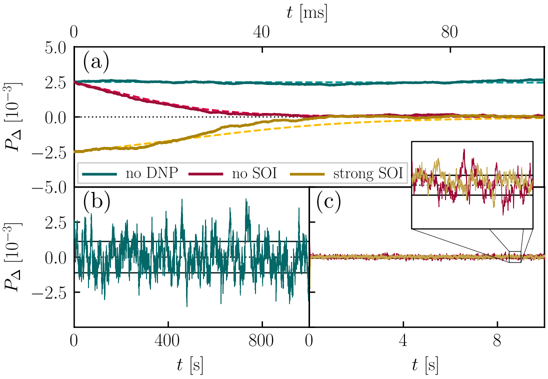

FIG. 5. Simulation of the polarization gradient $P_\Delta(t)$ without SOI (red solid lines), strong SOI (yellow solid lines), and without hyperfine-induced spin pumping ($A = 0$, green solid lines). The dashed lines show the solution of Eq. (19) using the same parameters. (a) Short-time evolution. Note that we used different initial conditions for clarity: $P_\Delta(0) = 0.0025$ for the red and green lines and $P_\Delta(0) = -0.0025$ for the yellow line; we always set $P_\Sigma(0) = 0$. (b) Long-time evolution for $A = 0$. The horizontal black lines indicate $\pm\sigma_0$. (c) Long-time evolution in the presence of spin pumping. The horizontal black lines now show $\pm\sigma$ as found from Eq. (22) (see inset). See the main text for all other parameters used.

function to be

$$\mathcal{P}(P_\Delta) = \exp\left\{\int^{P_\Delta} dP'_\Delta\, 2N\frac{\gamma_\Delta^+ - \gamma_\Delta^-}{\gamma_\Delta^+ + \gamma_\Delta^-}\right\}, \tag{21}$$

where $\gamma_\Delta^\pm = \frac{1}{2}(\gamma_L^\pm - \gamma_R^\pm)$ in terms of the flip rates as written in Eq. (18). The slope of the integrand close to the points where $\gamma_\Delta^+ - \gamma_\Delta^- = 0$ can thus be used to estimate the equilibrium rms deviation of P_Δ from those stable points. In the absence of pumping, i.e., for $F(\Delta) \to 0$, we find a peak in the distribution around the point $P_\Delta = 0$ with a variance $\sigma_0^2 = 1/2N$. Including pumping, and assuming that the second term in Eq. (19) dominates around the stable point, we find a peak in $\mathcal{P}(P_\Delta)$ at $P_\Delta \approx -2\Delta_{\text{so}}/A$, where

$$\sigma^2 \approx \sigma_0^2 \frac{E_B^2 + \frac{1}{4}\Gamma_B^2}{AE_B}\left(1 + 8\frac{E_Z^2N^2}{A^2\tau}\frac{\Gamma_B + 2\Gamma_t}{\Gamma_B^2 + 4\Gamma_t^2}\right). \tag{22}$$

In Fig. 4 we show the resulting suppression of the fluctuations σ^2/σ_0^2 as a function of detuning ϵ and strength of the SOI, parametrized by η, where we fixed the total tunnel coupling to $t = 7.5$ μeV and then used $t_x^2 + t_y^2 = t^2\sin^2\eta$ and $t_z^2 + t_s^2 = t^2\cos^2\eta$. In this way, $\eta = 0$ corresponds to having no SOI and $\eta \sim \pi/4$ to strong SOI. We further used $A = 250$ μeV, $E_Z = 12.5$ μeV, $\Gamma = 75$ μeV, $N = 4 \times 10^5$, and $\tau = 5$ s. For these parameters we observe a significant suppression of the fluctuations in the whole range we plotted. We see that the suppression is most effective for strong SOI (where $\eta \to \pi/4$), but still of the same order of magnitude in the absence of SOI (where $\eta = 0$).

D. Numerical simulations

We complement our analytic results with a numerical simulation of the electron-nuclear spin dynamics, discretizing time in small steps of Δt. We start with two initial polarizations $P_L(0)$ and $P_R(0)$ on the two dots and then solve for the eigenvalues ε_i and eigenmodes $\hat{\rho}_i$ of the superoperator Λ that describes the coherent evolution and decay of the density matrix,

$$\Lambda\hat{\rho} = -i[\hat{H}, \hat{\rho}] - \tfrac{1}{2}\{\hat{\Gamma}, \hat{\rho}\}, \tag{23}$$

where $\hat{\Gamma}$ is a diagonal matrix containing the decay rates of the five basis states [52]. Each of the 25 eigenmodes of Λ can then be written as $\hat{\rho}_i = |n\rangle\langle m|$, where $|n\rangle$ and $|m\rangle$ are picked from a (new) five-dimensional basis. The corresponding eigenvalue ε_i has the form $\varepsilon_i = -i(E_n - E_m) - \frac{1}{2}(\gamma_n + \gamma_m)$, where $E_{n,m}$ and $\gamma_{n,m}$ give the effective energies and decay rates of the two states $|n\rangle$ and $|m\rangle$. From knowing all ε_i and $\hat{\rho}_i$ we can thus derive the appropriate basis states, their effective energies, and their decay rates. To find the steady-state occupation probabilities for these five states, we evaluate their weight in the (1,1) subspace, $w_n = \langle n|(\mathbb{1} - \hat{P}_{02})|n\rangle$, from which the occupation probabilities follow as $p_n = w_n\gamma_n^{-1}/\sum_i w_i\gamma_i^{-1}$.

Now we have all ingredients we need to evaluate the spin-flip rates on both dots. We rewrite Eq. (18) including the detailed dependence on all energy differences and decay rates,

$$\gamma_d^\pm = \frac{A^2}{N^2}\sum_{i,j}\frac{p_i(\gamma_i + \gamma_j)|\langle j|\hat{S}_d^\mp|i\rangle|^2}{4(E_i - E_j)^2 + (\gamma_i + \gamma_j)^2}N_d^\mp + \gamma N_d^\mp, \tag{24}$$

where i, j now run over the actual eigenstates found numerically as outlined above. Then we pick random numbers of spin-flip events $k_d^\pm$ on both dots and in both directions, using a Poisson distribution $(\gamma_d^\pm\Delta t)^{k_d^\pm}e^{\gamma_d^\pm\Delta t}/(k_d^\pm)!$, and we update the polarizations $P_d(\Delta t) = P_d(0) + (2/N)(k_d^+ - k_d^-)$. This process can then be repeated as many times as desired to simulate the evolution of $P_{L,R}(t)$ over longer times. We note that we make sure that Δt is small enough so that most of the $k_d^\pm$ turn out 0 or 1.

We show the results of our simulations as solid lines in Fig. 5, where we plot $P_\Delta(t)$ for three different cases: (i) strong SOI, where $t_{x,y,z} = 3.12$ μeV and $t = 5.21$ μeV (yellow), (ii) no SOI, with $t_{x,y,z} = 0$ and $t = 7.5$ μeV (red), and (iii) no hyperfine interaction (green). The other parameters used were $A = 125$ μeV, $E_Z = 12.5$ μeV, $\delta = 100$ μeV, $\Gamma = 75$ μeV, $N = 4 \times 10^5$, $\tau = 5$ s, and $\Delta t = 10$ μs. We used as initial conditions $P_\Delta(0) = 0.0025$ (red and green), $P_\Delta(0) = -0.0025$ (yellow), and $P_\Sigma(0) = 0$ (always). We note that, in order to make the comparison more straightforward, we set $\Delta_{\text{so}} = 0$ in all cases, including the case of strong SOI.

In Fig. 5(a) we show the first 0.1 s of the evolution. We see that the hyperfine interaction accelerates the dynamics of the polarizations and tends to suppress the gradient to zero. We added dashed lines that show time-dependent solutions of Eq. (19), which indeed seems to predict the average dynamics of the polarization gradient to reasonable accuracy. In Figs. 5(b) and 5(c) we show longer time traces to illustrate the magnitude of the fluctuations around the stable point $P_\Delta = 0$. In Fig. 5(b) the fluctuations are clearly much larger than in Fig. 5(c), which is what we expected. The horizontal lines show the magnitude of the fluctuations as predicted by Eq. (22): For the parameters used we find $\sigma_0 = 1.1 \times 10^{-3}$ (to be compared with the green trace), and $\sigma = 7.8 \times 10^{-5}$ (red trace) and $\sigma = 7.5 \times 10^{-5}$ (yellow trace).

In both simulations that include spin pumping (red and yellow lines) the average polarization P_Σ tends to drift to negative values, stabilizing at ~ -0.02. This can be understood in qualitative terms from Figs. 2(b) and 2(c): With strong SOI [Fig. 2(b)] the state $|T_+\rangle$ decays more efficiently than $|T_-\rangle$ since it is closer in energy to $|S_{02}\rangle$ and Γ is finite. This makes in general spin flips from $|D\rangle$ slightly more likely to happen to $|T_+\rangle$, resulting in a net average transfer of negative angular momentum to the nuclear spins. Without SOI [Fig. 2(c)], the bright state $|B\rangle$ is closer in energy to $|T_-\rangle$ than to $|T_+\rangle$ (assuming $\delta > 0$), resulting in the flip rate $|T_-\rangle \to |B\rangle$ to be larger than $|T_+\rangle \to |B\rangle$. This should indeed also result in a small net negative pumping of the average polarization. These effects are not reflected in Eq. (20) since in that section we neglected all energy differences in the (1,1) subspace compared to E_Z, which, in turn, was assumed negligible compared to Γ.

E. Conclusion

We found that embedding a double quantum dot in the spin-blockade regime in a transport setup, the flow of electrons induces dynamic nuclear spin polarization that tends to suppress the polarization gradient over the two dots. This mechanism not only works in the case of strong SOI, but also with weak SOI or in the absence of SOI. We derived simple analytic equations to describe the dynamics of the polarization gradient (which we corroborated with numerical simulations), and we found that, over a large range of parameters, the rms value of the random polarization gradient can be suppressed by one to two orders of magnitude. This could present a straightforward way to extend the coherence time of double-dot-based spin qubits.

III. EXCHANGE-ONLY QUBIT

A. The qubit

Exchange-only qubits are usually hosted in a linear triple quantum dot, with one electron in each dot. The eight-dimensional (1,1,1) subspace consists of one spin quadruplet $|Q\rangle$ and two doublets $|D_1\rangle$ and $|D_2\rangle$. An external magnetic field lifts the degeneracy of states with different total S_z, and when the system is then tuned close to the border of the (1,1,1) region, exchange effects due to finite interdot tunneling can lift the remaining degeneracies. The qubit is then commonly defined in the two doublet states with spin projection $S_z = +\frac{1}{2}$, and turns out to be fully controllable via electric fields only.

In Fig. 6(a) we sketch the charge stability diagram close to the (1,1,1)-(1,0,2)-(2,0,1) triple point, as a function of the two tuning parameters $\epsilon = \frac{1}{2}(V_R - V_L)$ and $\epsilon_M = V_C - \frac{1}{2}(V_L + V_R)$, where $V_{L,C,R}$ denote the gate-induced potentials on the left, central, and right dot, respectively. We include energy offsets such that the triple point is defined to be at $(\epsilon_M, \epsilon) = (0, 0)$. In this regime, the low-energy part of the spectrum consists of 12 states: In addition to the eight (1,1,1) states mentioned above, we also need to include a doublet $|D_L\rangle$ in a (2,0,1) configuration and a doublet $|D_R\rangle$ in a (1,0,2) configuration.

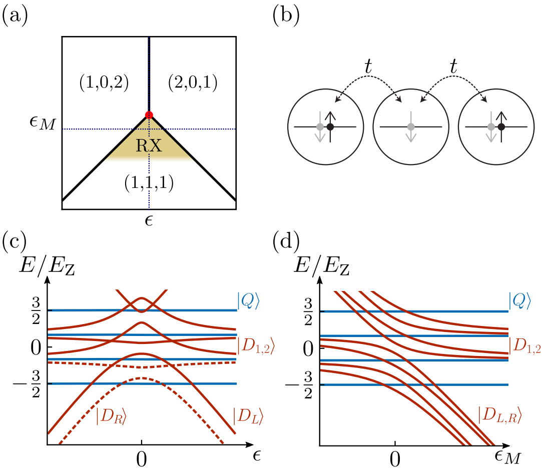

FIG. 6. (a) Sketch of the charge stability diagram of a linear triple quantum dot tuned close to the (1,1,1)-(1,0,2)-(2,0,1) triple point. (b) Cartoon of the setup. (c), (d) Lowest part of the spectrum along the horizontal and vertical dashed line, respectively.

We can then write a similar Hamiltonian as before,

$$\hat{H}_0 = \hat{H}_e + \hat{H}_t + \hat{H}_Z. \tag{25}$$

Now we have

$$\hat{H}_e = \sum_{\alpha=\pm} \{ -(\epsilon_M + \epsilon)|D_L^\alpha\rangle\langle D_L^\alpha| - (\epsilon_M - \epsilon)|D_R^\alpha\rangle\langle D_R^\alpha| \}, \tag{26}$$

where $\alpha = \pm$ labels the spin projection $S_z = \pm\frac{1}{2}$ of the doublet state. The tunneling Hamiltonian is

$$\begin{aligned} \hat{H}_t =& \frac{t}{2} \sum_{\alpha=\pm} \alpha \{ \sqrt{3}|D_1^\alpha\rangle[\langle D_R^\alpha| - \langle D_L^\alpha|] \\ &+ |D_2^\alpha\rangle[\langle D_R^\alpha| + \langle D_L^\alpha|] \} + \text{H.c.}, \end{aligned} \tag{27}$$

where we assumed the left and right tunneling couplings to be equal, for simplicity. The Zeeman term is

$$\hat{H}_Z = g\mu_B B \hat{S}_z^{\text{tot}}, \tag{28}$$

in terms of the total spin-z projection operator for the three electrons.

In the region marked “RX” in Fig. 6(a) the central electron can become delocalized over the three dots [see Fig. 6(b)], yielding relatively strong exchange effects. To illustrate, we sketch in Fig. 6(c) the spectrum of $\hat{H}_0$ along the dotted line in (a), where we set $t = 3E_Z$. The two dashed lines (the lowest doublet states with $S_z^{\text{tot}} = +\frac{1}{2}$) form the qubit subspace, where $|1\rangle = |D_2^+\rangle$ and $|0\rangle = |D_1^+\rangle$ at $\epsilon = 0$. Close to that point, the projected qubit Hamiltonian is

$$\hat{H}_q = \frac{J}{2}\hat{\sigma}_z - \frac{\sqrt{3}j}{2}\hat{\sigma}_x, \tag{29}$$

with $J = \frac{1}{2}(J_L + J_R)$ and $j = \frac{1}{2}(J_L - J_R)$, in terms of the exchange energies $J_{L,R}$ associated with virtual tunneling to the left or right dot, respectively. To lowest order in t [valid not too close to the borders of the (1,1,1) region] we have $J_{L,R} = -t^2/(\epsilon_M \pm \epsilon)$. From this it is clear that the exchange-only qubit allows for electric control of rotations around two different axes of the Bloch sphere, by tuning J and j through ϵ and ϵ_M, whereas the singlet-triplet qubit offered electric control over only one axis.

As in the double-dot system, the main effect of the hyperfine interaction with the nuclear spin bath can be described on a mean-field level using three random effective nuclear fields,

$$\hat{H}_{\rm hf,mf} = \mathbf{K}_L \cdot \hat{\mathbf{S}}_L + \mathbf{K}_C \cdot \hat{\mathbf{S}}_C + \mathbf{K}_R \cdot \hat{\mathbf{S}}_R. \tag{30}$$

Projected onto the qubit subspace, this yields

$$\hat{H}_{\rm hf,q} = -\frac{2}{3}\delta K_M^z \hat{\sigma}_z - \frac{1}{\sqrt{3}}\delta K_{LR}^z \hat{\sigma}_x, \tag{31}$$

where $\delta K_M^z = -\frac{1}{2}(\delta K_{LC}^z - \delta K_{CR}^z)$ and $\delta K_{LR}^z = \frac{1}{2}(K_L^z - K_R^z)$, in terms of the field gradients $\delta K_{ij}^z = \frac{1}{2}(K_i^z - K_j^z)$ over neighboring dots. We thus see that, also in this case, the random nuclear fields can be an important source of qubit decoherence. Besides, the quadruplet state $|Q_{+1/2}\rangle$ that cannot be split off by increasing the external field B is coupled to the states $|0\rangle$ and $|1\rangle$ through the same gradients δK_M^z and δK_{LR}^z, which can thus cause leakage out of the qubit subspace. To be able to control or suppress the field gradients could therefore again dramatically increase the qubit quality.

B. Transport-induced nuclear spin pumping: Qualitative picture

Inspired by our findings for the double dot, we now investigate possibilities to suppress the nuclear field gradients by running a current through the system while tuning it to some sort of spin-blockade regime. In contrast to the double-dot setup, there are several different types of spin blockade in a linear triple dot [53], which differ in the geometry of drains and sources and relative detuning of the three dots. In a simplest setup where the source and drain are attached to the outer dots, all regimes of spin blockade effectively behave as a double dot connected to one isolated dot containing one "inert" spin. Transport through such a setup would thus only suppress the field gradient between the two interacting dots.

To address both field gradients we use a setup where the source is connected to the *central* dot and both of the outer dots are connected to a drain [see Fig. 7(a)]. Applying a source-drain bias voltage in vicinity of the triple point shown in Fig. 6(a) can then give rise to a current through the system via the two transport cycles $(1,1,1) \to (2,0,1)/(1,0,2) \to (1,0,1) \to (1,1,1)$. Again we will assume that the system is in the open regime where the rates $\Gamma_{\rm in,out}$ are the largest energy scales, such that the interesting dynamics happen during the $(1,1,1) \to (2,0,1)/(1,0,2)$ transitions, which involves the 12 spin states discussed above. For simplicity, we will assume a symmetric situation, where $\epsilon = 0$ and $\epsilon_M > 0$ [see Fig. 6(d)], $t_l = t_r$, and $\Gamma_{{\rm out},l} = \Gamma_{{\rm out},r}$.

In the absence of spin-mixing processes, the only (1,1,1) states that couple to $|D_L\rangle$ and $|D_R\rangle$ are the doublets $|D_{1,2}\rangle$, and the current is spin blocked in either of the four quadruplet states. This blockade may be lifted by SOI, which affects the system in the same way as before: (i) Variations in the effective g-factor over the dots yield spin-orbit-induced Zeeman gradients $\Delta_{{\rm so},ij} = \frac{1}{2}(g_i - g_j)\mu_{\rm B}B$ and (ii) tunneling between dots can be accompanied by a spin flip. It is easy to show that, in contrast to the double-dot case, in the presence of SOI there are no dark states, even when all total Zeeman gradients $\Delta_{ij} = \Delta_{{\rm so},ij} + \delta K_{ij}^z$ are zero. SOI thus always fully lifts the spin blockade and competes with the flip-flop terms in the hyperfine interaction, thereby reducing the efficiency of spin pumping. Below we will only focus on the case without SOI, which is experimentally also most relevant since with strong SOI there is no spin blockade that can be used for initialization or read-out.

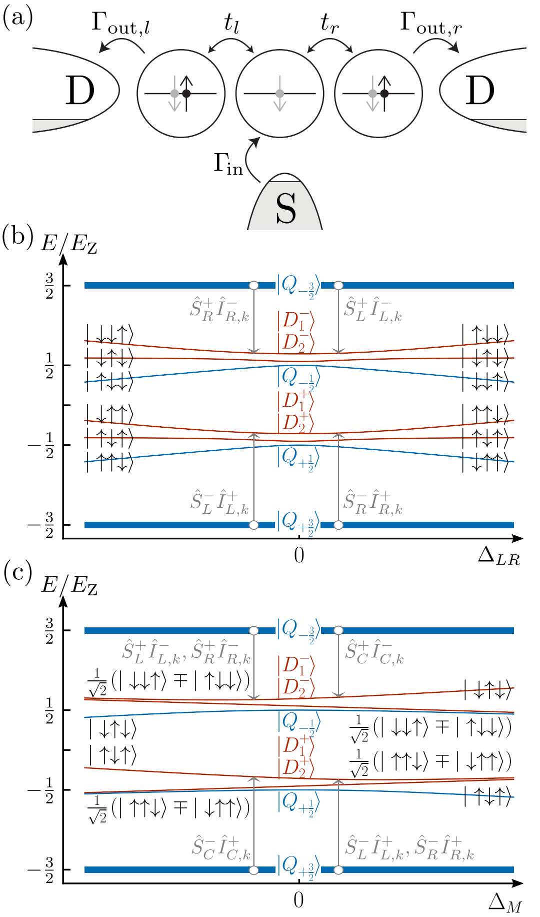
(a)
$\Gamma_{{\rm out},l}$
t_l
t_r
$\Gamma_{{\rm out},r}$
D
D
$\Gamma_{\rm in}$
S
(b)
E/E_Z
$\frac{3}{2}$
$\frac{1}{2}$
$-\frac{1}{2}$
$-\frac{3}{2}$
$|Q_{-\frac{3}{2}}\rangle$
$\hat{S}_R^+\hat{I}_{R,k}^-$
$\hat{S}_L^+\hat{I}_{L,k}^-$
$|D_1^-\rangle$
$|D_2^-\rangle$
$|{\downarrow\downarrow\uparrow}\rangle$
$|{\downarrow\uparrow\downarrow}\rangle$
$|{\uparrow\downarrow\downarrow}\rangle$
$|Q_{-\frac{1}{2}}\rangle$
$|D_1^+\rangle$
$|D_2^+\rangle$
$|{\downarrow\uparrow\uparrow}\rangle$
$|{\uparrow\downarrow\uparrow}\rangle$
$|{\uparrow\uparrow\downarrow}\rangle$
$|Q_{+\frac{1}{2}}\rangle$
$\hat{S}_L^-\hat{I}_{L,k}^+$
$\hat{S}_R^-\hat{I}_{R,k}^+$
$|Q_{+\frac{3}{2}}\rangle$
0
Δ_{LR}
(c)
E/E_Z
$\hat{S}_L^+\hat{I}_{L,k}^-, \hat{S}_R^+\hat{I}_{R,k}^-$
$\hat{S}_C^+\hat{I}_{C,k}^-$
$\frac{1}{\sqrt{2}}(|{\downarrow\downarrow\uparrow}\rangle \mp |{\uparrow\downarrow\downarrow}\rangle)$
$|{\downarrow\uparrow\downarrow}\rangle$
$|{\uparrow\downarrow\uparrow}\rangle$
$\frac{1}{\sqrt{2}}(|{\uparrow\uparrow\downarrow}\rangle \mp |{\downarrow\uparrow\uparrow}\rangle)$
$\hat{S}_C^-\hat{I}_{C,k}^+$
$\hat{S}_L^-\hat{I}_{L,k}^+, \hat{S}_R^-\hat{I}_{R,k}^+$
Δ_M

FIG. 7. (a) The central dot is connected to a source and the two outer dots are connected to drains; an applied bias voltage then enables electrons to flow through the system to either of the drains. (b), (c) Spectrum of the (1,1,1) states in the absence of SOI, as a function of the gradients (b) Δ_{LR} and (c) Δ_M, where the thickness of the lines indicates the occupation probabilities. Preferred spin-flip rates are indicated by gray arrows.

Let us now develop an intuitive picture of the electron-nuclear spin dynamics in this spin-blockade situation, similar to the discussion in Sec. II B. When the gradients Δ_{LR} and Δ_M are zero, the electrons are trapped in one of the four quadruplet states with equal probability $\frac{1}{4}$. As before, due to the symmetric spin structure of all states at this point there will be no net spin pumping. A nonzero gradient mixes states with the same total S_z^{tot}, giving all six states with $S_z^{\text{tot}} = \pm\frac{1}{2}$ a finite coupling to $|D_{L,R}^{\pm}\rangle$, whereas the two fully polarized quadruplets remain spin blocked, each with occupation probability $\frac{1}{2}$. For small gradients, the doublets have a much larger coupling to $|D_{L,R}^{\pm}\rangle$ than $|Q_{\pm 1/2}\rangle$ and spin-flip processes are thus dominated by transitions from $|Q_{\pm 3/2}\rangle$ to a doublet state.

We first show that transitions to $|D_2^{\pm}\rangle$ do not contribute strongly to spin pumping. When $\Delta_{LR} \neq 0$, the states $|D_2^{\pm}\rangle$ develop a dominating $\uparrow\downarrow\uparrow$ and $\downarrow\uparrow\downarrow$ character, respectively [see Fig. 7(b)]. This results in an increased spin-flip rate γ_C^+ from transitions $|Q_{+3/2}\rangle \to |D_2^+\rangle$ as well as an increased rate γ_C^- from $|Q_{-3/2}\rangle \to |D_2^-\rangle$. One thus does not expect a strong net effect. For $\Delta_M \neq 0$ the situation is similar: $|D_2^+\rangle$ ($|D_2^-\rangle$) gains a larger weight of $\uparrow\uparrow\downarrow$ and $\downarrow\uparrow\uparrow$ ($\downarrow\downarrow\uparrow$ and $\uparrow\downarrow\downarrow$). The spin-flip rates from $|Q_{+3/2}\rangle \to |D_2^+\rangle$ and $|Q_{-3/2}\rangle \to |D_2^-\rangle$ are thus affected in a symmetric way and there is no net spin pumping.

The doublet states $|D_1^{\pm}\rangle$, however, have the largest coupling to the outgoing states $|D_{L,R}^{\pm}\rangle$, and effectively pump the field gradients toward zero. For a positive gradient $\Delta_{LR} > 0$, the state $|D_1^+\rangle$ ($|D_1^-\rangle$) evolves into a state with a slight $\uparrow\uparrow\downarrow$ ($\uparrow\downarrow\downarrow$) character [see Fig. 7(b)]. This increases γ_R^+ (γ_L^-) and thus drives Δ_{LR} toward lower values. For a negative gradient $\Delta_{LR} < 0$, the situation is exactly opposite, again driving Δ_{LR} to zero. A similar argument holds for the other gradient Δ_M: When $\Delta_M > 0$, the state $|D_1^-\rangle$ gets a slight $\downarrow\uparrow\downarrow$ character and $|D_1^+\rangle$ obtains stronger $\downarrow\downarrow\uparrow$ and $\uparrow\downarrow\downarrow$ components [see Fig. 7(c)]. This increases the rates γ_L^+, γ_C^-, and γ_R^+, thereby effectively reducing Δ_M. For $\Delta_M < 0$ the situation is again opposite, yielding a positive pumping of Δ_M.

C. Analytic results

We now use the same approach as in Sec. II C to derive time-evolution equations for the three nuclear polarizations, valid for small P_d. The time-evolution equation for the electronic density matrix in the triple dot reads

$$\frac{d\hat{\rho}}{dt} = -i[\hat{H}, \hat{\rho}] + \mathbf{\Gamma}\hat{\rho}, \tag{32}$$

with $\hat{H} = \hat{H}_0 + \hat{H}_{\text{hf,mf}}$. We describe the transitions $(2,0,1)/(1,0,2) \to (1,0,1) \to (1,1,1)$ with the term $\mathbf{\Gamma}\hat{\rho} = -\frac{1}{2}\Gamma\{\hat{P}_{\text{dec}}, \hat{\rho}\} + \frac{1}{8}\Gamma(\mathbb{1} - \hat{P}_{\text{dec}})\rho_{\text{dec}}$, where the operator $P_{\text{dec}} = \sum_{i=D_{L,R}^{\alpha}} |i\rangle\langle i|$ projects to the subspace that is coupled to the drain leads and $\rho_{\text{dec}} = \sum_{i=D_{L,R}^{\alpha}} \rho_{i,i}$.

Assuming that Γ is the largest energy scale involved, we again separate timescales and write the effective (1,1,1) Hamiltonian

$$\hat{H}^{(1,1,1)} = \sum_{\alpha=\pm} -\alpha\frac{3}{2}E_Z|Q_{\alpha 3/2}\rangle\langle Q_{\alpha 3/2}| + \hat{H}_{\frac{1}{2}}^{\alpha}, \tag{33}$$

using the two 3×3 blocks

$$\begin{aligned}\hat{H}_{\frac{1}{2}}^{\alpha} &= -\alpha\frac{1}{2}E_Z + 3E_D|D_1^{\alpha}\rangle\langle D_1^{\alpha}| + E_D|D_2^{\alpha}\rangle\langle D_2^{\alpha}| \\ &\quad + \alpha\begin{pmatrix} 0 & -\frac{\sqrt{2}}{3}\Delta_M & \sqrt{\frac{2}{3}}\Delta_{LR} \\ -\frac{\sqrt{2}}{3}\Delta_M & -\frac{1}{3}\Delta_M & -\frac{1}{\sqrt{3}}\Delta_{LR} \\ \sqrt{\frac{2}{3}}\Delta_{LR} & -\frac{1}{\sqrt{3}}\Delta_{LR} & \frac{1}{3}\Delta_M \end{pmatrix},\end{aligned} \tag{34}$$

acting on the subspaces $\{|Q_{\alpha 1/2}\rangle, |D_1^{\alpha}\rangle, |D_2^{\alpha}\rangle\}$. Here, E_Z contains the contribution $\frac{1}{3}(K_L^z + K_C^z + K_R^z)$ from the average nuclear spin polarization. We assumed E_Z to be large enough that we can neglect the transverse components $K_d^{x,y}$ that couple states with different S_z^{tot}. The projection to the (1,1,1) subspace introduced the exchange energy

$$E_D = \frac{2t^2\epsilon_M}{4\epsilon_M^2 + \Gamma^2}, \tag{35}$$

and makes the states $|D_1^{\pm}\rangle$ and $|D_2^{\pm}\rangle$ decay with rates $\Gamma_1 = 3\Gamma_D$ and $\Gamma_2 = \Gamma_D$, respectively, where

$$\Gamma_D = \frac{2t^2\Gamma}{4\epsilon_M^2 + \Gamma^2}. \tag{36}$$

Assuming that the exchange energy E_D is much larger than the gradients Δ_{LR} and Δ_M, we diagonalize $\hat{H}_{\frac{1}{2}}^{\pm}$ using perturbation theory and thusly find expressions for the eigenstates and their decay rates valid to lowest order in the gradients [54]. For nonzero gradients, the occupation probabilities are approximately $\frac{1}{2}$ for $|Q_{\pm 3/2}\rangle$ and zero for the remaining six states. As for the double dot, we then calculate the hyperfine-induced flip-flop rates perturbatively using Fermi's golden rule (18), and translate the resulting flip rates to evolution equations for the average polarization $P_\Sigma = \frac{1}{3}(P_L + P_C + P_R)$, and the two polarization gradients $P_{LR} = \frac{1}{2}(P_L - P_R)$ and $P_M = P_C - \frac{1}{2}(P_L + P_R)$. This gives, to lowest order in the field gradients Δ_{LR} and Δ_M,

$$\frac{dP_{LR}}{dt} = -\left[G + \frac{1}{\tau}\right]P_{LR} - \frac{G}{E_D}\Delta_{LR}, \tag{37}$$

$$\frac{dP_M}{dt} = -\left[\frac{5}{3}G + \frac{1}{\tau}\right]P_M - GP_\Sigma - \frac{2G}{3E_D}\Delta_M, \tag{38}$$

$$\frac{dP_\Sigma}{dt} = -\left[\frac{4}{3}G + \frac{1}{\tau}\right]P_\Sigma - \frac{2}{9}GP_M, \tag{39}$$

with $G = A^2\Gamma_D/4N^2E_Z^2$, where we again assumed equal N on all dots, for simplicity.

As in the double dot, all polarization gradients thus acquire an effectively enhanced relaxation rate. We further find that the polarization dynamics of P_M and P_Σ are coupled, which is a result of the geometry of the source and drains. However, for typical parameters the last terms in Eqs. (37) and (38) dominate, predicting an efficient suppression of both gradients, similar to the double-dot case.

Using these results, we can again investigate the stochastic fluctuations around stable points, using a linear Fokker-Planck equation that describes the time-dependent probability distribution $\mathcal{P}(n, m, l, t)$, where $n = \frac{3}{2}NP_\Sigma$, $m = NP_{LR}$, and

$l = \frac{2}{3}NP_M$. In the continuous limit, and to lowest order in the gradients, we find a covariance matrix that reads

$$\sigma_{LR}^2 = \frac{1}{2N}\frac{2E_D}{2E_D + A}, \tag{40}$$

$$\sigma_M^2 = \frac{3}{2N}\frac{E_D(81E_D + 10A)}{81E_D^2 + 27AE_D + 2A^2}, \tag{41}$$

$$\sigma_\Sigma^2 = \frac{1}{3N}\left[1 - \frac{AE_D}{81E_D^2 + 27AE_D + 2A^2}\right], \tag{42}$$

$$\sigma_{LR,M}^2 = \frac{2}{N}\frac{AE_D}{81E_D^2 + 27AE_D + 2A^2}. \tag{43}$$

Realistically $A \gg E_D$, so the rms of the fluctuations of the two gradients are suppressed by a factor $\sim\sqrt{E_D/A}$, whereas the fluctuations of P_Σ are barely affected, similar to what we found for the double dot.

D. Numerical simulations

Using the same method as in Sec. II D we performed numerical simulations to corroborate our analytic results. In Figs. 8(a) and 8(b) we first illustrate the coupled dynamics of P_{LR} and P_M. We set $P_\Sigma = 0$, $A = 125$ μeV, $E_Z = 12.5$ μeV, $N = 4 \times 10^5$, $\tau = 5$ s, $\epsilon_M = 100$ μeV, $\epsilon = 0$, $\Gamma = 75$ μeV, and $t = 7.5$ μeV, and then we plot in color the rates of change dP_{LR}/dt [Fig. 8(a)] and dP_M/dt [Fig. 8(b)] as a function of P_{LR} and P_M as found using Eq. (24). In both plots we also included the (same) vector field $(dP_M/dt, dP_{LR}/dt)$, represented by the black arrows, illustrating how both field gradients are indeed pumped toward zero. The insets show line cuts along the red dotted lines, i.e., they show the rate of change of each polarization gradient as a function of the same gradient, where the other one is set to zero. The dashed orange lines indicate the slope of the pumping curve at the stable point, as predicted by Eqs. (37)–(39), showing indeed good agreement with the numerical results.

In Figs. 8(c) and 8(d) we then show simulations of the stochastic dynamics of the two polarization gradients, performed in the same way as we did in Sec. II D for the double dot. We started with initial polarizations $P_{LR}(0) = 0.001$, $P_M(0) = 0.002$, and $P_\Sigma = 0$ and performed a simulation with the parameters given above (red lines) and one without spin pumping ($A = 0$, green lines). Panels (i) show the short-time dynamics, where the dashed lines correspond to the result predicted by Eqs. (37)–(39), and panels (ii) and (iii) show the long-time dynamics, where the horizontal solid lines indicate the rms value of the fluctuations as predicted from Eqs. (40)–(43). We see that in all cases our analytic expressions agree reasonably well with the simulated dynamics of the gradients. We further note that, for similar reasons as in the double dot, the average polarization P_Σ drifts toward negative values, stabilizing around ~ -0.004. Due to the way the dynamics of P_M depend on P_Σ [see Eq. (38)] one expects that the long-time stable polarization of P_M is not at zero but at a small positive value; a careful look at Fig. 8(d)(iii) shows that this is indeed the case in our simulations.

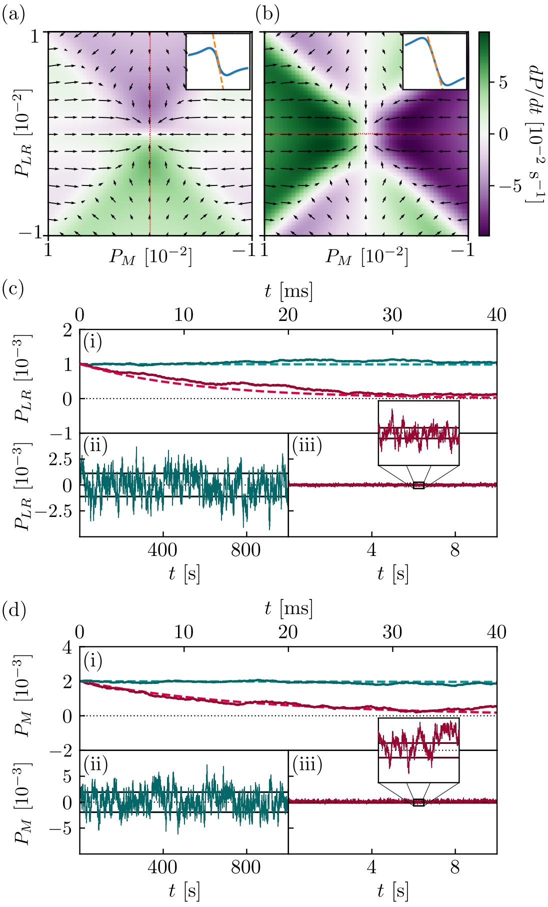

FIG. 8. (a) dP_{LR}/dt and (b) dP_M/dt as a function of P_{LR} and P_M (color plots), calculated numerically using Eq. (24). The insets show line cuts along the red dashed lines, where the orange dashed lines indicate the slope of dP/dt at the stable point as predicted by Eqs. (37) and (38). In both plots we also included the (same) vector field $(dP_M/dt, dP_{LR}/dt)$, represented by the black arrows. See the main text for all parameters used. (c), (d) Simulated stochastic dynamics of (c) P_{LR} and (d) P_M with initial conditions $P_{LR}(0) = 0.001$, $P_M(0) = 0.002$, and $P_\Sigma = 0$. For the red lines we used the same parameters as in (a) and (b); the green lines show the dynamics in the absence of spin pumping (for $A = 0$). Panels (i) show the short-time suppression toward zero gradients, where the dashed lines show the dynamics predicted by Eqs. (37)–(39). Panels (ii) and (iii) illustrate the fluctuations around the stable gradients at longer times.

E. Conclusion

We found that electron transport through a linear triple quantum dot—with a source connected to the central dot and drains connected to the outer dots—tuned to the regime of a Pauli spin blockade can yield a hyperfine-induced feedback cycle that dynamically suppresses the two nuclear polarization gradients in the triple dot. To find the approximate magnitude of the rms value of the remaining nuclear-field fluctuations, we derived simple perturbative analytical expressions to describe the coupled dynamics of the polarization gradients. This predicts a similar suppression of the fluctuations of the gradients as in the double-dot case, i.e., a suppression of one to two orders of magnitude. We corroborated these analytic results with numerical simulations of the coupled electron-nuclear spin dynamics, finding good agreement between the two.

IV. CONCLUSION

In multielectron qubits, such as the double-dot-based two-electron singlet-triplet qubit and triple-dot-based three-electron exchange-only qubits, the main source of decoherence is usually the fluctuating nuclear-spin polarization gradients over neighboring dots. These random gradients couple to the spins of the electrons in the dots and can thereby add to the qubit splitting or couple the two qubit states to each other as well as to other nearby states outside of the computational basis.

In this paper, we investigated the effect of running a DC current through such systems on the nuclear polarization gradients, while tuning to a regime of a Pauli spin blockade. We found that transport through the dots can give rise to a dynamical feedback cycle between the electronic and nuclear spins that results in an active suppression of the nuclear polarization gradients.

We considered a double-dot setup with and without a significant spin-orbit interaction as well as a triple-dot setup without a spin-orbit interaction. For all cases we derived approximate analytical evolution equations for the nuclear polarization gradients, which all predict the possibility of a significant suppression of the fluctuations of the gradients. We corroborated these results with numerical simulations of the stochastic coupled electron-nuclear spin dynamics which confirmed a reduction in the random fluctuations of the nuclear polarization gradients by one to two orders of magnitude. These suppression mechanisms could thus present a straightforward way to significantly reduce the hyperfine-induced decoherence in multielectron qubits.

ACKNOWLEDGMENTS

This work is part of FRIPRO-project 274853, which is funded by the Research Council of Norway (RCN), and was also partly supported by the Centers of Excellence funding scheme of the RCN, Project No. 262633, QuSpin.

---

[1] R. Hanson, L. P. Kouwenhoven, J. R. Petta, S. Tarucha, and L. M. K. Vandersypen, Rev. Mod. Phys. **79**, 1217 (2007).

[2] F. A. Zwanenburg, A. S. Dzurak, A. Morello, M. Y. Simmons, L. C. L. Hollenberg, G. Klimeck, S. Rogge, S. N. Coppersmith, and M. A. Eriksson, Rev. Mod. Phys. **85**, 961 (2013).

[3] L. M. K. Vandersypen, H. Bluhm, J. S. Clarke, A. S. Dzurak, R. Ishihara, A. Morello, D. J. Reilly, L. R. Schreiber, and M. Veldhorst, npj Quantum Inf. **3**, 34 (2017).

[4] D. Loss and D. P. DiVincenzo, Phys. Rev. A **57**, 120 (1998).

[5] F. H. L. Koppens, C. Buizert, K. J. Tielrooij, I. T. Vink, K. C. Nowack, T. Meunier, L. P. Kouwenhoven, and L. M. K. Vandersypen, Nature (London) **442**, 766 (2006).

[6] J. R. Petta, A. C. Johnson, J. M. Taylor, E. A. Laird, A. Yacoby, M. D. Lukin, C. M. Marcus, M. P. Hanson, and A. C. Gossard, Science **309**, 2180 (2005).

[7] J. M. Taylor, J. R. Petta, A. C. Johnson, A. Yacoby, C. M. Marcus, and M. D. Lukin, Phys. Rev. B **76**, 035315 (2007).

[8] Z. Shi, C. B. Simmons, J. R. Prance, J. K. Gamble, T. S. Koh, Y.-P. Shim, X. Hu, D. E. Savage, M. G. Lagally, M. A. Eriksson, M. Friesen, and S. N. Coppersmith, Phys. Rev. Lett. **108**, 140503 (2012).

[9] D. Kim, Z. Shi, C. B. Simmons, D. R. Ward, J. R. Prance, T. S. Koh, J. K. Gamble, D. E. Savage, M. G. Lagally, M. Friesen, and S. N. Coppersmith, Nature (London) **511**, 70 (2014).

[10] E. A. Laird, J. M. Taylor, D. P. DiVincenzo, C. M. Marcus, M. P. Hanson, and A. C. Gossard, Phys. Rev. B **82**, 075403 (2010).

[11] L. Gaudreau, G. Granger, A. Kam, G. C. Aers, S. A. Studenikin, P. Zawadzki, M. Pioro-Ladrière, Z. R. Wasilewski, and A. S. Sachrajda, Nat. Phys. **8**, 54 (2012).

[12] J. Medford, J. Beil, J. M. Taylor, S. D. Bartlett, A. C. Doherty, E. I. Rashba, D. P. DiVincenzo, H. Lu, A. C. Gossard, and C. M. Marcus, Nat. Nanotechnol. **8**, 654 (2013).

[13] J. Medford, J. Beil, J. M. Taylor, E. I. Rashba, H. Lu, A. C. Gossard, and C. M. Marcus, Phys. Rev. Lett. **111**, 050501 (2013).

[14] J. M. Taylor, V. Srinivasa, and J. Medford, Phys. Rev. Lett. **111**, 050502 (2013).

[15] D. P. DiVincenzo, D. Bacon, J. Kempe, G. Burkard, and K. B. Whaley, Nature (London) **408**, 339 (2000).

[16] M. Russ and G. Burkard, J. Phys.: Condens. Matter **29**, 393001 (2017).

[17] I. A. Merkulov, A. L. Efros, and M. Rosen, Phys. Rev. B **65**, 205309 (2002).

[18] A. V. Khaetskii, D. Loss, and L. Glazman, Phys. Rev. Lett. **88**, 186802 (2002).

[19] J.-T. Hung, J. Fei, M. Friesen, and X. Hu, Phys. Rev. B **90**, 045308 (2014).

[20] C. G. Péterfalvi and G. Burkard, Phys. Rev. B **96**, 245412 (2017).

[21] X. Hu and S. Das Sarma, Phys. Rev. Lett. **96**, 100501 (2006).

[22] M. Russ and G. Burkard, Phys. Rev. B **91**, 235411 (2015).

[23] F. Martins, F. K. Malinowski, P. D. Nissen, E. Barnes, S. Fallahi, G. C. Gardner, M. J. Manfra, C. M. Marcus, and F. Kuemmeth, Phys. Rev. Lett. **116**, 116801 (2016).

[24] M. D. Reed, B. M. Maune, R. W. Andrews, M. G. Borselli, K. Eng, M. P. Jura, A. A. Kiselev, T. D. Ladd, S. T. Merkel, I. Milosavljevic, E. J. Pritchett, M. T. Rakher, R. S. Ross, A. E. Schmitz, A. Smith, J. A. Wright, M. F. Gyure, and A. T. Hunter, Phys. Rev. Lett. **116**, 110402 (2016).

[25] Y.-P. Shim and C. Tahan, Phys. Rev. B **93**, 121410(R) (2016).

[26] F. K. Malinowski, F. Martins, P. D. Nissen, S. Fallahi, G. C. Gardner, M. J. Manfra, C. M. Marcus, and F. Kuemmeth, Phys. Rev. B **96**, 045443 (2017).

[27] C. Zhang, X.-C. Yang, and X. Wang, Phys. Rev. A **97**, 042326 (2018).

[28] J. T. Muhonen, J. P. Dehollain, A. Laucht, F. E. Hudson, R. Kalra, T. Sekiguchi, K. M. Itoh, D. N. Jamieson, J. C. McCallum, A. S. Dzurak, and A. Morello, Nat. Nanotechnol. **9**, 986 (2014).

[29] K. Eng, T. D. Ladd, A. Smith, M. G. Borselli, A. A. Kiselev, B. H. Fong, K. S. Holabird, T. M. Hazard, B. Huang, P. W. Deelman, I. Milosavljevic, A. E. Schmitz, R. S. Ross, M. F. Gyure, and A. T. Hunter, Sci. Adv. **1**, e1500214 (2015).

[30] M. Veldhorst, J. C. C. Hwang, C. H. Yang, A. W. Leenstra, B. de Ronde, J. P. Dehollain, J. T. Muhonen, F. E. Hudson, K. M. Itoh, A. Morello, and A. S. Dzurak, Nat. Nanotechnol. **9**, 981 (2014).

[31] J. Yoneda, K. Takeda, T. Otsuka, T. Nakajima, M. R. Delbecq, G. Allison, T. Honda, T. Kodera, S. Oda, Y. Hoshi, N. Usami, K. M. Itoh, and S. Tarucha, Nat. Nanotechnol. **13**, 102 (2018).

[32] M. Friesen, S. Chutia, C. Tahan, and S. N. Coppersmith, Phys. Rev. B **75**, 115318 (2007).

[33] D. Culcer, X. Hu, and S. Das Sarma, Phys. Rev. B **82**, 205315 (2010).

[34] S. F. Neyens, R. H. Foote, B. Thorgrimsson, T. J. Knapp, T. McJunkin, L. M. K. Vandersypen, P. Amin, N. K. Thomas, J. S. Clarke, D. E. Savage, M. G. Lagally, M. Friesen, S. N. Coppersmith, and M. A. Eriksson, Appl. Phys. Lett. **112**, 243107 (2018).

[35] C. Tahan and R. Joynt, Phys. Rev. B **89**, 075302 (2014).

[36] A. Sala and J. Danon, Phys. Rev. B **98**, 245409 (2018).

[37] A. Sala and J. Danon, Phys. Rev. B **95**, 241303(R) (2017).

[38] M. Russ, J. R. Petta, and G. Burkard, Phys. Rev. Lett. **121**, 177701 (2018).

[39] A. Sala, J. H. Qvist, and J. Danon, Phys. Rev. Research **2**, 012062(R) (2020).

[40] F. K. Malinowski, F. Martins, P. D. Nissen, E. Barnes, Ł. Cywiński, M. S. Rudner, S. Fallahi, G. C. Gardner, M. J. Manfra, C. M. Marcus, and F. Kuemmeth, Nat. Nanotechnol. **12**, 16 (2016).

[41] J. R. Petta, J. M. Taylor, A. C. Johnson, A. Yacoby, M. D. Lukin, C. M. Marcus, M. P. Hanson, and A. C. Gossard, Phys. Rev. Lett. **100**, 067601 (2008).

[42] D. J. Reilly, J. M. Taylor, J. R. Petta, C. M. Marcus, M. P. Hanson, and A. C. Gossard, Science **321**, 817 (2008).

[43] S. Foletti, H. Bluhm, D. Mahalu, V. Umansky, and A. Yacoby, Nat. Phys. **5**, 903 (2009).

[44] H. Bluhm, S. Foletti, D. Mahalu, V. Umansky, and A. Yacoby, Phys. Rev. Lett. **105**, 216803 (2010).

[45] C. Echeverría-Arrondo and E. Y. Sherman, Phys. Rev. B **87**, 081410(R) (2013).

[46] S. M. Frolov, J. Danon, S. Nadj-Perge, K. Zuo, J. W. W. van Tilburg, V. S. Pribiag, J. W. G. van den Berg, E. P. A. M. Bakkers, and L. P. Kouwenhoven, Phys. Rev. Lett. **109**, 236805 (2012).

[47] J. Danon and Y. V. Nazarov, Phys. Rev. B **80**, 041301(R) (2009).

[48] Using a different nuclear spin, such as $\frac{3}{2}$ (as it is for both Ga and As), yields unimportant overall numerical prefactors of order 1.

[49] D. J. Reilly, J. M. Taylor, J. R. Petta, C. M. Marcus, M. P. Hanson, and A. C. Gossard, Phys. Rev. Lett. **104**, 236802 (2010).

[50] J. Danon, I. T. Vink, F. H. L. Koppens, K. C. Nowack, L. M. K. Vandersypen, and Y. V. Nazarov, Phys. Rev. Lett. **103**, 046601 (2009).

[51] I. T. Vink, K. C. Nowack, F. Koppens, J. Danon, Y. V. Nazarov, and L. M. K. Vandersypen, Nat. Phys. **5**, 764 (2009).

[52] We added an infinitesimal decay rate of 10^{-9} μeV to all (1,1) states to avoid singularities.

[53] C. Y. Hsieh, Y. P. Shim, and P. Hawrylak, Phys. Rev. B **85**, 085309 (2012).

[54] Here, we keep only the effect of E_D on the structure of the basis, i.e., we disregard Γ_D.

Paper III

J. H. Qvist and J. Danon.

Anisotropic g-tensors in hole quantum dots: The role of the transverse confinement direction.

Physical review B **105**, 075303 (2022).

PHYSICAL REVIEW B **105**, 075303 (2022)

Anisotropic g-tensors in hole quantum dots: Role of transverse confinement direction

Jørgen Holme Qvist and Jeroen Danon
Center for Quantum Spintronics, Department of Physics, Norwegian University of Science and Technology, NO-7491 Trondheim, Norway

(Received 26 November 2021; accepted 28 January 2022; published 9 February 2022)

Qubits encoded in the spin state of heavy holes confined in Si- and Ge-based semiconductor quantum dots are currently leading the efforts toward spin-based quantum information processing. The virtual absence of spinful nuclei in purified samples yields long qubit coherence times and the intricate coupling between spin and momentum in the valence band can provide very fast spin-orbit-based qubit control, e.g., via electrically induced modulations of the heavy-hole g-tensor. A thorough understanding of all aspects of the interplay between spin-orbit coupling, the confining potentials, and applied magnetic fields is thus essential for the development of the optimal hole-spin-based qubit platform. Here we theoretically investigate the manifestation of the effective g-tensor and effective mass of heavy holes in two-dimensional hole gases as well as in lateral quantum dots. We include the effects of the anisotropy of the effective Luttinger Hamiltonian (particularly relevant for Si-based systems) and we focus on the detailed role of the orientation of the transverse confining potential. We derive general analytic expressions for the anisotropic g-tensor and we present a general and straightforward way to calculate corrections to this g-tensor for localized holes due to various types of spin-orbit interaction, exemplifying the approach by including a simple linear Rashba-like term. Our results thus contribute to the understanding needed to find optimal points in parameter space for hole-spin qubits, where confinement is effective and spin-orbit-mediated electric control over the spin states is efficient.

DOI: 10.1103/PhysRevB.105.075303

I. INTRODUCTION

Electron-spin-based qubits hosted in gate-defined semiconductor quantum dot structures have long been a promising candidate for easily scalable quantum information processors [1–3]. Although GaAs-based devices have propelled the field forward for more than a decade, yielding many encouraging features such as full electric control and fast operation times [4–9], their coherence times are intrinsically limited due to the coupling between the electron spins and the nuclear spin bath of the host material [10–12]. A potential solution to this problem is to host the qubits in group-IV materials, such as Si or Ge, which can be made almost nuclear spin free by isotopic purification [13–17]. However, this approach comes with the complication of an extra valley degree of freedom for confined electrons, which is hard to control and provides an extra channel for leakage and dephasing [18,19].

Lately there has been dramatic progress with Si- and Ge-based spin qubits that use instead of electron spin the spin of valence-band holes [20–28]. These holes provide a similar protection against magnetic noise as the electrons, due to the virtual absence of nuclear spins in purified samples, but they do not have the complicating valley degree of freedom. However, since the orbitals that constitute the valence band are of p type [29], the corresponding states have a total sixfold angular momentum degree of freedom, possibly leading to highly anisotropic dynamics. Compared to the valley mixing of the electronic states, however, these dynamics are relatively predictable, and the built-in mixing of orbital and spin degrees of freedom can yield strong effective spin-orbit coupling that allows for fast qubit operation [30–36]. Moreover, the p-type orbital nature of the valence band has the additional advantage of weaker effective hyperfine coupling to any residual spinful nuclei, due to the wave function having a node at the atomic site [37].

Recent experiments on two-dimensional hole quantum wells and quantum dots have indeed shown wildly varying and anisotropic effective hole masses [38–40] and g-factors [41–52], depending on choice of material, hole densities, and on the details of the confinement. In this paper we theoretically investigate these anisotropic properties of confined holes in detail, with a focus on the role of the precise orientation of the confinement potentials with respect to the crystal orientation. We will pay special attention to the case of Si, which has particularly strong anisotropic properties as compared to most other common materials, such as Ge, GaAs, and InAs [29].

We assume a semiconductor heterostructure containing a thin layer to which a two-dimensional hole gas (2DHG) is confined. Further in-plane confinement into quantum dots can then be realized using electrostatic top gates. We do not restrict our analysis to confinement planes along the common crystal growth directions, but investigate the more general case where the 2DHG can be oriented along any arbitrary direction. Although from a fabricational point of view it is maybe not straightforward to realize arbitrary confinement directions (or directions that are incommensurate with the primitive lattice vectors), exploring the fully general case will allow us to identify orientations with optimally tuned parameters for spin-qubit implementations in different materials, such as minimal effective masses, maximal in-plane g-factors, and maximal electrical tunability of the g-tensor.

©2022 American Physical Society

Apart from revealing analytical insights in the relation between the orientation of the 2DHG and the most important effective parameters of the resulting quantum dots, our results could thus also serve as inspiration for exploring possibilities to create confinement planes in less common crystallographic directions.

In Sec. II we present the effective 4×4 Luttinger Hamiltonian we use to describe the hole dynamics in the top part of the valence band. We then write the Hamiltonian as a function of two Euler (rotation) angles such that the z direction can be made to point in any desired direction.

In Sec. III we add a strong confinement potential along the (arbitrary) z direction, assuming that the corresponding confinement energy scale dominates all other relevant scales in the system. The terms in the Luttinger Hamiltonian that break spherical symmetry allow the confinement to mix states with different angular momentum along the out-of-plane direction, thereby introducing anisotropy in the effective hole parameters. Under the assumption of strong confinement we thus diagonalize the dominating part of the Hamiltonian and extract analytic expressions for the in-plane effective hole masses. Then we add a Zeeman Hamiltonian describing the coupling of the hole spins to an applied magnetic field. We transform this Hamiltonian to the same eigenbasis defined by the transverse confinement and extract analytic expressions for the full anisotropic g-tensor for the lowest two-hole spin states, as a function of the two Euler angles. We map out the full orientation dependence of the g-tensor for the case of Si, showing a great variation of magnitude and sign in its components.

Finally, in Sec. IV, we add in-plane confinement into quantum dots, assuming the corresponding orbital energy scale to be much smaller than the out-of-plane orbital energy. Although we assume a circularly symmetric confining potential, the anisotropic effective hole mass makes the confinement effectively elliptic. We add the effect of the out-of-plane component of the applied magnetic field and use a diagonalized version of a single quantum-dot Hamiltonian in terms of bosonic ladder operators. Expressing the hole momentum operators in terms of the same ladder operators allows for a straightforward and versatile perturbative evaluation of the effect of spin-orbit interaction (SOI) on the dynamics of the confined holes. We exemplify this approach by including a simple linear Rashba-like SOI that can result from the out-of-plane confinement, and we derive analytic expressions for the resulting corrections to the g-tensor for the confined holes. As we point out below, including other types of SOI that might dominate depending on choice of material and details of confinement is simple in our approach, and our results can straightforwardly be used to produce analytic expressions for the g-tensor corrections due to any desired type of SOI. The SOI-induced corrections to the g-tensor of localized holes can used for fast spin manipulation through electrical g-tensor modulation [42,47,53,54], and developing a thorough understanding of the detailed interplay of SOI, confinement, and applied magnetic fields is thus crucial [55–57].

II. HAMILTONIAN

In semiconductors with diamond or zinc-blende structure the states in the valence band are comprised of atomic orbitals with angular momentum $l = 1$ and spin $s = \frac{1}{2}$. The band thus has a sixfold degree of freedom that can be classified in terms of total angular momentum $j = l + s$. Spin-orbit interaction splits off the two states with $j = \frac{1}{2}$ from the other four by an energy of the order ~100 meV, and for the low-energy dynamics one can thus focus on the four $j = \frac{3}{2}$ states. Using $\boldsymbol{k} \cdot \boldsymbol{p}$ theory, one can derive an effective 4×4 Hamiltonian for this subspace, which reads in the cubic approximation

TABLE I. Luttinger parameters $\gamma_{1,2,3}$ and bare effective g-factors κ and q in Si, Ge, GaAs, and InAs [29].

	Si	Ge	GaAs	InAs
γ_1	4.285	13.38	6.85	20.40
γ_2	0.339	4.24	2.10	8.30
γ_3	1.446	5.69	2.90	9.10
κ	−0.42	3.41	1.20	7.60
q	0.01	0.06	0.01	0.39

$$H_{\mathrm{L}} = \frac{p^2}{2m_0}\left(\gamma_1 + \frac{5}{2}\gamma_2\right) - \frac{\gamma_2}{m_0}\left(p_x^2 J_x^2 + \text{c.p.}\right) - \frac{2\gamma_3}{m_0}(\{p_x, p_y\}\{J_x, J_y\} + \text{c.p.}), \tag{1}$$

where $\{A, B\} = \frac{1}{2}(AB + BA)$, m_0 is the electron rest mass, p_i are the momentum operators, with $i \in \{x, y, x\}$, J_i are the three spin-$\frac{3}{2}$ matrices, and c.p. denotes cyclic permutation. Furthermore, the dimensionless constants $\gamma_{1,2,3}$ are the three so-called Luttinger parameters, and are given in Table I for Si, Ge, GaAs, and InAs.

Although we will mainly focus on the dynamics governed by the Luttinger Hamiltonian (1), the effect of strain could easily be added by including the so-called Bir-Pikus Hamiltonian [58],

$$H_{\mathrm{BP}} = \left(-a + \frac{5}{4}b\right)(\epsilon_{xx} + \text{c.p.}) - b\left(\epsilon_{xx}J_x^2 + \text{c.p.}\right) - \frac{2d}{\sqrt{3}}(\epsilon_{xy}\{J_x, J_y\} + \text{c.p.}), \tag{2}$$

where $\bar{\epsilon}$ is the strain tensor, a is the Bir-Pikus hydrostatic deformation potential, and b and d are two Bir-Pikus shear deformation potentials [58]. This Hamiltonian has the same structure as the Luttinger Hamiltonian (1), which in principle allows for a straightforward inclusion of strain into the results we will report below.

In both Hamiltonians (1) and (2) it is assumed that the coordinate system $\{x, y, z\}$ is aligned with the main crystallographic axes. This is important since the terms proportional to $\gamma_{2,3}$, b, and d are not spherically symmetric, i.e., the structure of these two terms depends on the choice of coordinate system. In many common semiconductors such as GaAs, Ge, and InAs the difference $\delta \equiv \gamma_3 - \gamma_2$ is smaller than the (weighted) average $2\gamma_2 + 3\gamma_3$ (see Table I), which makes neglecting terms proportional to δ a good approximation. In that case, the Hamiltonian becomes spherically symmetric and no longer depends on the orientation of the coordinate system with respect to the crystal structure. However, since we specifically want to include Si in our consideration, for which

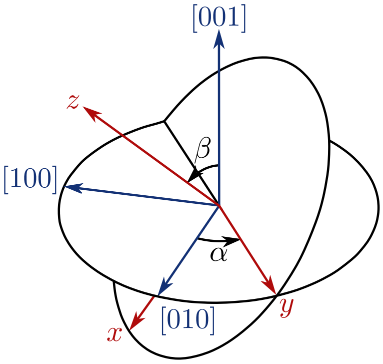

FIG. 1. Illustration of the rotation using the two Euler angles α and β. The crystallographic axes are shown in blue, the rotated coordinate system (x, y, z) is shown in red.

the spherical approximation is not particularly good, we will not neglect δ, and will take the actual crystal orientation into account.

A 2DHG is created by applying strong confinement along one direction. To find an effective in-plane two-dimensional Hamiltonian for the 2DHG we need to integrate out the coordinate along the direction of confinement, which we will call z. If z does not point along one of the main crystallographic axes, we first need to rotate the Hamiltonian to the correct coordinate system. This can be done as follows: (i) The original Hamiltonian is separated in a spherically symmetric part, which is invariant under rotations, and a cubic part that is comprised of the 0 and ±4 components of the rank-4 part of the tensor product of the two irreducible rank-2 tensors that can be formed from the elements $K_{ij} = \frac{3}{2}(p_i p_j + p_j p_i) - \delta_{ij} p^2$ and $L_{ij} = \frac{3}{2}(J_i J_j + J_j J_i) - \delta_{ij} J^2$ [59]. (ii) The cubic contribution can be rotated to the new coordinate system by applying the rotation matrix for $j = 4$ angular-momentum eigenfunctions $\mathbf{D}^{(4)}(\alpha, \beta, \gamma)$ to the components of the rank-4 tensor mentioned above, where $\{\alpha, \beta, \gamma\}$ are the Euler angles of the rotation [60]. In this work we will explore the full range of possible confinement planes and thus not restrict ourselves to the common crystal growth directions such as $[nnm]$.

Since any plane of confinement can be defined by two angles only, we fix $\gamma = 0$ to simplify our analytic expressions. The new coordinate system then results from a rotation by α about [001] followed by a rotation by β about the new y axis, as illustrated in Fig. 1. In that way the $[nnm]$ directions, as investigated in Refs. [29,59], can be obtained by simply setting $\alpha = \pi/4$. Most experiments use samples grown along the [001] and [110] directions, with the confinement created along the growth direction, and when presenting explicit results we will thus consider these highly used confinement directions. However, since we can obtain results for any general direction of confinement, it is straightforward to also explore less common directions, which could result in a 2DHG with more interesting or useful properties. There is no fundamental problem with growing structures along less common directions and by investigating all possible confinement orientations our text might identify new attractive orientations that motivate the production of the more exotic substrates required.

The resulting rotated Hamiltonian can always be written in the following form:

$$H(\alpha, \beta) = \begin{pmatrix} P-Q & -S & R & 0 \\ -S^\dagger & P+Q & 0 & R \\ R^\dagger & 0 & P+Q & S \\ 0 & R^\dagger & S^\dagger & P-Q \end{pmatrix}, \tag{3}$$

in the basis of the eigenstates $\{|\frac{3}{2}\rangle, |\frac{1}{2}\rangle, |-\frac{1}{2}\rangle, |-\frac{3}{2}\rangle\}$ of J_z with its quantization axis along the new z direction. The matrix elements P, Q, R, and S can be expressed in terms of dimensionless symmetric tensors M_{ij},

$$M = \frac{1}{2m_0} \sum_{i,j} M_{ij} \{p_i, p_j\}, \tag{4}$$

where $M \in \{P, Q, R, S\}$ and $i, j \in \{x, y, z\}$. The diagonal element P is invariant under rotations and follows from $P_{ij} = \delta_{ij}\gamma_1$; the other elements are more involved and explicit expressions for their M_{ij} as a function of α and β are given in Appendix A. The Bir-Pikus contribution to the Hamiltonian can easily be included in this notation, by adding a similar contribution $M \to M + \sum_{i,j} M_{ij}^{\mathrm{BP}} \epsilon_{ij}$, where the elements M_{ij}^{BP} can be obtained from M_{ij} by the substitution $\{\gamma_1, \gamma_2, \gamma_3\} \to \{-a, \frac{1}{2}b, \frac{1}{2\sqrt{3}}d\}$.

III. TWO-DIMENSIONAL HOLE GAS

In this section we investigate the dynamics of the holes in a 2DHG, and calculate their effective masses and g-tensor. The in-plane Hamiltonian for the confined holes is obtained by integrating out the coordinate along the direction of confinement, which we labeled z. Assuming no strain and an infinite-well-type of confinement for simplicity, one finds that all terms in H that are linear in p_z vanish, also in the presence of a finite magnetic field [29], and the terms quadratic in p_z integrate out to contributions $M_{zz}u_z$, where the confinement energy scale $u_z = \langle p_z^2 \rangle / 2m_0$ will be assumed much larger than the in-plane kinetic energy of the holes.

The next step is to diagonalize the part of the Hamiltonian that is proportional to u_z, which in general leads to a basis that no longer consists of pure $m_j = \pm\frac{3}{2}$ and $m_j = \pm\frac{1}{2}$ states. The two resulting pairs of spin-mixed eigenstates are the heavy and light holes (HHs and LHs), where the heavy holes are the ones with the lowest excitation energy. The light holes are split off by an energy $\Delta_{\mathrm{HL}} = 2u_z\sqrt{Q_{zz}^2 + |R_{zz}|^2 + |S_{zz}|^2}$, but can become mixed with the heavy holes by in-plane confinement or an applied magnetic field.

A. Effective masses

1. Spherical approximation, $\delta = 0$

Before investigating the anisotropic dynamics of the 2DHG, we briefly repeat the well-known results for the spherical approximation, which follows from neglecting all terms in the Hamiltonian proportional to $\delta = \gamma_3 - \gamma_2$. Then, the HH and LH states at the band edge are pure $m_j = \pm\frac{3}{2}$ and

$m_j = \pm\frac{1}{2}$ states, and one finds $S = 0$ and

$$Q = \frac{4\gamma_2 + 6\gamma_3}{5} u_z - \frac{1}{10m_0}(2\gamma_2 + 3\gamma_3)\big(p_x^2 + p_y^2\big), \tag{5}$$

$$R = -\frac{\sqrt{3}}{10m_0}(2\gamma_2 + 3\gamma_3)(p_x - ip_y)^2, \tag{6}$$

so that $\Delta_{\rm HL} = \frac{4}{5}(2\gamma_2 + 3\gamma_3)u_z$. We see that the Hamiltonian is indeed spherically symmetric in this limit and irrespective of the crystallographic orientation of the 2DHG the in-plane effective masses read to leading order in $1/u_z$ as $m^{\rm H(L)} = m_0/[\gamma_1 \pm \frac{1}{5}(2\gamma_2 + 3\gamma_3)]$ for the HHs and LHs, respectively.

2. *Anisotropic Hamiltonian, $\delta \neq 0$*

The spherical approximation is good in materials where $\delta/(2\gamma_2 + 3\gamma_3)$ is very small. For the case of Si, however, we have $\delta/(2\gamma_2 + 3\gamma_3) \approx 0.22$, which is not negligible, and we thus need to include the terms proportional to δ as well. In general this results in the HHs and LHs becoming mixtures of the $m_j = \pm\frac{3}{2}$ and $m_j = \pm\frac{1}{2}$ states, except for confinement along high-symmetry directions, such as [001] and [111], where $R_{zz} = S_{zz} = 0$ and the Hamiltonian becomes isotropic again.

Most generally, we find for the in-plane effective masses to leading order in $1/u_z$, cf. [29]

$$m^{\rm H,L}(\theta) = \frac{2m_0}{2\gamma_1 + s + r\cos(2\theta - 2\zeta)}, \tag{7}$$

where θ is the angle between the x axis and the direction of motion of the hole. The parameters s and r are different for the HHs and LHs,

$$s^{\rm H,L} = \mp {\rm Re}[\boldsymbol{n}_{zz} \cdot (\boldsymbol{v}_{xx} + \boldsymbol{v}_{yy})^*],$$

$$r^{\rm H,L} = \pm\sqrt{{\rm Re}[\boldsymbol{n}_{zz} \cdot (\boldsymbol{v}_{xx} - \boldsymbol{v}_{yy})^*]^2 + {\rm Re}[\boldsymbol{n}_{zz} \cdot \boldsymbol{v}_{xy}^*]^2},$$

where we introduced the vectors $\boldsymbol{v}_{\alpha\beta} \equiv \{Q_{\alpha\beta}, R_{\alpha\beta}, S_{\alpha\beta}\}$ and $\boldsymbol{n}_{\alpha\beta} \equiv \boldsymbol{v}_{\alpha\beta}/|\boldsymbol{v}_{\alpha\beta}|$, and the upper (lower) sign corresponds to the heavy (light) holes. The angle

$$\zeta = \frac{1}{2}\arctan\left(\frac{{\rm Re}[\boldsymbol{n}_{zz} \cdot \boldsymbol{v}_{xy}^*]}{2{\rm Re}[\boldsymbol{n}_{zz} \cdot (\boldsymbol{v}_{yy} - \boldsymbol{v}_{xx})^*]}\right) \tag{8}$$

determines what θ gives the smallest (largest) effective heavy (light) hole mass, while the largest (smallest) effective mass is always obtained when θ is an angle $\frac{\pi}{2}$ off from ζ. Inserting the expressions given in Appendix A reveals the explicit dependence of $m^{\rm H,L}(\theta)$ on the Euler angles that were used to rotate the Hamiltonian.

In Fig. 2 we illustrate how the effective HH masses in Si depend on the two Euler angles α and β. Figures 2(a) and 2(b) show the magnitudes of the smallest effective mass $m^{\rm H}(\zeta)/m_0$ and the largest effective mass $m^{\rm H}(\zeta + \frac{\pi}{2})/m_0$, respectively. In Fig. 2(c) we plot the anisotropy of the effective masses $m^{\rm H}(\zeta + \frac{\pi}{2})/m^{\rm H}(\zeta)$, while Fig. 2(d) shows how the angle ζ depends on α and β.

The three symbols in Fig. 2 mark three common confinement directions: [001] (circle), [110] (cross), and [112] (star). For the high-symmetry direction [001] the effective masses are isotropic, as expected. Inserting zero for α and β in Eq. (7) we find $m^{\rm H,L}_{[001]}(\theta) = m_0/(\gamma_1 \pm \gamma_2)$, which is indeed independent of θ since $r^{\rm H,L}_{[001]} = 0$. The largest anisotropy of the effective masses is obtained when the 2DHG is confined along [110], where $m^{\rm H}(\zeta + \frac{\pi}{2})/m^{\rm H}(\zeta) > 1.5$. Here, the parameter $r^{\rm H,L}$ in Eq. (7) is at its maximum, making the masses highly dependent on θ,

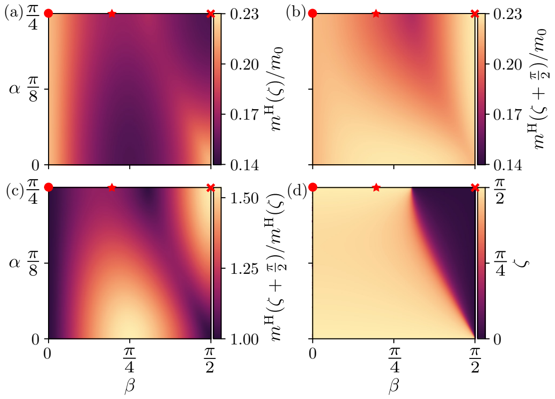

FIG. 2. The effective hole masses of Si as predicted by Eq. (7), plotted against the direction of confinement. (a) and (b) show the smallest and largest effective mass $m^{\rm H}(\zeta)$ and $m^{\rm H}(\zeta + \pi/2)$, respectively; (c) shows the anisotropy of the effective masses $m^{\rm H}(\zeta + \pi/2)/m^{\rm H}(\zeta)$; and (d) shows the angle ζ.

$$m^{\rm H,L}_{[110]}(\theta) = \frac{2m_0}{2\gamma_1 \pm \sqrt{\gamma_2^2 + 3\gamma_3^2} \pm 3\frac{|\gamma_3^2 - \gamma_2^2|}{\sqrt{\gamma_2^2 + 3\gamma_3^2}}\cos(2\theta)}. \tag{9}$$

We find a similar expression for the [112] direction,

$$m^{\rm H,L}_{[112]}(\theta) = \frac{2m_0}{2\gamma_1 \pm \sqrt{\gamma_2^2 + 3\gamma_3^2} \mp \frac{|\gamma_3^2 - \gamma_2^2|}{\sqrt{\gamma_2^2 + 3\gamma_3^2}}\cos(2\theta)}. \tag{10}$$

which has less anisotropy and opposite directions where the masses are largest and smallest, as compared to [110].

B. Heavy-hole Zeeman effect

We will now add a magnetic field and consider its coupling to the angular momentum of the HHs in a 2DHG through the Zeeman effect. The Hamiltonian describing this coupling for the four $j = \frac{3}{2}$ states in the upper valence band reads as [29,61]

$$H_{\rm Z} = 2\kappa\boldsymbol{B} \cdot \boldsymbol{J} + 2q\boldsymbol{B} \cdot \boldsymbol{\mathcal{J}}, \tag{11}$$

where κ is the effective g-factor of the isotropic coupling, $\boldsymbol{B}$ is the applied magnetic field, q sets the strength of the anisotropic coupling, $\boldsymbol{\mathcal{J}} = \{J_x^3, J_y^3, J_z^3\}$, and we use units where the Bohr magneton $\mu_{\rm B} = 1$. Since κ is usually two orders of magnitude larger than q (see Table I) we will neglect the anisotropic contribution to $H_{\rm Z}$. The goal of this section is to derive an effective g-tensor $\bar{g}$ for the HH subspace, such that the linear Zeeman Hamiltonian (11) for the HHs can be written as

$$H_{\rm Z}^{\rm H} = \tfrac{1}{2}\boldsymbol{\sigma} \cdot \bar{g} \cdot \boldsymbol{B}, \tag{12}$$

where $\boldsymbol{\sigma} = \{\sigma_x, \sigma_y, \sigma_z\}$ is the vector of Pauli matrices, acting in the HH subspace.

1. Spherical approximation, $\delta = 0$

Let us again first review the case where the spherical approximation $\delta \to 0$ is reasonable, such as for Ge. At the edge of the valence band, i.e., where $p_x = p_y = 0$, we have $R = S = 0$ and the two HH states are thus pure $m_j = \pm\frac{3}{2}$ states. In that case, the effective HH Zeeman Hamiltonian becomes to leading order in $1/u_z$

$$H_{\rm Z}^{\rm H} = 3\kappa B_z \sigma_z. \tag{13}$$

At the edge of the valence band, the coupling to the in-plane components of the magnetic field $B_{x,y}$ is a higher-order effect via the LH states and is thus proportional to $B_{x,y}^3/u_z^2$. In terms of the g-tensor this means that $g_{zz} = 6\kappa$ and all other elements are much smaller.

For a 2DHG with a finite density, the holes with nonzero in-plane momentum have a nonzero matrix element R, see Eq. (6). This means that for holes close to the Fermi level the resulting HH-LH mixing adds a finite coupling to the in-plane field, yielding an effective direction-dependent g-tensor

$$\bar{g} = \begin{pmatrix} g_\parallel \cos 2\varphi & -g_\parallel \sin 2\varphi & 0 \\ g_\parallel \sin 2\varphi & g_\parallel \cos 2\varphi & 0 \\ 0 & 0 & g_\perp \end{pmatrix}, \tag{14}$$

with $g_\perp = 6\kappa$ and $g_\parallel = 6\kappa p_{\rm F}^2/2m_0 u_z$, again up to order $O(1/u_z)$. Here $p_{\rm F}$ is the Fermi momentum and φ is the direction of propagation of the hole under consideration.

Using that we defined $u_z = \langle p_z^2 \rangle / 2m_0$, we arrive at an elegant expression for the ratio of the magnitudes of the in-plane and out-of-plane g-factors in the spherical approximation [29,62],

$$\frac{g_\parallel}{g_\perp} = \frac{p_{\rm F}^2}{\langle p_z^2 \rangle}. \tag{15}$$

Assuming parabolic dispersion for the range of energies of interest, we can consider a finite two-dimensional density of HHs ρ in the valence band and thus write for the ratio of g-factors at the Fermi level

$$\frac{g_\parallel}{g_\perp} = \frac{2\pi\rho}{\langle k_z^2 \rangle} = \frac{2}{\pi}\rho d^2, \tag{16}$$

where in the last step we again used our assumption of an infinite-well-type of confinement along z, resulting in $\langle k_z^2 \rangle = \pi^2/d^2$, where d is the width of the well.

2. Anisotropic Hamiltonian, $\delta \neq 0$

Going beyond the spherical approximation, as is necessary for Si, all HHs and LHs are mixtures of $m_j = \pm\frac{3}{2}$ and $m_j = \pm\frac{1}{2}$ states, thus resulting in general in a finite coupling to $B_{x,y}$ within the HH subspace, also in the absence of finite in-plane momentum. We thus transform the Zeeman Hamiltonian (11) to the basis where the part of H proportional to u_z is diagonal, which we then project to the HH subspace. To leading order in $1/u_z$, the resulting g-tensor can be written relatively compactly,

$$\frac{g_{zz}}{\kappa} = 2\frac{Q_{zz}}{\nu} + 4\frac{\nu}{\mu}, \tag{17}$$

$$\frac{g_{zx} - i g_{zy}}{\kappa} = 2\sqrt{3}\frac{S_{zz}}{\nu} - 2\frac{R_{zz}S_{zz}^*}{\mu\nu}, \tag{18}$$

$$\frac{g_{xz} + i g_{yz}}{\kappa} = 2\frac{R_{zz}S_{zz}}{\mu\nu}, \tag{19}$$

$$g_{xx} - i g_{xy} = g_{-+} + g_{++}, \tag{20}$$

$$g_{yy} + i g_{yx} = g_{-+} - g_{++}, \tag{21}$$

with

$$\begin{aligned} \frac{g_{-+}}{\kappa} &= -\sqrt{3}\frac{R_{zz}^*}{\mu}\left(1 + \frac{Q_{zz}}{\nu}\right) \\ &\quad - \frac{(S_{zz}^*)^2}{|S_{zz}|^2}\left(1 - \frac{Q_{zz}}{\nu}\right)\left(1 + \frac{\nu}{\mu}\right), \\ \frac{g_{++}}{\kappa} &= \sqrt{3}\frac{R_{zz}}{\mu}\frac{S_{zz}^2}{|S_{zz}|^2}\left(1 - \frac{Q_{zz}}{\nu}\right) \\ &\quad + \frac{R_{zz}^2}{|R_{zz}|^2}\left(1 + \frac{Q_{zz}}{\nu}\right)\left(1 - \frac{\nu}{\mu}\right), \end{aligned}$$

using the shorthand notation $\nu = \sqrt{Q_{zz}^2 + |S_{zz}|^2}$ and $\mu = \sqrt{Q_{zz}^2 + |S_{zz}|^2 + |R_{zz}|^2}$. These results generalize those presented in Refs. [61,63], where the focus was on confinement along $[nnm]$. Equations (18)–(21) are again valid to leading order in $1/u_z$; we note that with the spherical approximation we have $S_{zz} = R_{zz} = 0$, yielding $g_{zz} = 6\kappa$ as the only nonzero element, as expected.[1] We only included the leading-order terms in $1/u_z$ and assumed that $k_\parallel = 0$, i.e., formally we evaluate the g-tensor at the edge of the valence band. However, finite $k_\parallel$ also contributes to $\bar{g}$ in the anisotropic ($\delta \neq 0$) case, similar as in Sec. III B 1. That contribution typically becomes comparable to the one evaluated here when $k_\parallel d \sim 1$, the exact number being highly material dependent.

When the 2DHG is confined along a high-symmetry direction, such as [001] or [111], we obtain an out-of-plane g-factor $g_\perp = 6\kappa$ and in-plane g-factors $g_\parallel = 0$, as expected. For lower-symmetry directions also the g_{xx} and g_{yy} components become nonzero, and by taking [110] as an example we find straightforwardly

$$\frac{g_{zz}}{\kappa} = 2 + \frac{2(\gamma_2 + 3\gamma_3)}{\sqrt{\gamma_2^2 + 3\gamma_3^2}}, \tag{22}$$

$$\frac{g_{yy}}{\kappa} = -2 - \frac{2(\gamma_2 - 3\gamma_3)}{\sqrt{\gamma_2^2 + 3\gamma_3^2}}, \tag{23}$$

$$\frac{g_{xx}}{\kappa} = 2 - \frac{4\gamma_2}{\sqrt{\gamma_2^2 + 3\gamma_3^2}}, \tag{24}$$

---

[1] Although we here focus on the leading-order terms $\propto 1/u_z$, we note that the expressions in Eqs. (18)–(21) can be generalized to describe the g-tensor of any heavy hole governed by a Hamiltonian in the form of Eq. (3) by simply substituting $\{Q_{zz}, R_{zz}, S_{zz}\} \to \{Q, R, S\}$.

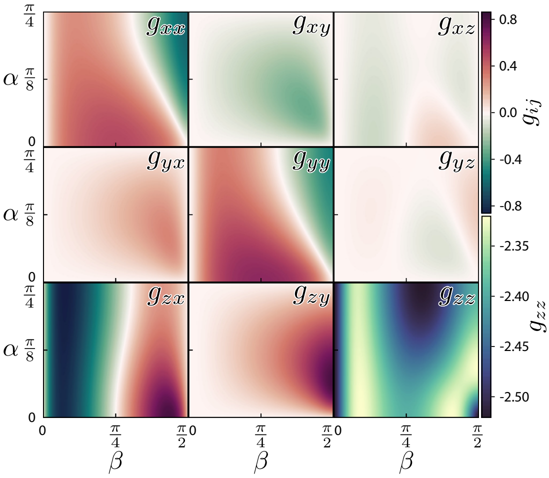

FIG. 3. The nine components of the heavy hole g-tensor given by Eqs. (18)–(21) plotted against the direction of confinement. We here used parameters for Si, see Table I.

and vanishing off-diagonal components. To obtain nonzero off-diagonal elements one has to consider less common directions. For example, for a 2DHG oriented along [112] one finds nonzero off-diagonal elements

$$\frac{g_{xz}}{\kappa} = \frac{2\sqrt{2}}{\sqrt{3}} \frac{(\gamma_3 - \gamma_2)^2}{\sqrt{\gamma_2^2 + 3\gamma_3^2}\sqrt{11\gamma_2^2 + 2\gamma_2\gamma_3 + 35\gamma_3^2}}, \tag{25}$$

$$\frac{g_{zx}}{\kappa} = \frac{2\sqrt{2}}{\sqrt{3}} \frac{6(\gamma_3 - \gamma_2)\sqrt{\gamma_2^2 + 3\gamma_3^2} - (\gamma_3 - \gamma_2)^2}{\sqrt{\gamma_2^2 + 3\gamma_3^2}\sqrt{11\gamma_2^2 + 2\gamma_2\gamma_3 + 35\gamma_3^2}}, \tag{26}$$

coupling the z component of the spin to the x component of $\boldsymbol{B}$ and vice-versa, making the g-tensor highly anisotropic. All these expressions follow straightforwardly from Eqs. (18)–(21) upon inserting the explicit expressions given in Appendix A. In Fig. 3 we plot the magnitude of all nine components of the HH g-tensor at the band edge as a function of the two confinement angles α and β, as given by Eqs. (18)–(21), where we again used parameters for Si. We see that by controlling the orientation of the confining potential one can design the qualitative form of the g-tensor, ranging from purely diagonal for high-symmetry directions to highly anisotropic for less common directions.

IV. CONFINED HEAVY HOLES

In the previous section we investigated the effects of confinement along the z direction on the g-tensor in a 2DHG. Further confinement along the in-plane coordinates x and y, often done via electrostatic gating, can then be used to localize the holes in lateral quantum dots, opening up the possibility to use them as a spin-qubit platform. The effective g-tensor for such localized holes can be affected by spin-orbit interaction (SOI) [2], the effect of which we will include in this section.

In this section we will restrict ourselves to a general linear Rashba-type SOI, which could be caused by the 2DHG confinement potential [64,65]. The Hamiltonian describing this type of interaction for the $j = \frac{3}{2}$ states in the upper valence band reads as [29,63,66]

$$H_{\rm so} = \beta_{\rm so}(p_y J_x - p_x J_y), \tag{27}$$

where we neglected the contribution proportional to $\mathcal{J}$, which is usually much weaker, and we assumed the electric field associated with the confining potential to point along z. The parameter $\beta_{\rm so}$ is material dependent and depends also in an intricate way on the exact shape of the transverse confining potential. By focusing solely on this Rashba term, we neglect the Dresselhaus contribution stemming from the lack of a crystallographic inversion center (which can contribute to the SOI in materials like GaAs and InAs) and we disregard the direct Rashba SOI due to HH-LH mixing [31–34,67] and the dipolar SOI [68]. Our choice is not meant to indicate that we believe that this type of SOI is dominant most often in realistic systems, but we think that it makes our presentation as pedagogical as possible: the straightforward derivation that follows below can serve as a clear blueprint for how the approach can be adapted to other, possibly more complex types of SOI.

In the remainder of this section we will start by calculating the level structure of holes confined in a quantum dot. This allows us then to project the spin-orbit Hamiltonian in Eq. (27) to this basis of localized heavy-hole states and calculate the SOI-induced corrections to the g-tensor using perturbation theory.

A. Level structure

The Luttinger Hamiltonian that governs the in-plane motion of the effective heavy holes was obtained by transforming the in-plane part of H in Eq. (3) to the basis where the part of H proportional to u_z is diagonal. We now add a circularly symmetric parabolic confinement potential $V(\mathbf{r}) = \lambda(x^2 + y^2)$, which can describe the confinement of the holes in a quantum dot,

$$H^{\rm H}_{{\rm L},\parallel} = \frac{p_{\tilde{x}}^2}{2m_-} + \frac{p_{\tilde{y}}^2}{2m_+} + \frac{m_-}{2}\omega_x^2\tilde{x}^2 + \frac{m_+}{2}\omega_y^2\tilde{y}^2. \tag{28}$$

Here, $m_- = m^{\rm H}(\zeta)$ and $m_+ = m^{\rm H}(\zeta + \pi/2)$ are the minimum and maximum HH effective masses, as given by Eq. (7), and the new in-plane coordinate system $\{\tilde{x}, \tilde{y}\}$ is thus rotated over an angle ζ along z with respect to the original system $\{x, y\}$. Further, the frequencies $\omega_x = \sqrt{2\lambda/m_-}$ and $\omega_y = \sqrt{2\lambda/m_+}$ determine the strength of the in-plane confinement and $\boldsymbol{p} = -i\hbar\partial_{\tilde{\boldsymbol{r}}} + e\boldsymbol{A}(\tilde{\boldsymbol{r}})$ is the canonical momentum, with $\boldsymbol{A}(\tilde{\boldsymbol{r}}) = B_z(-\tilde{y}/2, \tilde{x}/2, 0)$ being the vector potential for which we use the circular gauge and neglect in-plane components of the magnetic field, assuming strong confinement along z.

The eigenstates and eigenenergies of such an anisotropic two-dimensional oscillator in the presence of a magnetic field can be found in different ways, see, e.g., Refs. [69–71]. We follow the procedure presented in Ref. [72], resulting in a Hamiltonian that can be written in terms of two independent harmonic oscillators,

$$H^{\rm H}_{{\rm L},\parallel} = \hbar\omega_+\big(a_+^\dagger a_+ + \tfrac{1}{2}\big) + \hbar\omega_-\big(a_-^\dagger a_- + \tfrac{1}{2}\big), \tag{29}$$

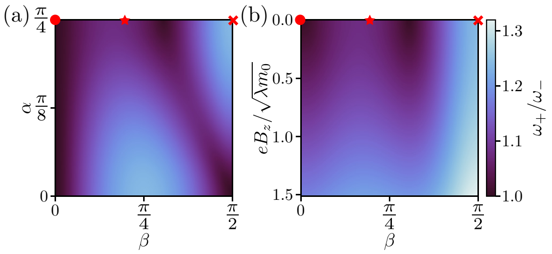

FIG. 4. Asymmetry in the confinement energy ω_+/ω_- as given by Eq. (31). (a) ω_+/ω_- as a function of the direction of confinement in the absence of a vector potential. (b) ω_+/ω_- as a function of the angle β and applied magnetic field $eB_z/\sqrt{\lambda m_0}$, setting $\alpha = \pi/4$ (which corresponds to focusing on confinement directions [*nnm*]). In both plots we used parameters for Si.

where $a_\pm^{(\dagger)}$ are bosonic creation and annihilation operators, and the (positive) oscillator frequencies are defined through

$$\omega_\pm^2 = \frac{1}{2}\omega_x^2 + \frac{1}{2}\omega_y^2 + 2\omega_c^2 \pm \frac{1}{2}\sqrt{\left(\omega_x^2 - \omega_y^2\right)^2 + 8\left(\omega_x^2 + \omega_y^2 + 2\omega_c^2\right)\omega_c^2}, \tag{30}$$

with $\omega_c^2 = e^2B_z^2/4m_+m_-$. We will assume throughout that the oscillator energies $\hbar\omega_\pm$ are much smaller than the energy u_z associated with the transverse confinement.

Since the masses $m_\pm$ depend on the orientation of the plane of the 2DHG (through the angles α and β, see Sec. III A) the level splitting in the dot will also vary as a function of that orientation, which can be shown more explicitly by inserting the maximum and minimum masses as given by Eq. (7),

$$\omega_\pm^2 = \frac{\lambda}{m_0}\left(2\gamma_1 + s + 2\chi_c^2 \pm \eta\right), \tag{31}$$

where we introduced the notation

$$\eta = \sqrt{b^2 + 4\chi_c^2\left(2\gamma_1 + s + \chi_c^2\right)}, \tag{32}$$

and used the dimensionless parameter

$$\chi_c = \frac{eB_z}{4\sqrt{\lambda m_0}}\sqrt{(2\gamma_1 + s)^2 - r^2}, \tag{33}$$

characterizing the magnitude of the cyclotron frequency compared to the harmonic oscillator frequencies. We used the same notation as in Sec. III A, where we omitted the superscript "H" from the coefficients r and s.

To illustrate the dependence of the confinement energies on the orientation of the 2DHG explicitly, we plot in Fig. 4(a) the anisotropy of the level splitting ω_+/ω_- as a function of the angles α and β in the absence of a vector potential, where we used parameters for Si. Naturally, since this anisotropy stems from the orientation dependence of the effective mass, it strongly resembles the results shown in Fig. 2(c). Figure 4(b) shows how a nonzero vector potential affects the anisotropy. We plot ω_+/ω_- as a function of $eB_z/\sqrt{\lambda m_0}$ and the angle β, fixing $\alpha = \pi/4$, which captures all confinement directions of the form [*nnm*]. We see that, as expected, the magnetic field increases the anisotropy, while retaining some of the orientation dependence.

B. Corrections to the *g*-tensor

Since the holes we now consider are localized, $H_{\rm so}$ does not couple the orbital ground states of the heavy holes directly, but does so only in higher order via virtually excited orbital states, this in contrast with the Zeeman Hamiltonian. To find the corrections to the *g*-tensor for the localized eigenstates of the Hamiltonian (28), we first transform $H_{\rm so}$ to the basis that diagonalizes the part of the Luttinger Hamiltonian (3) that is proportional to u_z, as we did in Sec. III B. This transformation thus amounts to performing the same rotation as we applied to $H_{\rm Z}$, meaning that the resulting Hamiltonian in the HH subspace can be written using the *g*-tensor we derived above. For a general spin-orbit Hamiltonian $\boldsymbol{f}(p_x, p_y) \cdot \boldsymbol{J}$ this results in $\frac{1}{4\kappa}\boldsymbol{\sigma} \cdot \bar{g} \cdot \boldsymbol{f}(p_x, p_y)$, and for the case of the linear Rashba Hamiltonian (27) we thus write

$$H_{\rm so}^{\rm H} = \frac{\beta_{\rm so}}{4\kappa}\boldsymbol{\sigma} \cdot \bar{g} \cdot \begin{pmatrix} p_y \\ -p_x \\ 0 \end{pmatrix}. \tag{34}$$

In this form the spin-orbit Hamiltonian contains the leading-order effect of HH-LH mixing.

We then express the in-plane momentum operators $p_{x,y}$ as linear combinations of the bosonic creation and annihilation operators $a_\pm^\dagger$ and $a_\pm$ (see Appendix B),

$$p_x = w_x^+ a_+ + w_x^- a_- + \text{H.c.}, \tag{35}$$

$$p_y = w_y^+ a_+ + w_y^- a_- + \text{H.c.}, \tag{36}$$

with

$$w_x^\pm = W^\mp\left[\pm\left(\frac{m_-^3}{m_+}\right)^{1/8}\sqrt{\eta \pm r \pm 2\chi_c^2}\cos\zeta - i\left(\frac{m_+^3}{m_-}\right)^{1/8}\sqrt{\eta \mp r \pm 2\chi_c^2}\sin\zeta\right], \tag{37}$$

$$w_y^\pm = W^\mp\left[i\left(\frac{m_+^3}{m_-}\right)^{1/8}\sqrt{\eta \mp r \pm 2\chi_c^2}\cos\zeta \pm \left(\frac{m_-^3}{m_+}\right)^{1/8}\sqrt{\eta \pm r \pm 2\chi_c^2}\sin\zeta\right], \tag{38}$$

where the common prefactor reads as

$$W^\pm = \left(\frac{\hbar^2\lambda}{16\eta^2}\right)^{1/4}\left[\left(2\gamma_1 + s + 2\chi_c^2 - \eta\right)\sqrt{\frac{m_+m_-}{m_0^2}}\right]^{\pm 1/4}, \tag{39}$$

and the angle ζ was defined in (8).

By inserting Eqs. (35) and (36) for p_x and p_y in the spin-orbit Hamiltonian (34) we see that we can write

$$H_{\rm so}^{\rm H} = \frac{\beta_{\rm so}}{4\kappa}\sigma_\alpha A_\alpha^\gamma a_\gamma + \text{H.c.}, \tag{40}$$

in terms of bosonic creation and annihilation operators, which makes performing perturbation theory in the SOI very straightforward. Summation over repeated indices $\alpha \in \{x, y, z\}$ and $\gamma \in \{+, -\}$ is implied and we introduced the vectors

$$A^{\pm}_{\alpha} = g_{\alpha x} w^{\pm}_{y} - g_{\alpha y} w^{\pm}_{x}. \tag{41}$$

Similar expressions for other types of SOI can straightforwardly be derived along the same lines.

Using this form of the spin-orbit Hamiltonian we now perform second-order perturbation theory on the eigenstates of the unperturbed Hamiltonian $H_0 = H^{\rm H}_{{\rm L},\parallel} + H^{\rm H}_{\rm Z}$, as given in Eqs. (12) and (29). To order $\beta^2_{\rm so}/\omega^2_{\pm}$ this yields a correction that follows from projecting

$$V_{\rm so} = \sum_{\gamma=\pm} \left\{ H^{\rm H}_{\rm so} \left[\gamma \frac{1}{2} E_{\rm Z} - H_0 \right]^{-1} H^{\rm H}_{\rm so}, P_{\gamma} \right\}, \tag{42}$$

to the HH subspace. Here $E_Z = |\bar{g} \cdot \boldsymbol{B}|$ is the magnitude of the HH Zeeman splitting, the operator $P_{\pm} = |\pm\rangle\langle\pm|$ projects to the two eigenstates of $H^{\rm H}_{Z}$ and can be written explicitly as $P_{\pm} = \frac{1}{2}(1 \pm \boldsymbol{b} \cdot \boldsymbol{\sigma})$ with $\boldsymbol{b} = \bar{g} \cdot \boldsymbol{B}/E_Z$ the unit vector pointing in the direction of the Zeeman field. We then evaluate (42) and extract the spin-orbit-induced contribution to the g-tensor from the linear dependence of $V_{\rm so}$ on $\boldsymbol{B}$. This yields the relatively compact expression

$$g^{\rm so}_{ij} = \frac{1}{16\kappa^2} \frac{l_0^2}{l_{\rm so}^2} \left[\cos^2 \zeta \left(\frac{g_{ix} g_{jx}}{L_-^3} + \frac{g_{iy} g_{jy}}{L_+^3} \right) + \sin^2 \zeta \left(\frac{g_{ix} g_{jx}}{L_+^3} + \frac{g_{iy} g_{jy}}{L_-^3} \right) + \sin(2\zeta) \frac{L_+ + L_-}{L_+^2 L_-^2} \epsilon_{ikl} g_{kx} g_{ly} \delta_{jz} \right], \tag{43}$$

where

$$L_{\pm} = \sqrt{2\gamma_1 + s \pm r}, \tag{44}$$

and we used the length scales $l_0 = (\hbar^2/m_0\lambda)^{\frac{1}{4}}$ (characterizing the in-plane confinement) and $l_{\rm so} = \hbar/m_0\beta_{\rm so}$ (the spin-orbit length). The first two terms in (43) arise due to the Zeeman shift of the ground and excited spin states, whereas the last term contains the contribution linear in ω_c and couples therefore only to B_z.

In Fig. 5 we show an example of the orientation dependence of the matrix elements $g^{\rm so}_{ij}$ as given by Eq. (43), where we again used parameters for Si, for consistency. The matrix elements are plotted in units of the dimensionless ratio $l_0/l_{\rm so}$, which characterizes the effect of the spin-orbit interaction in the quantum dots. The elements $g^{\rm so}_{ix}$ and $g^{\rm so}_{iy}$ are solely determined by the first two terms in Eq. (43), whereas the elements $g^{\rm so}_{iz}$ also include contributions from the last term. Similar to the unperturbed g-tensor as investigated in Sec. III B, many elements of the spin-orbit correction $\bar{g}^{\rm so}$ also vanish for high-symmetry confinement directions such as [001] and [111].

Depending on the details of the material and confinement potential of the hole gas, other types of SOI than the linear Rashba type of Eq. (34) could be dominating, such as an effectively cubic Rashba interaction $\propto p^3_+\sigma_- - p^3_-\sigma_+$. We emphasize again that the derivation presented in this section can easily be adapted to such other spin-orbit Hamiltonians, simply by substituting Eqs. (35), (36) into the spin-orbit Hamiltonian and evaluating the resulting correction (42). Working in the bosonic number basis this is a straightforward task.

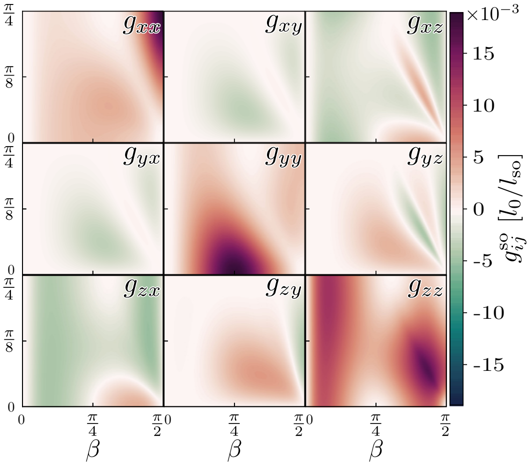

FIG. 5. The nine matrix elements of the spin-orbit correction to the g-tensor, as given by Eq. (43), plotted as a function of the direction of the confinement plane. The correction is shown in units of $l_0/l_{\rm so}$. In this plot we used again parameters for Si.

V. CONCLUSION

Depending on the choice of material, holes confined in two- or lower-dimensional semiconductor structures can possess anisotropic dynamics that are highly dependent on the details of the confinement potentials in the system. Such holes can have several interesting properties that arise from this anisotropy, such as highly anisotropic effective masses and g-tensors.

In this paper we investigated these anisotropies, with special focus on the detailed role of the orientation of the confinement potentials. Starting from a 4×4 Luttinger Hamiltonian, which we did not necessarily assume to be spherically symmetric, we assumed very strong transverse confinement in one direction, resulting in a 2DHG. We rotated our coordinate system such that the transverse direction could easily be integrated out for an arbitrary direction of confinement. This approach allowed us to extract very general analytic expressions for both the in-plane effective hole masses and the heavy-hole g-tensor, where we pointed out how the effect of strain can easily be included. We then investigated a strainless 2DHG and derived analytic expressions for the effective masses and the g-tensor. In our explicit results we focused on Si, which exhibits relatively strong anisotropies, but the expressions we presented are fully general.

We then assumed additional in-plane confinement, leading to the formation of quantum dots. We presented a straightforward approach to include the effects of spin-orbit coupling on the dynamics of the hole states localized in a quantum dot. As an example we considered the effect of a linear Rashba-like

SOI that could arise from the transverse confinement. By calculating the level splitting of the localized states, we projected the spin-orbit Hamiltonian to the basis of the localized states and used perturbation theory to obtain an electric-field-dependent correction to the g-tensor of the confined heavy holes. Our results are highly relevant for the ongoing efforts to use hole spins localized in Si- or Ge-based quantum dots as spin qubits. Finding optimal working points, providing fast qubit control through g-tensor modulation together with relative insensitivity to charge noise requires a thorough understanding of the intricate interplay of SOI, confinement, and applied magnetic fields.

ACKNOWLEDGMENTS

This work is part of FRIPRO-Project No. 274853, which is funded by the Research Council of Norway (RCN), and was also partly supported by the Centers of Excellence funding scheme of the RCN, Project No. 262633, QuSpin.

APPENDIX A: HAMILTONIAN TENSOR ELEMENTS

The rotated Luttinger (and Bir-Pikus) Hamiltonian can always be written in the following form:

$$H(\alpha,\beta) = \begin{pmatrix} P-Q & -S & R & 0 \\ -S^\dagger & P+Q & 0 & R \\ R^\dagger & 0 & P+Q & S \\ 0 & R^\dagger & S^\dagger & P-Q \end{pmatrix}, \qquad \text{(A1)}$$

in the basis of the eigenstates $\{|\frac{3}{2}\rangle, |\frac{1}{2}\rangle, |-\frac{1}{2}\rangle, |-\frac{3}{2}\rangle\}$ of J_z with its quantization axis along the new z direction.

For the Luttinger Hamiltonian the matrix elements P, Q, R, and S can be expressed in terms of dimensionless symmetric tensors M_{ij},

$$M = \frac{1}{2m_0}\sum_{i,j} M_{ij}\{p_i, p_j\}, \qquad \text{(A2)}$$

where $\{A, B\} = \frac{1}{2}(AB + BA)$, $M \in \{P, Q, R, S\}$ and $i, j \in \{x, y, z\}$. The diagonal element P is invariant under rotations and follows from $P_{ij} = \delta_{ij}\gamma_1$, while the tensor elements of Q, R, and S read

$$Q_{xx} = -\frac{1}{5}(2\gamma_2 + 3\gamma_3) - \frac{3\delta}{160}[3 + 5\cos(4\alpha) - 5\cos(4\beta)\{7 + \cos(4\alpha)\}], \qquad \text{(A3)}$$

$$Q_{yy} = -\frac{1}{5}(2\gamma_2 + 3\gamma_3) + \frac{3\delta}{40}[3 + 5\cos(4\alpha) + 10\cos(2\beta)\sin^2(2\alpha)], \qquad \text{(A4)}$$

$$Q_{zz} = \frac{2}{5}(2\gamma_2 + 3\gamma_3) - \frac{3\delta}{160}[9 + 20\cos(2\beta) + 35\cos(4\beta) + 40\cos(4\alpha)\sin^4\beta], \qquad \text{(A5)}$$

$$Q_{xy} = -\frac{3\delta}{2}\sin(4\alpha)\cos\beta\sin^2\beta, \qquad \text{(A6)}$$

$$Q_{yz} = -\frac{3\delta}{2}\sin(4\alpha)\sin^3\beta, \qquad \text{(A7)}$$

$$Q_{zx} = \frac{3\delta}{16}[4\sin^2(2\alpha)\sin(2\beta) + \sin(4\beta)\{7 + \cos(4\alpha)\}], \qquad \text{(A8)}$$

$$R_{xx} = -\frac{\sqrt{3}}{5}(2\gamma_2 + 3\gamma_3) + \frac{\sqrt{3}\delta}{160}\left[21 - 40\cos(2\beta) + 35\cos(4\beta) + 80\cos^2\beta\left\{e^{-4i\alpha}\cos^4\left(\frac{\beta}{2}\right) + e^{4i\alpha}\sin^4\left(\frac{\beta}{2}\right)\right\}\right], \qquad \text{(A9)}$$

$$R_{yy} = \frac{\sqrt{3}}{5}(2\gamma_2 + 3\gamma_3) - \frac{\sqrt{3}\delta}{40}[9 + 15\cos(4\alpha) - 10\sin^2(2\alpha)\cos(2\beta) - 20i\sin(4\alpha)\cos\beta], \qquad \text{(A10)}$$

$$R_{zz} = \frac{\sqrt{3}\delta}{8}\sin^2\beta[5 + 7\cos(2\beta) + \cos(4\alpha)\{3 + \cos(2\beta)\} - 4i\sin(4\alpha)\cos\beta], \qquad \text{(A11)}$$

$$R_{xy} = \frac{2\sqrt{3}i}{5}(2\gamma_2 + 3\gamma_3) + \frac{\sqrt{3}\delta}{40}[5\sin(4\alpha)\{7\cos\beta + \cos(3\beta)\} + 4i\{3 + 5\cos(4\alpha) - 10\sin^2(2\alpha)\cos(2\beta)\}], \qquad \text{(A12)}$$

$$R_{yz} = \frac{\sqrt{3}\delta}{8}[\sin(4\alpha)\{5\sin\beta + \sin(3\beta)\} - 8i\sin^2(2\alpha)\cos(2\beta)], \qquad \text{(A13)}$$

$$R_{zx} = -\frac{\sqrt{3}\delta}{8}\sin(2\beta)[3 - 7\cos(2\beta) - \cos(4\alpha)\{3 + \cos(2\beta)\} + 4i\sin(4\alpha)\cos\beta], \qquad \text{(A14)}$$

$$S_{xx} = -\frac{\sqrt{3}\delta}{16}[8\cos^2\beta\sin\beta\{\cos(4\alpha)\cos\beta - i\sin(4\alpha)\} - 2\sin(2\beta) + 7\sin(4\beta)], \qquad \text{(A15)}$$

$$S_{yy} = -\sqrt{3}\delta\sin(2\alpha)\sin\beta[\sin(2\alpha)\cos\beta + i\cos(2\alpha)], \qquad \text{(A16)}$$

$$S_{zz} = -\frac{\sqrt{3}\delta}{16}[8\sin^3\beta\{\cos(4\alpha)\cos\beta - i\sin(4\alpha)\} - 2\sin(2\beta) - 7\sin(4\beta)], \qquad \text{(A17)}$$

$$S_{xy} = -\sqrt{3}\delta\sin(2\alpha)\sin(2\beta)[\cos(2\alpha)\cos\beta - i\sin(2\alpha)], \tag{A18}$$

$$S_{yz} = -\frac{2\sqrt{3}i}{5}(2\gamma_2+3\gamma_3) - \frac{\sqrt{3}i\delta}{10}[3+5\cos(2\beta)+10\sin^2\beta\{\cos(4\alpha)-i\sin(4\alpha)\cos\beta\}], \tag{A19}$$

$$S_{zx} = \frac{2\sqrt{3}}{5}(2\gamma_2+3\gamma_3) - \frac{\sqrt{3}\delta}{40}[3+5\cos(4\alpha)\{1-\cos(4\beta)\}-35\cos(4\beta)-40i\sin(4\alpha)\cos\beta\sin^2\beta]. \tag{A20}$$

Also the Bir-Pikus Hamiltonian can easily be obtained from the tensor elements above. The matrix elements of the Hamiltonian take the form

$$M = \sum_{i,j} M_{ij}^{\mathrm{BP}}\epsilon_{ij}, \tag{A21}$$

where $\bar{\epsilon}$ is the strain tensor, and M_{ij}^{BP} can be obtained from M_{ij} by the substitution $\{\gamma_1,\gamma_2,\gamma_3\} \to \{-a, \frac{1}{2}b, \frac{1}{2\sqrt{3}}d\}$.

APPENDIX B: HARMONIC OSCILLATOR HAMILTONIAN

The Hamiltonian we consider has the form

$$H = \frac{\pi_x^2}{2m_-} + \frac{\pi_y^2}{2m_+} + \frac{m_-}{2}\omega_x^2x^2 + \frac{m_+}{2}\omega_y^2y^2, \tag{B1}$$

with $\boldsymbol{\pi} = \boldsymbol{p} + e\boldsymbol{A}(\boldsymbol{r})$, where $\boldsymbol{A}(\boldsymbol{r}) = B_z(-y/2, x/2, 0)$, and $\boldsymbol{p} = -i\hbar\partial_{\boldsymbol{r}}$ the kinetic momentum. We insert this expression for $\boldsymbol{p}$ and rewrite the Hamiltonian as

$$H = \frac{\bar{p}_x^2}{2\mu} + \frac{\bar{p}_y^2}{2\mu} + \omega_c\bar{p}_y\bar{x} - \omega_c\bar{p}_x\bar{y} + \frac{\mu}{2}\omega_1^2\bar{x}^2 + \frac{\mu}{2}\omega_2^2\bar{y}^2, \tag{B2}$$

using the frequencies $\omega_1 = \sqrt{\omega_x^2+\omega_c^2}$, $\omega_2 = \sqrt{[b]\omega_y^2+\omega_c^2}$, and $\omega_c = eB_z/2\mu$. We further rescaled $\bar{p}_x = p_x\sqrt{\mu/m_-}$, $\bar{p}_y = p_y\sqrt{\mu/m_+}$, $\bar{x} = x\sqrt{m_-/\mu}$, and $\bar{y} = y\sqrt{m_+/\mu}$, with $\mu = \sqrt{m_+m_-}$ being the geometric average of the two effective masses. In this way we rewrote the Hamiltonian as that for an electron with an isotropic mass μ in an elliptic harmonic potential in the presence of an out-of-plane magnetic field.

There are many ways to diagonalize such a Hamiltonian; we will follow the method outlined in Ref. [72], which leads straightforwardly to

$$H = \hbar\omega_+\left(a_+^\dagger a_+ + \tfrac{1}{2}\right) + \hbar\omega_-\left(a_-^\dagger a_- + \tfrac{1}{2}\right), \tag{B3}$$

with $\omega_\pm$ as defined in the main text and

$$a_\pm = \boldsymbol{u}^\pm \cdot \{\bar{x}, \bar{p}_x, \bar{y}, \bar{p}_y\}, \tag{B4}$$

which obey bosonic commutation relations. The vectors $\boldsymbol{u}^\pm$ read as

$$\boldsymbol{u}^\pm = \frac{1}{C_\pm}\big\{-i\mu\omega_\pm\left(\omega_\pm^2-\omega_y^2-2\omega_c^2\right), \omega_\pm^2-\omega_y^2, -\mu\omega_c\left(\omega_\pm^2+\omega_y^2\right), -2i\omega_c\omega_\pm\big\}, \tag{B5}$$

with

$$C_\pm = \sqrt{2\hbar\mu\omega_\pm\left[\left(\omega_\pm^2-\omega_y^2\right)^2+4\omega_c^2\omega_y^2\right]}. \tag{B6}$$

We can then solve Eq. (B4) to express the coordinate and kinetic momentum operators $\{\bar{x}, \bar{p}_x, \bar{y}, \bar{p}_y\}$ in terms of the bosonic operators $a_\pm$ and $a_\pm^\dagger$,

$$\bar{p}_x = \frac{u_3^-a_+ - u_3^+a_-}{2(u_3^-u_2^+ - u_2^-u_3^+)} + \text{H.c.}, \tag{B7}$$

$$\bar{p}_y = \frac{-u_1^-a_+ + u_1^+a_-}{2(u_4^-u_1^+ - u_1^-u_4^+)} + \text{H.c.}, \tag{B8}$$

$$\bar{x} = \frac{u_4^-a_+ - u_4^+a_-}{2(u_4^-u_1^+ - u_1^-u_4^+)} + \text{H.c.}, \tag{B9}$$

$$\bar{y} = \frac{-u_2^-a_+ + u_2^+a_-}{2(u_3^-u_2^+ - u_2^-u_3^+)} + \text{H.c.} \tag{B10}$$

After scaling back to the original operators $\{x, p_x, y, p_y\}$, the canonical momenta

$$\pi_x = \sqrt{\frac{m_-}{\mu}}\bar{p}_x - \frac{eB_z}{2}\sqrt{\frac{\mu}{m_+}}\bar{y}, \tag{B11}$$

$$\pi_y = \sqrt{\frac{m_+}{\mu}}\bar{p}_y + \frac{eB_z}{2}\sqrt{\frac{\mu}{m_-}}\bar{x}, \tag{B12}$$

are expressed in terms of the bosonic operators. Such a form of the momentum operators is very convenient to use in perturbation theory: In this bosonic framework one can straightforwardly work exclusively in the bosonic Fock space, where no explicit knowledge of the electronic wave functions is required.

[1] D. Loss and D. P. DiVincenzo, Phys. Rev. A **57**, 120 (1998).

[2] R. Hanson, L. P. Kouwenhoven, J. R. Petta, S. Tarucha, and L. M. K. Vandersypen, Rev. Mod. Phys. **79**, 1217 (2007).

[3] A. Chatterjee, P. Stevenson, S. De Franceschi, A. Morello, N. P. de Leon, and F. Kuemmeth, Nature Rev. Phys. **3**, 157 (2021).

[4] D. P. DiVincenzo, D. Bacon, J. Kempe, G. Burkard, and K. B. Whaley, Nature (London) **408**, 339 (2000).

[5] M. Russ and G. Burkard, J. Phys.: Condens. Matter **29**, 393001 (2017).

[6] E. A. Laird, J. M. Taylor, D. P. DiVincenzo, C. M. Marcus, M. P. Hanson, and A. C. Gossard, Phys. Rev. B **82**, 075403 (2010).

[7] L. Gaudreau, G. Granger, A. Kam, G. C. Aers, S. A. Studenikin, P. Zawadzki, M. Pioro-Ladrière, Z. R. Wasilewski, and A. S. Sachrajda, Nature Phys. **8**, 54 (2011).

[8] J. Medford, J. Beil, J. M. Taylor, S. D. Bartlett, A. C. Doherty, E. I. Rashba, D. P. DiVincenzo, H. Lu, A. C. Gossard, and C. M. Marcus, Nature Nanotechnol. **8**, 654 (2013).

[9] J. Medford, J. Beil, J. M. Taylor, E. I. Rashba, H. Lu, A. C. Gossard, and C. M. Marcus, Phys. Rev. Lett. **111**, 050501 (2013).

[10] A. V. Khaetskii, D. Loss, and L. Glazman, Phys. Rev. Lett. **88**, 186802 (2002).

[11] J.-T. Hung, J. Fei, M. Friesen, and X. Hu, Phys. Rev. B **90**, 045308 (2014).

[12] C. G. Péterfalvi and G. Burkard, Phys. Rev. B **96**, 245412 (2017).

[13] M. Veldhorst, J. C. C. Hwang, C. H. Yang, A. W. Leenstra, B. de Ronde, J. P. Dehollain, J. T. Muhonen, F. E. Hudson, K. M. Itoh, A. Morello, and A. S. Dzurak, Nature Nanotechnol. **9**, 981 (2014).

[14] J. T. Muhonen, J. P. Dehollain, A. Laucht, F. E. Hudson, R. Kalra, T. Sekiguchi, K. M. Itoh, D. N. Jamieson, J. C. McCallum, A. S. Dzurak, and A. Morello, Nature Nanotechnol. **9**, 986 (2014).

[15] K. Eng, T. D. Ladd, A. Smith, M. G. Borselli, A. A. Kiselev, B. H. Fong, K. S. Holabird, T. M. Hazard, B. Huang, P. W. Deelman, I. Milosavljevic, A. E. Schmitz, R. S. Ross, M. F. Gyure, and A. T. Hunter, Sci. Adv. **1**, e1500214 (2015).

[16] J. Yoneda, K. Takeda, T. Otsuka, T. Nakajima, M. R. Delbecq, G. Allison, T. Honda, T. Kodera, S. Oda, Y. Hoshi, N. Usami, K. M. Itoh, and S. Tarucha, Nature Nanotechnol. **13**, 102 (2018).

[17] R. W. Andrews, C. Jones, M. D. Reed, A. M. Jones, S. D. Ha, M. P. Jura, J. Kerckhoff, M. Levendorf, S. Meenehan, S. T. Merkel, A. Smith, B. Sun, A. J. Weinstein, M. T. Rakher, T. D. Ladd, and M. G. Borselli, Nature Nanotechnol. **14**, 747 (2019).

[18] F. A. Zwanenburg, A. S. Dzurak, A. Morello, M. Y. Simmons, L. C. L. Hollenberg, G. Klimeck, S. Rogge, S. N. Coppersmith, and M. A. Eriksson, Rev. Mod. Phys. **85**, 961 (2013).

[19] D. Culcer, X. Hu, and S. Das Sarma, Phys. Rev. B **82**, 205315 (2010).

[20] R. Maurand, X. Jehl, D. Kotekar-Patil, A. Corna, H. Bohuslavskyi, R. Laviéville, L. Hutin, S. Barraud, M. Vinet, M. Sanquer, and S. De Franceschi, Nature Commun. **7**, 13575 (2016).

[21] S. D. Liles, R. Li, C. H. Yang, F. E. Hudson, M. Veldhorst, A. S. Dzurak, and A. R. Hamilton, Nature Commun. **9**, 3255 (2018).

[22] H. Watzinger, J. Kukučka, L. Vukušić, F. Gao, T. Wang, F. Schäffler, J.-J. Zhang, and G. Katsaros, Nature Commun. **9**, 3902 (2018).

[23] L. Vukušić, J. Kukučka, H. Watzinger, J. M. Milem, F. Schäffler, and G. Katsaros, Nano Lett. **18**, 7141 (2018), 1803.01775.

[24] A. Crippa, R. Ezzouch, A. Aprá, A. Amisse, R. Laviéville, L. Hutin, B. Bertrand, M. Vinet, M. Urdampilleta, T. Meunier, M. Sanquer, X. Jehl, R. Maurand, and S. De Franceschi, Nature Commun. **10**, 2776 (2019).

[25] G. Scappucci, C. Kloeffel, F. A. Zwanenburg, D. Loss, M. Myronov, J.-J. Zhang, S. D. Franceschi, G. Katsaros, and M. Veldhorst, Nature Rev. Mater. **6**, 926 (2020).

[26] D. Jirovec, A. Hofmann, A. Ballabio, P. M. Mutter, G. Tavani, M. Botifoll, A. Crippa, J. Kukucka, O. Sagi, F. Martins, J. Saez-Mollejo, I. Prieto, M. Borovkov, J. Arbiol, D. Chrastina, G. Isella, and G. Katsaros, Nature Mater. **20**, 1106 (2021).

[27] W. I. L. Lawrie, M. Russ, F. v. Riggelen, N. W. Hendrickx, S. L. d. Snoo, A. Sammak, G. Scappucci, and M. Veldhorst, arXiv:2109.07837.

[28] N. W. Hendrickx, W. I. L. Lawrie, M. Russ, F. v. Riggelen, S. L. d. Snoo, R. N. Schouten, A. Sammak, G. Scappucci, and M. Veldhorst, Nature (London) **591**, 580 (2021).

[29] R. Winkler, *Spin–Orbit Coupling Effects in Two-Dimensional Electron and Hole Systems* (Springer, Berlin, 2003).

[30] N. Ares, G. Katsaros, V. N. Golovach, J. J. Zhang, A. Prager, L. I. Glazman, O. G. Schmidt, and S. De Franceschi, Appl. Phys. Lett. **103**, 263113 (2013).

[31] C. Kloeffel, M. Trif, and D. Loss, Phys. Rev. B **84**, 195314 (2011).

[32] C. Kloeffel, M. J. Rančić, and D. Loss, Phys. Rev. B **97**, 235422 (2018).

[33] S. Bosco, M. Benito, C. Adelsberger, and D. Loss, Phys. Rev. B **104**, 115425 (2021).

[34] S. Bosco, B. Hetényi, and D. Loss, PRX Quantum **2**, 010348 (2021).

[35] F. N. M. Froning, L. C. Camenzind, O. A. H. v. d. Molen, A. Li, E. P. A. M. Bakkers, D. M. Zumbühl, and F. R. Braakman, Nature Nanotechnol. **16**, 308 (2021).

[36] Z. Wang, E. Marcellina, A. R. Hamilton, J. H. Cullen, S. Rogge, J. Salfi, and D. Culcer, npj Quant. Inf. **7**, 54 (2021).

[37] J. Fischer, W. A. Coish, D. V. Bulaev, and D. Loss, Phys. Rev. B **78**, 155329 (2008).

[38] Y. T. Chiu, M. Padmanabhan, T. Gokmen, J. Shabani, E. Tutuc, M. Shayegan, and R. Winkler, Phys. Rev. B **84**, 155459 (2011).

[39] W. J. Hardy, C. T. Harris, Y. H. Su, Y. Chuang, J. Moussa, L. N. Maurer, J. Y. Li, T. M. Lu, and D. R. Luhman, Nanotechnol. **30**, 215202 (2019).

[40] M. Lodari, A. Tosato, D. Sabbagh, M. A. Schubert, G. Capellini, A. Sammak, M. Veldhorst, and G. Scappucci, Phys. Rev. B **100**, 041304(R) (2019).

[41] S. P. Koduvayur, L. P. Rokhinson, D. C. Tsui, L. N. Pfeiffer, and K. W. West, Phys. Rev. Lett. **100**, 126401 (2008).

[42] B. Voisin, R. Maurand, S. Barraud, M. Vinet, X. Jehl, M. Sanquer, J. Renard, and S. De Franceschi, Nano Lett. **16**, 88 (2016).

[43] H. Watzinger, C. Kloeffel, L. Vukušić, M. D. Rossell, V. Sessi, J. Kukučka, R. Kirchschlager, E. Lausecker, A. Truhlar, M. Glaser, A. Rastelli, A. Fuhrer, D. Loss, and G. Katsaros, Nano Lett. **16**, 6879 (2016).

[44] M. Brauns, J. Ridderbos, A. Li, E. P. A. M. Bakkers, and F. A. Zwanenburg, Phys. Rev. B **93**, 121408(R) (2016).

[45] A. Bogan, S. A. Studenikin, M. Korkusinski, G. C. Aers, L. Gaudreau, P. Zawadzki, A. S. Sachrajda, L. A. Tracy, J. L. Reno, and T. W. Hargett, Phys. Rev. Lett. **118**, 167701 (2017).

[46] T. M. Lu, C. T. Harris, S.-H. Huang, Y. Chuang, J.-Y. Li, and C. W. Liu, Appl. Phys. Lett. **111**, 102108 (2017).

[47] A. Crippa, R. Maurand, L. Bourdet, D. Kotekar-Patil, A. Amisse, X. Jehl, M. Sanquer, R. Laviéville, H. Bohuslavskyi, L. Hutin, S. Barraud, M. Vinet, Y.-M. Niquet, and S. De Franceschi, Phys. Rev. Lett. **120**, 137702 (2018).

[48] C. Gradl, R. Winkler, M. Kempf, J. Holler, D. Schuh, D. Bougeard, A. Hernández-Mínguez, K. Biermann, P. V. Santos, C. Schüller, and T. Korn, Phys. Rev. X **8**, 021068 (2018).

[49] F. K. de Vries, J. Shen, R. J. Skolasinski, M. P. Nowak, D. Varjas, L. Wang, M. Wimmer, J. Ridderbos, F. A. Zwanenburg, A. Li, S. Koelling, M. A. Verheijen, E. P. A. M. Bakkers, and L. P. Kouwenhoven, Nano Lett. **18**, 6483 (2018).

[50] A. Sammak, D. Sabbagh, N. W. Hendrickx, M. Lodari, B. P. Wuetz, A. Tosato, L. Yeoh, M. Bollani, M. Virgilio,

M. A. Schubert, P. Zaumseil, G. Capellini, M. Veldhorst, and G. Scappucci, Adv. Funct. Mater. **29**, 1807613 (2019).
[51] A. Hofmann, D. Jirovec, M. Borovkov, I. Prieto, A. Ballabio, J. Frigerio, D. Chrastina, G. Isella, and G. Katsaros, arXiv:1910.05841.
[52] A. J. Miller, M. Brickson, W. J. Hardy, C.-Y. Liu, J.-Y. Li, A. Baczewski, M. P. Lilly, T.-M. Lu, and D. R. Luhman, arXiv:2102.01758.
[53] Y. Kato, R. C. Myers, D. C. Driscoll, A. C. Gossard, J. Levy, and D. D. Awschalom, Science **299**, 1201 (2003).
[54] B. Venitucci, L. Bourdet, D. Pouzada, and Y.-M. Niquet, Phys. Rev. B **98**, 155319 (2018).
[55] L. A. Terrazos, E. Marcellina, Z. Wang, S. N. Coppersmith, M. Friesen, A. R. Hamilton, X. Hu, B. Koiller, A. L. Saraiva, D. Culcer, and R. B. Capaz, Phys. Rev. B **103**, 125201 (2021).
[56] V. P. Michal, B. Venitucci, and Y.-M. Niquet, Phys. Rev. B **103**, 045305 (2021).
[57] C. Adelsberger, M. Benito, S. Bosco, J. Klinovaja, and D. Loss, arXiv:2110.15039.
[58] Y. Sun, S. E. Thompson, and T. Nishida, *Strain effect in semiconductors: theory and device applications* (Springer Science & Business Media, Berlin, 2009).
[59] G. Fishman, Phys. Rev. B **52**, 11132 (1995).
[60] M. Tinkham, *Group Theory and Quantum Mechanics* (McGraw-Hill Book Company, New York, 1964).
[61] R. Winkler, S. J. Papadakis, E. P. DePoortere, and M. Shayegan, Phys. Rev. Lett. **85**, 4574 (2000).
[62] E. Marcellina, A. Srinivasan, D. S. Miserev, A. F. Croxall, D. A. Ritchie, I. Farrer, O. P. Sushkov, D. Culcer, and A. R. Hamilton, Phys. Rev. Lett. **121**, 077701 (2018).
[63] R. Winkler, D. Culcer, S. J. Papadakis, B. Habib, and M. Shayegan, Semicond. Sci. Technol. **23**, 114017 (2008).
[64] H. Nakamura, T. Koga, and T. Kimura, Phys. Rev. Lett. **108**, 206601 (2012).
[65] R. Moriya, K. Sawano, Y. Hoshi, S. Masubuchi, Y. Shiraki, A. Wild, C. Neumann, G. Abstreiter, D. Bougeard, T. Koga, and T. Machida, Phys. Rev. Lett. **113**, 086601 (2014).
[66] R. Winkler, Phys. Rev. B **62**, 4245 (2000).
[67] J.-X. Xiong, S. Guan, J.-W. Luo, and S.-S. Li, Phys. Rev. B **103**, 085309 (2021).
[68] P. Philippopoulos, S. Chesi, D. Culcer, and W. A. Coish, Phys. Rev. B **102**, 075310 (2020).
[69] T. Rebane, Theor. Exp. Chem. **5**, 1 (1972).
[70] B. Schuh, J. Phys. A: Math. Gen. **18**, 803 (1985).
[71] F. N. M. Froning, M. J. Rančić, B. Hetényi, S. Bosco, M. K. Rehmann, A. Li, E. P. A. M. Bakkers, F. A. Zwanenburg, D. Loss, D. M. Zumbühl, and F. R. Braakman, Phys. Rev. Research **3**, 013081 (2021).
[72] L. Qiong-Gui, Commun. Theor. Phys. **38**, 667 (2002).

Paper IV

J. H. Qvist and J. Danon.

Probing details of spin–orbit coupling through Pauli spin blockade.

arXiv:2204.12546 (2022).

arXiv:2204.12546v1 [cond-mat.mes-hall] 26 Apr 2022

Probing details of spin–orbit coupling through Pauli spin blockade

Jørgen Holme Qvist and Jeroen Danon
Center for Quantum Spintronics, Department of Physics,
Norwegian University of Science and Technology, NO-7491 Trondheim, Norway

(Dated: April 28, 2022)

Spin–orbit interaction (SOI) plays a fundamental role in many low-dimensional semiconductor and hybrid quantum devices. In the rapidly evolving field of semiconductor spin qubits, SOI is an essential ingredient that can allow for ultrafast qubit control. The exact manifestation of SOI in a given device is, however, often both hard to predict theoretically and probe experimentally. Here, we develop a detailed theoretical connection between the leakage current through a double quantum dot in Pauli spin blockade and the underlying SOI in the system. We present a general analytic expression for the leakage current, which allows to connect experimentally observable features to both the magnitude and orientation of the effective spin–orbit field acting on the moving carriers. Motivated by the large recent interest in hole-based quantum devices, we further zoom in on the case of Pauli blockade of hole spins, assuming a strong transverse confinement potential. In this limit we also find an analytic expression for the current at low external magnetic field, that includes the effect of hyperfine coupling of the hole spins to randomly fluctuating nuclear spin baths. This result can be used to extract detailed information about both hyperfine and spin–orbit coupling parameters for hole spins in devices with a significant fraction of non-zero nuclear spins.

I. INTRODUCTION

Spin–orbit interaction (SOI) couples the spin degree of freedom of a charge carrier moving in an electromagnetic field to its momentum. This interaction is an essential ingredient for many semiconductor-based quantum devices. In semiconductor-superconductor hybrid structures, SOI plays a crucial role for the realization of Majorana bound states [1–6], with potential applications in topologically protected quantum computation [7–10]. For spin-based quantum technologies SOI enables spin manipulation via electric control, allowing for enhanced spin-cavity couplings [11–13] and electric dipole spin resonance [14–16].

In the field of semiconductor spin qubits [17–21], the electric control over spin provided by SOI enables fast qubit operation [22, 23], while also being a source of qubit decoherence and relaxation [24–26]. Lately, there has been substantial progress with Si- and Ge-based spin qubits that use the spin of valence-band holes instead of conduction-band electrons [27–34]. The p-type nature of the valence band leads to a mixing of the orbital and spin degrees of freedom of the carriers, yielding a potentially strong effective SOI that depends on the details of the confinement. This can give rise to several interesting phenomena such as a highly anisotropic and electrically tunable g-tensor [35–46], and it could also allow for very fast spin-qubit manipulation [47–53].

Despite SOI being crucial for the working of many semiconductor quantum devices, its exact manifestation for a given system is often hard to predict or deduce from experiments. This is partly a result of the total SOI having often several, qualitatively different contributions in strongly confined systems [54, 55]. Common contributions are Rashba terms stemming from structural inversion asymmetry, e.g., created by a confining potential, and Dresselhaus terms originating from the lack of a crystallographic inversion center in semiconductors with zinc-blende structure. In addition to this, both the so-called dipolar SOI [56] and strain-induced mixing of different hole states [57] can strongly affect the total effective SOI for valence-band spins.

In an experiment, the relevant spin–orbit parameters often emerge on a phenomenological level as an effective spin–orbit field that acts on the moving carriers. The manifestation of this field can be probed using several different approaches, the most common ones being dispersive gate sensing [58] and current measurements as a function of the orientation of an externally applied magnetic field [59–62]. Since such measurements are the most straightforward way to access the details of the effective spin–orbit field, it is essential to develop a thorough understanding of the connection between the experimentally accessible quantities and the underlying SOI.

In this paper, we focus on a double quantum dot tuned to the regime of Pauli spin blockade, where the most important effect of SOI is that it effectively allows for interdot tunneling accompanied by a spin rotation [63], which fundamentally changes the nature of the blockade. We theoretically investigate the leakage current through the system, focusing on its dependence on the details of the SOI. Building on the approach of Refs. [64, 65], which found expressions for the current in absence of SOI, we derive a general analytic expression for the leakage current including SOI. Based on this result we present a straightforward connection between the details of the emerging spin–orbit field and the dependence of the current on experimentally tunable parameters. We also discuss the role of the hyperfine interaction between the localized spins and randomly fluctuating nuclear spins of the host material, most relevant for devices based on III-V semiconductors. For the case of hole-based systems defined in a strongly confined two-dimensional hole gas we present an analytic expression that captures the combined effects on the leakage current of SOI and coupling to randomly polarized nuclear spin baths. Comparing this expression to an experimentally measured current could reveal details about both the effective nuclear fields on the dots and the spin–orbit field in the system.

The rest of the paper is organized as follows. In Sec. II we present our model Hamiltonian used to describe the double-dot system. In Sec. III we then derive an analytic expression for the leakage current as a function of arbitrarily oriented spin–orbit and Zeeman fields. Based on this expression we characterize special points in parameter space where the current vanishes. In Sec. IV we consider the collection of these stopping points and we present straightforward connections between clear features of the current (such as sharp minima) and the orientation and magnitude of the effective spin–orbit field in the system. In Sec. IV A we assume fully controllable Zeeman fields on the two dots and in Sec. IV B we assume a homogeneously applied field but allow for additional random nuclear fields on the dots, focusing on hole-spin systems with strong transverse confinement.

II. MODEL

The system we consider consists of two tunnel coupled quantum dots that both are connected to a lead, as illustrated in Fig. 1. We assume that the system is tuned close to the (1,1)–(0,2) charge transition, where (n, m) indicates a state with $n(m)$ excess charges on the left(right) dot, which can be either electrons or holes. Applying a voltage bias between the two leads can then induce a current to run through the double dot, say from the left to the right lead. Assuming a large on-site orbital level splitting (typically $\sim$ meV) compared to the applied bias voltage, states involving excited orbitals can be disregarded, and the Pauli exclusion principle then dictates that the two charges in the (0,2) configuration must be in a spin-singlet state, $|S_{02}\rangle$. In the (1,1) charge configuration all four spin states are accessible, three triplets $|T_{\pm,0}\rangle$ and one singlet $|S\rangle$. This can lead to a so-called spin blockade, where the system is stuck in one of the (1,1) triplet states, which cannot transition to $|S_{02}\rangle$.

We include two spin-mixing ingredients that can modify or lift this blockade. Firstly, each of the two dots experiences a Zeeman field, $\boldsymbol{B}_{L,R}$, which we allow to be different on the two dots. These effective magnetic fields can originate from an externally applied field, nearby on-chip micromagnets, or hyperfine interaction between the localized spins and the nuclear spins of the host material. Secondly, we also allow for strong spin–orbit coupling. This can result in spin flips during tunneling between the dots, but it can also renormalize the g-tensors on the two dots, potentially contributing to a difference in the effective Zeeman fields on the two dots.

Focusing on the five levels mentioned above, we describe the system with a simple model Hamiltonian,

$$H = H_e + H_t + H_B. \tag{1}$$

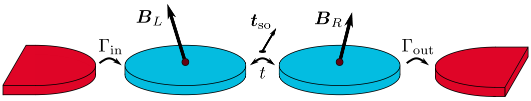

FIG. 1. Illustration of the two tunnel coupled quantum dots connected to two leads, showing the orientation of the different fields: The spin-orbit vector is assumed to be pointing along $\hat{z}$, whereas the Zeeman fields $E_{Z,i}$ and Overhauser fields K_i are arbitrary.

Here

$$H_e = -\delta|S_{02}\rangle\langle S_{02}| \tag{2}$$

accounts for the relative detuning δ of the four (1,1) states with respect to the (0,2) singlet. The interdot tunnel coupling is described by

$$H_t = t_s|S\rangle\langle S_{02}| + i\boldsymbol{t}_{\rm so}\cdot|\boldsymbol{T}\rangle\langle S_{02}| + \text{H.c.}, \tag{3}$$

where $|\boldsymbol{T}\rangle = \{|T_x\rangle, |T_y\rangle, |T_z\rangle\}$ is the vector of unpolarized triplet states along the three orthogonal coordinate axes [63]. The first term in H_t accounts for spin-conserving tunneling, whereas the second term parametrizes the effect of spin–orbit interaction on the interdot tunneling, effectively yielding spin-non-conserving tunneling terms. The magnitude and orientation of the vector $\boldsymbol{t}_{\rm so}$ depend on microscopic details of the spin–orbit interaction. Finally, due to the singlet nature of $|S_{02}\rangle$, magnetic fields only yield a Zeeman effect within the (1,1) subspace, which we describe by

$$H_B = \frac{1}{2}\left[(\boldsymbol{B}_L\cdot\boldsymbol{\sigma}_L)\otimes\mathbb{1}_R + \mathbb{1}_L\otimes(\boldsymbol{B}_R\cdot\boldsymbol{\sigma}_R)\right], \tag{4}$$

with $\boldsymbol{\sigma}_{L(R)}$ being the vector of Pauli matrices acting on the left(right) spin and $\boldsymbol{B}_{L(R)}$ being the total Zeeman field on the left(right) dot. These fields can contain a contribution from externally applied magnetic fields as well as the Overhauser fields that are due to hyperfine interaction with the spinful nuclei in each dot.

III. LEAKAGE CURRENT

The current through the double dot, and thus the degree of spin blockade, is governed by an interplay between the structure of the coupling Hamiltonian (3) and the degree of spin mixing within the (1,1) subspace due to the fields $\boldsymbol{B}_{L,R}$. Because of the resulting complexity it will be convenient to perform a basis transformation which makes the Hamiltonian take a simple form, from which the current can be calculated analytically.

The first step is to define the z-direction of our coordinate system to point along $\boldsymbol{t}_{\rm so}$. This rotates the coupling Hamiltonian into $H_t = t_s|S\rangle\langle S_{02}| + it_{\rm so}|T_0\rangle\langle S_{02}| + \text{H.c.}$, where $|T_0\rangle = \frac{1}{\sqrt{2}}[|{\uparrow\downarrow}\rangle + |{\downarrow\uparrow}\rangle]$ is the (usual) unpolarized spin triplet along $\hat{z}$ and $t_{\rm so}$ is the magnitude of the spin–orbit vector $\boldsymbol{t}_{\rm so}$. We then introduce a dimensionless parameter $\eta = \arctan\left[t_{\rm so}/t_s\right]$ that parameterizes the relative strength of the spin–orbit-induced tunnel coupling and apply a basis transformation to all (1,1) states

$$|\tilde{\psi}\rangle = e^{i\frac{\eta}{2}(\sigma_L^z - \sigma_R^z)}|\psi\rangle. \tag{5}$$

In this new basis we find that $|\tilde{S}\rangle = \cos\eta\,|S\rangle + i\sin\eta\,|T_0\rangle$ is a "bright" state that is coupled to $|S_{02}\rangle$ with strength $t \equiv \sqrt{t_s^2 + t_{\rm so}^2}$, and $|\tilde{T}_0\rangle = i\sin\eta\,|S\rangle + \cos\eta\,|T_0\rangle$ is a "dark" state that is not coupled; the polarized triplet states $|\tilde{T}_\pm\rangle = |T_\pm\rangle$ are unchanged by the transformation. Therefore, in the new basis only one (1,1) state is coupled to $|S_{02}\rangle$, the price to pay being that the transformed Zeeman Hamiltonian $e^{-i\frac{\eta}{2}(\sigma_L^z - \sigma_R^z)}H_B e^{i\frac{\eta}{2}(\sigma_L^z - \sigma_R^z)}$ acquired an η-dependence and now incorporates all spin–orbit effects included in our model. The transformation thus gauges away the spin–orbit interaction, yielding a Hamiltonian that can be mapped exactly to the case without spin–orbit coupling ($\boldsymbol{t}_{\rm so} = \boldsymbol{0}$), simply by redefining the two effective Zeeman fields. For the case without spin–orbit interaction steady-state expressions for the current have been derived before [64, 65] and one can thus apply a similar approach to include spin–orbit coupling.

We assume the system to be tuned to the open regime, where the couplings to the reservoirs, characterized by the tunneling rates $\Gamma_{\rm in,out}$ (see Fig. 1), are the largest relevant energy scales. This ensures that the sequential tunneling process $(0,2) \to (0,1) \to (1,1)$ is effectively instantaneous, and the interesting dynamics happen during the transition $(1,1) \to (0,2)$ which involves only the five levels we included in the Hamiltonian (1). An analytical expression for the current is then obtained by solving the steady-state Master equation (see App. A for more details). In the limit $\Gamma \gg \delta, t, B_{L,R}$ we find the relatively compact expression (setting $\hbar = 1$ from here on),

$$\frac{I}{e\Gamma_s} = \frac{|e^{2i\eta}B_R^- B_L^z - B_L^- B_R^z|^2 + {\rm Im}\{e^{2i\eta}B_R^- B_L^+\}^2}{\Gamma_s^2 Q_+^2\left[3 + \frac{16Q_+^2Q_-^2}{(B_L^2 - B_R^2)^2}\right] + B_L^2 B_R^2}, \tag{6}$$

where we used $B_{L,R} = |\boldsymbol{B}_{L,R}|$ and we introduced the rate $\Gamma_s \equiv t^2/\Gamma$, which sets the scale of the effective decay rate of the (1,1) states. We also introduced the notations $B^\pm = B^x \pm iB^y$ and

$$\begin{aligned} Q_\pm^2 = {} & {\rm Re}\{\tfrac{1}{2}e^{i\eta}(B_L^+ \pm B_R^-)\}^2 \\ & + {\rm Im}\{\tfrac{1}{2}e^{i\eta}(B_L^+ \mp B_R^-)\}^2 + \tfrac{1}{4}(B_L^z \pm B_R^z)^2. \end{aligned} \tag{7}$$

This expression thus describes the current through a double quantum dot in the spin-blockade regime, including the effect of spin–orbit coupling and two possibly different Zeeman fields on the two dots.

Eq. (6) is the most important analytic result of this work; it generalizes the result presented in Ref. [65], by including arbitrarily oriented non-spin-conserving interdot tunneling processes. The relative importance of these processes is described by the parameter $\eta = \arctan[t_{\rm so}/t_s]$, so that $e^{i\eta} = (t_s/t) + i(t_{\rm so}/t)$, and the direction of the vector $\boldsymbol{t}_{\rm so}$ is encoded in the choice of coordinate system, by defining the z-direction along $\boldsymbol{t}_{\rm so}$.

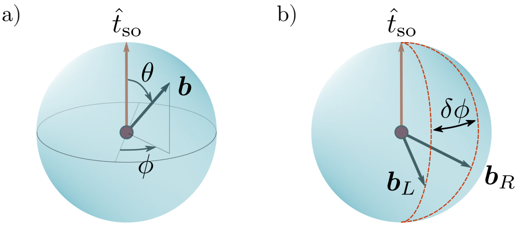

FIG. 2. (a) For two Zeeman fields with the same orientation $\boldsymbol{b} = \boldsymbol{B}/B$ but different magnitudes the current only vanishes when the two fields are oriented along the spin–orbit vector marked in red. (b) Tuning the Zeeman fields away from the spin–orbit vector, the current vanish along the red lines on the sphere where the relative orientation of the two Zeeman vectors $\boldsymbol{b}_{L,R}$ satisfy $\delta\phi = 2\eta$.

From Eq. (6) we can identify special configurations of $\boldsymbol{B}_{L,R}$ for which the current vanishes, so-called "stopping points" [64, 65]. We find four of such points: (i) The first arises when the magnitude of the two Zeeman fields is equal, $B_L = B_R$, making the term $16Q_+^2Q_-^2/(B_L^2 - B_R^2)^2$ in the denominator diverge. The blockade at this point can be understood from considering the (1,1) states in the basis of spin up and down along the local fields on the left and right dot. In this basis, the two states $|{\uparrow\downarrow}\rangle$ and $|{\downarrow\uparrow}\rangle$ are both eigenstates of H_B with zero total Zeeman energy. This means that they can be rearranged into a bright and a dark state (again in terms of coupling to $|S_{02}\rangle$) and the system will thus get blocked in the dark state. (ii) The three other points are obtained for field configurations where the numerator in Eq. (6) vanishes. One configuration for which this happens is when either of the two fields is zero, $B_{L,R} = 0$, resulting in two doubly degenerate subspaces which can again be rearranged in dark and bright states. (iii) The numerator also vanishes when both fields are parallel or antiparallel to the spin–orbit vector $\boldsymbol{t}_{\rm so}$, i.e., $B_{L,R}^\pm = 0$. In this case the two triplets $|T_\pm\rangle$ are eigenstates of H_B that are not coupled to $|S_{02}\rangle$, resulting in a blockade of the current. (iv) The last stopping point occurs when $e^{2i\eta} = B_L^- B_R^z / B_R^- B_L^z$. Writing the two fields in spherical coordinates $\{B, \theta, \phi\}$, where $\theta = 0$ corresponds to the z-direction (which is aligned with $\boldsymbol{t}_{\rm so}$), as illustrated in Fig. 2(a), we see that this condition corresponds to having $\phi_R - \phi_L = 2\eta$ if $\theta_L = \theta_R$ and $\phi_R - \phi_L = 2\eta + \pi$ if $\theta_L = \pi - \theta_R$. This configuration corresponds to the two fields having the same "latitude" but a relative azimuthal angle of $\delta\phi = 2\eta$, as illustrated in Fig. 2(b) (or one of the two fields can have an overall minus sign compared to this situation). This stopping point can be understood from considering the non-spin-conserving tunneling that underlies the coupling Hamiltonian (3): H_t can be interpreted as being a projection to our five-level basis of the general non-spin-conserving tunneling Hamiltonian

$$H_t = \frac{1}{\sqrt{2}} \hat{c}^\dagger_{L,\alpha} [t_s \mathbb{1} + i \boldsymbol{t}_{\rm so} \cdot \boldsymbol{\sigma}]_{\alpha\beta} \hat{c}_{R,\beta} + \text{H.c.}, \qquad (8)$$

where $\hat{c}^\dagger_{L(R),\sigma}$ is the creation operator of a charge with spin σ on the left(right) dot. With the z-axis oriented along $\boldsymbol{t}_{\rm so}$ we see that this tunneling Hamiltonian reduces to $H_t = \frac{1}{\sqrt{2}} \hat{c}^\dagger_{L,\alpha} [t \, e^{i\eta\sigma_z}]_{\alpha\beta} \hat{c}_{R,\beta}$ + H.c., which describes charge tunneling with amplitude t that is accompanied by a z-rotation of the spin over an angle of $\pm 2\eta$ (depending on the direction of tunneling). With this in mind we understand that the eigenstate of H_B where both spins are aligned with (or exactly opposite to) two local fields that have a relative azimuthal angle of 2η will evolve during the interdot tunneling into a fully polarized spin-1 state, which has no overlap with $|S_{02}\rangle$.

IV. EFFECTS OF SPIN–ORBIT COUPLING

A. Independently controllable Zeeman fields

The collection of stopping points provides a potentially useful tool for characterizing the spin–orbit interaction in a double-dot system, allowing to identify both the orientation and magnitude of the spin–orbit tunneling vector $\boldsymbol{t}_{\rm so}$. Assuming that one has full control over the two Zeeman fields on the dots, either through local control of the applied magnetic fields or, e.g., via local manipulation of the g-tensor, one can in principle map out all the stopping points discussed above.

If one makes sure that the two Zeeman fields are both non-zero and have different magnitudes, then only the last two stopping points will be probed. In this case, the orientation of the spin–orbit vector (up to a sign) can be identified from making the two Zeeman fields parallel to each other and finding the field orientation for which the current vanishes, i.e., by probing stopping point (iii) [66]. Knowing the orientation of the spin–orbit vector, its magnitude can then be found by identifying stopping points of type (iv): One tilts both fields away from $\boldsymbol{t}_{\rm so}$, in any direction, and then one rotates one of the fields along $\boldsymbol{t}_{\rm so}$ while measuring the leakage current. From the point where the current vanishes the parameter η, and thus the relative magnitude $t_{\rm so}/t_s$, follows via $\eta = (\phi_R - \phi_L)/2$, see Fig. 2(b). We note here that there is no requirement on the actual magnitude of the difference $|B_L - B_R|$: As long as the line shape of the resulting leakage current can be detected, the stopping points can be located. Also if the fields are equal in magnitude but there still is a sizable leakage current due to, e.g., spin relaxation processes, then the stopping points related to $\boldsymbol{t}_{\rm so}$ are still detectable by locating the minima of the current.

In the above we assumed accurate control over the two Zeeman fields $\boldsymbol{B}_{L,R}$ separately. In many systems, however, especially in devices based on III-V materials such as GaAs and InAs, but also in some Si- and Ge-based systems, atoms that carry finite nuclear spin yield small quasistatic, but random effective magnetic fields acting on the localized spins, sometimes of the order of a few mT when there is a significant fraction of spinful nuclei. This means that the total Zeeman fields $\boldsymbol{B}_{L,R} = \boldsymbol{B}^{\rm ext}_{L,R} + \boldsymbol{K}_{L,R}$ are the sum of the externally applied fields $\boldsymbol{B}^{\rm ext}_{L,R}$ and random components $\boldsymbol{K}_{L,R}$ that cannot be controlled.

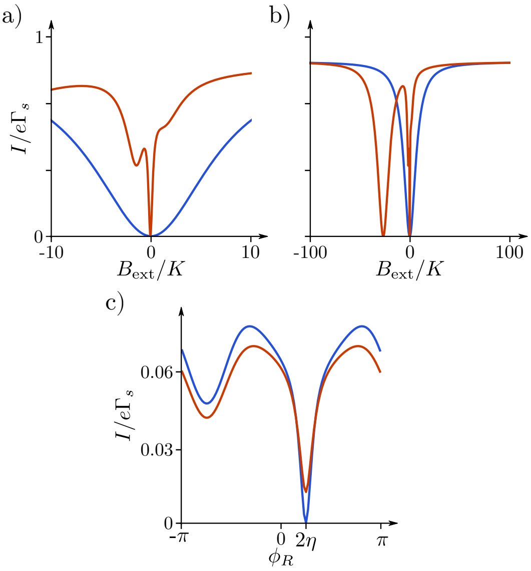

FIG. 3. (a,b) Calculated current as a function of the magnitude of a uniformly applied external field $B_{\rm ext}$, assuming two different g-tensors on the two dots. In this plot we used $\boldsymbol{B}_L = \{0.76, 0.32, 0.34\} B_{\rm ext}$ and $\boldsymbol{B}_R = \{1, 0, 0\} B_{\rm ext}$ with $\Gamma_s = 0.1$ μeV. The blue lines show the case with no nuclear spins present, and the red lines show how adding two small random nuclear fields $\boldsymbol{K}_{L,R}$, drawn from a normal distribution with an r.m.s. value of 0.1 μeV, drastically changes the behaviour of the current at small fields. (c) Current as a function of ϕ_R with $B_L = 0.9$, $B_R = 1$, $\theta_L = \theta_R = 3\pi/8$, and $\phi_L = 0$. In the absence of nuclear fields (blue line) the current vanishes when the relative azimuthal angle $\delta\phi$ of two fields of different magnitude is equal to 2η. Averaging the current over random nuclear fields (red line) with the same distribution as used in (a,b), the current still has its minimum at $\delta\phi = 2\eta$.

However, since only the direction of the two total Zeeman fields matters for the procedure described above, the effect of the random contribution from the nuclear fields can be suppressed simply by working in the large-field limit $B^{\rm ext}_{L,R} \gg K$, where K is the typical magnitude of the nuclear fields on the dots; residual details depending on the specific configuration of $\boldsymbol{K}_{L,R}$ will average out in a typical experiment, where the total measurement time exceeds the correlation time of the nuclear fields.

We illustrate this in Fig. 3. First, in Fig. 3(a,b) we exemplify the effect of one single static configuration of $\boldsymbol{K}_{L,R}$ on the leakage current: The blue lines show the current as given by Eq. (6), as a function of a uniformly applied magnetic field $B_{\rm ext}$, in the absence of nuclear fields but assuming different g-tensors on the two dots (see the caption for the details). For the red lines we added two randomly oriented nuclear fields with magnitudes drawn from a normal distribution with $\langle K_{L,R}^2\rangle^{1/2} \equiv K = 0.1$ μeV. We see that the difference is substantial at small fields, but vanishes at larger applied field. In Fig. 3(c) we assume two external fields with $B_L = 0.9$, $B_R = 1$ and $\theta_L = \theta_R = 3\pi/8$, looking for the current minimum as a function of their relative angle $\delta\phi$, in the absence of nuclear fields (blue line) and after averaging over many (finite) nuclear field configurations (red line). Fig. 3(c) confirms that the averaging removes all sharp features, allowing again to locate the minimum in the current that is related to spin–orbit coupling, in the same way as in the case without nuclear fields.

B. Homogeneous external field:
Hole-spin qubits with strong transverse confinement

Finally, we turn our attention to the more common situation where one can only control a homogeneous external field, yielding more or less equal Zeeman fields on the two dots. Since the situation with $B_L = B_R$ corresponds to one of the stopping configurations discussed above, in this case finite nuclear fields are in fact required for obtaining a finite leakage current (in the absence of other spin relaxation processes). Eq. (6) thus has to be averaged over the random fields $\boldsymbol{K}_{L,R}$ to find the leakage current that would be measured in a typical experiment, which is in general hard to do analytically.

One case, however, that can be treated analytically is potentially relevant for hole-based transport in quantum dots hosted in a quasi-two-dimensional carrier gas. The valence band of most semiconductors is of p-type, which adds another threefold orbital angular momentum degree of freedom to the hole states. Spin–orbit coupling splits off the states with total (orbital and spin) angular momentum $J = \frac{1}{2}$, leaving a four-dimensional $J = \frac{3}{2}$ low-energy subspace. Out-of-plane confinement, used to create a two-dimensional hole gas, results in further splitting inside this subspace, lowering the energy of the so-called heavy holes (HHs) with $J_z = \pm\frac{3}{2}$ relative to the light holes (LHs) with $J_z = \pm\frac{1}{2}$. For strong confinement this HH–LH splitting can become significant, in which case the low-energy confined states on the dots will mostly have a HH character. Due to the $\pm\frac{3}{2}$ angular momentum carried by the two basis states, these states are to lowest order not expected to be coupled directly by the in-plane angular momentum operators $J^{\pm}$. This is the reason why in the absence of significant HH–LH mixing most spin-dependent phenomena are usually highly anisotropic in the HH subspace: The in-plane g-factor can be up to an order of magnitude smaller than the out-of-plane one [35–38, 41–43, 45, 46], hyperfine interaction with the residual nuclear spins could become effectively almost purely Ising-like [67–70] (although some experiments suggest that a significant d-shell state admixture can result in a much less anisotropic coupling than naively expected [71, 72]), and also spin–orbit coupling inside the HH subspace will in general be more efficient along J^z.

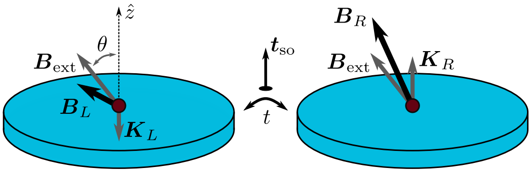

FIG. 4. Illustration of the orientation of the fields used for the analytical derivation in Sec. IV B: The spin-orbit vector $\boldsymbol{t}_{\rm so}$ and both nuclear fields $\boldsymbol{K}_{L,R}$ are assumed to be pointing along $\hat{z}$. The external Zeeman field $\boldsymbol{B}_{\rm ext}$ is equal on the two dots, but can point in any direction.

In this highly anisotropic limit we can thus assume that (i) the two nuclear fields are purely out-of-plane and (ii) the spin–orbit vector $\boldsymbol{t}_{\rm so}$ is also most likely to be out-of-plane. In that case, the current (6) becomes a function of the fields $\boldsymbol{B}_{L,R} = \boldsymbol{B}_{\rm ext} + K_{L,R}^z\hat{z}$, as illustrated in Fig. 4. The experimentally measured current then follows from averaging Eq. (6) over $K_{L,R}^z$,

$$\mathcal{I}_{\rm av} = \int dK_L^z dK_R^z \, \frac{e^{-[(K_L^z)^2+(K_R^z)^2]/2K^2}}{4\pi K^2} \, I(\boldsymbol{B}_L, \boldsymbol{B}_R), \quad (9)$$

where we have assumed the nuclear-field distributions to be Gaussian with mean zero and variance K^2. Signatures of the hyperfine interaction that survive this averaging are again expected to be most prominent at small fields, where $B_{\rm ext} \lesssim K$. We will thus focus on the small-field limit, $\Gamma_s \gg K, B_{\rm ext}$, where we find the approximate analytic result

$$\begin{aligned}\frac{\mathcal{I}_{\rm av}\Gamma_s}{eK^2} &= 2f\left(\alpha + ib^z\right)\left\{1 + 6f\left(\tfrac{1}{2}\beta\right)\beta^2\right\} \\ &\quad - f\left(\tfrac{1}{2}\alpha + ib^z\right)\left\{2 + 3f\left(\tfrac{1}{2}\beta\right)\beta^2\right\}, \end{aligned} \quad (10)$$

where we have used the function

$$f(x) = \frac{\sqrt{\pi}}{3}\,{\rm Re}\left\{x\right\}{\rm Re}\left\{e^{x^2}{\rm erfc}\left(x\right)\right\} - \frac{1}{3}, \quad (11)$$

with erfc(x) being the complementary error function. Furthermore, we introduced $\alpha = b^{\parallel}\cos\eta$ and $\beta = b^{\parallel}\sin\eta$ where $b^z = B_{\rm ext}^z/K$ and $b^{\parallel} = \sqrt{(B_{\rm ext}^x)^2 + (B_{\rm ext}^y)^2}/K$ give the out-of-plane and in-plane component of the external Zeeman field, respectively, in units of K.

In Fig. 5 we plot the current given by Eq. (10) as a function of the magnitude of the external magnetic field, for different orientations of the field and different strengths of spin–orbit coupling. The four plots (a–d) show the

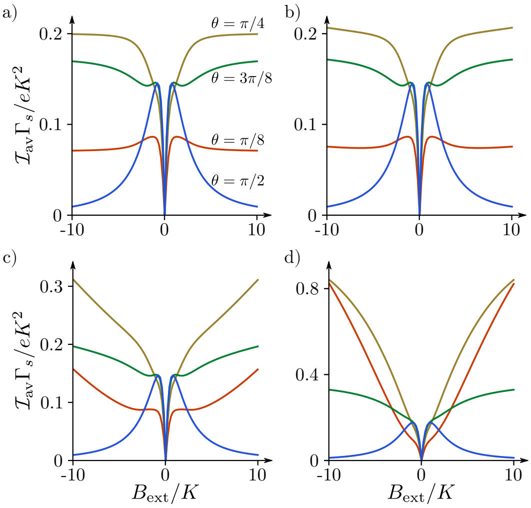

FIG. 5. The current as given by Eq. (10), as a function of the magnitude of the applied field $\boldsymbol{B}_{\rm ext}$. The four plots have an increasing magnitude of spin–orbit interaction: (a) $\eta = 0$, (b) $\eta = 0.02$, (c) $\eta = 0.1$ and (d) $\eta = 0.5$. In each plot the four traces correspond to four different orientations of the applied field, the corresponding polar angles of $\boldsymbol{B}_{\rm ext}$ are indicated in (a) (same colors represent same orientations in all plots).

current for different magnitudes of spin–orbit coupling ($\eta = 0$, $\eta = 0.02$, $\eta = 0.1$ and $\eta = 0.5$, respectively) and each plot contains four traces that assume a different orientation of $\boldsymbol{B}_{\rm ext}$, the angle θ being the polar angle of the applied field (see Fig. 4). In all plots we used the parameters $\Gamma_s = 15$ μeV and $K = 0.1$ μeV.

For all values of η the current vanishes when the Zeeman field points along $\hat{z}$ (i.e., is parallel to $\boldsymbol{K}_{L,R}$ and $\boldsymbol{t}_{\rm so}$) and at the point where $B_{\rm ext} = 0$, both of which are cases of the third stopping point mentioned above.

The spin–orbit-free case $\eta = 0$ is shown in Fig. 5(a). For most orientations of $\boldsymbol{B}_{\rm ext}$, but most prominently for an in-plane field, we observe a peak in the current around zero field, with a width $\sim K$, that is split into a double peak by the stopping point at $B_{\rm ext} = 0$. For large fields the current converges towards a direction-dependent limiting value $\mathcal{I}_{\rm av}^{\infty} \approx 2(e/\Gamma_s)K^2 \sin^2\theta/(4 + \tan^2\theta)$. This large-field current vanishes for $\theta = 0$ (see above), but also for $\theta = \pi/2$, where the nuclear fields do not affect the magnitude of the total fields to leading order, resulting effectively in a blockade due to stopping point (i).

As illustrated in Fig. 5(b–d), adding a finite spin–orbit coupling changes the current profiles: On top of the narrow current peaks caused by the nuclear fields, we observe in most cases the characteristic spin–orbit-induced low-field current dip, the shape and width of which depend on η and the direction of the applied field. The large-field limiting current is typically larger than in the case of $\eta = 0$, due to the efficient spin–orbit-induced spin mixing, which becomes more effective at larger fields.

Comparing Eq. 10 with the experimentally measured low-field leakage current could thus give insight in the typical magnitude of the effective nuclear fields in the system as well as the total strength of the effective spin–orbit field, for the case of hole-based transport in systems with strong transverse confinement. We note here that features similar to some observed in Fig. 5 (such as a low-field split peak on the background of a wider zero-field dip in the current) are indeed sometimes observed in such systems [60, 61].

V. CONCLUSION

Spin–orbit interaction is an important ingredient in low-dimensional semiconductor and hybrid structures, and understanding the detailed manifestation of the interaction is therefore essential. One of the mechanisms that couples the spin dynamics of localized carriers to the more easily detectable charge dynamics is the Pauli spin blockade that can occur in multi-quantum-dot structures.

In this paper we investigated in detail how the leakage current of a double quantum dot in spin blockade is affected by spin–orbit interaction. The main effect of spin–orbit interaction in such a situation is that it yields effectively a non-spin-conserving interdot tunnel coupling. Using a simple few-level model Hamiltonian to describe the coupled spin-charge dynamics in the system, we derived a relatively compact analytic expression describing the leakage current through the blockade, including the detailed effect of the spin–orbit coupling. From this result we could identify different so-called stopping points, for which the current vanishes, which allowed us to connect qualitative features in the current to both the magnitude and orientation of the effective spin–orbit field acting on the tunneling carriers. This connection could thus provide a tool for characterizing the relevant spin–orbit parameters in multi-quantum-dot devices.

We then investigated the leakage current in more detail in the presence of randomly fluctuating nuclear spin baths that can couple to the localized carriers. For the case of hole spins in a strongly confined two-dimensional hole gas, we derived an analytic expression for the low-field leakage current that includes averaging over the random effective nuclear field configurations on the two dots. Comparing these results with the experimentally measured leakage current at small fields could provide additional information about the details of both the hyperfine and spin–orbit coupling in a system.

ACKNOWLEDGMENTS

This work is part of FRIPRO-Project No. 274853, which is funded by the Research Council of Norway

(RCN), and was also partly supported by the Centers of Excellence funding scheme of the RCN, Project No. 262633, QuSpin.

Appendix A: Derivation of the current

We write the Hamiltonian (1) in the rotated basis $|\tilde{\psi}\rangle = e^{i\frac{\eta}{2}(\sigma_L^z - \sigma_R^z)}|\psi\rangle$ of one bright and three dark states, as explained in the main text. Then, we introduce the (anti)symmetric magnetic fields $\boldsymbol{B}_\pm = \frac{1}{2}(\boldsymbol{B}_L \pm \boldsymbol{B}_R)$ and we define the auxiliary fields $\boldsymbol{E}_\pm = \{B^x_\pm \cos\eta - B^y_\mp \sin\eta, B^y_\pm \cos\eta + B^x_\mp \sin\eta, B^z_\pm\}$ that incorporate the η-dependence of the Zeeman Hamiltonian. In terms of these new fields, we can write the Zeeman terms as

$$
\begin{aligned}
H_B = \frac{1}{\sqrt{2}} \sum_\pm \Big[&(E^x_+ \pm i E^y_+)|\tilde{T}_0\rangle\langle\tilde{T}_\pm| \\
&+ (\mp E^x_- - i E^y_-)|\tilde{S}\rangle\langle\tilde{T}_\pm| + \text{H.c.}\Big] \\
&+ E^z_+\{|\tilde{T}_+\rangle\langle\tilde{T}_+| - |\tilde{T}_-\rangle\langle\tilde{T}_-|\} \\
&+ E^z_-\{|\tilde{S}\rangle\langle\tilde{T}_0| + |\tilde{T}_0\rangle\langle\tilde{S}|\},
\end{aligned}
\tag{A1}
$$

which has exactly the same form as the usual (1,1) Zeeman Hamiltonian (4) when written in a singlet-triplet basis [64], under the substitution $\boldsymbol{B}_\pm \to \boldsymbol{E}_\pm$.

The 3×3 block of the Hamiltonian governing the subspace $\{|\tilde{T}_+\rangle, |\tilde{T}_0\rangle, |\tilde{T}_-\rangle\}$ thus describes a spin-1 system coupled to the spin–orbit-rotated effective field $\boldsymbol{E}_+$. Applying the appropriate spin-1 rotation $\exp(i\alpha \boldsymbol{J}\cdot\hat{\boldsymbol{n}})$ (where $\boldsymbol{J}$ is the vector of spin-1 matrices and $\hat{\boldsymbol{n}}$ is the unit vector of rotation), we can diagonalize this block such that the full five-level Hamiltonian becomes

$$
H = \begin{pmatrix}
E_+ & 0 & 0 & c & 0 \\
0 & 0 & 0 & -d & 0 \\
0 & 0 & -E_+ & -c & 0 \\
c & -d & -c & 0 & t \\
0 & 0 & 0 & t & -\delta
\end{pmatrix},
\tag{A2}
$$

where $t = \sqrt{t_s^2 + t_{\text{so}}^2}$, and the (real) couplings between the triplets and the bright state $|\tilde{S}\rangle$ read

$$
\begin{aligned}
c = \frac{E_-}{\sqrt{2}} \Big\{ &[\cos\theta_+ \sin\theta_- \cos(\phi_+ - \phi_-) - \cos\theta_- \sin\theta_+]^2 \\
&+ \sin^2\theta_- \sin^2(\phi_+ - \phi_-) \Big\}^{1/2},
\end{aligned}
\tag{A3}
$$

$$
d = E_- \left[\cos\theta_- \cos\theta_+ + \sin\theta_- \sin\theta_+ \cos(\phi_+ - \phi_-)\right],
\tag{A4}
$$

with

$$
\theta_\pm = \arccos\left[\frac{E^z_\pm}{E_\pm}\right], \qquad \phi_\pm = \arg\left[E^x_\pm + iE^y_\pm\right],
\tag{A5}
$$

being the angles that define the orientation of the fields $\boldsymbol{E}_\pm$. Having the Hamiltonian on this form is advantageous when calculating the current since it reduces the number of independent parameters from eight to five.

To obtain an analytical expression for the current through the system we then solve the master equation in steady state

$$
\frac{\partial\hat{\rho}}{\partial t} = -i[H, \hat{\rho}] + \boldsymbol{\Gamma}(\hat{\rho}) = 0,
\tag{A6}
$$

where $\hat{\rho}$ is the five-level density matrix and $\boldsymbol{\Gamma}(\hat{\rho}) = -\frac{1}{2}\Gamma\{\hat{P}_{02}, \hat{\rho}\} + \frac{1}{4}\Gamma(\mathbb{1} - \hat{P}_{02})\hat{\rho}_{02,02}$ the superoperator describing the fast tunneling processes to and from the reservoirs. Here, Γ is the characteristic rate of decay of $|S_{02}\rangle$ and subsequent reloading of one of the (1,1) states, and $\hat{P}_{02} = |S_{02}\rangle\langle S_{02}|$ is the projector onto the state $|S_{02}\rangle$. After solving Eq. (A6) for the steady-state density matrix $\hat{\rho}^{\text{ss}}$, the current through the double dot can be calculated from the expression $I = e\Gamma\hat{\rho}^{\text{ss}}_{02,02}$, giving

$$
\begin{aligned}
\frac{8e\Gamma t^2 c^2 d^2 E_+^2}{I} = {}& 4c^4 d^2(4E_+^2 + \Gamma^2 + 4\delta^2) \\
&+ d^2[4E_+^6 + 4E_+^2 t^4 + d^4(4E_+^2 + \Gamma^2 + 4\delta^2) - 2d^2 E_+^2(4E_+^2 - 4t^2 + \Gamma^2 + 4\delta^2)] \\
&+ 2c^2[E_+^2 t^4 + 2d^4(4E_+^2 + \Gamma^2 + 4\delta^2) + 2d^2 E_+^2(4E_+^2 + 2t^2 + \Gamma^2 + 4\delta^2)].
\end{aligned}
\tag{A7}
$$

Eq. (6) in the main text then follows from assuming that we are in the strong-coupling regime, where $\Gamma \gg \delta, B_\pm$, and introducing the rate $\Gamma_s \equiv t^2/\Gamma$, which sets the scale of the effective decay of the (1,1) states.

[1] J. D. Sau, R. M. Lutchyn, S. Tewari, and S. Das Sarma, Phys. Rev. Lett. **104**, 040502 (2010).

[2] R. M. Lutchyn, J. D. Sau, and S. Das Sarma, Phys. Rev.

Lett. **105**, 077001 (2010).
[3] Y. Oreg, G. Refael, and F. von Oppen, Phys. Rev. Lett. **105**, 177002 (2010).
[4] M. Leijnse and K. Flensberg, Semicond. Science and Techn. **27**, 124003 (2012).
[5] C. Beenakker, Ann. Rev.of Cond. Matt. Phys. **4**, 113 (2013).
[6] R. M. Lutchyn, E. P. A. M. Bakkers, L. P. Kouwenhoven, P. Krogstrup, C. M. Marcus, and Y. Oreg, Nat. Rev. Mater. **3**, 52 (2018).
[7] A. Y. Kitaev, Ann. Phys. **303**, 2 (2003).
[8] C. Nayak, S. H. Simon, A. Stern, M. Freedman, and S. Das Sarma, Rev. Mod. Phys. **80**, 1083 (2008).
[9] S. Das Sarma, M. Freedman, and C. Nayak, npj Quant. Inf. **1**, 1 (2015).
[10] T. D. Stanescu, *Introduction to Topological Quantum Matter & Quantum Computation* (CRC Press, 2016).
[11] K. D. Petersson, L. W. McFaul, M. D. Schroer, M. Jung, J. M. Taylor, A. A. Houck, and J. R. Petta, Nature **490**, 380 (2012).
[12] N. Samkharadze, G. Zheng, N. Kalhor, D. Brousse, A. Sammak, U. C. Mendes, A. Blais, G. Scappucci, and L. M. K. Vandersypen, Science **359**, 1123 (2018).
[13] G. Burkard, M. J. Gullans, X. Mi, and J. R. Petta, Nat. Rev. Phys. **2**, 129 (2020).
[14] E. I. Rashba and Al. L. Efros, Phys. Rev. Lett. **91**, 126405 (2003).
[15] I. Žutić, J. Fabian, and S. Das Sarma, Rev. Mod. Phys. **76**, 323 (2004).
[16] S. Nadj-Perge, S. M. Frolov, E. P. A. M. Bakkers, and L. P. Kouwenhoven, Nature **468**, 1084 (2010).
[17] D. Loss and D. P. DiVincenzo, Phys. Rev. A **57**, 120 (1998).
[18] R. Hanson, L. P. Kouwenhoven, J. R. Petta, S. Tarucha, and L. M. K. Vandersypen, Rev. Mod. Phys. **79**, 1217 (2007).
[19] C. Kloeffel and D. Loss, Annu. Rev. Condens. Matter Phys. **4**, 51 (2013).
[20] A. Chatterjee, P. Stevenson, S. De Franceschi, A. Morello, N. P. de Leon, and F. Kuemmeth, Nat. Rev. Phys. **3**, 157 (2021).
[21] G. Burkard, T. D. Ladd, J. M. Nichol, A. Pan, and J. R. Petta, arXiv:2112.08863 (2021).
[22] V. N. Golovach, M. Borhani, and D. Loss, Phys. Rev. B **74**, 165319 (2006).
[23] C. Flindt, A. S. Sørensen, and K. Flensberg, Phys. Rev. Lett. **97**, 240501 (2006).
[24] A. V. Khaetskii and Y. V. Nazarov, Phys. Rev. B **61**, 12639 (2000).
[25] A. V. Khaetskii and Y. V. Nazarov, Phys. Rev. B **64**, 125316 (2001).
[26] V. N. Golovach, A. Khaetskii, and D. Loss, Phys. Rev. Lett. **93**, 016601 (2004).
[27] R. Maurand, X. Jehl, D. Kotekar-Patil, A. Corna, H. Bohuslavskyi, R. Laviéville, L. Hutin, S. Barraud, M. Vinet, M. Sanquer, and S. De Franceschi, Nat. Comm. **7**, 13575 (2016).
[28] H. Watzinger, J. Kukučka, L. Vukušić, F. Gao, T. Wang, F. Schäffler, J.-J. Zhang, and G. Katsaros, Nat. Comm. **9**, 3902 (2018).
[29] L. Vukušić, J. Kukučka, H. Watzinger, J. M. Milem, F. Schäffler, and G. Katsaros, Nano Lett. **18**, 7141 (2018).
[30] A. Crippa, R. Ezzouch, A. Aprá, A. Amisse, R. Laviéville, L. Hutin, B. Bertrand, M. Vinet, M. Urdampilleta, T. Meunier, M. Sanquer, X. Jehl, R. Maurand, and S. De Franceschi, Nat. Comm. **10**, 2776 (2019).
[31] G. Scappucci, C. Kloeffel, F. A. Zwanenburg, D. Loss, M. Myronov, J.-J. Zhang, S. D. Franceschi, G. Katsaros, and M. Veldhorst, Nat. Rev. Mat. **6**, 926 (2020).
[32] D. Jirovec, A. Hofmann, A. Ballabio, P. M. Mutter, G. Tavani, M. Botifoll, A. Crippa, J. Kukucka, O. Sagi, F. Martins, J. Saez-Mollejo, I. Prieto, M. Borovkov, J. Arbiol, D. Chrastina, G. Isella, and G. Katsaros, Nat. Mat. **20**, 1106 (2021).
[33] W. I. L. Lawrie, M. Russ, F. van Riggelen, N. W. Hendrickx, S. L. de Snoo, A. Sammak, G. Scappucci, and M. Veldhorst, arXiv:2109.07837 (2021).
[34] N. W. Hendrickx, W. I. L. Lawrie, M. Russ, F. van Riggelen, S. L. de Snoo, R. N. Schouten, A. Sammak, G. Scappucci, and M. Veldhorst, Nature **591**, 580 (2021).
[35] H. Watzinger, C. Kloeffel, L. Vukušić, M. D. Rossell, V. Sessi, J. Kukučka, R. Kirchschlager, E. Lausecker, A. Truhlar, M. Glaser, A. Rastelli, A. Fuhrer, D. Loss, and G. Katsaros, Nano Lett. **16**, 6879 (2016).
[36] M. Brauns, J. Ridderbos, A. Li, E. P. A. M. Bakkers, and F. A. Zwanenburg, Phys. Rev. B **93**, 121408(R) (2016).
[37] A. Bogan, S. A. Studenikin, M. Korkusinski, G. C. Aers, L. Gaudreau, P. Zawadzki, A. S. Sachrajda, L. A. Tracy, J. L. Reno, and T. W. Hargett, Phys. Rev. Lett. **118**, 167701 (2017).
[38] T. M. Lu, C. T. Harris, S.-H. Huang, Y. Chuang, J.-Y. Li, and C. W. Liu, Appl. Phys. Lett. **111**, 102108 (2017).
[39] A. Crippa, R. Maurand, L. Bourdet, D. Kotekar-Patil, A. Amisse, X. Jehl, M. Sanquer, R. Laviéville, H. Bohuslavskyi, L. Hutin, S. Barraud, M. Vinet, Y.-M. Niquet, and S. De Franceschi, Phys. Rev. Lett. **120**, 137702 (2018).
[40] E. Marcellina, A. Srinivasan, D. S. Miserev, A. F. Croxall, D. A. Ritchie, I. Farrer, O. P. Sushkov, D. Culcer, and A. R. Hamilton, Phys. Rev. Lett. **121**, 077701 (2018).
[41] C. Gradl, R. Winkler, M. Kempf, J. Holler, D. Schuh, D. Bougeard, A. Hernández-Mínguez, K. Biermann, P. V. Santos, C. Schüller, and T. Korn, Phys. Rev. X **8**, 021068 (2018).
[42] A. Hofmann, D. Jirovec, M. Borovkov, I. Prieto, A. Ballabio, J. Frigerio, D. Chrastina, G. Isella, and G. Katsaros, arXiv:1910.05841 (2019).
[43] A. J. Miller, M. Brickson, W. J. Hardy, C.-Y. Liu, J.-Y. Li, A. Baczewski, M. P. Lilly, T.-M. Lu, and D. R. Luhman, arXiv:2102.01758 (2021).
[44] F. N. M. Froning, M. J. Rančić, B. Hetényi, S. Bosco, M. K. Rehmann, A. Li, E. P. A. M. Bakkers, F. A. Zwanenburg, D. Loss, D. M. Zumbühl, and F. R. Braakman, Phys. Rev. Research **3**, 013081 (2021).
[45] S. D. Liles, F. Martins, D. S. Miserev, A. A. Kiselev, I. D. Thorvaldson, M. J. Rendell, I. K. Jin, F. E. Hudson, M. Veldhorst, K. M. Itoh, O. P. Sushkov, T. D. Ladd, A. S. Dzurak, and A. R. Hamilton, Phys. Rev. B **104**, 235303 (2021).
[46] J. H. Qvist and J. Danon, Phys. Rev. B **105**, 075303 (2022).
[47] N. Ares, G. Katsaros, V. N. Golovach, J. J. Zhang, A. Prager, L. I. Glazman, O. G. Schmidt, and S. De Franceschi, Appl. Phys. Lett. **103**, 263113 (2013).
[48] C. Kloeffel, M. Trif, and D. Loss, Phys. Rev. B **84**, 195314 (2011).
[49] C. Kloeffel, M. J. Rančić, and D. Loss, Phys. Rev. B **97**,

235422 (2018).

[50] S. Bosco, M. Benito, C. Adelsberger, and D. Loss, Phys. Rev. B **104**, 115425 (2021).

[51] S. Bosco, B. Hetényi, and D. Loss, PRX Quantum **2**, 010348 (2021).

[52] F. N. M. Froning, L. C. Camenzind, O. A. H. v. d. Molen, A. Li, E. P. A. M. Bakkers, D. M. Zumbühl, and F. R. Braakman, Nat. Nanotech. **16**, 308 (2021).

[53] Z. Wang, E. Marcellina, A. R. Hamilton, J. H. Cullen, S. Rogge, J. Salfi, and D. Culcer, npj Quant. Inf. **7**, 54 (2021).

[54] R. Winkler, *Spin–Orbit Coupling Effects in Two-Dimensional Electron and Hole Systems* (Springer Berlin Heidelberg, 2003).

[55] E. Marcellina, A. R. Hamilton, R. Winkler, and D. Culcer, Phys. Rev. B **95**, 075305 (2017).

[56] P. Philippopoulos, S. Chesi, D. Culcer, and W. A. Coish, Phys. Rev. B **102**, 075310 (2020).

[57] L. A. Terrazos, E. Marcellina, Z. Wang, S. N. Coppersmith, M. Friesen, A. R. Hamilton, X. Hu, B. Koiller, A. L. Saraiva, D. Culcer, and R. B. Capaz, Phys. Rev. B **103**, 125201 (2021).

[58] L. Han, M. Chan, D. de Jong, C. Prosko, G. Badawy, S. Gazibegovic, E. P. A. M. Bakkers, L. P. Kouwenhoven, F. K. Malinowski, and W. Pfaff, arXiv:2203.06047 (2022).

[59] D. Q. Wang, O. Klochan, J.-T. Hung, D. Culcer, I. Farrer, D. A. Ritchie, and A. R. Hamilton, Nano Lett. **16**, 7685 (2016).

[60] J.-Y. Wang, G.-Y. Huang, S. Huang, J. Xue, D. Pan, J. Zhao, and H. Xu, Nano Lett. **18**, 4741 (2018).

[61] M. Marx, J. Yoneda, Á. G. Rubio, P. Stano, T. Otsuka, K. Takeda, S. Li, Y. Yamaoka, T. Nakajima, A. Noiri, D. Loss, T. Kodera, and S. Tarucha, arXiv:2003.07079 (2020).

[62] A. Sala and J. Danon, Phys. Rev. B **104**, 085421 (2021).

[63] J. Danon and Y. V. Nazarov, Phys. Rev. B **80**, 041301 (2009).

[64] O. N. Jouravlev and Y. V. Nazarov, Phys. Rev. Lett. **96**, 176804 (2006).

[65] J. Danon, X. Wang, and A. Manchon, Phys. Rev. Lett. **111**, 066802 (2013).

[66] The current also vanishes for $\theta = \pi/2$ and $\eta = \pi/2$, where the couplings between $|S_{02}\rangle$ and $\{|\uparrow\downarrow\rangle, |\downarrow\uparrow\rangle\}$ (in the eigenbasis of the local fields) are zero. However, the case $\eta = \pi/2$ corresponds to the extreme case where $t_{\rm so} = t$ and $t_s = 0$, which we will ignore here.

[67] J. Fischer, W. A. Coish, D. V. Bulaev, and D. Loss, Phys. Rev. B **78**, 155329 (2008).

[68] C. Testelin, F. Bernardot, B. Eble, and M. Chamarro, Phys. Rev. B **79**, 195440 (2009).

[69] J. H. Prechtel, A. V. Kuhlmann, J. Houel, A. Ludwig, S. R. Valentin, A. D. Wieck, and R. J. Warburton, Nat. Mat. **15**, 981 (2016).

[70] S. Bosco and D. Loss, Phys. Rev. Lett. **127**, 190501 (2021).

[71] E. A. Chekhovich, M. M. Glazov, A. B. Krysa, M. Hopkinson, P. Senellart, A. Lemaître, M. S. Skolnick, and A. I. Tartakovskii, Nat. Phys. **9**, 74 (2013).

[72] P. Machnikowski, K. Gawarecki, and L. Cywiński, Phys. Rev. B **100**, 085305 (2019).

This document was typeset using the typographical look-and-feel `classicthesis` developed by André Miede and Ivo Pletikosić. The style was inspired by Robert Bringhurst's seminal book on typography *"The Elements of Typographic Style"*. `classicthesis` is available for both LaTeX and LyX:

`https://bitbucket.org/amiede/classicthesis/`

ISBN 978-82-326-6300-2 (printed ver.)
ISBN 978-82-326-6443-6 (electronic ver.)
ISSN 1503-8181 (printed ver.)
ISSN 2703-8084 (online ver.)

NTNU
Norwegian University of
Science and Technology